

NASA/TM-2005-213545



Trailing Edge Blowing on a Two-Dimensional Six-Percent Thick Elliptical Circulation Control Airfoil Up to Transonic Conditions

*Michael G. Alexander, Scott G. Anders, Stuart K. Johnson,
Jennifer P. Florance, and Donald F. Keller
Langley Research Center, Hampton, Virginia*

March 2005

The NASA STI Program Office . . . in Profile

Since its founding, NASA has been dedicated to the advancement of aeronautics and space science. The NASA Scientific and Technical Information (STI) Program Office plays a key part in helping NASA maintain this important role.

The NASA STI Program Office is operated by Langley Research Center, the lead center for NASA's scientific and technical information. The NASA STI Program Office provides access to the NASA STI Database, the largest collection of aeronautical and space science STI in the world. The Program Office is also NASA's institutional mechanism for disseminating the results of its research and development activities. These results are published by NASA in the NASA STI Report Series, which includes the following report types:

- **TECHNICAL PUBLICATION.** Reports of completed research or a major significant phase of research that present the results of NASA programs and include extensive data or theoretical analysis. Includes compilations of significant scientific and technical data and information deemed to be of continuing reference value. NASA counterpart of peer-reviewed formal professional papers, but having less stringent limitations on manuscript length and extent of graphic presentations.
- **TECHNICAL MEMORANDUM.** Scientific and technical findings that are preliminary or of specialized interest, e.g., quick release reports, working papers, and bibliographies that contain minimal annotation. Does not contain extensive analysis.
- **CONTRACTOR REPORT.** Scientific and technical findings by NASA-sponsored contractors and grantees.

- **CONFERENCE PUBLICATION.** Collected papers from scientific and technical conferences, symposia, seminars, or other meetings sponsored or co-sponsored by NASA.
- **SPECIAL PUBLICATION.** Scientific, technical, or historical information from NASA programs, projects, and missions, often concerned with subjects having substantial public interest.
- **TECHNICAL TRANSLATION.** English-language translations of foreign scientific and technical material pertinent to NASA's mission.

Specialized services that complement the STI Program Office's diverse offerings include creating custom thesauri, building customized databases, organizing and publishing research results ... even providing videos.

For more information about the NASA STI Program Office, see the following:

- Access the NASA STI Program Home Page at <http://www.sti.nasa.gov>
- E-mail your question via the Internet to help@sti.nasa.gov
- Fax your question to the NASA STI Help Desk at (301) 621-0134
- Phone the NASA STI Help Desk at (301) 621-0390
- Write to:
NASA STI Help Desk
NASA Center for AeroSpace Information
7121 Standard Drive
Hanover, MD 21076-1320

NASA/TM-2005-213545



Trailing Edge Blowing on a Two-Dimensional Six-Percent Thick Elliptical Circulation Control Airfoil Up to Transonic Conditions

*Michael G. Alexander, Scott G. Anders, Stuart K. Johnson,
Jennifer P. Florance, and Donald F. Keller
Langley Research Center, Hampton, Virginia*

National Aeronautics and
Space Administration

Langley Research Center
Hampton, Virginia 23681-2199

March 2005

Acknowledgments

The authors would like to acknowledge the assistance of those individuals who's efforts made this test possible. They include: from the TDT, Mr. Chuck McClish and Mr. Wesley Goodman, from Lockheed-Martin, Mr. Jerome Cawthorne, and from the Naval Surface Warfare Center, Carderock Division, Dr. Ernest Rogers and Ms. Jane Abramson.

Available from:

NASA Center for AeroSpace Information (CASI)
7121 Standard Drive
Hanover, MD 21076-1320
(301) 621-0390

National Technical Information Service (NTIS)
5285 Port Royal Road
Springfield, VA 22161-2171
(703) 605-6000

Contents

List of Tables	v
List of Figures	v
Abstract	1
Introduction	1
Symbols	2
Model Description	3
Circulation Control Airfoil (CCA)	3
Baseline Airfoil	3
Reference Chord	4
CCA Planform Characteristics	4
Coanda Surface Definition	4
Slot Definition	5
Half Height Slot	6
Aft Surfaces	6
End Plate	7
t/2 Tip	7
Internal Plenum	7
Internal Screens	8
Boundary Layer Trip	8
Facility	9
Model Support	9
Data Acquisition and Processing	10
Air Supply	10
Critical Flow Venturi	10
Burst Disk	11
CCA Instrumentation	11
Static Pressures	11
Coanda Surface Static Pressures	11
Plenum Total Pressures	12
CCA Wake Pressures	12
Plenum Thermocouples	13
Test Procedures and Conditions	13
Lift and Pitching Moment	13
Momentum Coefficient	13
Drag	14
Single Slot	14
Dual Slots	14
Test Conditions	14
Data Corrections	15

Discussion of Results	15
Baseline Airfoil Aerodynamic Performance (No Blowing)	15
Chordwise Pressure Distribution.....	15
Comparison of End Plate and t/2 Tip Configurations	16
Mach 0.3	16
Mach 0.8	16
Blowing Performance	17
Mach = 0.3 at $\alpha = 6^\circ$	17
Coanda Surface Effect.....	17
Slot Height Effect.....	18
Slot Blowing Position Effect.....	18
Pressure Distributions	18
Main Airfoil Body	18
Coanda Bulb	18
Mach = 0.8 at $\alpha = 3^\circ$	19
Coanda Surface Effect.....	19
Slot Height Effect.....	19
2.98:1 Coanda with h/c = 0.0012 Slot	20
Mach Number Effect.....	20
Angle-of-Attack Effect.....	20
Slot Blowing Position Effect.....	21
Pressure Distributions	21
Main Airfoil Body	21
Coanda Bulb	21
Drag	22
Dual Slot Blowing.....	22
Slot Blowing Position Effect.....	22
Coanda 1.78:1 with h/c = 0.0012 Slot	22
Coanda 2.98:1 with h/c = 0.0012 Slot	22
Angle-of-Attack Effect.....	22
Coanda 2.98:1 with h/c = 0.0012 Slot	22
Summary of Results	23
Appendix A – Gap and Chord Length Measurements	24
Appendix B - Critical Flow Venturi Calibration.....	26
References	31

List of Tables

Table 1	CCA Chord Lengths for Each Coanda Surface.....	4
Table 2	Coanda Radius and Slot Height Dimensions	5
Table 3	Slot and Chord Measurements	6
Table 4	Critical Flow Venturi Information	11
Table 5	Range of Test Conditions.....	14
Table 6	Lift Curve Slopes (Per Radian) For Circulation Control Airfoil for $C_{\mu} = 0$	16
Table B1	Discharge Coefficients.....	30

List of Figures

Figure 1	Tangential blowing over a Coanda surface.....	1
Figure 2	CCA wind tunnel model mounted in the TDT (looking downstream).....	3
Figure 3	Baseline elliptical airfoil section.....	4
Figure 4	Typical CCA airfoil section	4
Figure 5	Coanda surfaces	5
Figure 6	Coanda surface installed - end view.....	5
Figure 7	Half height slot.....	6
Figure 8	Aft surface identification.....	6
Figure 9	CCA end plate.....	7
Figure 10	CCA "t/2 tip"	7
Figure 11	CCA internal plenum section cut	8
Figure 12	Center body internal screen and upper plenum layout.....	8
Figure 13	TDT schematic.....	9
Figure 14	CCA model installed on splitter plate (looking downstream).....	9
Figure 15	Air supply.....	10
Figure 16	Coanda surface static pressure tap locations	11
Figure 17	Plenum total pressure tap locations.....	12
Figure 18	Wake rake	12
Figure B1	Typical cross-section and its assembly	26
Figure B2	Venturis s/n 47 & 48 installation	27
Figure B3	Temperature effects plot	29
Figure 19	Airfoil performance, Mach number effect, no blowing	33

Figure 20	Chordwise pressure distribution, angle of attack effect, no blowing, Coanda (2.98:1), slot ($h/c = 0.0012$)	37
Figure 21	Center of pressure versus angle of attack, Mach number effect, no blowing Coanda (2.98:1), slot ($h/c = 0.0012$)	39
Figure 22	End plate effects, Mach = 0.3	40
Figure 23	End plate effects, Mach = 0.8	41
Figure 24	ΔC_l & ΔC_m versus C_{μ} , Coanda surface effect, upper slot blowing, Mach = 0.3, $\alpha = 6^\circ$	42
Figure 25	ΔC_l & ΔC_m versus C_{μ} , Coanda surface effect, lower slot blowing, Mach = 0.3, $\alpha = 6^\circ$	43
Figure 26	ΔC_l & ΔC_m versus C_{μ} , Coanda surface effect, dual slot blowing, Mach = 0.3, $\alpha = 6^\circ$	44
Figure 27	Lift augmentation ratio versus C_{μ} , Coanda surface effect, upper slot blowing, Mach = 0.3, $\alpha = 6^\circ$	45
Figure 28	Lift augmentation ratio versus velocity ratio, Coanda surface effect, upper slot blowing, Mach = 0.3, $\alpha = 6^\circ$	46
Figure 29	Lift augmentation ratio versus C_{μ} , Coanda surface effect, lower slot blowing, Mach = 0.3, $\alpha = 6^\circ$	47
Figure 30	Lift augmentation ratio versus velocity ratio, Coanda surface effect, lower slot blowing, Mach = 0.3, $\alpha = 6^\circ$	48
Figure 31	ΔC_l versus nozzle pressure ratio, Coanda surface effect, upper slot blowing, Mach = 0.3, $\alpha = 6^\circ$	49
Figure 32	ΔC_l & ΔC_m versus C_{μ} , slot height effect, upper slot blowing, Mach = 0.3, $\alpha = 6^\circ$	50
Figure 33	ΔC_l & ΔC_m versus C_{μ} , slot height effect, lower slot blowing, Mach = 0.3, $\alpha = 6^\circ$	51
Figure 34	ΔC_l & ΔC_m versus C_{μ} , slot height effect, dual slot blowing, Mach = 0.3, $\alpha = 6^\circ$	52
Figure 35	Lift augmentation ratio versus C_{μ} , slot height effect, upper slot blowing, Mach = 0.3, $\alpha = 6^\circ$	53
Figure 36	Lift augmentation ratio versus velocity ratio, slot height effect, upper slot blowing, Mach = 0.3, $\alpha = 6^\circ$	54
Figure 37	Lift augmentation ratio versus C_{μ} , slot height effect, lower slot blowing, Mach = 0.3, $\alpha = 6^\circ$	55
Figure 38	Lift augmentation ratio versus velocity ratio, slot height effect, lower slot blowing, Mach = 0.3, $\alpha = 6^\circ$	56
Figure 39	ΔC_l & ΔC_m versus C_{μ} , slot position effect, Coanda (1.78:1), slot ($h/c = 0.0012$)	57
Figure 40	Upper and lower chordwise pressure distribution, Coanda (1.78:1), slot ($h/c = 0.0012$), Mach = 0.3, $\alpha = 6^\circ$	58
Figure 41	Upper and lower surface Coanda bulb pressure distribution, Coanda (1.78:1), slot ($h/c = 0.0012$), Mach = 0.3, $\alpha = 6^\circ$	60

Figure 42	Coanda bulb pressure distribution, dual slot blowing, Coanda (1.78:1), slot ($h/c = 0.0012$), Mach = 0.3, $\alpha = 6^\circ$	61
Figure 43	ΔC_1 & ΔC_m versus C_μ , Coanda surface effect, upper slot blowing, Mach = 0.8, $\alpha = 3^\circ$	62
Figure 44	ΔC_1 & ΔC_m versus C_μ , Coanda surface effect, lower slot blowing, Mach = 0.8, $\alpha = 3^\circ$	63
Figure 45	ΔC_1 & ΔC_m versus C_μ , Coanda surface effect, dual slot blowing, Mach = 0.8, $\alpha = 3^\circ$	64
Figure 46	Lift augmentation ratio versus C_μ , Coanda surface effect, upper slot blowing, Mach = 0.8, $\alpha = 3^\circ$	65
Figure 47	Lift augmentation ratio versus velocity ratio, Coanda surface effect, upper slot blowing, Mach = 0.8, $\alpha = 3^\circ$	66
Figure 48	Lift augmentation ratio versus C_μ , Coanda surface effect, lower slot blowing, Mach = 0.8, $\alpha = 3^\circ$	67
Figure 49	Lift augmentation ratio versus velocity ratio, Coanda surface effect, lower slot blowing, Mach = 0.8, $\alpha = 3^\circ$	68
Figure 50	ΔC_1 versus nozzle pressure ratio, Coanda surface effect, upper slot blowing Mach 0.8, $\alpha = 3^\circ$	69
Figure 51	ΔC_1 & ΔC_m versus C_μ , slot height effect, upper slot blowing, Mach = 0.8, $\alpha = 3^\circ$	70
Figure 52	ΔC_1 & ΔC_m versus C_μ , slot height effect, lower slot blowing, Mach = 0.8, $\alpha = 3^\circ$	71
Figure 53	ΔC_1 & ΔC_m versus C_μ , slot height effect, dual slot blowing, Mach = 0.8, $\alpha = 3^\circ$	72
Figure 54	Lift augmentation ratio versus C_μ , slot height effect, upper slot blowing, Mach = 0.8, $\alpha = 3^\circ$	73
Figure 55	Lift augmentation ratio versus velocity ratio, slot height effect, upper slot blowing, Mach = 0.8, $\alpha = 3^\circ$	74
Figure 56	Lift augmentation ratio versus C_μ , slot height effect, lower slot blowing, Mach = 0.8, $\alpha = 3^\circ$	75
Figure 57	Lift augmentation ratio versus velocity ratio, slot height effect, lower slot blowing, Mach = 0.8, $\alpha = 3^\circ$	76
Figure 58	ΔC_1 & ΔC_m versus C_μ , Mach number effect, upper slot blowing, Coanda (2.98:1), slot ($h/c = 0.0012$).....	77
Figure 59	ΔC_1 & ΔC_m versus C_μ , Mach number effect, lower slot blowing, Coanda (2.98:1), slot ($h/c = 0.0012$).....	80
Figure 60	Lift augmentation ratio versus C_μ or velocity ratio, Mach number effect, upper slot blowing, Coanda (2.98:1), slot ($h/c = 0.0012$).....	83
Figure 61	Lift augmentation ratio versus C_μ or velocity ratio, Mach number effect, lower slot blowing, Coanda (2.98:1), slot ($h/c = 0.0012$).....	86
Figure 62	Center of pressure location versus C_μ , Mach number effect, Coanda (2.98:1), slot ($h/c = 0.0012$).....	89

Figure 63	ΔC_l & ΔC_m versus C_{μ} , angle of attack effect, upper slot blowing, Coanda (2.98:1), slot ($h/c = 0.0012$)	90
Figure 64	ΔC_l & ΔC_m versus C_{μ} , angle of attack effect, lower slot blowing, Coanda (2.98:1), slot ($h/c = 0.0012$)	92
Figure 65	Lift augmentation ratio versus C_{μ} or velocity ratio, angle of attack effect, upper slot blowing, Coanda (2.98:1), slot ($h/c = 0.0012$)	94
Figure 66	Lift augmentation ratio versus C_{μ} or velocity ratio, angle of attack effect, lower slot blowing, Coanda (2.98:1), slot ($h/c = 0.0012$)	96
Figure 67	C_l versus C_{μ} , angle of attack effect, upper slot blowing, Coanda (2.98:1), slot ($h/c = 0.0012$)	98
Figure 68	C_l versus C_{μ} , angle of attack effect, lower slot blowing, Coanda (2.98:1), slot ($h/c = 0.0012$)	100
Figure 69	C_l versus velocity ratio, angle of attack effect, upper slot blowing, Coanda (2.98:1), slot ($h/c = 0.0012$)	102
Figure 70	C_l versus velocity ratio, angle of attack effect, lower slot blowing, Coanda (2.98:1), slot ($h/c = 0.0012$)	104
Figure 71	ΔC_l & ΔC_m versus C_{μ} , slot position effect, Coanda (2.98:1), slot ($h/c = 0.0012$)	106
Figure 72	Upper and lower chordwise surface pressure distribution, C_{μ} effect, upper slot blowing, Coanda (2.98:1), slot ($h/c = 0.0012$), $\alpha = 3^\circ$	108
Figure 73	Upper and lower chordwise surface pressure distribution, C_{μ} effect, lower slot blowing, Coanda (2.98:1) slot ($h/c = 0.0012$), $\alpha = 3^\circ$	109
Figure 74	Upper and lower chordwise surface pressure distribution, C_{μ} effect, dual slot blowing, Coanda (2.98:1) slot ($h/c = 0.0012$), $\alpha = 3^\circ$	110
Figure 75	Upper surface Coanda bulb pressure distribution, C_{μ} effect, upper slot blowing, Coanda (2.98:1), slot ($h/c = 0.0012$), $\alpha = 3^\circ$	111
Figure 76	Lower surface Coanda bulb pressure distribution, C_{μ} effect, lower slot blowing, Coanda (2.98:1), slot ($h/c = 0.0012$), $\alpha = 3^\circ$	112
Figure 77	Coanda bulb pressure distribution, dual slot blowing, Coanda (2.98:1), slot ($h/c = 0.0012$), Mach = 0.84, $\alpha = 3^\circ$	113
Figure 78	Coanda bulb pressure distribution, dual slot blowing, Coanda (2.98:1), slot ($h/c = 0.0012$), Mach = 0.8, $\alpha = 3^\circ$	114
Figure 79	Coanda bulb pressure distribution, dual slot blowing, Coanda (2.98:1), slot ($h/c = 0.0012$), Mach = 0.7, $\alpha = 3^\circ$	115
Figure 80	Coanda bulb pressure distribution, dual slot blowing, Coanda (2.98:1), slot ($h/c = 0.0012$), Mach = 0.3, $\alpha = 3^\circ$	116
Figure 81	C_d versus C_{μ} , Coanda surface effect, dual slot blowing, slot ($h/c = 0.0012$)	117
Figure 82	C_d versus C_{μ} , angle of attack effect, dual slot blowing, Coanda (2.98:1), slot ($h/c = 0.0012$)	118

Figure 83	C_d versus C_μ , slot position effect, Coanda (1.78:1), slot ($h/c = 0.0012$)	119
Figure 84	C_d versus C_μ , slot position effect, Coanda (2.98:1), slot ($h/c = 0.0012$)	120
Figure 85	C_d versus C_μ , angle of attack effect, upper slot blowing, Coanda (2.98:1), slot ($h/c = 0.0012$)	121
Figure 86	C_d versus C_μ , angle of attack effect, lower slot blowing, Coanda (2.98:1), slot ($h/c = 0.0012$)	122

Abstract

A wind tunnel test was conducted in the NASA Langley Transonic Dynamics Tunnel (TDT) on a six percent thick slightly cambered elliptical circulation control airfoil with both upper and lower surface blowing capability. Parametric evaluations of jet slot heights and Coanda surface shapes were conducted at momentum coefficients ($C\mu$) from 0.0 to 0.12. Test data were acquired at Mach numbers of 0.3, 0.5, 0.7, 0.8, and 0.84 at Reynolds numbers per foot of 2.43×10^5 to 1.05×10^6 . For a transonic condition, (Mach = 0.8 at $\alpha = 3^\circ$), it was generally found the smaller slot and larger Coanda surface combination was overall more effective than other slot/Coanda surface combinations. Lower surface blowing was not as effective in producing lift and pitching moment increments at transonic conditions as the upper surface blowing over the same range of momentum coefficients. No appreciable Coanda surface, slot height, or slot blowing position preference was indicated transonically with the dual slot blowing. Subsonically (Mach = 0.3 at $\alpha = 6^\circ$), it was generally found the smaller slot and smaller Coanda surface combination was more effective overall than other slot/Coanda surface combinations. At Mach = 0.3 and $\alpha = 6^\circ$, the 1.78:1 Coanda with the upper slot blowing position with a slot height of $h/c = 0.0012$ gave the maximum ΔCl generated of 0.75 at a $C\mu = 0.085$. At Mach = 0.8 and $\alpha = 3^\circ$, the 2.98:1 Coanda with the upper slot blowing position having a slot height of $h/c = 0.001$, slightly outperformed the lower slot position, with the upper slot generating a maximum ΔCl of 0.25 at a $C\mu = 0.008$. Both subsonic and transonic trailing edge blowing influenced the flow field upstream of the slot.

Introduction

Circulation control is considered one of the most efficient methods for lift augmentation at low Mach numbers (ref. 1). The device augments an airfoil's lifting capability by tangentially ejecting a thin jet of high momentum air over a rounded trailing edge (ref. 2). When the jet sheet velocity is greater than the local external flow, the jet sheet remains attached over the curved surface by means of the Coanda effect (ref. 3-5). The Coanda effect is created when a tangentially blowing slot ejects a jet sheet of air over a curved or "Coanda surface" and remains attached to the surface due to a balance between the low static pressures generated by the jet and the centrifugal force acting on the curving jet (ref. 6) (figure 1). The jet not only moves the separation point around the trailing edge toward the lower surface of the wing, but also entrains the external flow field to follow the jet. This entrainment and separation point movement produces a net increase in the circulation of the wing resulting in lift augmentation (ref. 7).

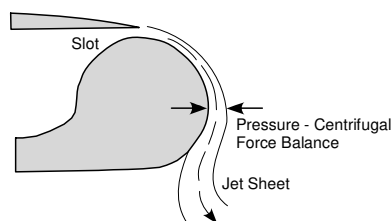


Figure 1 - Tangential blowing over a Coanda surface.

Numerous experimental circulation control tests using the Coanda effect to enhance lift have been conducted at subsonic velocities on thick airfoil sections (ref. 8-14). However, a void exists for transonic data on thin circulation control airfoils. Therefore, it is the focus of this experiment to evaluate the effectiveness of trailing edge circulation control on a thin airfoil section at transonic Mach numbers. A wind tunnel test was conducted on a six percent thick slightly cambered elliptical airfoil with both upper and lower surface slot blowing capability. Parametric evaluations of slot heights and Coanda surface shapes

were conducted at momentum coefficients (C_{μ}) ranging from 0.0 to 0.12. Test data were acquired in the Langley Transonic Dynamics Tunnel at multiple Mach numbers and angles of attack at Reynolds numbers per foot ranging from 2.43×10^5 to 1.05×10^6 .

Symbols

α	angle of attack (degrees)	h	average measured slot height (inch)
Δ	delta (incremental change)	h/c	non dimensional slot height
ρ	density (lbm/ft ³)	l/d	lift to drag ratio
γ	ratio of specific heat	M	Mach number
A	area (ft ²)	\dot{m}	mass flow (lbm/sec)
b	model span (inch)	NPR	nozzle pressure ratio
c	chord (inch)	P_s or P_{∞}	freestream static pressure (psia)
c_{ref}	reference chord (30 inch)	P_o	total pressure (psia)
CCA	circulation control airfoil	q	dynamic pressure (psi)
CD	discharge coefficient	r	radius
C_d	sectional drag coefficient	R	gas constant $\left(53.34 \frac{ft-lbf}{lbm-\circ R} \right)$
$C_{d_{rake}}$	uncorrected drag measured at the wake rake	Rn/ft	Reynolds number per foot
C_l	sectional lift coefficient	S	Model surface area (in ²)
Cl_{α}	lift curve slope	t	airfoil thickness
C_m or $C_{m_{0.25c_{ref}}}$	sectional 0.25c _{ref} pitching moment coefficient	TDT	Transonic Dynamics Tunnel
C_{m_0}	pitching moment independent of angle of attack	T_o	total temperature (R)
$C_{m_{\alpha}}$	pitching moment curve slope	U	Typically jet velocity (ft/sec)
C_p	pressure coefficient	V	Typically tunnel velocity (ft/sec)
CP	center of pressure (xcp/c)	x	chordwise distance (inch)
CP*	critical pressure coefficient	x/c	non dimensional chordwise distance
C_{μ}	momentum coefficient	xcp	distance center of pressure is from reference point (inches)
$\Delta Cl/C_{\mu}$	lift augmentation ratio	y	span distance (inch)
$\Delta Cl/C_{\mu} = \left(\frac{C_l - C_l_{C_{\mu} = 0}}{C_{\mu}} \right)$		y/b	non dimensional span location
DAS	data acquisition system	<u>Subscripts</u>	
ESP	electronically scanned pressures	jet	air flow exiting nozzle
g_c	gravitation constant $\left(32.174 \frac{lbm-ft}{ft-s} \right)$	l	lower
		max	maximum value
		s	slot
		TE	trailing edge
		u	upper
		∞	freestream

Model Description

The configuration tested in this experimental investigation was a semi-span circulation control airfoil (CCA) having zero leading and trailing edge sweep and an end plate on its tip (figure 2). The model was mounted in the TDT on a splitter plate located approximately 3 feet from the tunnel wall. The model incorporated circulation control by blowing tangentially from a full span rectangular slot located upstream of a trailing edge "Coanda surface". The rectangular slot exit is located at $x/c_{ref} = 0.9$ and extends full width (60 inches) of the model. The model has two separate and isolated internal plenums that provide air to either the upper or lower rectangular slot. The model is instrumented with a total of 157 static and total pressure taps, one accelerometer, and a type J thermocouple located in each plenum. The model has a surface finish of 32μ inch, and the Coanda surface finish from upper slot exit to lower slot exit is 16μ inch finish.

A wake rake was placed one reference chord length (30 inches) downstream of the CCA trailing edge and was used to acquire the CCA wake total and static pressures. The wake pressures were then integrated to determine drag.



Figure 2 - CCA wind tunnel model mounted in the TDT (looking downstream).

Circulation Control Airfoil (CCA)

The CCA was derived from a baseline elliptical airfoil truncated at $x/c_{ref} = 0.90$ where the nozzle of the rectangular slot occurred. All other baseline airfoil attributes remained the same.

Baseline Airfoil

In determining an airfoil to use in this experimental effort, a NACA-64A series was initially considered. However, an elliptical section was chosen based on discussions in reference 15 which examine desirable pressure distributions for transonic circulation control airfoils. A 6 percent thick section with 0.75 percent camber was chosen based primarily on reference 5 that indicates this would nearly achieve an optimum thickness to generate maximum ΔC_l 's at Mach numbers from 0.8 to 0.85.

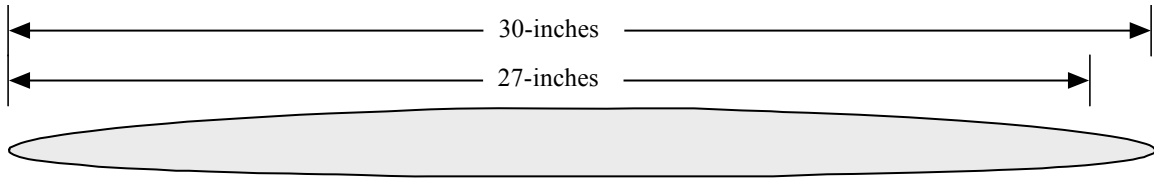


Figure 3 - Baseline elliptical airfoil section.

Reference Chord

The CCA sectional profile was sized with a 30 inch chord length without a Coanda surface. In order to have a consistent non dimensional nozzle height parameter (h/c), it was decided to establish the chord length of each CCA trailing edge configuration as seen in table 1.

	Coanda		
y/b	1.78:1	2.38:1	2.98:1
0.5	27.82-in.	28.09-in.	28.36-in.

Table 1 - CCA chord lengths for each Coanda surface.

CCA Planform Characteristics

The CCA section is a simple six percent thick elliptical airfoil having 0.75 percent camber (figure 4). The model span (b) is 60 inches with zero leading and trailing edge sweep. A reference chord (c_{ref}) of 30 inches gave the model an aspect ratio of two and a taper ratio of one. Common practice for testing semispan models on a reflection plane is to refer to this as an aspect ratio four wing. To accommodate the trailing edge Coanda surfaces, the reference airfoil was truncated at $x/c_{ref} = 0.90$ (27 inches). The CCA model tip was capable of accommodating either a 30 inch diameter circular end plate to promote two dimensional flow or a "t/2" tip used to evaluate three dimensional effects.

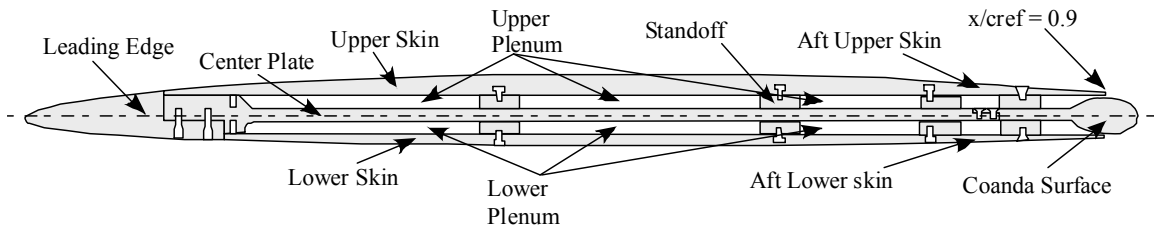


Figure 4 – Typical CCA airfoil section.

Coanda Surface Definition

Three elliptical trailing edge surfaces (referred to as Coanda surfaces) were manufactured with length to height ratios of 1.78:1, 2.38:1, and 2.98:1 (as illustrated in figure 5) and installed on the CCA model shown in figure 6. The minor axis of the Coanda surface was aligned with the slot exit to ensure the minimum exit area occurred at the exit ($x/c_{ref} = 0.9$). The horizontal axis of the ellipse was mapped to the camber line of the elliptical airfoil and formed a 5 degree converging nozzle at the exit. The Coanda surface spanned the entire model (60 inches). Table 2 lists the Coanda surface characteristics.

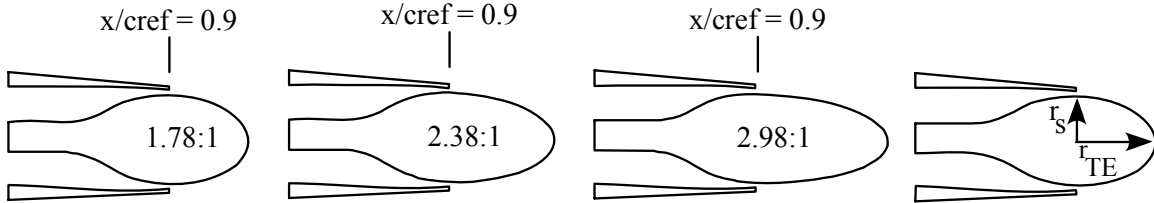


Figure 5 - Coanda surfaces.



Figure 6 - Coanda surface installed - end view.

Suggested guidelines from reference 15 for Coanda surface radii of curvatures are listed in table 2. It was not possible to meet the entire guideline radius of curvatures on a six percent thick airfoil, and it was decided preference would be given to the slot radius of curvature in an effort to achieve initial attachment of the jet flow. For this reason, a family of elliptical Coanda surfaces was chosen which has larger slot radii of curvature and small trailing edge radii of curvature.

Chord (in.)	Coanda		
	1.78 : 1	2.38 : 1	2.98 : 1
$h1/r_s$	0.024	0.014	0.009
$h2/r_s$	0.039	0.022	0.014
$h3/r_s$	0.051	0.028	0.018
$h1/r_{TE}$	0.14	0.18	0.23
$h2/r_{TE}$	0.22	0.30	0.37
$h3/r_{TE}$	0.29	0.38	0.48
Guidelines			
h/r	0.01 to 0.08		

Chord (in.)	Coanda		
	1.78 : 1	2.38 : 1	2.98 : 1
r_s (in.)	1.44	2.57	4.02
r_{TE} (in.)	0.25	0.19	0.15
r_s/c	0.052	0.091	0.142
r_{TE}/c	0.009	0.007	0.005
Guidelines			
r/c	0.02 to 0.06		

Table 2 - Coanda Radius and Slot Height Dimensions.

Slot Definition

Three upper and lower slot heights for each Coanda surface were possible for this wind tunnel investigation. The aft upper and lower removable surfaces were designed to set the slot heights by varying the internal mold line while not disturbing the outer mold line of the model. Average measured slot height

(h) and chord lengths were used to determine the height to chord ratio (h/c) of each slot. Table 3 below lists the measured average slot height and the resulting h/c. Actual measurements are recorded in Appendix A.

Slot	h(avg) (inch)	h/c
1	0.035	0.0012
2	0.056	0.0020
3	0.073	0.0026
4	0.021	0.0007

Table 3 - Slot and Chord Measurements.

Half Height Slot

A fourth slot height (4, table 3)) was constructed during the test using the upper surface small slot (h/c = 0.0012) aft skin by applying four layers of tape at 0.0035 inches per layer for a total thickness of 0.014 inches (figure 7). The resulting "half height" slot was used with the 2.98:1 Coanda, resulting in an exit h = 0.021 inches or h/c = 0.0007.



Figure 7 – Half height slot.

Aft Surfaces

Three sets of aft surfaces were manufactured and attached to the main airfoil body to form the upper and lower external airfoil contour as well as the internal convergent nozzle contour (figure 8). The aft skins also contained chordwise surface static pressure taps at $y/b = 0.5$. Any aft surface in combination with any Coanda surface ensured the minimum nozzle area was located at the nozzle exit. Each aft surface also established a discrete slot height above the Coanda surface.

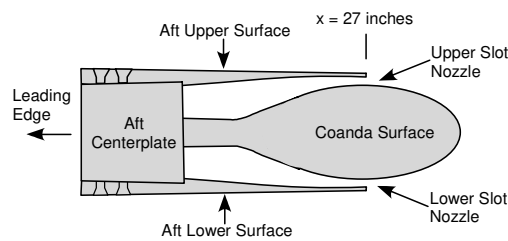


Figure 8 - Aft surface identification.

End Plate

The purpose of the circular end plate was to promote two dimensional flow across the span so the chordwise pressure measurements at mid chord would represent the performance of a two dimensional, infinite span airfoil. As seen in figure 9, the end plate is a 30 inch diameter circular plate constructed from a 0.25 inch thick aluminum plate with the outside edge beveled. The forward edge of the end plate was flush with the airfoil leading edge and centered vertically with the airfoil. This resulted in the end plate extending past the trailing edge of the airfoil by 1.7 to 2.3 inches, depending on which Coanda surface was installed. A removable cutout located at its trailing edge was used to allow Coanda surface removal and replacement. The design of the end plate was based on sizing criteria found in reference 16.

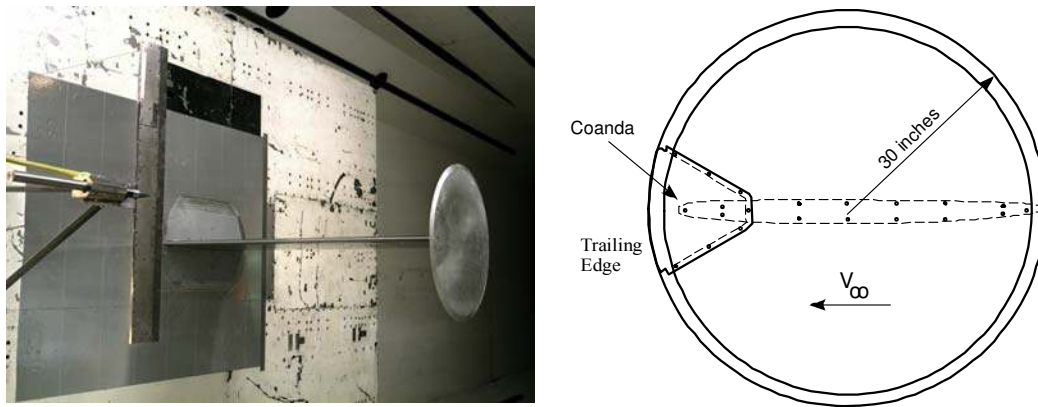


Figure 9 - CCA end plate.

t/2 Tip

A “ $t/2$ tip” was designed to close out the airfoil in a manner representative of a three dimensional wing (figure 10). The rounded tip had a radius equal to one half the local thickness and is referred to as the “ $t/2$ tip” configuration. The data acquired from this configuration were used to evaluate the effects of the end plate.



Figure 10 - CCA “ $t/2$ tip”.

Internal Plenum

As seen in figure 11, the airfoil section is divided into contiguous, separate, and isolated upper and lower plenums. The ratio of the slot height to plenum height ranged from 3.8 to 12.8 depending on the slot

height. This ensured low flow velocities in the plenum that helped maintain uniform plenum pressures. Each plenum has the capability of accepting three high loss screens to promote flow uniformity. This test used only the most aft screen that ran full span and parallel to the slot nozzle.

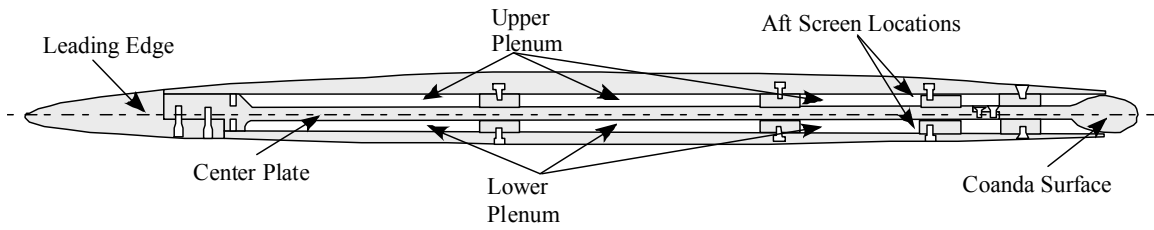


Figure 11 - CCA internal plenum section cut.

Internal Screens

The model has the capability to hold six removable, 0.050 inch thick, high pressure loss screens (figure 12). The screens were fastened to the model center plate and extended to the plenum ceiling. Each screen has a porosity of 30 percent and was sized using the method described in reference 17. It was determined through bench testing to use only one screen in each plenum in the aft most position. The aft screen was located approximately $x/c_{ref} = 0.72$ and ran full spanwise, parallel to the slot.

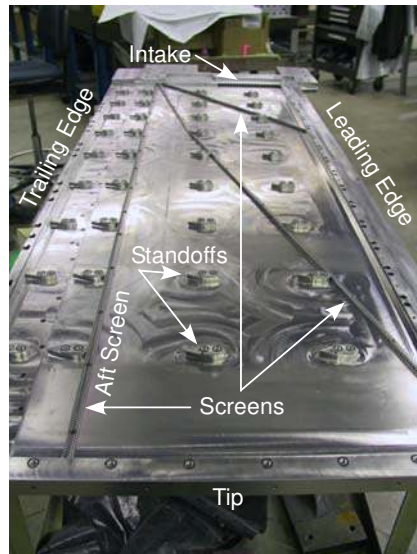


Figure 12 - Center body internal screen and upper plenum layout.

Boundary Layer Trip

A boundary layer trip strip (ref. 18) was located 1.5 inches (measured along the surface) aft of the leading edge on both the upper and lower surfaces. The trip strip used epoxy dots with a diameter of 0.038 inch, a thickness of 0.015 inch, and an edge to edge spacing distance between the epoxy dots of 0.098 inch.

Facility

This wind tunnel investigation was conducted in the Langley Transonic Dynamics Tunnel (TDT) (ref. 19). The TDT is a closed circuit, continuous flow, variable pressure wind tunnel with a 16 foot square test section with cropped corners (figure 13). The tunnel has the capability of using either air or R134a gas as the test medium. The current investigation was conducted in air. The tunnel can operate up to Mach 1.2 and is capable of maximum Reynolds numbers of approximately three million per foot and dynamic pressures up to 2.29 psi in air. Tunnel stagnation pressure can be varied from near vacuum to atmosphere.

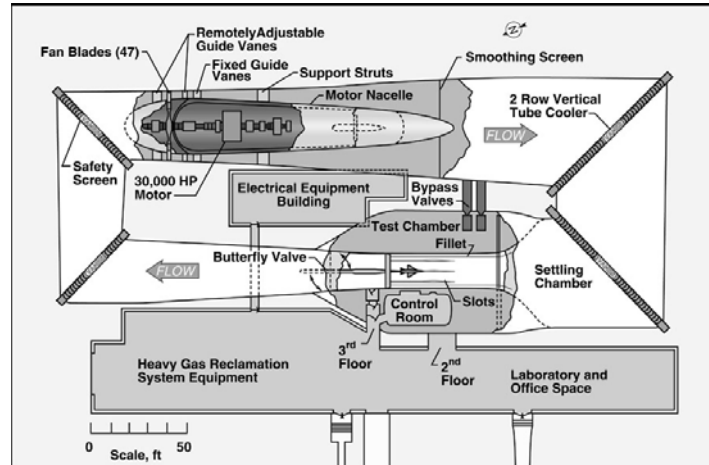


Figure 13 - TDT schematic.

Model Support

The TDT model support systems used for this test were a sidewall turntable and splitter plate as seen in figure 14. The splitter plate was located approximately 3 feet from the tunnel walls using wall standoffs. The rigid support and the model instrumentation were placed inside an aerodynamic shape or "canoe" located between the splitter plate and the tunnel sidewall.

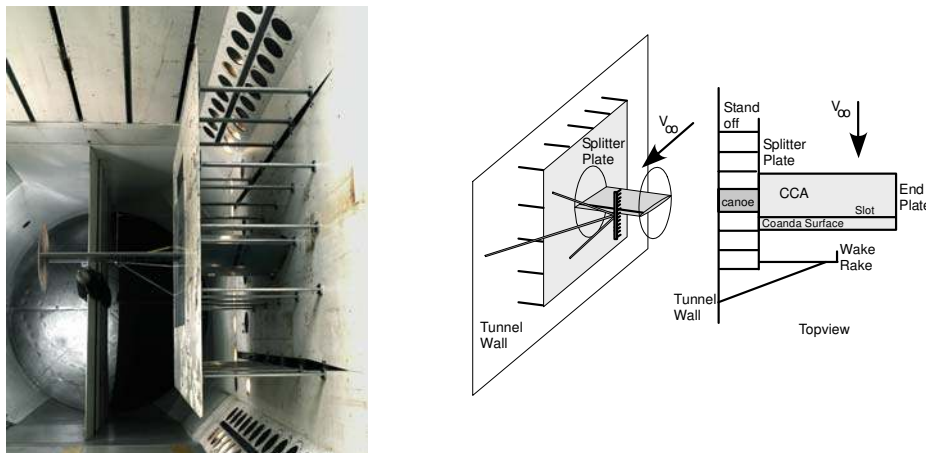


Figure 14 - CCA model installed on splitter plate (looking downstream).

Data Acquisition and Processing

The TDT open architecture dynamic data acquisition system (DAS) allowed real time acquisition and display of measured static and dynamic data as well as online analysis of the acquired data.

The DAS hardware is comprised of three subsystems with each switch connectable to a subset of four NEFF "front ends". Each NEFF provides signal conditioning, filtering, and sample and hold analog to digital conversion for 64 channels for a total capability of 256 channels. Data can be sampled at an aggregate rate approaching 300,000 samples per second, which typically provides data acquisition at a rate of at least 1000 samples per second for all available model instrumentation. The computer systems supporting the DAS perform basic data acquisition, archiving, and continuous buffering necessary to provide high quality dynamic data during tests. All computers and terminals are connected, via networks, to workstations at the TDT or at remote sites, which provide a distributed real time data display capability.

For this test, the DAS handled typical model instrumentation arrangements such as strain gage balances, potentiometers for position indication, and electronically scanned pressure (ESP) transducers.

Labview that resided on a personal computer in the TDT control room further processed data. Labview acquired the raw data from the tunnel data acquisition computer, reduced the data, and presented near real-time force and pressure information in a graphical format as well as data files.

Air Supply

Air was supplied to the model via two 1 inch high pressure flex lines delivering a maximum of 1 lbf/sec at 200 psia. The supply total temperature to the model was uncontrolled and ranged from -13°F to 70°F. Each supply line was attached to a control valve that regulated total pressure to the CCA model (figure 15). A manually operated crossover line located upstream of the control valve allowed mass flow to be diverted from one line to another. After the control valve, the supply air went through its dedicated critical flow venturi and then entered the model plenum.

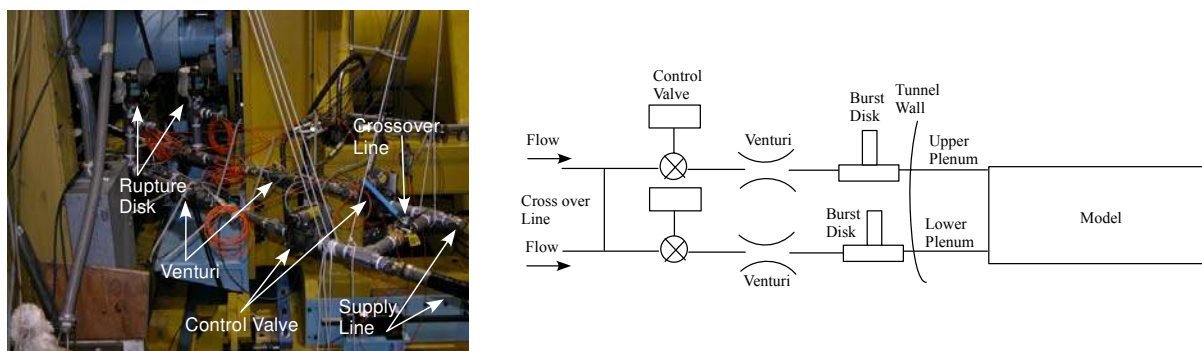


Figure 15 - Air supply.

Critical Flow Venturi

The two critical flow venturis, serial numbers 47 and 48, were used in this wind tunnel test and can be seen in table 4. They required 1 inch diameter input/exit lines and have a venturi throat diameter of 0.505 inch. Each venturi had a total pressure keel probe located upstream of the venturi throat and a static

pressure and a total temperature probe located at the venturi throat. Located upstream of the venturi was the remotely operated control valve that controlled the upstream total pressure prior to entering the venturi. Further information about the venturis and their calibration can be found in Appendix B.

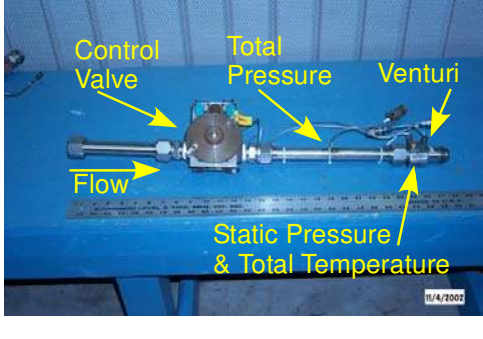
	Venturi Serial Number	47 (upper plenum)	48 (lower plenum)
	Throat Area (ft ²)	0.0014	0.0014
	Discharge Coefficient	0.971	0.982

Table 4 - Critical flow venturi information

Burst Disk

To ensure safe operations with high pressure air, a 1 inch diameter burst disk was located downstream of each venturi. The burst disks were rated to 112 psia with a five percent uncertainty band (106.4 to 112 psia) and were placed in line on a 1 inch carbon steel safety holder.

CCA Instrumentation

Static Pressures

Eighty-three (42 upper and 41 lower) external static surface pressure taps were located at $y/b = 0.5$ on the upper and lower airfoil surface. There were two spanwise rows of ten static pressures taps located at $x/c_{ref} = 0.5$ and 0.8 on the upper and lower airfoil surface.

Coanda Surface Static Pressures

Each Coanda has 19 surface static pressure taps located at approximately $y/b = 0.5$ (figure 16). Some taps were slightly offset in span from $y/b = 0.5$ to accommodate manufacturability.

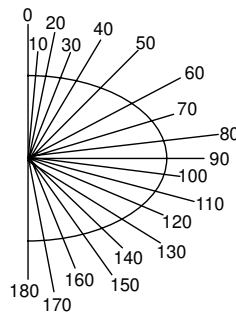


Figure 16 - Coanda surface static pressure tap locations.

Plenum Total Pressures

Each plenum had six total pressure taps with five taps located behind the high loss screens as seen in figure 17. Pressure taps two through six were located upstream of the slot, and tap one was used to determine the total pressure entering the plenum from the intake nozzle. Total pressure taps two through six were averaged together to obtain the nozzle exit total pressure.

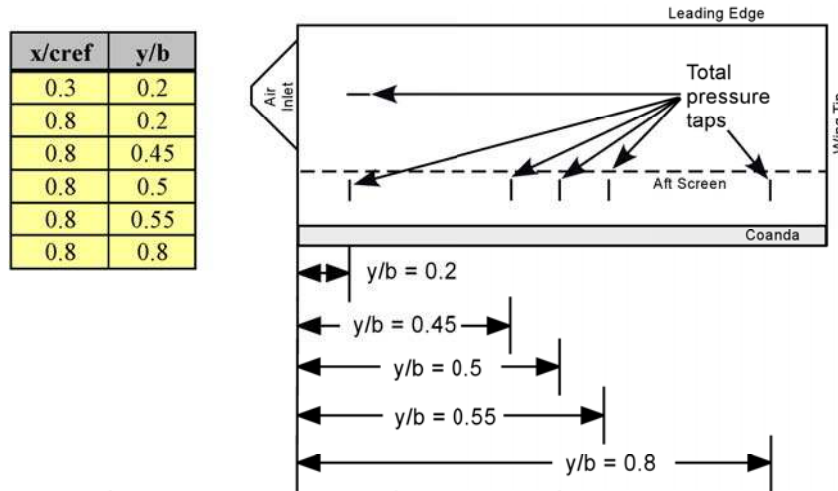


Figure 17 - Plenum total pressure tap locations.

CCA Wake Pressures

The wake rake was mounted in the tunnel using a tripod mounting arrangement (figures 2 and 18) with two of the legs attaching to the splitter plate and the aft leg attaching to the tunnel wall. The fixed rake is 48 inches in length and was used to obtain the total and the static pressure distributions in the model wake on the model centerline. The measured pressures were integrated to determine the drag. The plane of the total pressure tubes was located 30 inches or one reference chord length from the baseline airfoil's trailing edge. The wake rake has a total of 87 pressures with 79 total pressures and eight static pressures taps. The total pressure tubing was stainless steel tubing having a 0.062 inch outside diameter with a wall thickness of 0.010 inch. The static pressure probes used a four hole system that provided an integrated static pressure from each probe. The static probes were manufactured using the criteria found in reference 20.

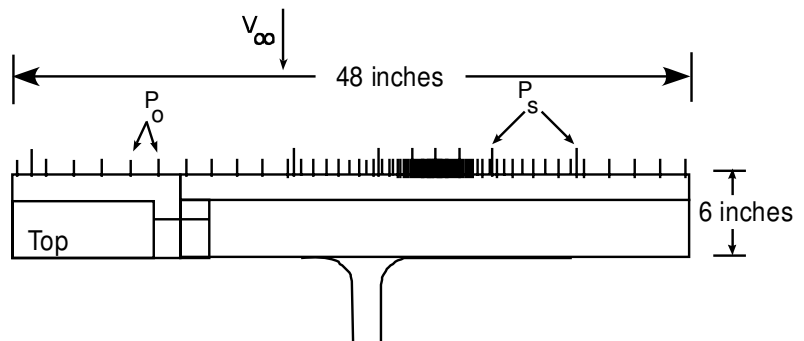
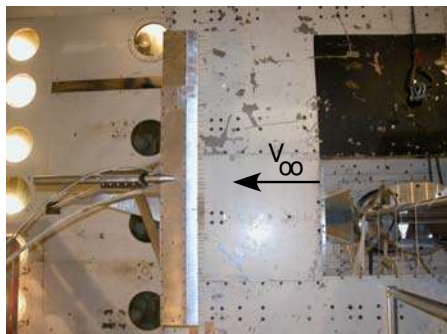


Figure 18 - Wake rake.

Plenum Thermocouples

The plenum has 2 iron constantan, type J thermocouples located in each plenum to measure plenum total temperature.

Test Procedures and Conditions

Lift and Pitching Moment

The sectional lift coefficient (equation 1) and quarter-chord pitching moment coefficient (equation 2) were obtained by numerically integrating (using the trapezoidal method) the local pressure coefficient at each $y/b = 0.5$ chordwise orifice from the upper and lower surface of the model.

$$C_l = \int_0^1 (C_{p_l} - C_{p_u}) d\left(\frac{x}{c}\right) * \cos \alpha \quad (1)$$

$$C_{m.25} = \int_0^1 (C_{p_l} - C_{p_u}) \left(0.25 - \left(\frac{x}{c}\right)\right) d\left(\frac{x}{c}\right) \quad (2)$$

Momentum Coefficient

The momentum coefficient was calculated using equation 3.

$$C_\mu = \left(\frac{\dot{m} U_{jet}}{q_\infty S} \right) \quad (3)$$

The ideal jet velocity (U_{jet}) (ft/s) was calculated (ref. 21) based on the assumption that the slot jet flow expands isentropically to the free stream static pressure (equation 4).

$$U_{jet} = \sqrt{2 * R * T_o * g_c * \left(\frac{\gamma}{\gamma - 1}\right) * \left[1 - \left(\frac{P_\infty}{P_{o plenum}}\right)^{\frac{\gamma - 1}{\gamma}} \right]} \quad (4)$$

Mass flow was determined using equation 5. The discharge coefficient (CD) was obtained from critical flow venturi calibrations conducted in the Langley Jet Exit Test Facility (Appendix B).

$$\dot{m} = CD(AV\rho)_{throat} \quad (5)$$

Drag

The sectional drag coefficient was obtained by numerically integrating (using the trapezoidal method) the rake total pressures to solve for the momentum loss across the deficit in the wake. The wake deficit integration used the procedure of Baals and Mourhess (ref. 22). This method, however, fails to account for the additional momentum introduced in the control volume by the jet at the trailing edge. To

correct the drag for the added momentum, the term $C_{\mu} \left(\frac{V_{\infty}}{U_{jet}} \right)$ was subtracted from the drag coefficient

(ref. 21) (equations 6 & 7).

Cd_{rake} = uncorrected integrated drag from rake

Single Slot

$$C_d = Cd_{rake} - C_{\mu} \left(\frac{V_{\infty}}{U_{jet}} \right) \quad (6)$$

Dual Slots

$$C_d = Cd_{rake} - C_{\mu} \left(\frac{V_{\infty}}{U_{jet_{up_slot}}} \right) - C_{\mu} \left(\frac{V_{\infty}}{U_{jet_{low_slot}}} \right) \quad (7)$$

The drag term used for developing l/d came from reference 21 and is seen in equation 8 below. This drag equation takes into consideration the additional penalty for mass intake (ram drag).

$$C_d = Cd_{rake} + C_{\mu} \left(\frac{U_{jet}}{2V_{\infty}} \right) + C_{\mu} \left(\frac{V_{\infty}}{U_{jet}} \right) \quad (8)$$

Test Conditions

The test conditions and ranges are presented in table 5 below.

Mach	P _o (psia)	P _s (psia)	T _o (°F)	Rn/ft
0.3	2.7 – 4.1	2.6 – 3.8	67 – 94	3.6x10 ⁵ – 5.5 x 10 ⁵
0.5	3.3 – 3.5	2.8 – 2.9	82 – 85	6.8x10 ⁵ – 7.2 x 10 ⁵
0.7	3.3 – 4.0	2.3 – 2.9	90 – 113	8.2 x 10 ⁵ – 1.0 x 10 ⁶
0.8	3.0 – 4.1	2.0 – 2.7	95 – 125	7.8 x 10 ⁵ – 1.0 x 10 ⁶
0.84	2.1 – 2.7	1.3 – 1.7	102 – 117	5.8 x 10 ⁵ – 7.4 x 10 ⁵

Table 5 - Range of Test Conditions

Data Corrections

No corrections were applied to the data to account for tunnel flow angularity, wall interference, thrust, or end plate effects.

Discussion of Results

Baseline Airfoil Aerodynamic Performance (No Blowing)

Figure 19 presents the no blowing longitudinal aerodynamic coefficients for the baseline airfoil. The baseline trailing edge configuration includes the 2.98:1 Coanda surface, having the upper and lower slot height (h/c) of 0.0012. Due to an unexplained data anomaly in the no blowing Mach = 0.3 data, the Mach = 0.3 data presented in figure 19 are from the model configuration having a slot height of $h/c = 0.0020$.

The angle of attack range was limited to $+10^\circ$ due to model stress analysis; therefore, a Cl_{max} was not observed. In figure 19(a), the slope of the $C_L - \alpha$ graph, Cl_α , is linear from -5° to $+8^\circ$ at all Mach numbers with Cl_0 occurring at a slightly negative angle of attack. Typical two dimensional airfoil subsonic Mach number effects on Cl_α are observed which show an increasing Cl_α with increasing Mach number.

In figures 19(b) and 19(c), from Mach numbers 0.3 to 0.7, the baseline airfoil is statically unstable with a Cm_0 occurring at $\alpha = 5^\circ$ ($C_l \sim 0.7$). At Mach = 0.8, no Cm_0 is observed, but Cm_α indicates a slight statically unstable airfoil until a reversal is encountered at $\alpha = 5^\circ$ ($C_l \sim 0.7$). At Mach = 0.84, Cm_α indicates a statically stable airfoil up to $\alpha = 6^\circ$ ($C_l \sim 0.9$) where Cm_α reverses and indicates an unstable airfoil. The Cm_0 at this Mach number occurs at $\alpha \sim -4^\circ$. Seen in figure 19(d), a maximum l/d of 44 occurs at a lift coefficient of 0.5 at Mach = 0.7. At Mach numbers above 0.7, $1/d_{max}$ diminishes which may be in part due to the transonic drag rise.

A drag increase associated with increasing angle of attack, Mach number, and C_l is observed in figures 19(e), and 19(f). The transonic drag rise can also be seen in figure 19(g) beginning at approximately Mach = 0.7.

Chordwise Pressure Distribution

The no blowing chordwise pressure distributions are observed in figure 20. Subsonic Mach numbers (0.3 and 0.5) display a very strong leading edge pressure spike that is followed by an equally strong pressure recovery over a very short chordwise distance. The first presence of an upper surface shock is seen at Mach = 0.7 at $\alpha = 5^\circ$ and gains further strength and moves aft with increasing angles of attack and Mach numbers. However, the shock is seen to move forward on the upper surface for $\alpha > 8^\circ$ at Mach = 0.8 and $\alpha > 6^\circ$ at Mach = 0.84. It is also noted the chordwise pressures at $\alpha = 0^\circ$ remain mostly positive throughout the angle of attack and Mach number range. With the chordwise pressure distributions seen in figure 20 and the center of pressure data in figure 21, it is conjectured the airfoil shock system is gaining strength with increasing angle of attack and Mach number which allow for the center of pressure to move further aft until a large region of separated flow occurs at the trailing edge. This is possibly due to a shock interaction or a stall causing the Cm_α reversals seen in figure 19(b).

Comparison of End Plate and t/2 Tip Configurations

Several runs were made with the tip configuration as shown in figure 10. Runs with the t/2 tip configuration were made with the 2.98:1 Coanda surface and the h/c = 0.0012 slot only. Comparisons are presented in Figures 22 and 23 for unblown and blown data taken at Mach = 0.3 at $\alpha = 6^\circ$ and at Mach = 0.8 at $\alpha = 3^\circ$. Based on C_l , the endplate does not produce a strong effect.

Mach 0.3

The unblown airfoil performance at Mach = 0.3 is shown in figure 22(a). A jump in the $C_l - \alpha$ curve occurs between 1° and 3° . McLachlan (ref. 23) found a similar jump in their blowing data which was attributed to the state of the boundary layer proceeding the slot location. It is assumed the shift shown here is also due to Reynolds number. The Reynolds number based on chord was 1×10^6 . The $C_l - \alpha$ slope before and after the jump appears to be nearly the same. In spite of the jump, the results show the end plate did little to affect the $C_l - \alpha$ curve. The slope of the t/2 tip curve is only slightly less than the end plate slope, but the difference is too small to make any strong conclusions.

The $\Delta C_l - C_\mu$ performance at Mach = 0.3 for $\alpha = 6.0^\circ$ is shown in figure 22(b). The slope of the $\Delta C_l - C_\mu$ graph, typically referred to as the augmentation ratio, is 27 up to $C_\mu = 0.01$. Abramson and Rogers (ref. 6) report augmentation ratios of up to 72. Typical good circulation airfoils should achieve augmentation ratios in the 50 to 70 range. In contrast, jet flaps attain augmentation ratios of approximately 14. The augmentation ratio of 27 indicates the airfoil lift control performing between the two regimes. The control method found for this experiment might be more accurately described as a Coanda jet flap. The $\Delta C_l - C_\mu$ slope falls off to 4.3 for $C_\mu > 0.03$, and the last datum point indicates the peak ΔC_l may be 0.66.

Mach 0.8

The unblown airfoil performance at Mach = 0.8 is shown in figure 23(a). The slope of the end plate $C_l - \alpha$ curve is higher than the t/2 tip slope. The lower slope occurs because of the upper and lower flowfield communication allowed by the t/2 tip configuration. Table 6 lists several $C_l - \alpha$ slopes for comparison. The empirical values from Raymer (ref. 24) are for wing lift curve slopes (per radian) for preliminary aircraft design purposes. The experimental values do not quite reach the empirical values but are close considering the approximation. The empirical values also give insight to how much improvement might be expected from the end plate.

	M=0.3	M=0.8
Theoretical: $2\pi/(1-M^2)^{1/2}$		
Subsonic 2D Ideal	6.6	10.5
Empirical Results:		
End Plate	4.5	6.9
T/2 Tip	4.1	5.9
From Experiment:		
End Plate	4	6.3
T/2 Tip	3.8	5.6

Table 6 - Lift Curve Slopes (Per Radian) for Circulation Control Airfoil for $C_\mu = 0$

The $\Delta C_l - C_{\mu}$ performance at Mach = 0.8 for $\alpha = 3.0^\circ$ is shown in figure 23(b). The $\Delta C_l - C_{\mu}$ slope remains constant at a value of 37 up to near the maximum ΔC_l point. The augmentation ratio is actually increased over the Mach = 0.3 results. However, it is still below what has historically been considered characteristic of circulation control performance ($\Delta C_l / C_{\mu} > 50$). Abramson and Rogers (ref. 6) achieved augmentation ratios of 58 at Mach = 0.6 for one of their 16% thick airfoil configurations. They found the augmentation ratio dropped to 27 for Mach = 0.7. The only slope available from their data set at Mach = 0.8 was 10.

Blowing Performance

Mach = 0.3 at $\alpha = 6^\circ$

Coanda Surface Effect

In figures 24, 25, and 26, incremental lift and pitching moment data for Coanda surface effects are presented for the upper, lower, and dual slot blowing, respectively. Each Coanda surface at this Mach number and angle of attack is capable of generating incremental lift and pitching moment at each blowing condition with the exception of dual slot blowing. Dual slot blowing negates the contributions of the upper and lower slot blowing configurations and does not create any appreciable forces and moments. Increasing C_{μ} during upper slot blowing creates positive lift increments and negative pitching moment increments. Conversely, increasing C_{μ} during lower slot blowing creates negative lift and positive pitching moment increments. Upper and lower slot blowing data trends for each Coanda surface appear to be somewhat asymptotic, and the Coanda surfaces may even decrease in effectiveness at higher blowing rates. The trend generally observed in figures 24, 25, and 26 is the smaller the Coanda surface, the greater the lift and pitching moment increment. Also observed in figure 24 and somewhat in figure 25 data, a preferred Coanda surface configuration changes with slot exit height by increasing the slot exit h/c . In figure 24, at a slot $h/c = 0.0012$, the apparent preferred Coanda is the smaller Coanda surface (1.78:1). As the slot size increases from $h/c = 0.0012$ to $h/c = 0.0020$, the data indicate all three Coanda surfaces are essentially equivocal. By increasing the slot height to $h/c = 0.0026$ from 0.0020, the larger Coanda surface (2.98:1) generates the larger magnitudes at the larger slot exit h/c , albeit overall still smaller than Coanda surface size of 1.78:1 and a slot height of 0.0012. In figure 25 at $h/c = 0.0026$, the 2.98:1 and 2:38:1 Coanda surfaces are essentially equivocal in effectiveness. Using the upper slot blowing position with a slot height of $h/c = 0.0012$, the maximum ΔC_l generated is 0.75 at a C_{μ} of 0.085.

The Coanda surface effect is observed in the lift augmentation ratio as seen in figures 27 and 28 for upper slot blowing and figures 29 and 30 for lower slot blowing. Dual slot blowing is not presented since it was not effective at generating appreciable lift increments. Data are presented in the above figures as $\Delta C_l / C_{\mu}$ versus C_{μ} or versus U_{jet} / V_{∞} . The data in these plots suggest that with increasing C_{μ} or velocity ratio, the lift augmentation diminishes. The data also indicate the smaller the Coanda surface and slot size (h/c), the greater the augmentation. Generally seen in figures 27 and 28 in the lower C_{μ} values of the $h/c = 0.0020$ or 0.0026 data, the 2.98:1 Coanda surface values typically increase in magnitude over a small C_{μ} range, while at the same C_{μ} range, the lift augmentation of smaller Coanda surfaces decreases in value.

A Coanda surface effect is observed in figure 31, ΔC_l versus nozzle pressure ratio (NPR), on upper slot blowing only. The same type of trends observed in figures 24, 25, and 26 is observed in figure 31.

Slot Height Effect

A slot height effect is observed in the incremental lift and pitching moment data shown in figures 32, 33, and 34 for the upper, lower, and dual blowing slots respectively. The trend generally indicates that the smaller the slot h/c , the greater the lift and moment increment generated. No appreciable slot preference is indicated with the dual slot blowing. Also observed is an apparent 'pinch down' in the $h/c = 0.0012$ and 0.0020 slot in the upper and lower blowing data from $C_{\mu} = 0.06$ to 0.08 that diminished as the Coanda surface size increased. This may indicate a jet reattachment (in the immediate region of the slot) followed by a lull where there is little flow turning with C_{μ} increment. The lull is followed by a period of flow turning around the Coanda bulb due to the increased C_{μ} . Typically observed are no significant differences in upper or lower slot blowing, and they appear to be somewhat equivocal in force and moment generation with the expected differences in signs.

A slot height effect on the lift augmentation ratio is observed in figures 35 and 36 for upper slot blowing and figures 37 and 38 for lower slot blowing. Similar trends are observed as seen in the Coanda surface effects on the lift augmentation data. The data indicate the smaller slot height is preferred on any Coanda surface with the exception of $h/c = 0.0007$ on the 2.98:1 Coanda during upper slot blowing (figures 35 and 36). At this blowing configuration the slot height of $h/c = 0.0007$ performs no greater than the larger slot height. However, at the same blowing configuration for lower slot blowing (figures 37 and 38), slot $h/c = 0.0007$ is the better performer, and the trend of the smallest slot for any Coanda surface holds true for lower slot blowing.

Slot Blowing Position Effect

The effect of slot blowing position on the 1.78:1 Coanda using the $h/c = 0.0012$ slot at two Mach numbers and angles of attack can be observed in figure 39. At these Mach numbers and angles of attack, the upper slot blowing position generated the largest ΔCl of all the slot positions.

Pressure Distributions

Main Airfoil Body

The effect on the upper and lower surface pressure distribution due to upper, lower, and dual slot blowing can be observed in figure 40. In figure 40(a), a C_{μ} effect from upper slot blowing is observed on the upper surface leading edge suction peak of the airfoil. As C_{μ} increases, the pressure footprint grows and moves aft up to a C_{μ} value of 0.046 where the remaining values of C_{μ} have no further effect on the leading edge suction peak. Little C_{μ} effect on the leading edge pressure peak is observed during lower slot blowing (figure 40(b)) and none for dual slot blowing (figure 40(c)). In figures 40(a) and 40(b), it appears the surface flow near 80-90% x/c accelerates due to flow entrainment caused by the trailing edge blowing jet that result in a decrease of the surface static pressures near the nozzle exit. No induced shocks due to blowing are observed at this Mach number ($M = 0.3$).

Coanda Bulb

Figures 41 and 42 display the Coanda bulb surface static pressures generated by upper and lower slot blowing (figure 41) and dual slot blowing (figure 42). An expansion at the slot is immediately followed by a compression before the flow accelerates again. Also observed in each figure is the aft movement of the shock with increasing C_{μ} .

$Mach = 0.8$ at $\alpha = 3^\circ$

Coanda Surface Effect

The incremental lift and pitching moments shown in figures 43, 44, and 45 are presented for the upper, lower, and dual slot blowing respectively. Increasing incremental lift and moments are observed with increasing blowing rates with upper slot blowing generating positive lift increments and negative pitching moment increments. Lower slot blowing generates negative lift and positive pitching moment increments. Dual slot blowing seen in figure 45 follows the $Mach = 0.3$ data trends, producing no appreciable incremental lift or pitching moments at any Coanda surface type. Generally, the data in figure 43 (upper slot blowing) display three distinct regions with the first region characterized by an increasing lift increment with increasing C_{μ} followed by a plateau region in most cases and then finally, a region of decreasing lift increment with further increasing C_{μ} . As the Coanda surfaces lengthened, the regions were stretched out further with increasing C_{μ} . The Coanda surface effect observed in this data indicates the larger Coanda surface is more effective over the mid to high C_{μ} range, while all three Coanda surfaces are equivocal in the low C_{μ} range. The data suggest the jet on the longer Coanda surface remains attached longer over a larger range of momentum coefficients while conversely, the jet separates much sooner on the smaller Coanda surfaces. This data trend is generally followed in figure 44 for lower slot blowing. However, the lower slot blowing is not as effective in producing lift and pitching moment increments as the upper slot blowing over the same range of momentum coefficients. Also, as seen in figure 44, none of the Coanda surfaces tested were capable of generating incremental lift or pitching moment for $h/c = 0.0026$. Note the contrast to this in figure 43 at $h/c = 0.0026$, for the 2.98:1 Coanda surface which shows that it does not diminish in effectiveness but appears to be somewhat asymptotic, reaching a maximum increment and maintaining that increment over the upper C_{μ} range. At $Mach = 0.8$ at $\alpha = 3^\circ$, the upper slot position slightly outperformed the lower slot position, with the upper slot generating a maximum ΔCl of 0.25 at a C_{μ} of 0.008.

The Coanda surface effect using the lift augmentation ratio is observed in figures 46 and 47 for upper slot blowing and figures 48 and 49 for lower slot blowing. Dual slot blowing data are not presented since no appreciable increments were generated. Data are presented in the above figures as $\Delta Cl / C_{\mu}$ versus C_{μ} or versus U_{jet} / V_{∞} . The data generally follow the same trend as the $Mach 0.3$ data where with increasing C_{μ} or velocity ratio values, the lift augmentation diminishes. In figure 46, at very low C_{μ} values, the 1.78:1 Coanda surface initially generates the largest lift augmentation values, but its effectiveness rapidly diminishes as C_{μ} and slot heights are increased where the apparent preferred Coanda surface becomes the larger 2.98:1 Coanda surface. It is also observed as the slot h/c increases, the maximum lift augmentation value attained decreases for each Coanda surface. Similar trends are observed in figure 47. In figures 48 and 49 for lower slot blowing, generally no significant Coanda effects are observed, with each Coanda surface essentially equivocal.

A Coanda surface effect is observed in figure 50, ΔCl versus nozzle pressure ratio (NPR), on upper slot blowing only. Figure 50 generally follows the same trends as reported above in figures 43, 44, and 45.

Slot Height Effect

A slot height effect using incremental lift and pitching moments due to upper, lower, and dual slot blowing can be observed in figures 51, 52, and 53 respectively. The same type of data regions found in the Coanda effect (figure 43) is also observed in the slot height effect data. The data in figures 51 and 52 indicate that the smaller slot sizes are more effective over the Coanda surface range. On the 2.98:1 Coanda surface, the data indicate that the $h/c = 0.0007$ slot is equivocal in effectiveness as the $h/c = 0.0012$ slot. It can be seen in the aforementioned figures that as the Coanda surface size increases, the C_{μ} value where

incremental lift and pitching moments are equal to zero increases in magnitude. Dual slot blowing, seen in figure 53, follows previously shown dual slot blowing trends, which display the inability for it to produce appreciable incremental lift or pitching moments at any slot height.

A slot height effect using the lift augmentation ratio for upper slot blowing is observed in figures 54 and 55 and for lower slot blowing in figures 56 and 57. On upper and lower slot blowing, generally the data indicate the smaller the slot height the greater the increment magnitude. Additionally, the data in figure 56, lower slot blowing, also suggest that at $C_{\mu} > 0.02$ on any given Coanda, the slots are equivocal in effectiveness. Similar trends are observed in figure 49.

2.98:1 Coanda with $h/c = 0.0012$ Slot

It was demonstrated for transonic conditions that the 2.98:1 Coanda surface using the $h/c = 0.0012$ slot was the preferred trailing edge circulation control configuration of all possible combinations. This section expands the results specifically for this preferred trailing edge configuration for upper and lower slot blowing operations. Due to the large C_{μ} range at Mach = 0.3, some of its incremental data was truncated in an effort to show the effects at lower C_{μ} ranges.

Mach Number Effect

The Mach number effect can be observed in figures 58 and 59, for upper and lower slot blowing respectively. In figures 58 and 59, the data suggest that generally this trailing edge configuration becomes less effective as the Mach number and C_{μ} is increased. This is in agreement with the data from reference 6. The corresponding lift augmentation ratios are observed in figures 60 and 61.

Mach number effects on the center of pressure location can be observed in figure 62 for upper and lower slot blowing. The large shift in the center of pressure at higher blowing rates is attributed to the jet detaching from the Coanda bulb surface.

Angle of Attack Effect

Figures 63 and 64 display an angle of attack effect for upper and lower slot blowing respectively. In figure 63 at Mach = 0.3 and 0.84, it appears the lower the angles of attack, the greater the slot effectiveness is. However, at Mach = 0.7 and 0.8, at higher C_{μ} values the opposite appears to be true, with the higher angles of attack appearing to be more effective than the lower angles of attack. For the lower slot blowing cases shown in figure 64, for Mach = 0.3 and 0.84, the effectiveness of the slot increases as angle of attack increases to $\alpha = 3$. However, at larger angles of attack, the slot becomes less effective. This may be due to an increased flow separation on the wing. But at Mach 0.7 and 0.8, the data generally indicate that as the angle of attack increases, the slot effectiveness decreases. However, it is noted in both figures 63 and 64 the performance differences between the angles of attack are very marginal, and in some cases the effectiveness across the angles of attack could be considered equivocal.

The angle of attack effect on the lift augmentation ratio can be observed in figures 65 and 66, upper and lower slot blowing respectively. Similar angle of attack effect trends that were observed in figures 63 and 64 are observed in figures 65 and 66.

In figures 67 and 68, an angle of attack effect can be observed on the lift coefficient (C_l) using upper and lower slot blowing. In these figures, as the Mach number increases, the lift increases with increasing angles of attack. Beginning at Mach = 0.8, C_l reaches a maximum magnitude and remains somewhat

constant over a discrete C_{μ} range, and then diminishes as C_{μ} increases. Similar trends are observed in figures 69 and 70 with the velocity ratio (U_{jet} / V_{∞}) on the independent axis.

Slot Blowing Position Effect

In figure 71, at Mach = 0.3 and $\alpha = 3^{\circ}$, the upper and lower slots are essentially equivocal in performance. However as angle of attack is increased to 6° (Mach = 0.3), the upper slot blowing is slightly more effective than the lower slot blowing. As the Mach number is increased, the upper slot blowing becomes slightly more effective than lower slot blowing.

Pressure Distributions

Main Airfoil Body

The effect of upper, lower, and dual slot blowing on the upper and lower surface pressures at $\alpha = 3^{\circ}$ is observed in figures 72 (upper slot blowing), 73 (lower slot blowing), and 74 (dual slot blowing). In figure 72 at Mach = 0.3 and 0.7, a slight blowing effect can be seen across the upper airfoil surface. As the flow nears the slot exit, the pressure data indicate the flow accelerates and lowers the upper surface pressures resulting in an aft loading of the airfoil. At the same Mach numbers in figure 73, lower slot blowing, a different trend is seen. In lieu of decreasing the upper surface pressures as the upper slot blowing did, the lower slot blowing increased those pressures suggesting that lower slot blowing may enhance the environment to promote separated flow on the upper surface. In figures 72, 73, and 74, at Mach = 0.84, the overall trend for the upper surface pressures is to slightly decrease with increasing C_{μ} . In figure 72, Mach = 0.84, upper slot blowing, initially with increasing C_{μ} , the aft shock tends to move aft towards the Coanda surface, and as C_{μ} increases further, the shock reverses and moves forward towards the leading edge of the airfoil. This shock movement is caused by the slot blowing influencing the flow field upstream of the slot. In figure 73, lower slot blowing, the opposite is observed at Mach = 0.84 where initially the shock moves forward towards the leading edge, then as C_{μ} increases further, the shock reverses and moves aft towards the Coanda surface. For dual slot blowing at Mach = 0.84, as seen in figure 74, the shock moves forward towards the leading edge of the airfoil with increasing C_{μ} .

In figure 72, upper slot blowing, at Mach = 0.8, what appears to be a leading edge shock tends to weaken with increasing C_{μ} . However, in figure 73, lower slot blowing, this possible leading edge shock seems to slightly increase in strength with increasing C_{μ} . In figure 74, as anticipated, dual slot blowing had no apparent blowing effect on the shock. In figures 72, 73, and 74, no significant blowing effects are observed on the leading edge below Mach = 0.7.

Coanda Bulb

Figures 75 and 76 are the pressure distributions at $\alpha = 3^{\circ}$ of the upper and lower surface of the 2.98:1 Coanda bulb using the $h/c = 0.0012$ slot at various Mach numbers. In figure 75 (upper slot blowing) with increasing C_{μ} , a shock is observed on the bulb just aft of the slot exit. Once the shock forms, generally as C_{μ} increases, the shock appears to move aft on the bulb. At C_{μ} values greater than or equal to 0.017 and Mach numbers ≥ 0.8 , the jet appears to detach from the bulb, and the pressures generally recover near to its no blowing static pressure values. No such jet detachment is observed in the Mach = 0.7 and 0.3 data. These same trends and Mach numbers are observed in figure 58 (lower slot blowing). The dual slot blowing data are seen in figures 77 through 80. At Mach = 0.84 (figure 77), increasing $C_{\mu} > 0.019$ apparently has the effect of detaching the jet from the bulb surface, and then the bulb surface pressure recovers to near its no blowing static pressure values.

Drag

Dual Slot Blowing

Dual slot blowing is where the upper and lower slots had the same slot h/c value and were blown simultaneously at the same C_{μ} . Dual slot blowing tests were conducted primarily to evaluate drag reduction effects obtained by using the jet to eliminate separation and fill the wake for the blunt Coanda trailing edges. Drag measurements were acquired by integrating the wake rake pressures and accounting for the additional momentum introduced into the test section, making them equivocal to what a balance would measure if induced effects could be eliminated (ref. 26).

Presented in figure 81 are dual slot blowing drag coefficient plots at two Mach numbers at different angles of attack. The $C_{\mu} = 0$ drag coefficient at both Mach = 0.3 at $\alpha = 6^{\circ}$ and Mach = 0.8 at $\alpha = 3^{\circ}$ is approximately 0.012. Ideal thrust curves are also provided in figure 81 for reference to indicate the thrust only effects of dual blowing. At Mach = 0.3, the dual slot blowing decreases the drag along the ideal thrust curve, indicating a net 100% thrust efficiency. This net efficiency is a result of the slot nozzle losses being offset by reduced drag of the baseline airfoil due to blowing. At Mach = 0.8, the dual slot blowing decreases the drag below the ideal thrust curve (greater than 100% efficiency), clearly indicating the baseline drag is reduced by dual blowing. This effect is greatest at $C_{\mu} = 0.005$ and is most likely caused by the elimination of flow separation on the blunt trailing edge. In figure 82, an angle of attack effect is observed in both Mach numbers with $\alpha = 10^{\circ}$ displaying the greater drag.

Slot Blowing Position Effect

Coanda 1.78:1 with $h/c = 0.0012$ Slot

In figure 83 a slot blowing position effect on drag can be observed at two different Mach numbers and angles of attack. The data in figure 83 at Mach = 0.3 suggest when compared to the ideal thrust curve, over the C_{μ} range, no loss or gain in drag is observed in the dual slot blowing, and only a marginal decrease in drag is observed using just the lower slot. However, a rise in drag from upper slot blowing is observed over the C_{μ} range. At Mach = 0.8, the data indicate dual slot blowing decreases the drag along the ideal thrust curve up to a $C_{\mu} = 0.015$ where it increases the drag for all C_{μ} 's > 0.015. In relationship to the ideal thrust curve, the upper and lower slots generally increase the drag at Mach = 0.8.

Coanda 2.98:1 with $h/c = 0.0012$ Slot

In figure 84 a slot position effect on drag can be observed at two different Mach numbers and angles of attack. The data at Mach = 0.3 and 0.8 follow the same trends seen in figure 83 (Coanda 1.78:1, $h/c = 0.0012$) with the exception of dual slot blowing at Mach = 0.8, where the data indicate dual slot blowing marginally reduces the drag over the C_{μ} range when compared against the ideal thrust curve.

Angle of Attack Effect

Coanda 2.98:1 with $h/c = 0.0012$ Slot

Presented in figures 85 and 86 is an angle of attack effect on upper and lower slot blowing respectively, on the drag coefficient at Mach = 0.3 and Mach = 0.8. The data generally indicate that at both

slot positions and over the C_{μ} range, higher angles of attack result in larger drag. Also seen in figures 85 and 86, as C_{μ} increases, the drag diminishes.

Summary of Results

1. A wind tunnel experiment was conducted in the NASA Langley Transonic Dynamics Tunnel (TDT) at Mach numbers of 0.3, 0.5, 0.7, 0.8, and 0.84 on a two dimensional, six percent thick airfoil with a modified trailing edge used to enhance the Coanda effect by tangential jet slot blowing.
2. The endplate does not produce a strong effect on the results.
3. The Mach = 0.3 and 0.5 data trend generally indicated that the smaller the Coanda surface and slot h/c, greater were the lift and pitching moment increments.
4. The Mach 0.7, 0.8, and 0.84 data trend generally indicated that the larger the Coanda surface and slot h/c, greater were the lift and pitching moment increments.
5. Increasing incremental lift and moments are observed with increasing blowing rate, with upper slot blowing creating positive lift increments and negative pitching moment increments, while lower slot blowing creates negative lift and positive pitching moment increments.
6. Lower slot blowing was not as effective in producing lift and pitching moment increments at transonic velocities as the upper slot blowing over the same range of momentum coefficients.
7. At Mach = 0.3 and $\alpha = 6^{\circ}$, the 1.78:1 Coanda with the upper slot blowing position having a slot height of $h/c = 0.0012$ gave the maximum ΔCl generated of 0.75 at a C_{μ} of 0.085.
8. At Mach = 0.8 and $\alpha = 3^{\circ}$, the 2.98:1 Coanda with the upper slot blowing position having a slot height of $h/c = 0.0012$ slightly outperformed the lower slot position, with the upper slot generating a maximum ΔCl of 0.25 at a C_{μ} of 0.008.
9. Trailing edge blowing influenced the flow field upstream of the slot.
10. The pressure distribution on all Coanda bulbs at Mach ≥ 0.8 suggests the jet detached from the bulb surface at the higher blowing rates, indicating a limit to the amount of blowing that can be accomplished without losing effectiveness.
11. At Mach 0.84, the trailing edge shock at the higher blowing rates moves forward possibly creating an area of flow separation thereby affecting the center of pressure location.
12. Based upon the ΔCl and ΔCm data, no appreciable Coanda surface and slot height preference were found with dual slot blowing.
13. Dual slot blowing resulted in the reduction of the airfoil's baseline drag at Mach = 0.8 and yielded near ideal slot thrust recovery at Mach = 0.3 and 0.8.
14. The movement of the airfoil shock (typically Mach = 0.84) at higher blowing rates is due to the flow field responding to the jet attachment and detachment on the Coanda bulb.

Appendix A

Gap and Chord Length Measurements

Below are gap height and chord length measurements at specific locations on the model.

Avg Gap Determination														
SLOT GAP	Span (inches)										Mean	Mean	Mean	Mean
Slot/Coanda	Position	7.5	15	22.5	24	30	36	37.5	45	52.5	h	h_all	h_all	h/c_all
Small/1.78:1	Upper	.036	.035	.035	.035	.037	.041	.041	.038	.032	.037	.00132	.0350	.0012
Small/1.78:1	Lower	.033	.034	.033	.033	.036	.036	.035	.029	.031	.033	.00120		
Small/2.38:1	Upper	.037	.036	.036	.036	.038	.037	.037	.038	.035	.037	.00131		
Small/2.38:1	Lower	.034	.037	.037	.032	.032	.035	.036	.032	.032	.034	.00121		
Small/2.98:1	Upper	.036	.033	.035	.035	.037	.041	.041	.037	.034	.037	.00129		
Small/2.98:1	Lower	.035	.036	.033	.033	.035	.034	.033	.028	.029	.033	.00116		
Med./1.78:1	Upper	.060	.056	.055	.056	.059	.060	.060	.061	.058	.058	.00210	.0562	.0020
Med./1.78:1	Lower	.051	.056	.054	.054	.053	.053	.054	.052	.048	.053	.00190		
Med./2.38:1	Upper	.062	.059	.058	.060	.062	.064	.064	.064	.068	.062	.00222		
Med./2.38:1	Lower	.049	.059	.052	.052	.054	.052	.054	.052	.050	.053	.00187		
Med./2.98:1	Upper	.060	.056	.054	.054	.059	.062	.063	.063	.062	.059	.00209		
Med./2.98:1	Lower	.051	.057	.053	.054	.053	.051	.051	.051	.045	.052	.00183		
Large/1.78:1	Upper	.074	.072	.073	.075	.076	.076	.075	.075	.074	.074	.00268	.0728	.0026
Large/1.78:1	Lower	.072	.074	.071	.070	.071	.071	.071	.069	.067	.071	.00254		
Large/2.38:1	Upper	.075	.075	.074	.075	.076	.075	.076	.077	.077	.076	.00269		
Large/2.38:1	Lower	.073	.072	.075	.074	.071	.072	.072	.069	.070	.072	.00256		
Large/2.98:1	Upper	.073	.070	.071	.073	.075	.075	.075	.075	.075	.074	.00259		
Large/2.98:1	Lower	.073	.076	.071	.070	.071	.069	.069	.069	.066	.070	.00248		

Half-Height (h4) 4-layers of tape @ 0.0035-in per layer taped on 'small' slot

SLOT GAP	Position	Actual				Average	
		h (avg)	Tape (in.)	h (in.)	h/c	h_all	h/c_all
Small/1.78:1	Upper	.037	.014	.023	.00081	.0210	.0007
Small/1.78:1	Lower	.033	.014	.019	.00069		
Small/2.38:1	Upper	.037	.014	.023	.00081		
Small/2.38:1	Lower	.034	.014	.020	.00072		
Small/2.98:1	Upper	.037	.014	.023	.00080		
Small/2.98:1	Lower	.033	.014	.019	.00067		

Chord Length						Chord (avg) inches
inches	0	7.5	30	45	60	
2y/b	0	0.125	0.5	0.75	1	
1.78:1	27.825	27.818	27.812	27.815	27.831	27.820
2.38:1	28.103	28.092	28.084	28.086	28.100	28.093
2.98:1	28.371	28.361	28.352	28.355	28.366	28.361

Span			
inches	0	15	30
x/c	0	0.5	1
1.78:1	59.994	60	
2.38:1	59.982	60	60.0021
2.98:1	59.994	60	

Plenum h/l											
HEIGHT UP	1	2	3	4	5	6	7	8	9	10	Length
	0.274	0.273	0.272	0.272	0.272	0.272	0.270	0.270	0.270	0.271	58.251
HEIGHT LOW	1	2	3	4	5	6	7	8	9	10	Length
	0.283	0.280	0.278	0.250	0.256	0.274	0.263	0.274	0.269	0.263	58.25

Appendix B

Critical Flow Venturi Calibration

Test Facility

The NASA Langley Jet Exit Facility is an indoor nozzle test stand which combines multiple flow air propulsion simulation with high pressure and high mass flow capabilities. Two individually controlled 1800 psia air lines supply the test model system(s), and each can provide flow rates up to 23 lbm per second. Supply air is heated to maintain room temperature conditions at critical model measurement stations. The mass flow rate of each air line is measured using a system of multiple critical venturi meters. Such systems allow accurate mass flow computations over a large range of flow rates. Pressurized air from one or both supply lines is directed through a selected model interface system into the propulsion simulation geometry and vented to atmosphere in the large test bay area. Exhaust flow is drawn outside the facility through two roof mounted ventilation systems, keeping the test bay conditions at atmospheric pressure.

The dual flow propulsion simulation system is designed for supply and control of two separate flow fields: a primary (core) flow and a secondary flow. It incorporates a 6 component strain gage force and moment balance with maximum axial force capacity of 1200 lbf. A nozzle installed to this rig can be tested at charging station total pressures up to 350 psi and total temperatures up to 90°F. Such conditions provide nozzle pressure ratios in excess of 20.

Venturi Description and Instrumentation

The two critical flow venturis, serial numbers 47 and 48, are identical and were assembled as shown in figure B1. They require 1 inch diameter input/exit lines and have a venturi throat diameter of 0.505 inch. Each venturi has a total pressure keel probe located upstream of the venturi throat and a static pressure and a total temperature probe located at the venturi throat. Located upstream of the venturi (figure B1) is the control valve which controlled the airflow to the venturi and was operated remotely from within the control room.

Typical Venturi Cross Section



Typical Venturi Cross-section

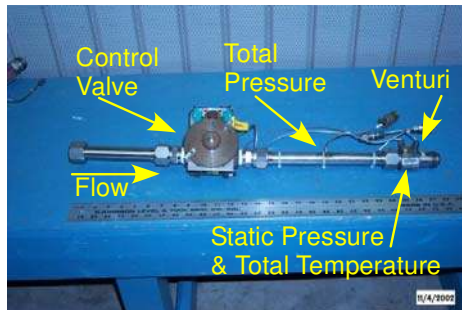


Figure B1 - Typical Venturi cross section and its assembly.

The in line venturi assemblies were attached to the Jet Exit Facility's secondary flow system that supplied a known quantity of mass flow measured by the upstream multiple critical venturi meters. The test venturi assemblies were attached to the secondary system's alternate cover plate as shown in figure B2. Thus, controlled and metered airflow was supplied to each venturi system for calibration of flow rate as a function of internal pressure.

The test venturis' total pressure and temperature measurements were correlated with the known mass flow and temperature from the secondary flow system to obtain the venturi calibrations. This test did not utilize the balance.

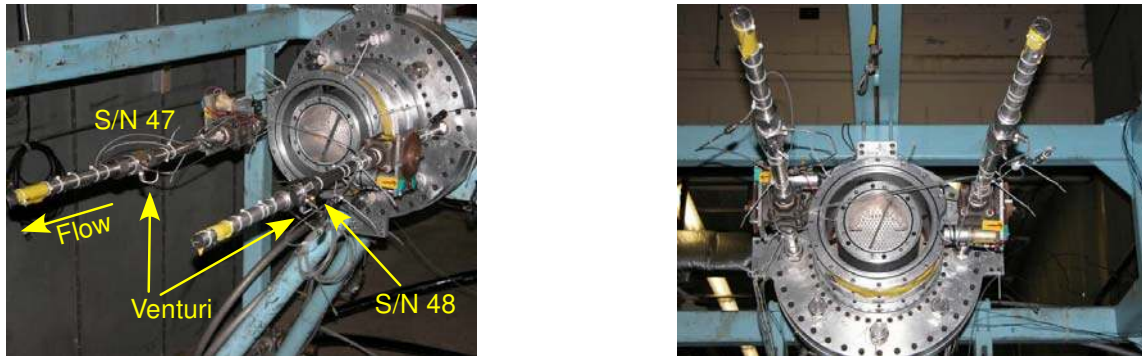


Figure B2 - Venturis s/n 47 & 48 installation.

Experimental Instrumentation

Upstream total pressure was acquired using a total pressure keel probe for each venturi. Throat static pressure and total temperature were also acquired. A Type J thermocouple was used to acquire the total temperature at the throat.

Calibration Conditions

The venturis were calibrated at two different air temperatures of 75° F and 55° F over a mass flow range from 0.6 to 2.0 lbms/sec at total pressures ranging from 0 psi to 400 psi. Mass flow data points were gathered in 0.1 lbms/sec increments to capture any unexpected non linearities from the venturis. Repeat points were taken at the end of each run to ensure data integrity.

Data Reduction

Jet Exit Facility data were reduced in accordance with reference 25. Venturi mass flow was determined from flow conditions at the facility Multiple Critical Venturis (MCV) according to the following relationships (equation B1).

For choked conditions $\left(\frac{p_{\infty}}{P_{O_S}} \right) \leq 0.5283$

$$\dot{m} = \left(A_{1,4} * P_{O_S} * \sqrt{\frac{\gamma g_c}{RT_o}} * \left(\frac{2}{\gamma + 1} \right)^{\frac{\gamma + 1}{2(\gamma - 1)}} \right) \text{lbms / sec} \quad (\text{B1})$$

where

$$A_1 = \text{MCV1_Throat_Area_}(0.00019 \text{ ft}^2)$$

$$A_4 = \text{MCV4_Throat_Area_}(0.00076 \text{ ft}^2)$$

$$P_{O_S} = \text{Total_Pressure_of_Supply_Air_}(psf)$$

$$p_{\infty} = \text{Atmospheric_Static_Pressure_}(psf)$$

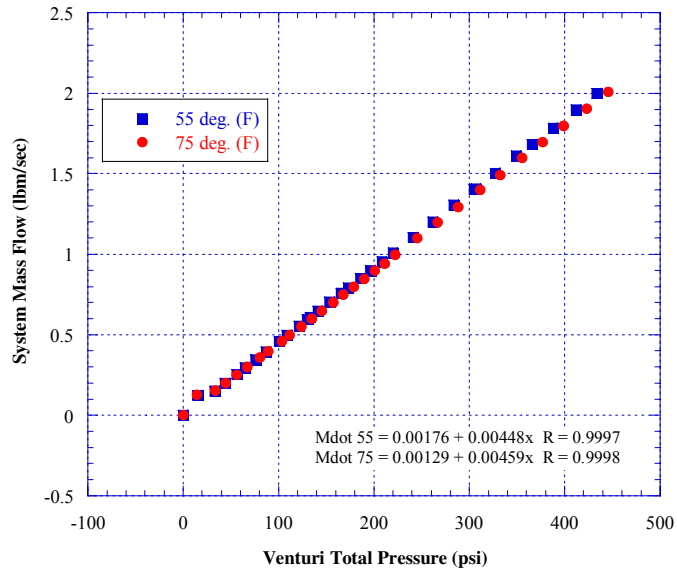
$$\gamma = 1.4$$

$$g_c = 32.174 \left(\frac{\text{lbm} \cdot \text{ft}}{\text{lbf} \cdot \text{s}^2} \right)$$

$$R = 53.34 \left(\frac{\text{ft} \cdot \text{lbf}}{\text{lbm} \cdot \text{R}} \right)$$

$$T_o = \text{Supply_Air_Temperature_}(Rankine)$$

**Temperature Effect
Left Venturi S/N 47**



**Temperature Effect
Right Venturi S/N 48**

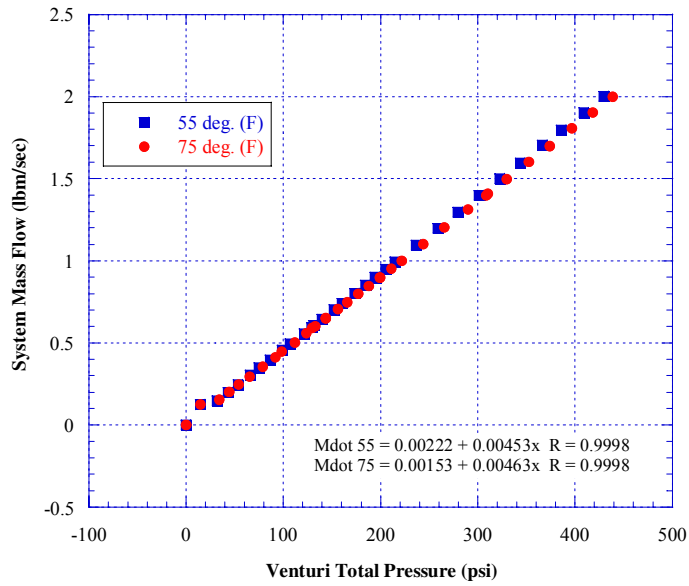


Figure B3 – Temperature effects plot.

Results

The test venturi calibrations are presented as curve fits to the system mass flow vs venturi total pressure as found in figure B3. Since the curve fits are very nearly linear, the calibration are expressed as a discharge coefficients as seen in equation B2.

where:

wP_{actual} = flow rate in lbm/sec from facility Multiple Critical Venturi (MCV) system.

wP_{ideal} = flow rate in lbm/sec calculated using 1-D flow equation using total pressure, total temperature and area at the test venturi.

$$CD = \left(\frac{wP_{actual}}{wP_{ideal}} \right) = discharge_coefficient \quad (B2)$$

Venturi Serial Number (S/N)	55°F	75°F
47	0.974	0.971
48	0.984	0.982

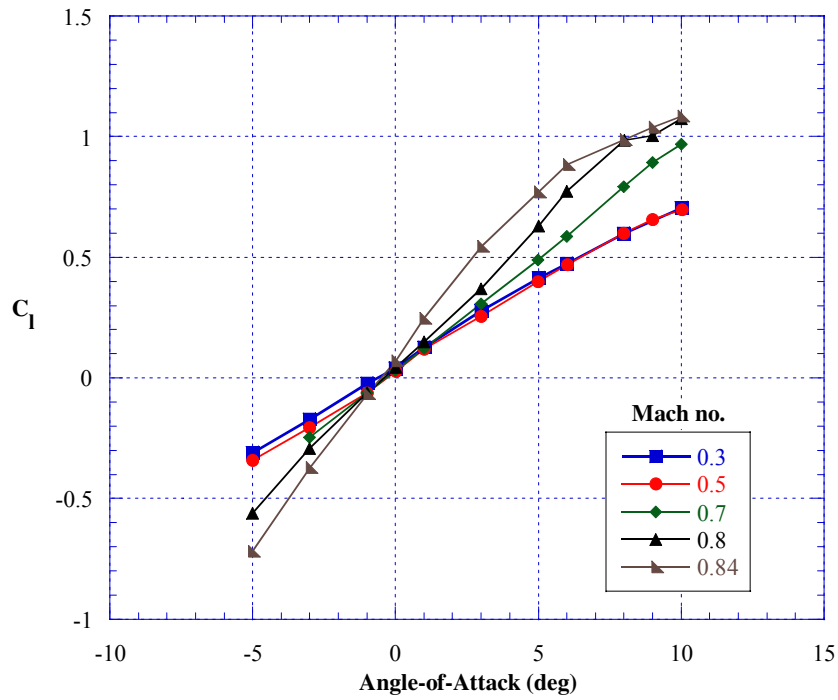
Table B1 – Discharge Coefficients

As seen in figure B3 and table B1, negligible temperature effects are observed in the venturi discharge coefficients. The discharge coefficients determined at 75°F were used for this experiment and were 0.971 and 0.982 for venturis S/N 47 and S/N 48, respectively.

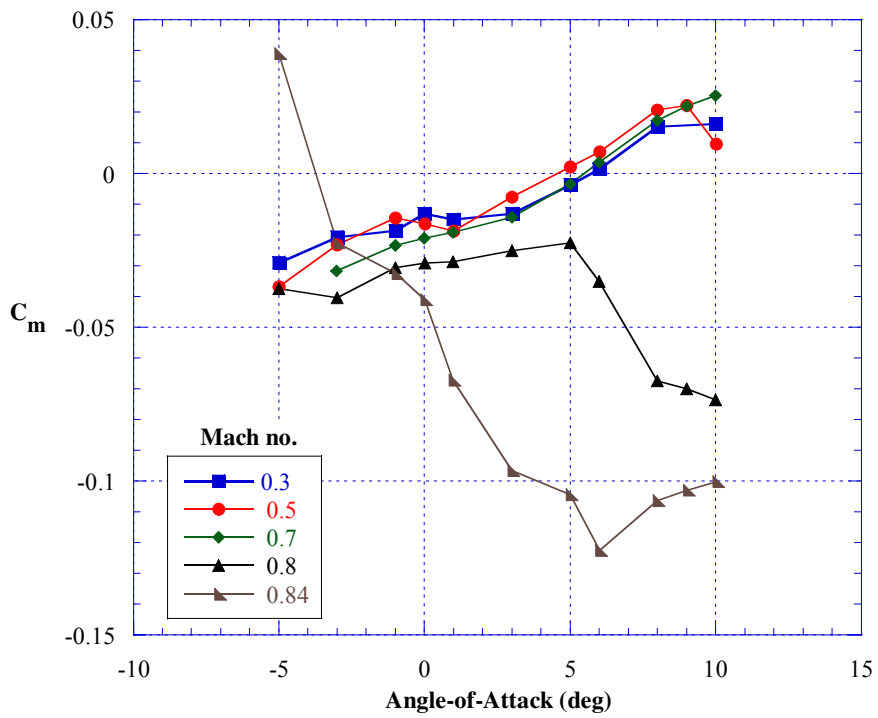
References

- 1) Novak, C.J.; Cornelius, K.C.; Road, R.K.: Experimental Investigations of Circular Wall Jet on a Circulation Control Airfoil. AIAA 87-0155, Jan. 1987.
- 2) Englar, R.J.: Investigations Into and Application of the High Velocity Circulation Control Wall Jet for High Lift and Drag Generation on STOL Aircraft. AIAA 74-502, June 1974.
- 3) Cheesman, I.C.; and Seed, A.R.: The Application of Circulation Control by Blowing to Helicopter Rotors. *Journal of Royal Aeronautical Society*, Vol. 71, No. 848, July 1966.
- 4) Englar, R.J.: Two Dimensional Transonic Wind Tunnel Tests of Three 15-Percent-Thick Circulation Control Airfoils. Naval Ship R&D Center Report ASED-182 (AD 882-075), December 1970.
- 5) Mavis, D.N.; Kirby, M.R.: Takeoff/Landing Assessment of an HSCT with Pneumatic Lift Augmentation. AIAA-99-0534, Jan. 1999.
- 6) Abramson, J.; Rogers, E.O.: High Speed Characteristics of Circulation Control Airfoils. AIAA 83-0265, Jan. 1983.
- 7) Abramson, J.: The Low Speed Characteristics of a 15-Percent Quasi-Elliptical Circulation Control Airfoil with Distributed Camber. David W. Taylor Naval Ship R&D Center Report DTNSRDC/ASED-79/07 (AD-A084-176), May 1979.
- 8) Nielsen, J. N.; and Bigger, J. C.: Recent Progress in Circulation Control Aerodynamics. AIAA Paper 87-0001, Jan. 1987.
- 9) Englar, R. J.: Circulation Control for High Lift and Drag Generation on STOL Airfoil. *Journal of Aircraft*, Vol. 12, No. 6, 1975, pp. 457-463.
- 10) Englar, R. J.; Trobaugh, L. A.; and Hemmerly, R. A.: STOL Potential of the Circulation Control Wing for High Performance Airfoil. *Journal of Aircraft*, Vol. 15, No. 3, 1978.
- 11) Nichols, J. H. Jr.; Englar, R. J.; Harris, M. J.; and Hason, G. G.: Experimental Development of an Advanced Circulation Control Wing System for Navy STOL Airfoil. ALKA Paper, 81-8151, 1981.
- 12) Englar, Robert J.; Smith, Marilyn J.; Kelley, Sean M.; and Rover III, Richard C.: Application of Circulation Control Technology to Advanced Subsonic Transport Aircraft, Part I: Airfoil 14 Development. AIAA Paper No. 93-0644; *Journal of Aircraft*, Vol. 31, No. 5, Sept-Oct. 1994, pp. 1160-1168.
- 13) Kind, R. J.; and Maull, D. J.: An Experimental Investigation of a Low-Speed Circulation-Controlled Aerofoil. *The Aeronautical Quarterly*, Vol. 19, May 1968, pp. 170-182.
- 14) Wood, N. J.; and Nielsen, J. N.: Circulation Control Airfoil-Past, Present, and Future. AIAA Paper 85-0204, Jan. 1985.
- 15) Rogers, E.O.: Development of Compressible Flow Similarity Concepts for Circulation Control Airfoils. AIAA-87-0153, January 1987.

- 16) Hoerner, Sighard, F.: Fluid-Dynamic Lift. Hoerner Fluid Dynamics, 2nd Edition, June 1992.
- 17) Blevins, Robert, D.: Applied Fluid Dynamics Handbook. Krieger Publishing Company, Reprint Edition June 2002.
- 18) Holmes, J. D.: Transition Trip Technique Study in the McAir Advanced Design Wind Tunnel. Technical Memorandum 4395, May 1984.
- 19) Staff, Aeroelasticity Branch.: *The Langley Transonic Dynamics Tunnel*. LWP-799, September 23, 1969.
- 20) Krause, Lloyd, N.: *Effects of Pressure-Rake Design Parameters on Static-Pressure Measurements for Rakes Used In Subsonic Flow*. NACA-TN 2520, Oct. 1951.
- 21) Englar, R.J.; Williams, R.M.: Test Techniques for High Lift, Two-Dimensional Airfoils with Boundary Layer and Circulation Control for Application to Rotary Aircraft. Naval Ship Research and Development Center, Report 4645, July 1975.
- 22) Baals, Donald D.; and Mourhess, Mary J.: *Numerical Evaluation of the Wake-Survey Equations for Subsonic Flow Including the Effect of Energy Addition*. NACA WR L-5 H27, 1945.
- 23) McLachlan, B.G.: *On The Effect of Leading Edge Blowing On Circulation Control Airfoil Aerodynamics*. Proceedings of the Circulation-Control Workshop, NASA Ames Research Center, NASA CP 2432, February 18-21, 1986.
- 24) Raymer, Daniel P.: Aircraft Design: A Conceptual Approach. 3rd Edition, 1999.
- 25) Staff of the Propulsion Aerodynamics Branch: *Data Reduction Formulas for the 16-Foot Transonic Tunnel*. Revision 2, NASA Technical Memorandum 107646, July 1992.
- 26) Englar, R. J. and R.M. Williams.: Test Techniques for High-Lift Airfoils with Boundary Layer and Circulation Control for Application to Rotary Wing Aircraft. *Canadian Aeronautics and Space Journal*, Vol. 19, No. 3, pp. 93-108, March 1973.



(a)



(b)

Figure 19 – Airfoil performance, Mach number effect, no blowing.

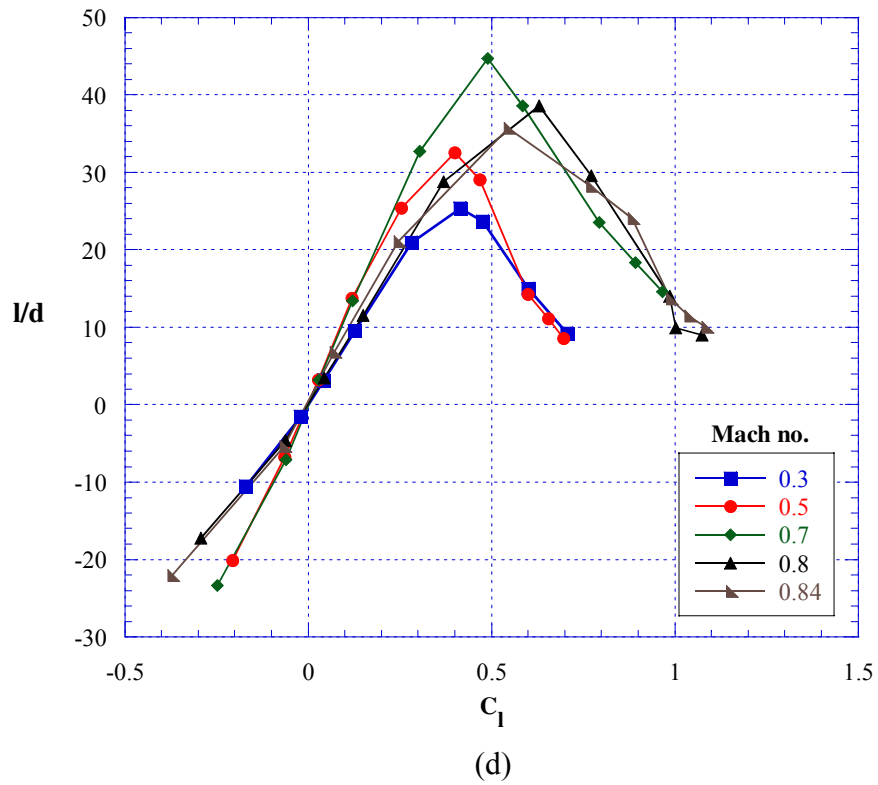
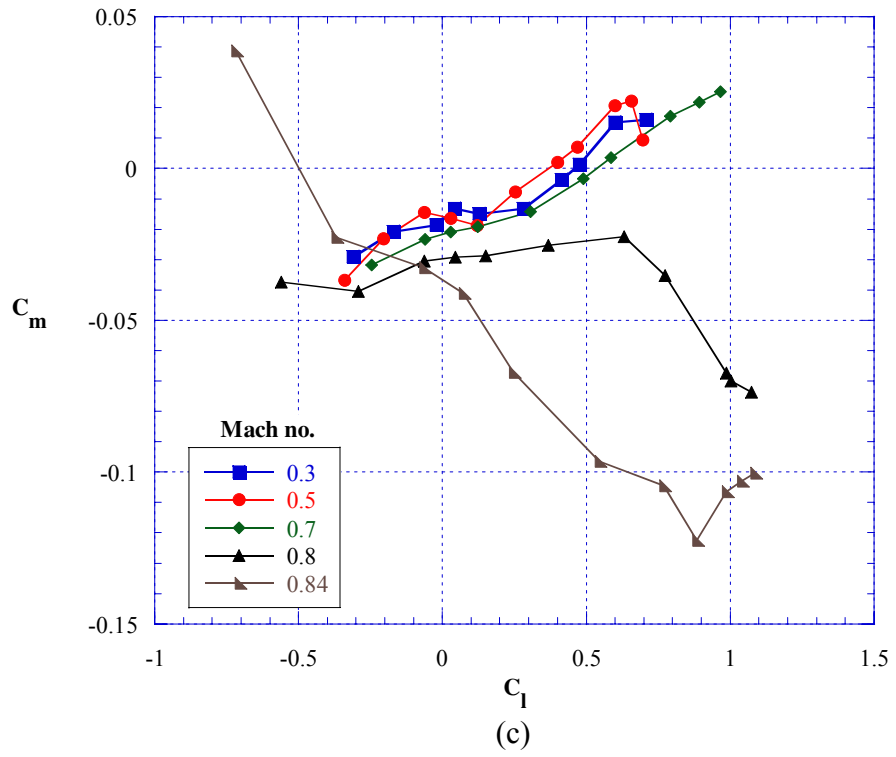
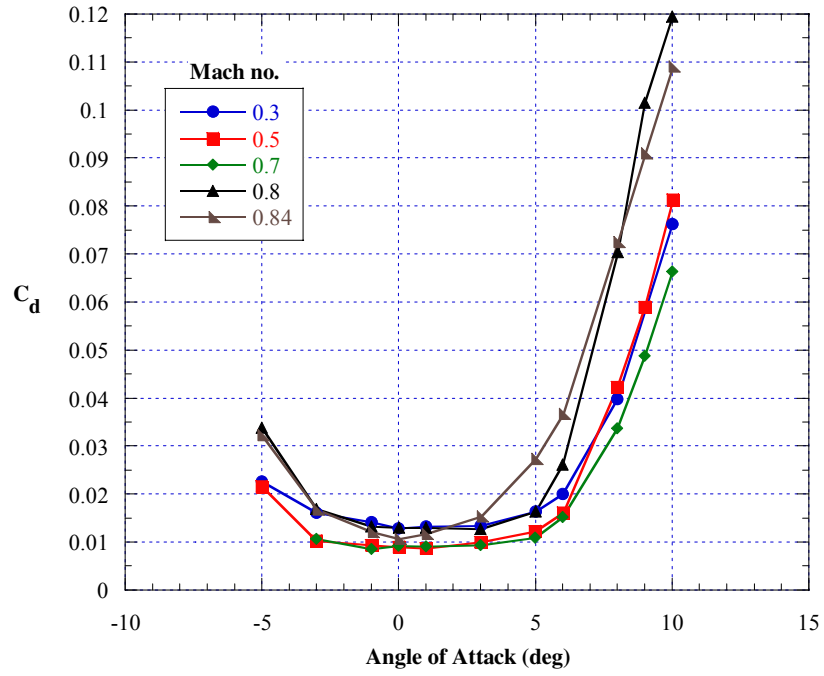
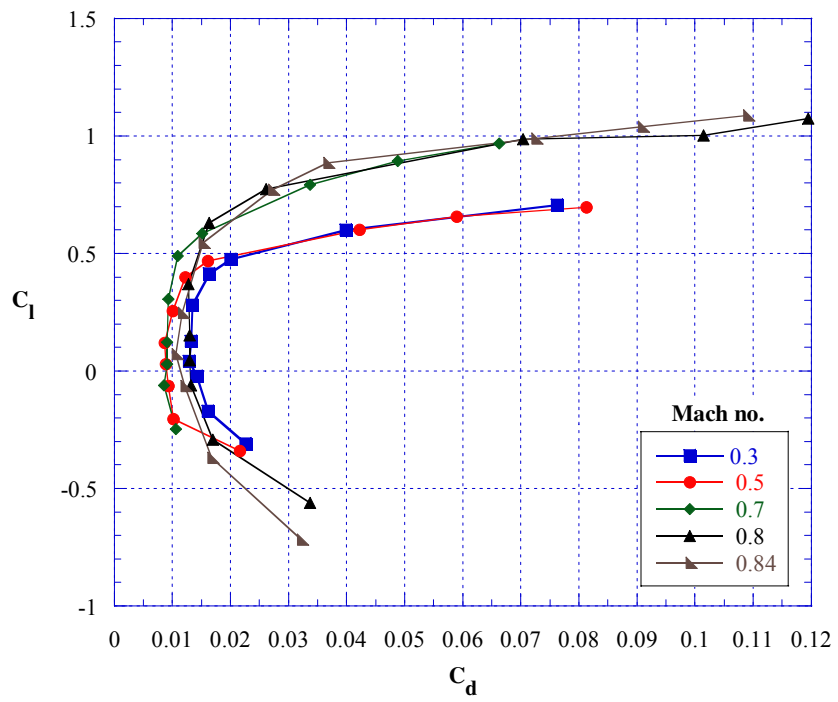


Figure 19 – Continued.

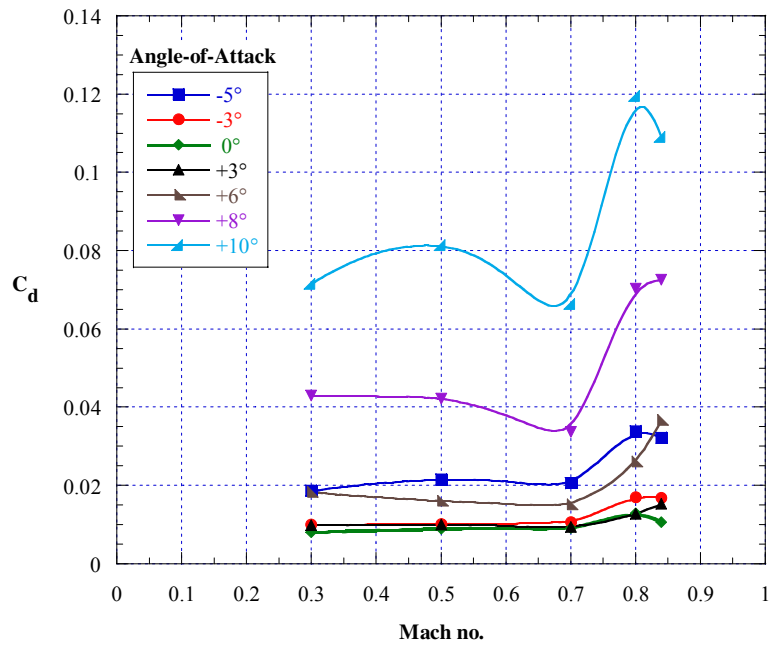


(e)



(f)

Figure 19 – Continued.



(g)

Figure 19 – Concluded.

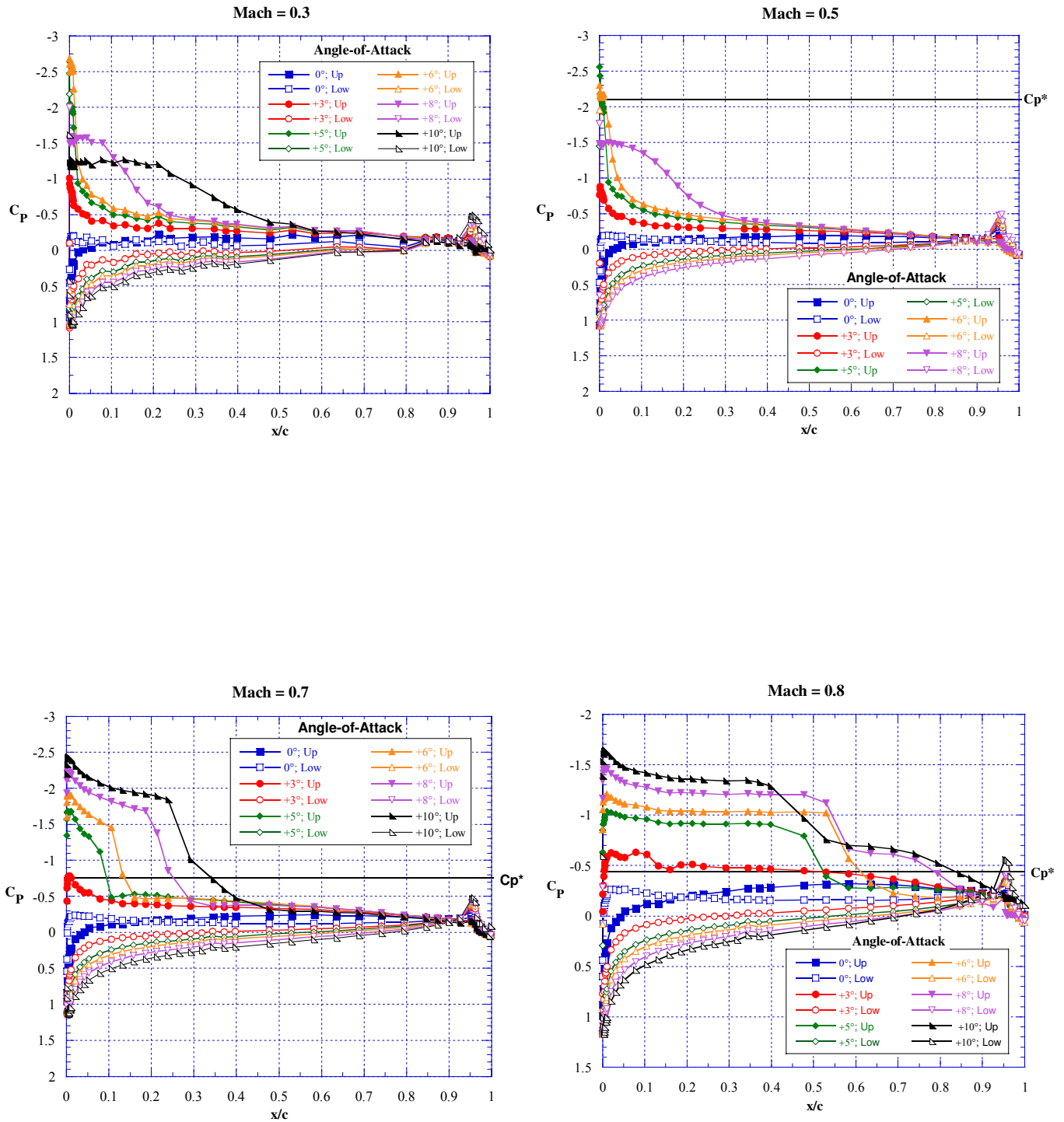


Figure 20 – Chordwise pressure distribution, angle of attack effect, no blowing, Coanda (2.98:1), slot ($h/c = 0.0012$).

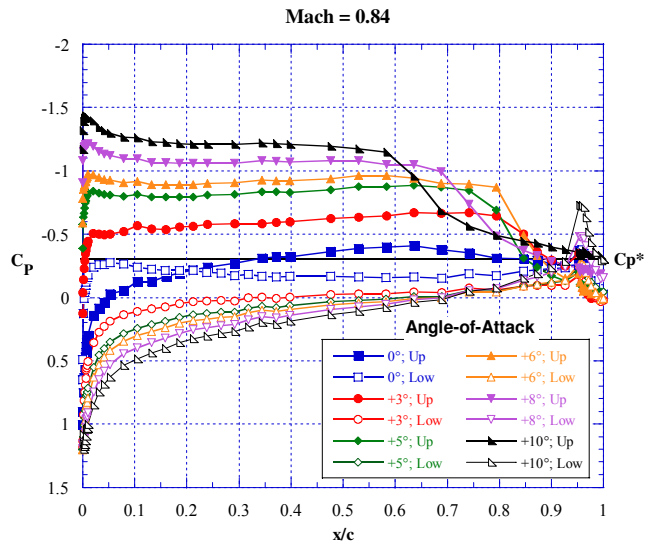


Figure 20 – Concluded.

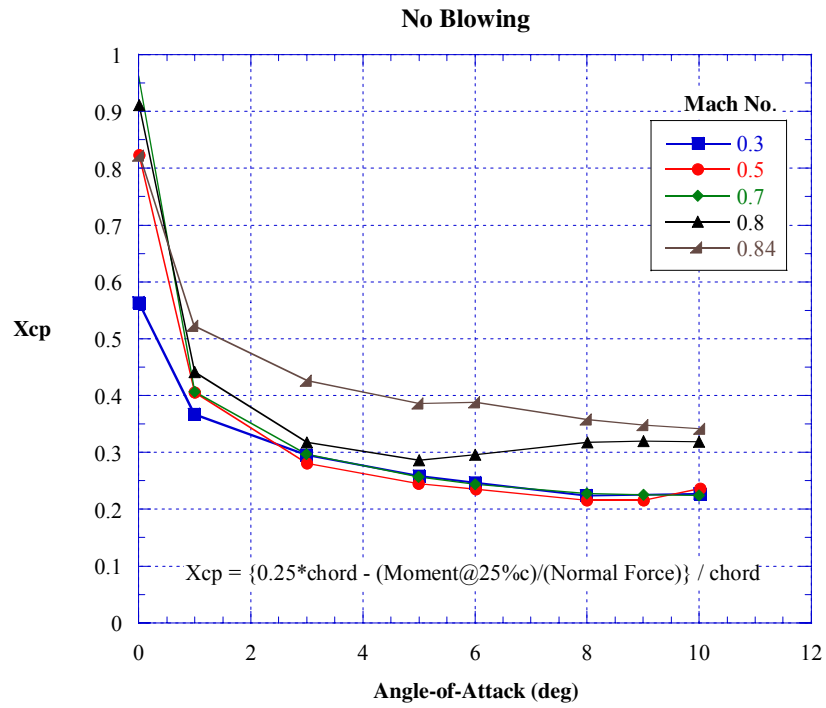
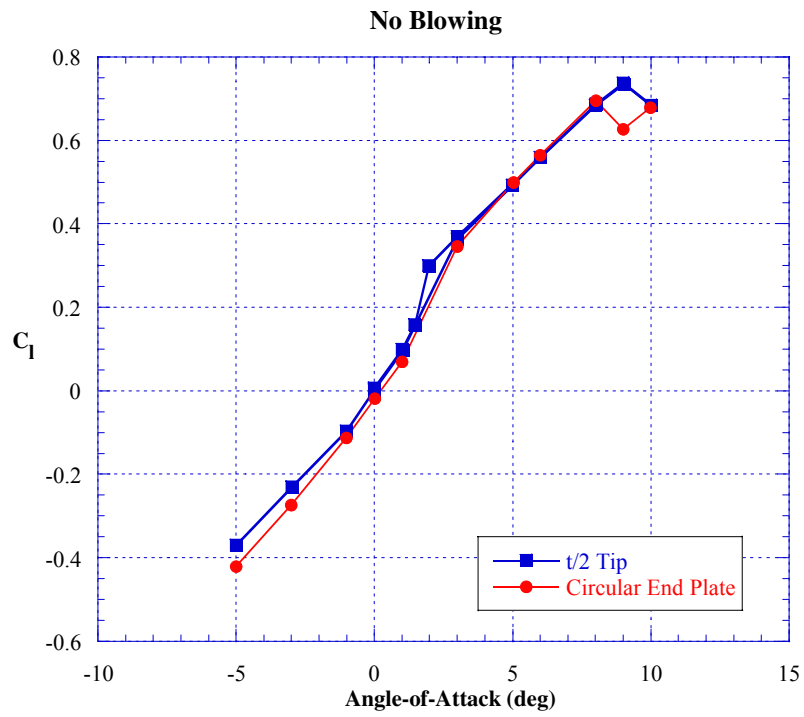
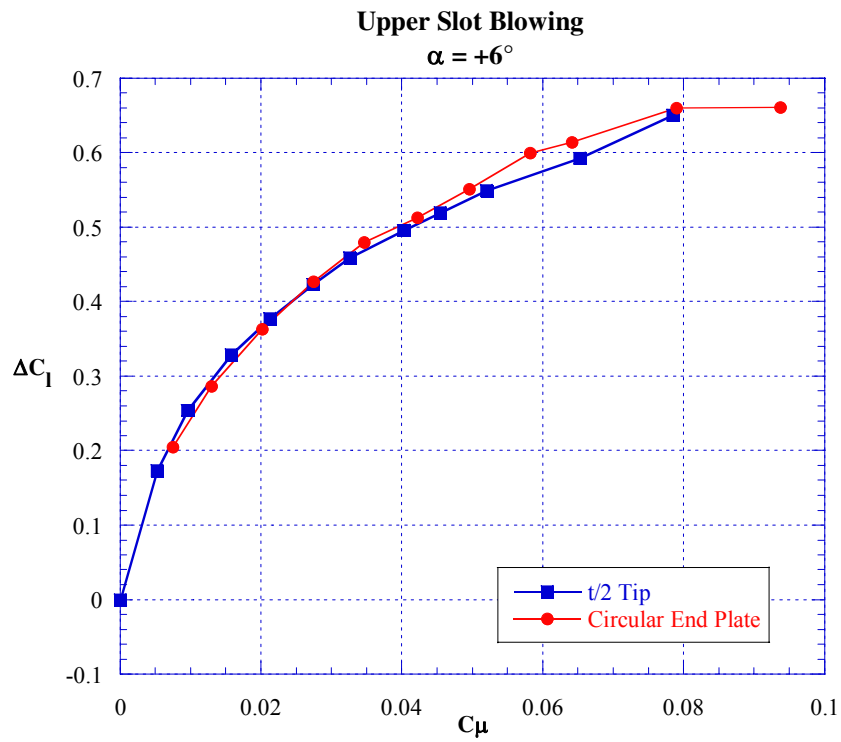


Figure 21 – Center of pressure versus angle of attack, Mach number effect no blowing, Coanda (2.98:1), slot ($h/c = 0.0012$).

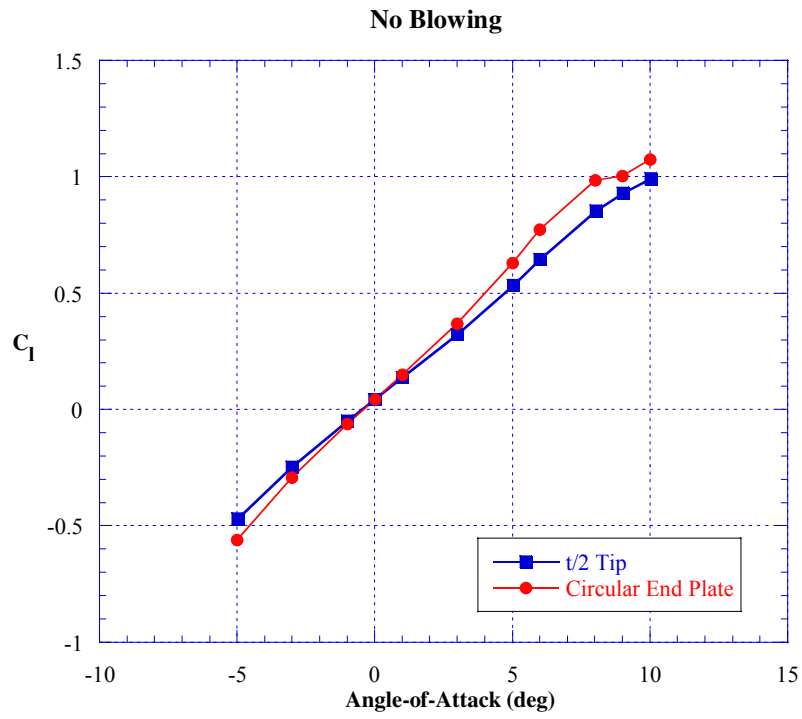


(a)

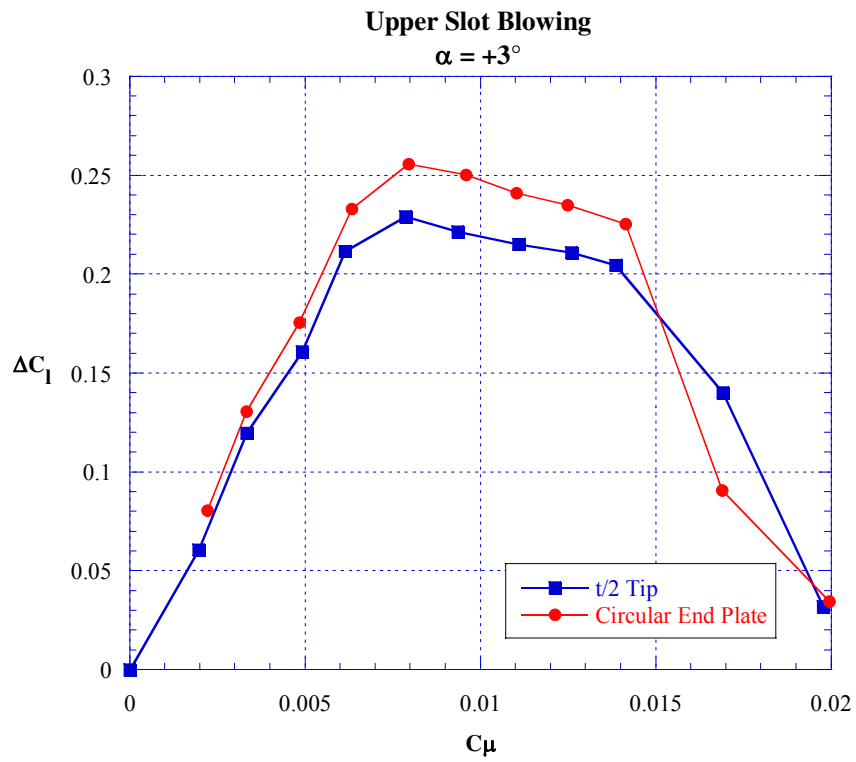


(b)

Figure 22 – End plate effects, Mach = 0.3.



(a)



(b)

Figure 23 – End plate effects, Mach = 0.8.

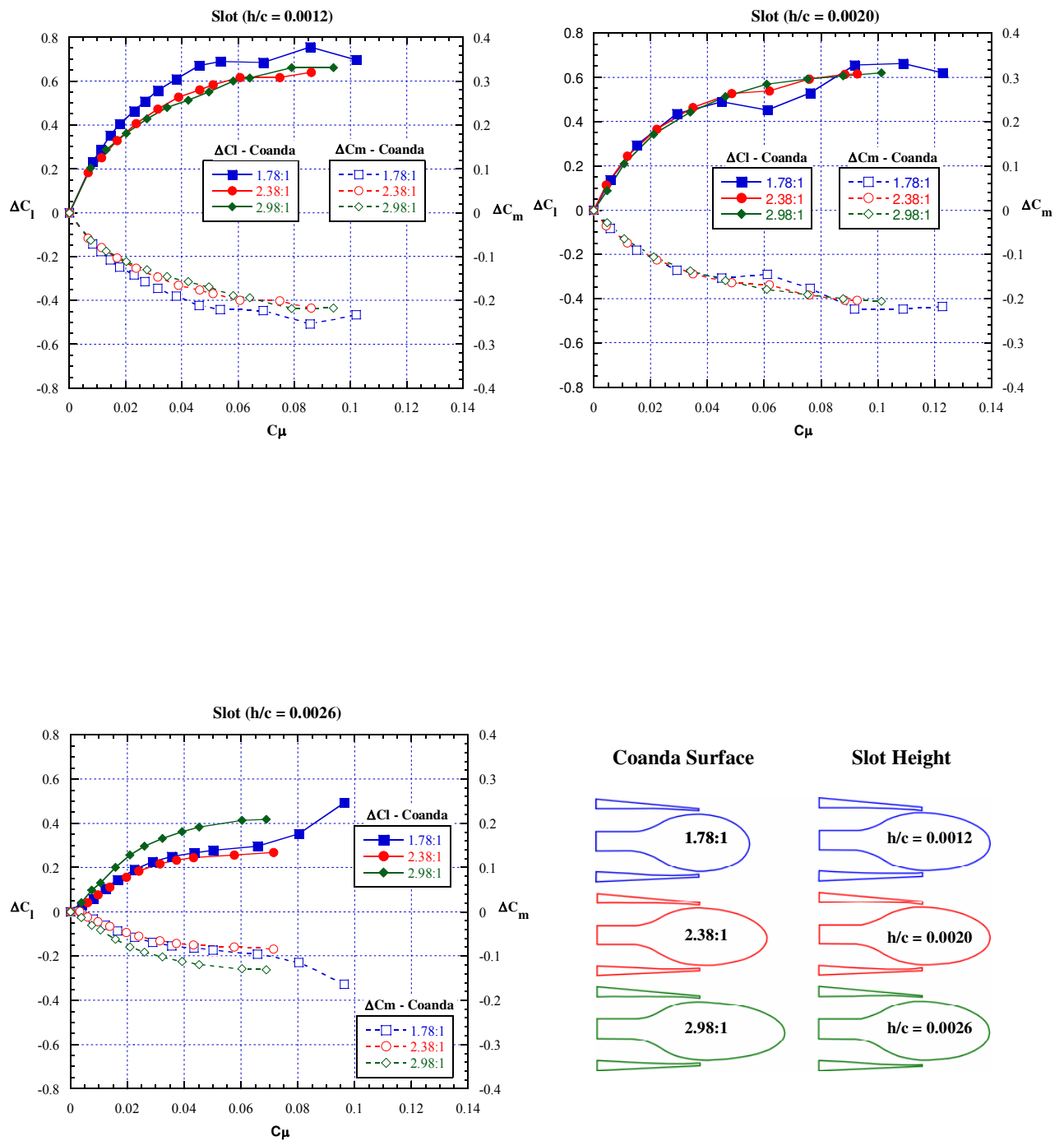


Figure 24 – ΔC_l & ΔC_m versus C_μ , Coanda surface effect, upper slot blowing, Mach = 0.3, $\alpha = 6^\circ$.

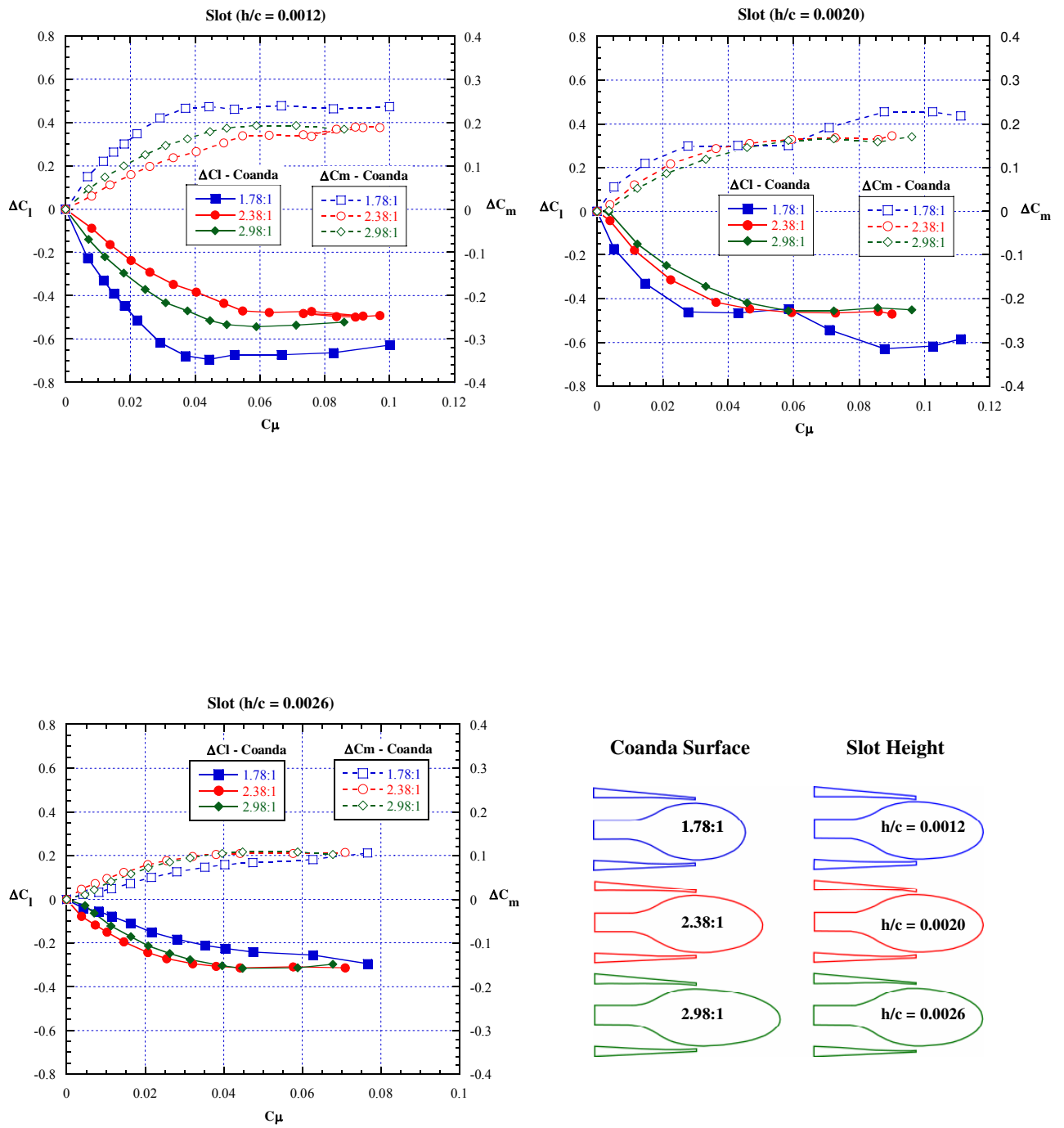


Figure 25 – ΔC_l & ΔC_m versus C_μ , Coanda surface effect, lower slot blowing, Mach = 0.3, $\alpha = 6^\circ$.

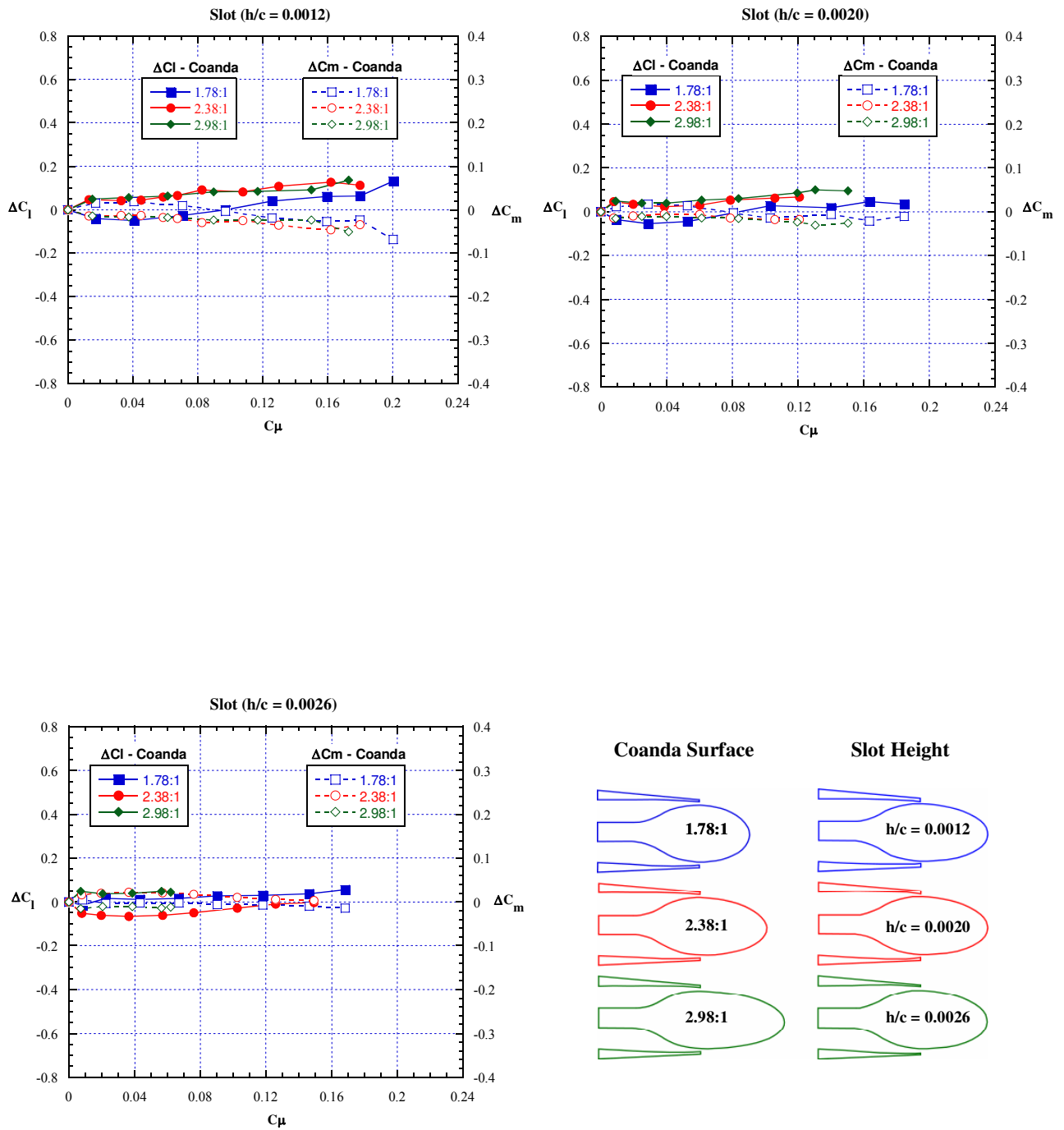


Figure 26 – ΔC_l & ΔC_m versus C_μ , Coanda surface effect, dual slot blowing, Mach = 0.3, $\alpha = 6^\circ$.

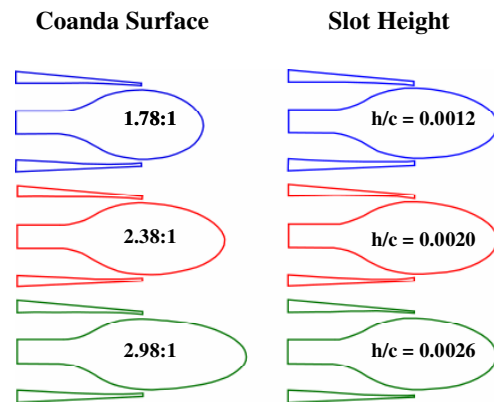
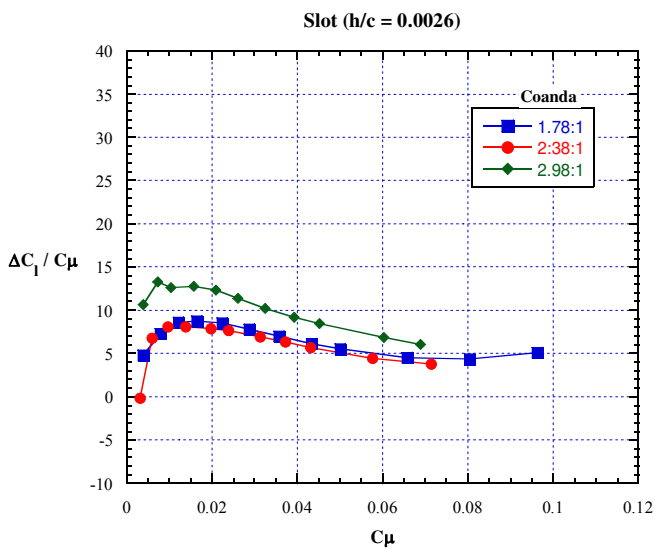
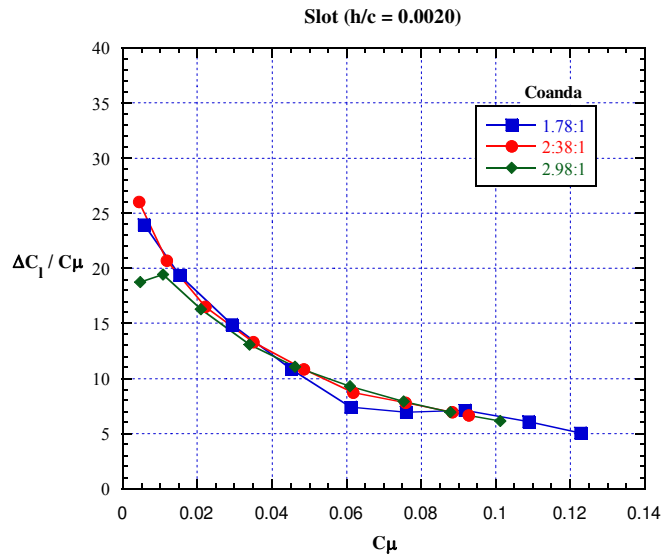
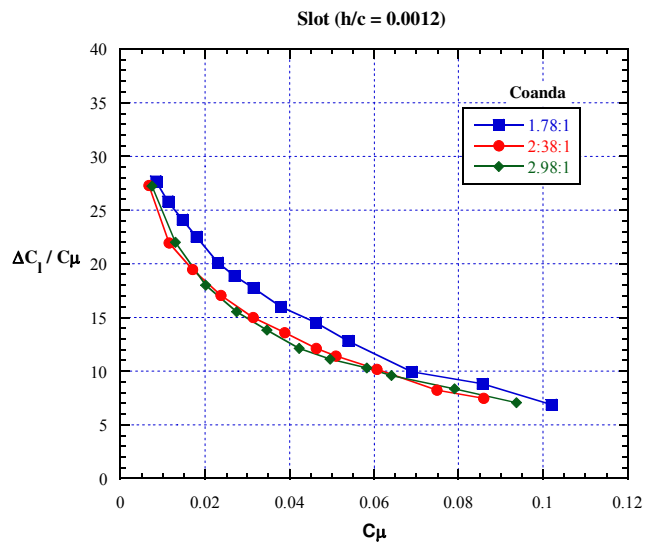


Figure 27 – Lift augmentation ratio versus C_μ , Coanda surface effect, upper slot blowing, Mach = 0.3, $\alpha = 6^\circ$.

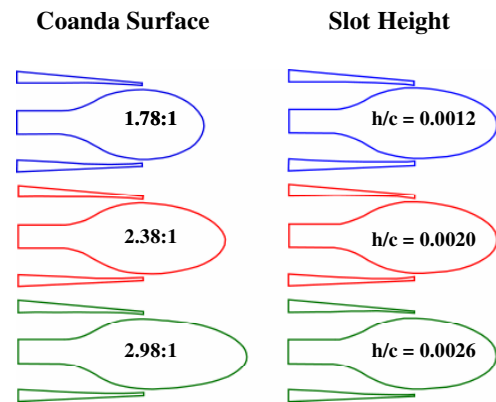
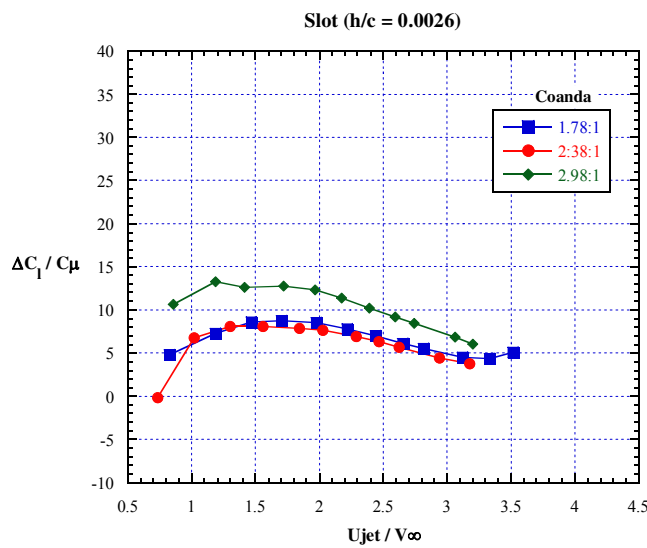
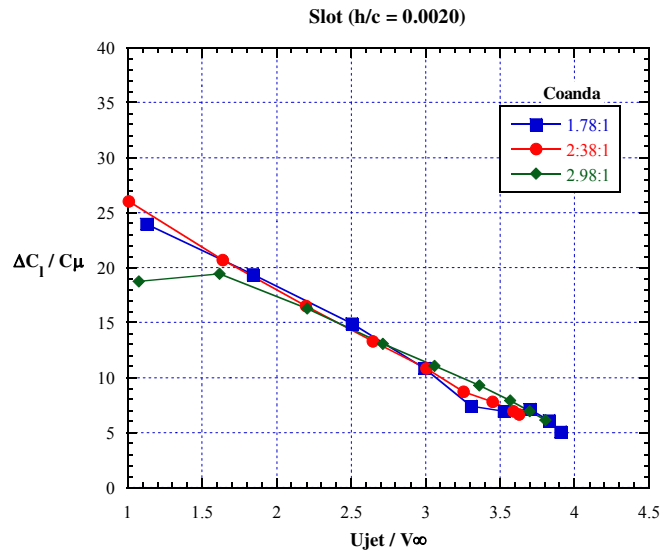
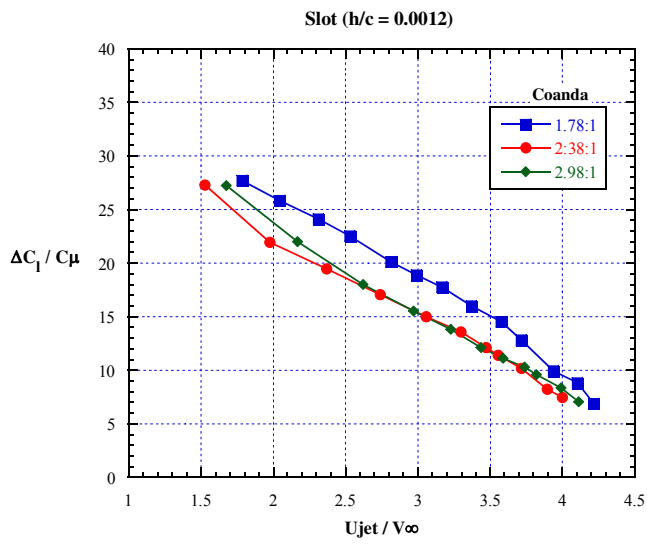


Figure 28 – Lift augmentation ratio versus velocity ratio, Coanda surface effect, upper slot blowing, Mach = 0.3, $\alpha = 6^\circ$.

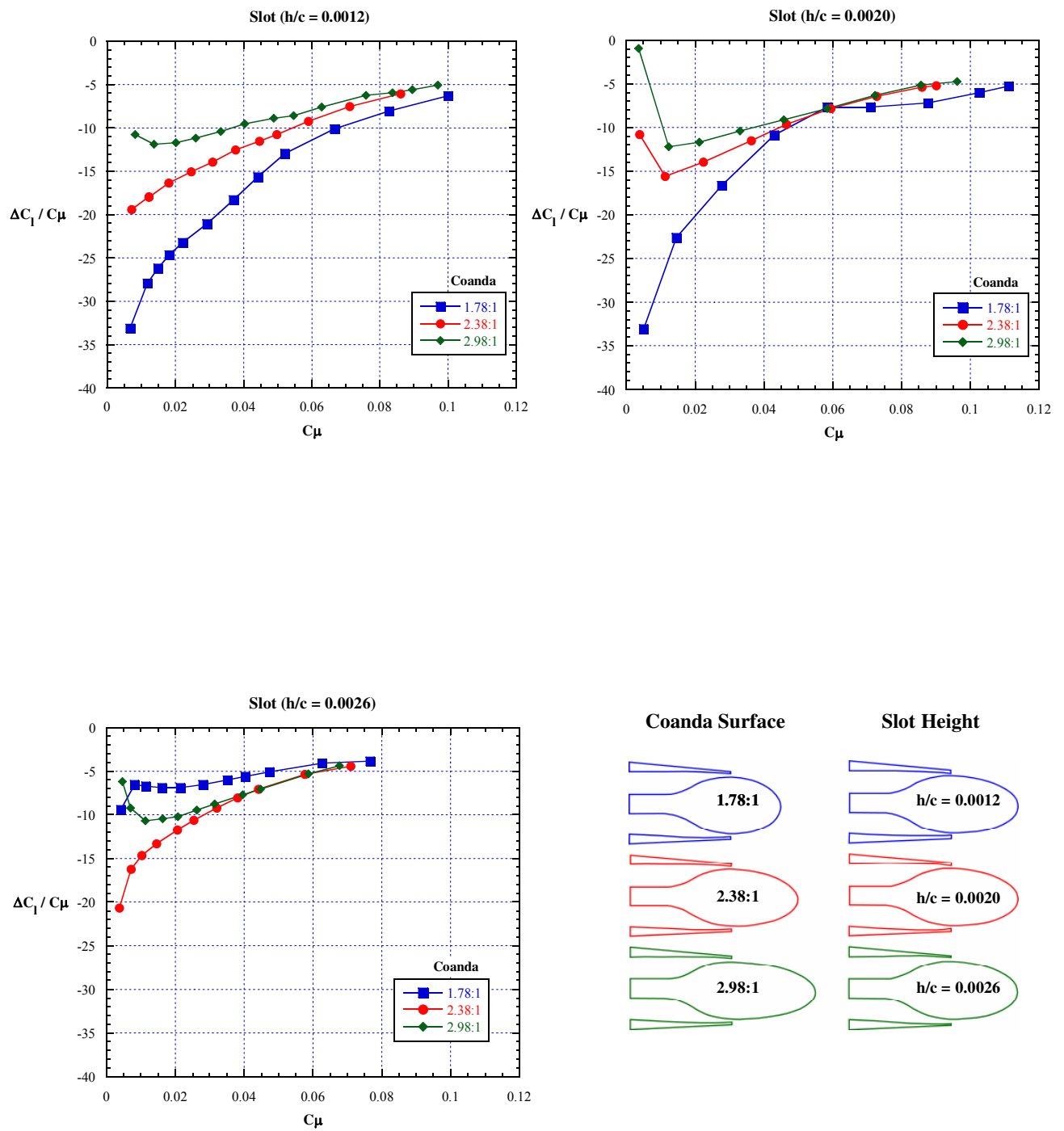


Figure 29 – Lift augmentation ratio versus C_{μ} , Coanda surface effect, lower slot blowing, Mach = 0.3, $\alpha = 6^\circ$.

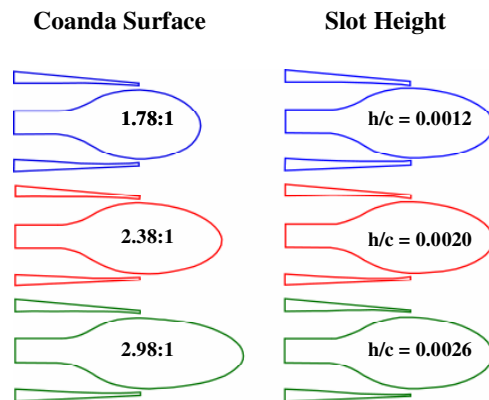
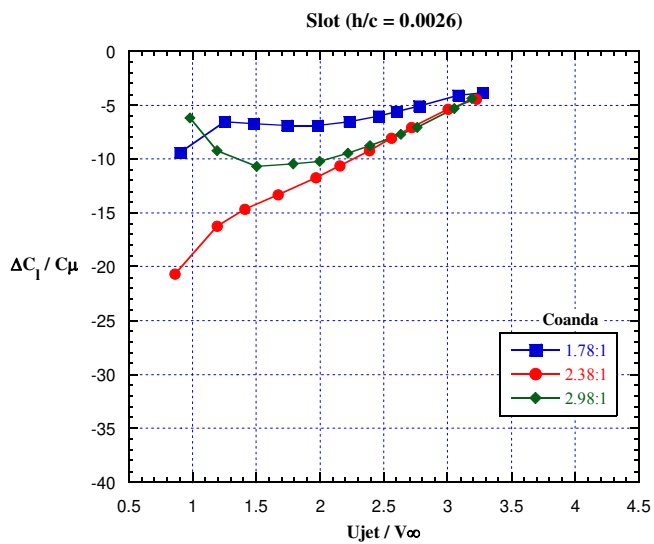
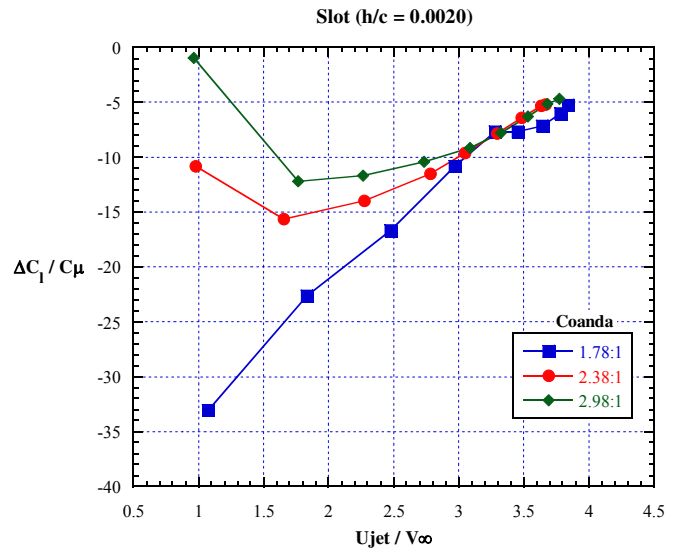
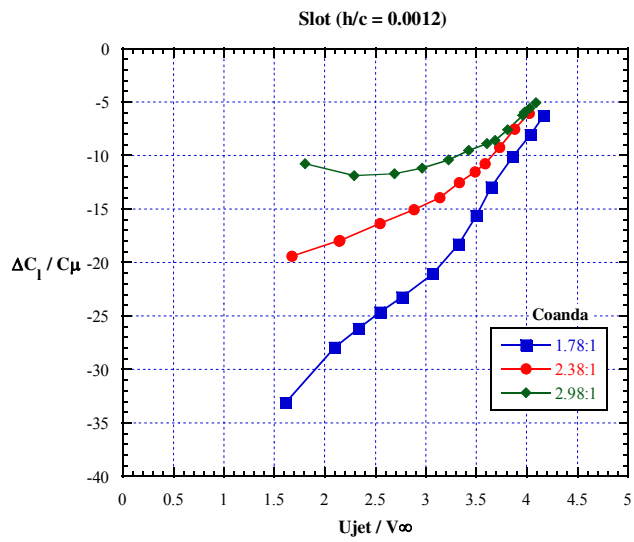


Figure 30 – Lift augmentation ratio versus velocity ratio, Coanda surface effect, lower slot blowing, Mach = 0.3, $\alpha = 6^\circ$.

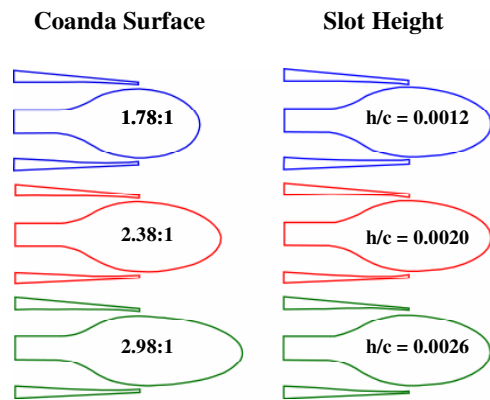
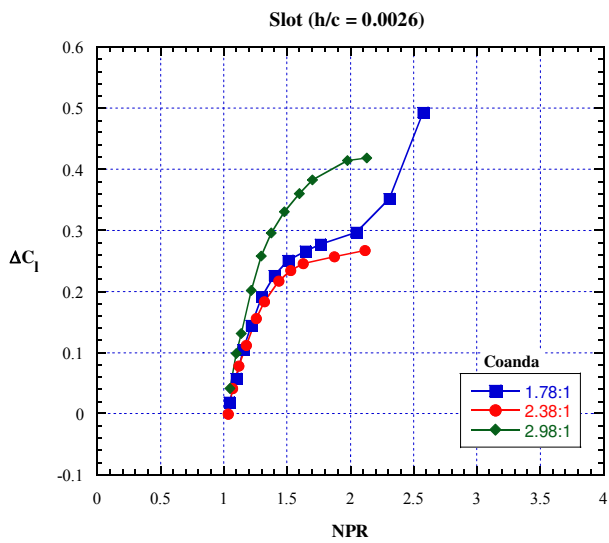
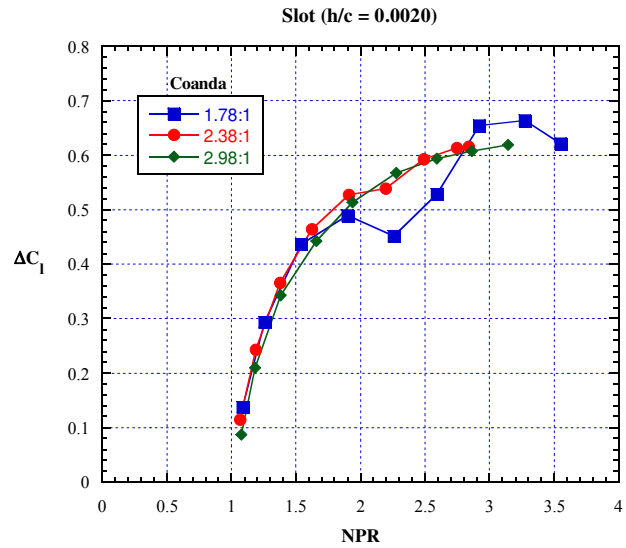
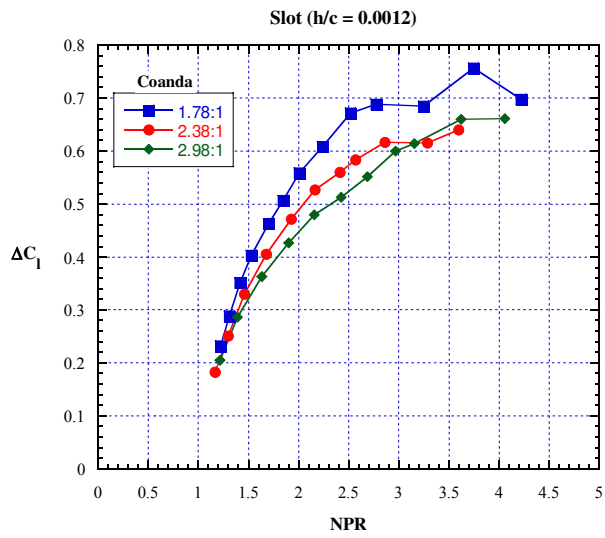


Figure 31 – ΔC_1 versus nozzle pressure ratio, Coanda surface effect, upper slot blowing, Mach = 0.3, $\alpha = 6^\circ$.

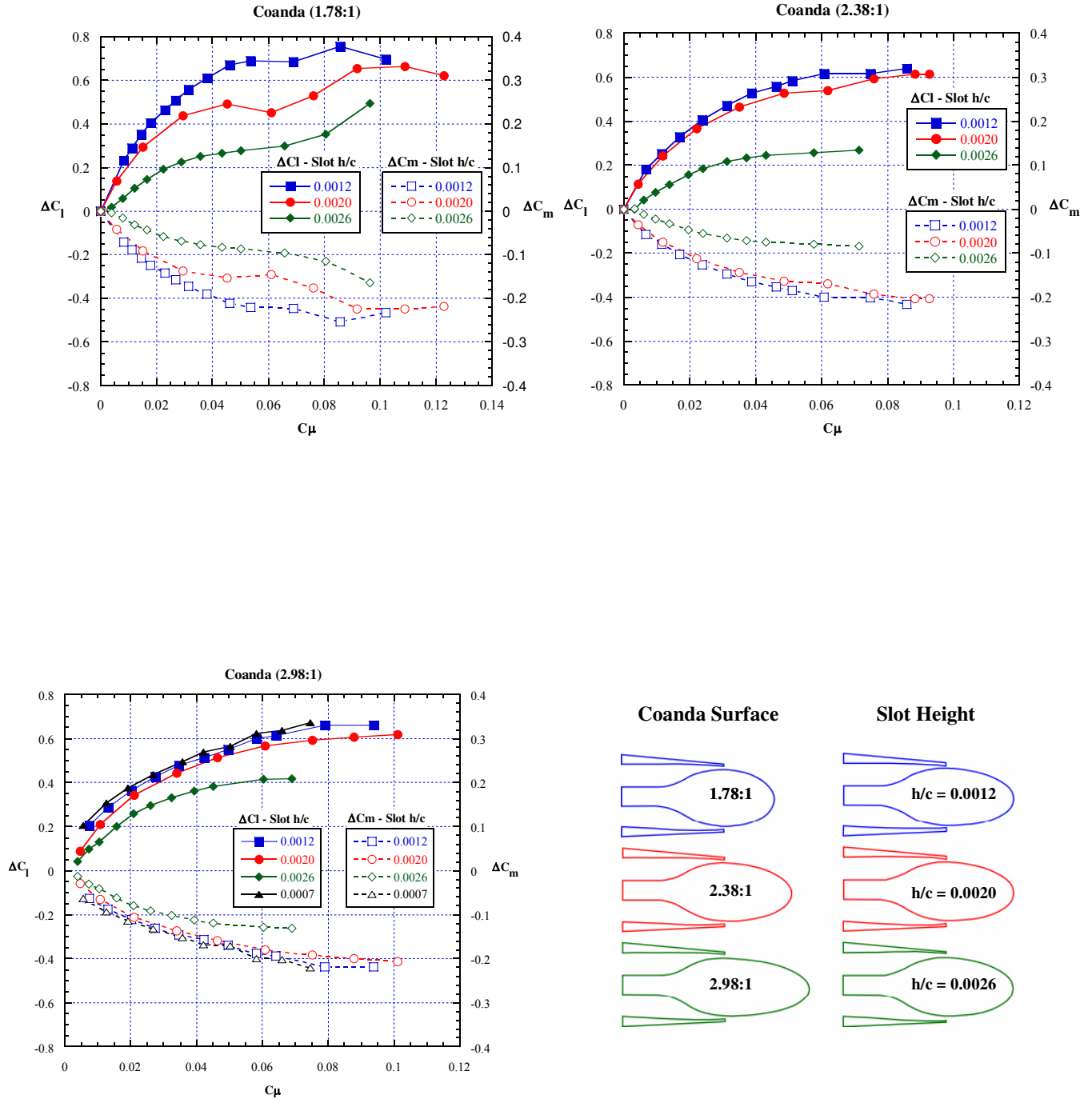


Figure 32 – ΔC_l & ΔC_m versus C_μ , slot height effect, upper slot blowing, Mach = 0.3, $\alpha = 6^\circ$.

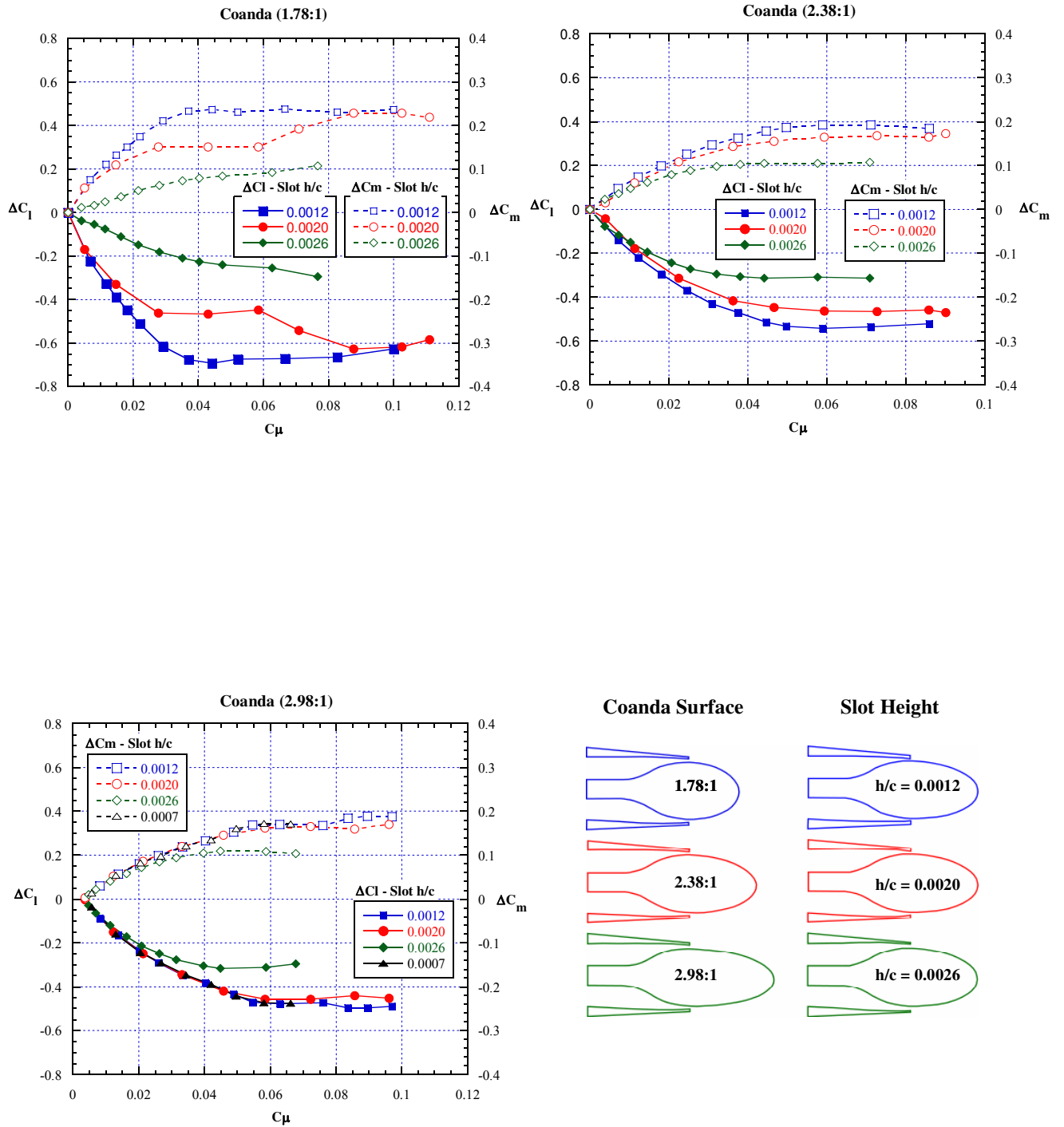


Figure 33 – ΔC_1 & ΔC_m versus C_μ , slot height effect, lower slot blowing, Mach = 0.3, $\alpha = 6^\circ$.

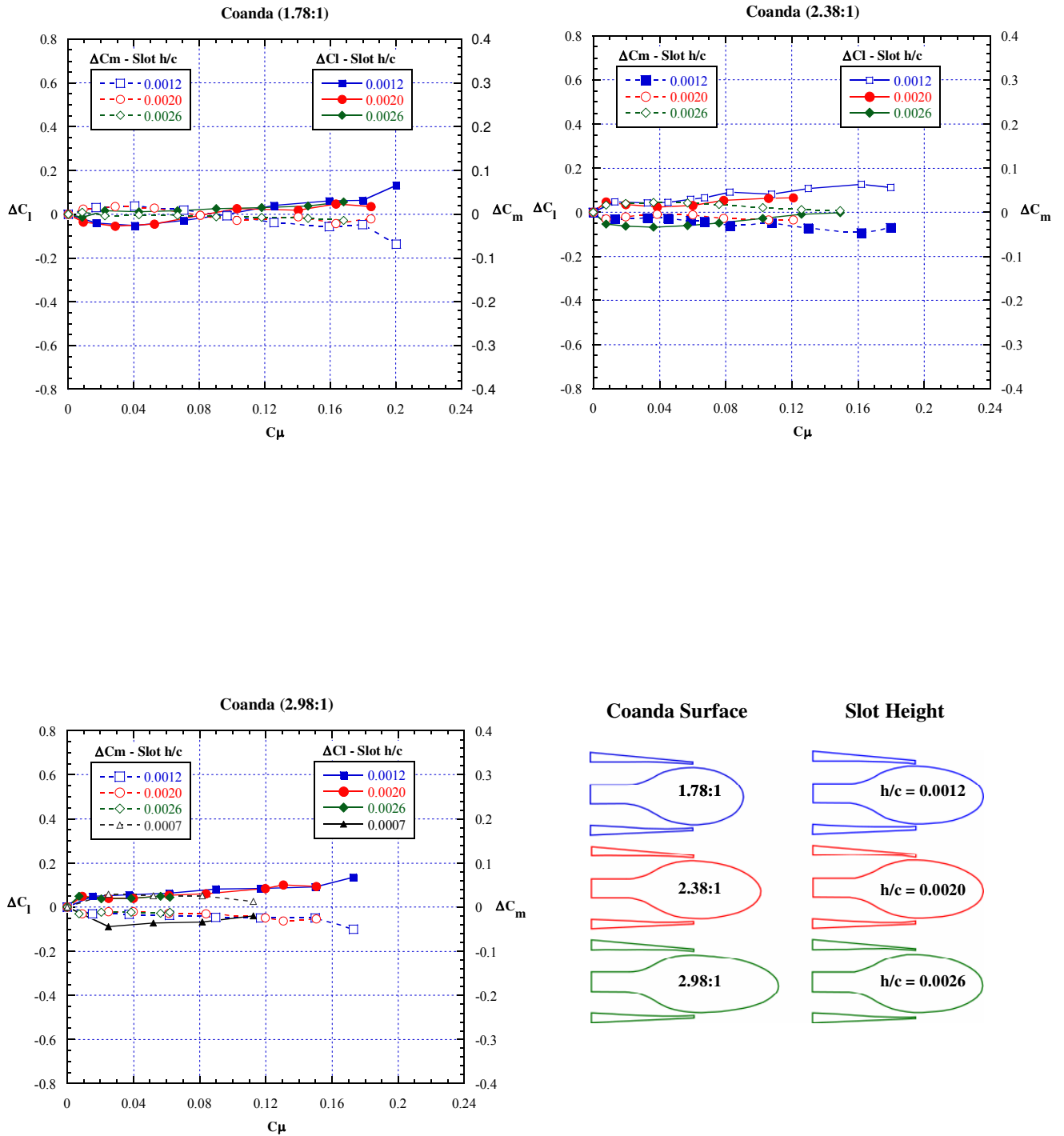


Figure 34 – ΔC_1 & ΔC_m versus C_μ , slot height effect, dual slot blowing, Mach = 0.3, $\alpha = 6^\circ$.

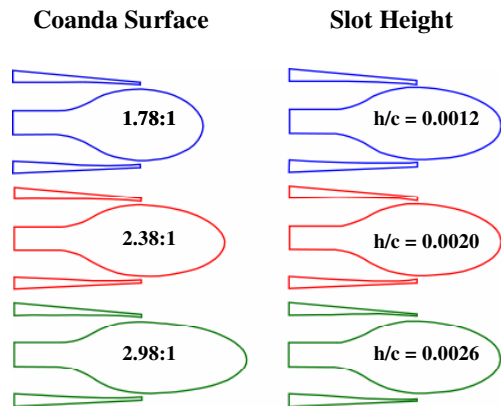
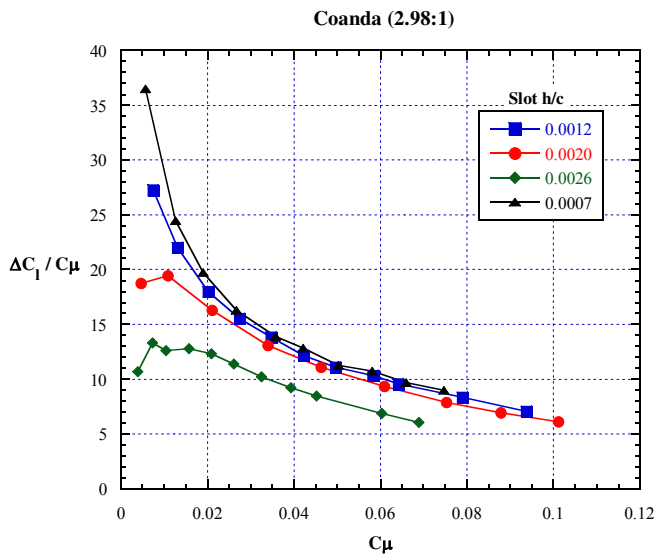
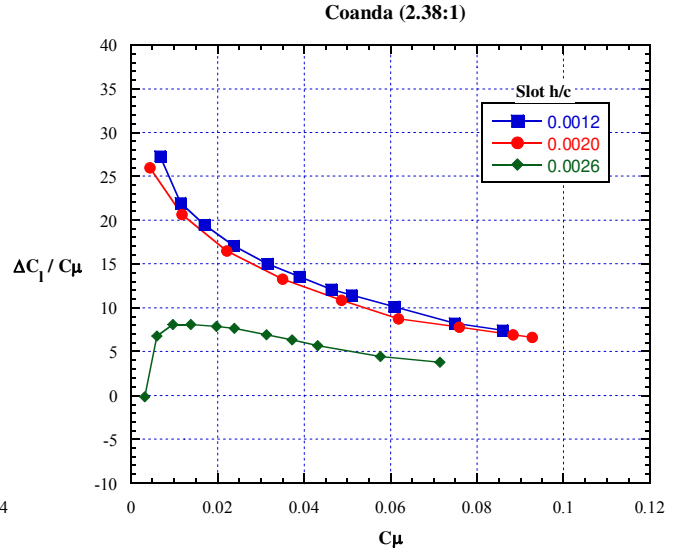
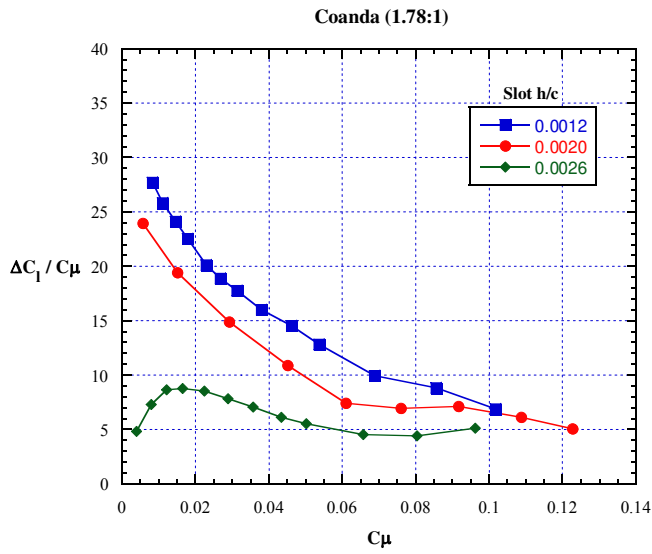


Figure 35 – Lift augmentation ratio versus C_μ , slot height effect, upper slot blowing, Mach = 0.3, $\alpha = 6^\circ$.

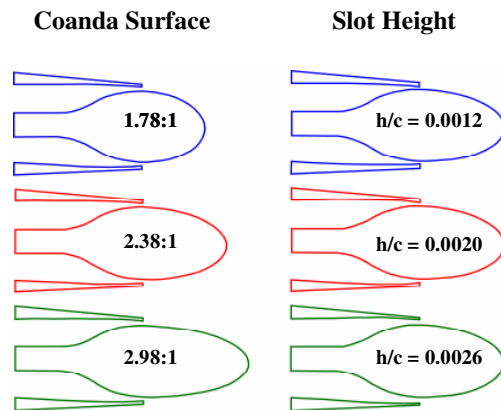
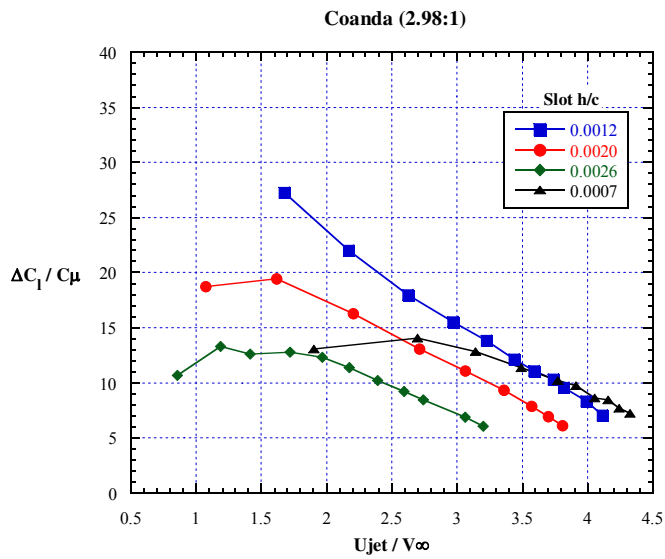
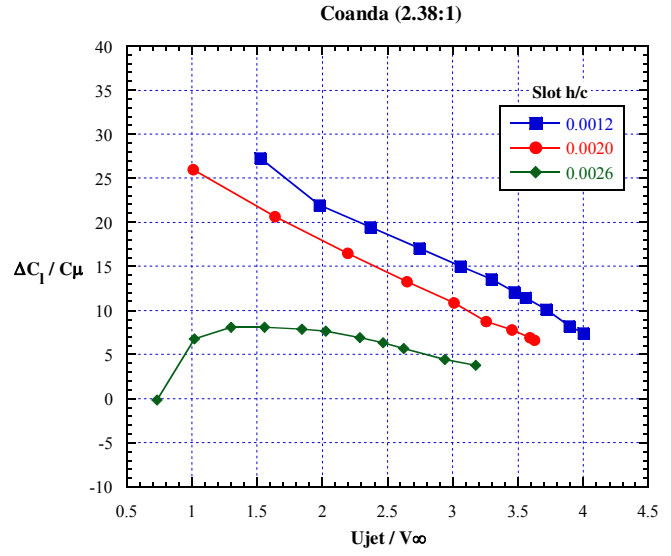
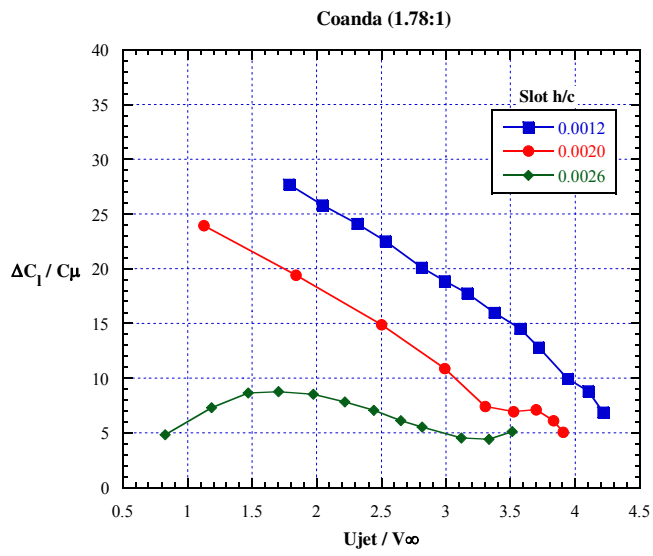


Figure 36 – Lift augmentation ratio versus velocity ratio, slot height effect, upper slot blowing, Mach = 0.3, $\alpha = 6^\circ$.

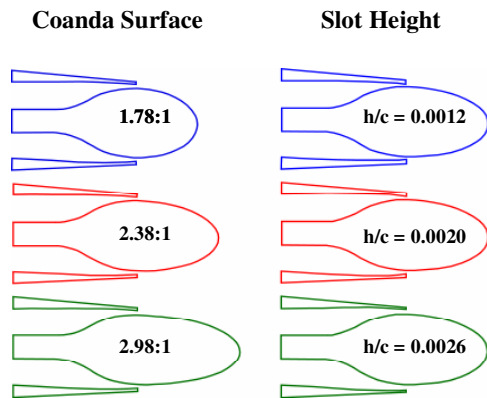
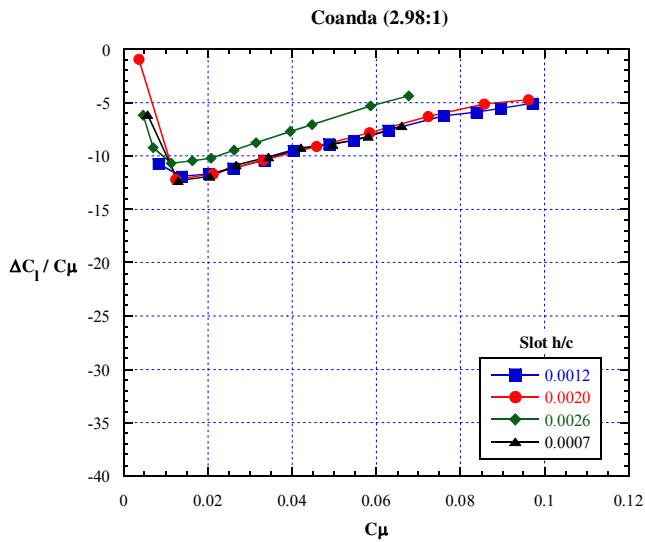
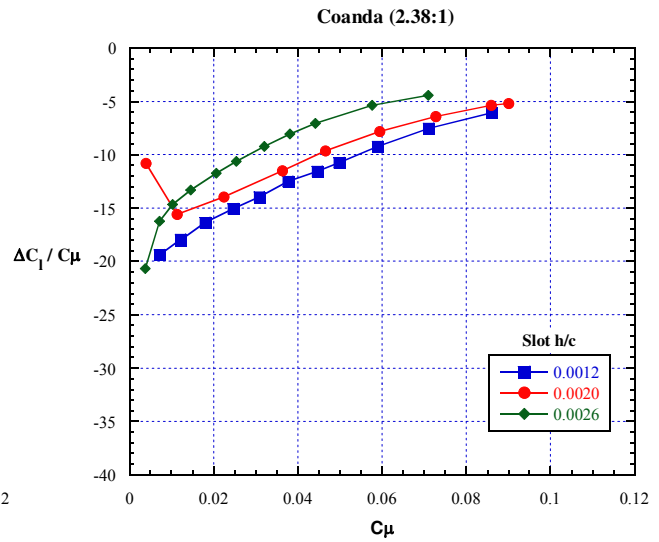
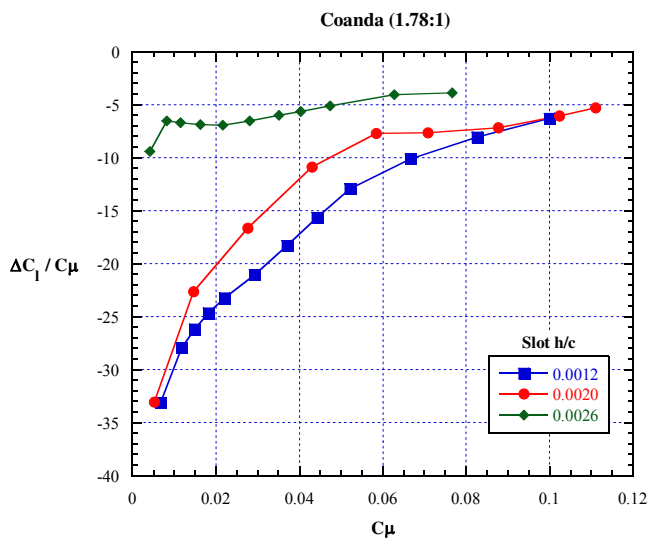


Figure 37 – Lift augmentation ratio versus C_{μ} , slot height effect, lower slot blowing, Mach = 0.3, $\alpha = 6^\circ$.

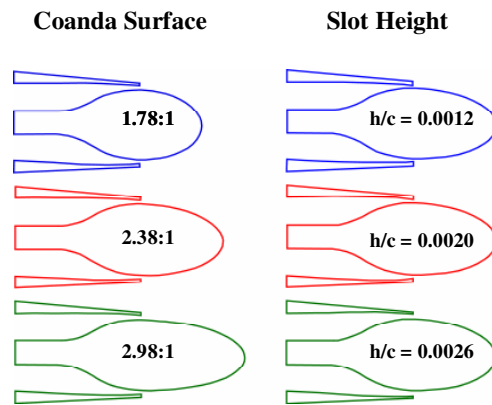
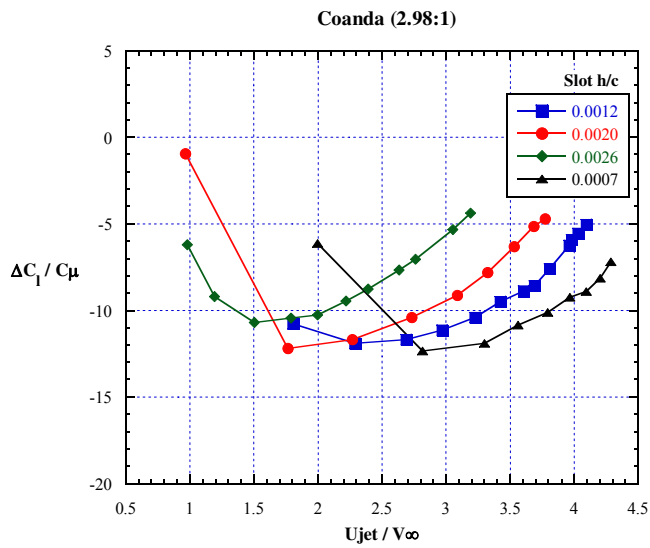
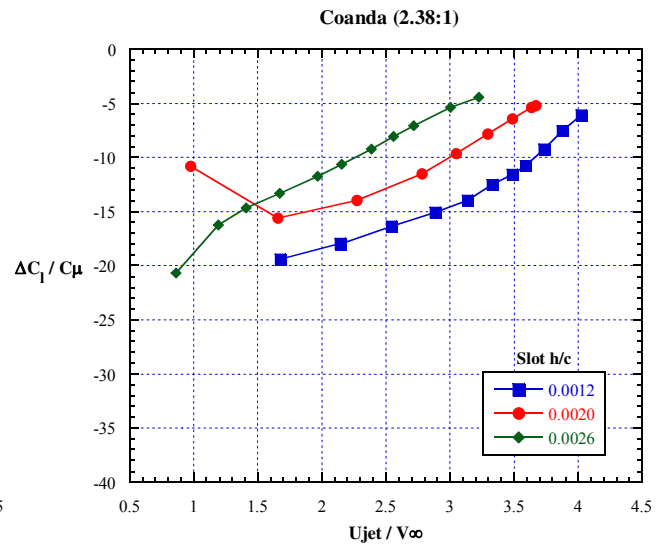
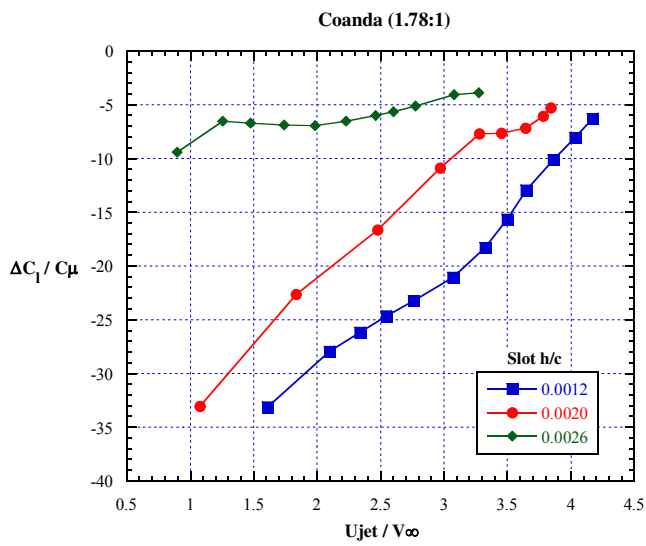


Figure 38 – Lift augmentation ratio versus velocity ratio, slot height effect, lower slot blowing, Mach = 0.3, $\alpha = 6^\circ$.

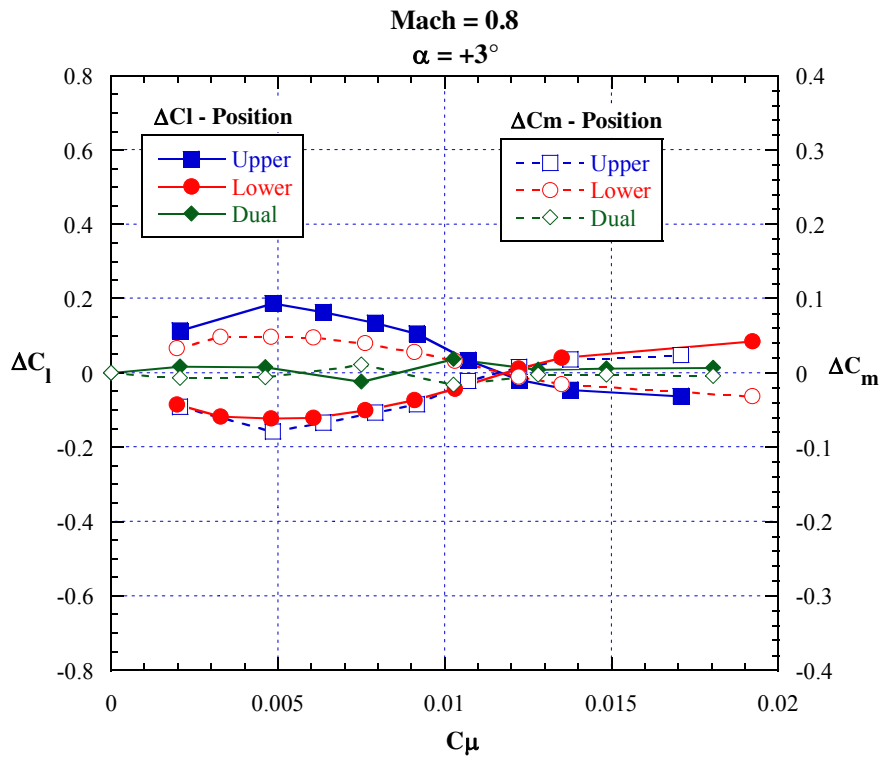
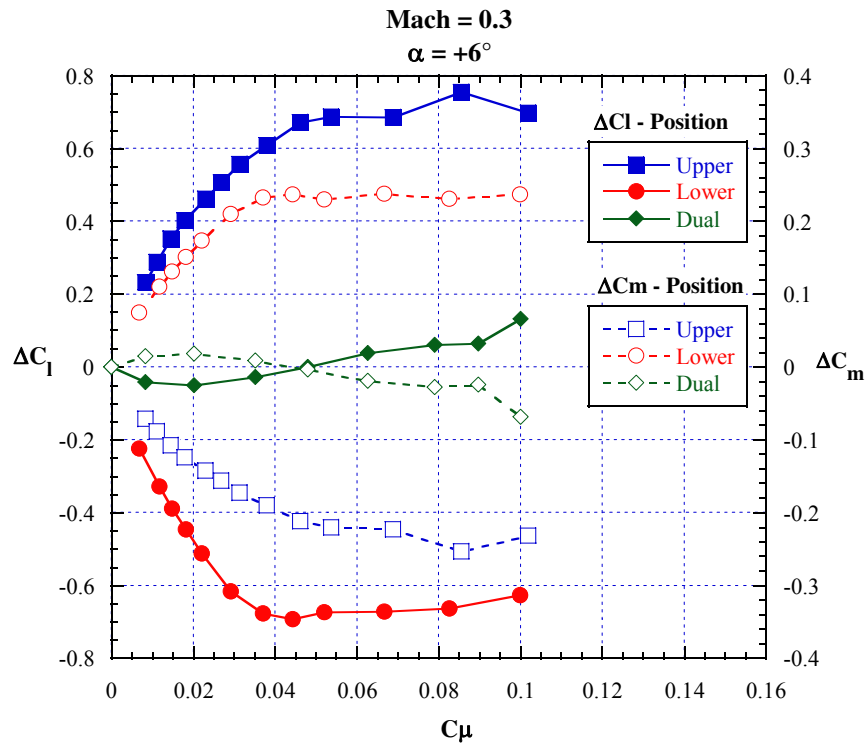


Figure 39 – ΔC_1 & ΔC_m versus C_μ , slot position effect, Coanda (1.78:1), slot ($h/c = 0.0012$).

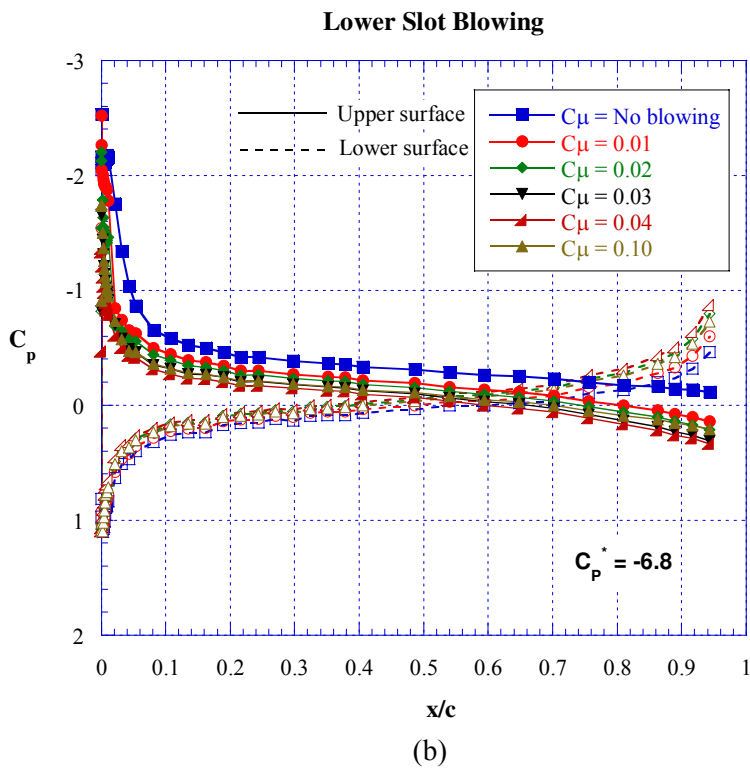
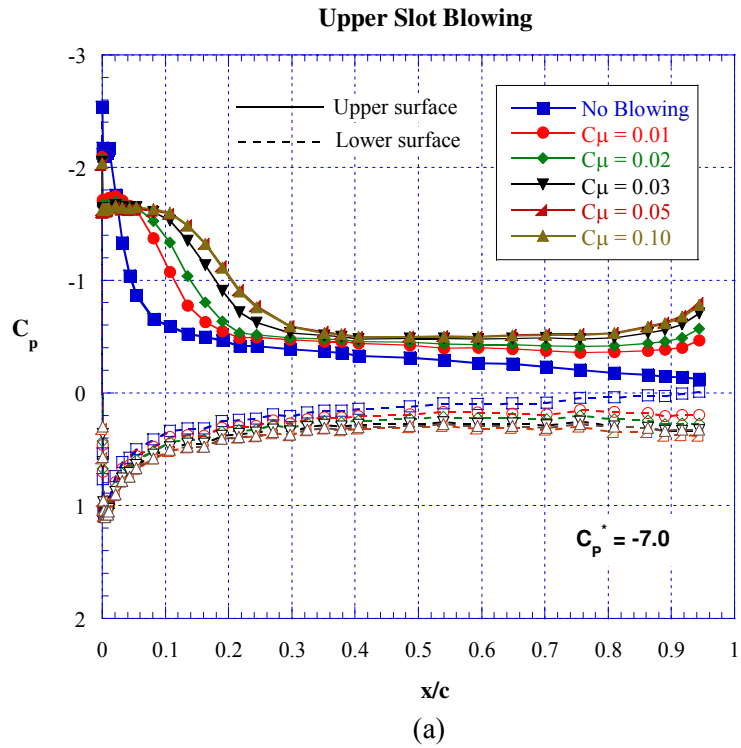
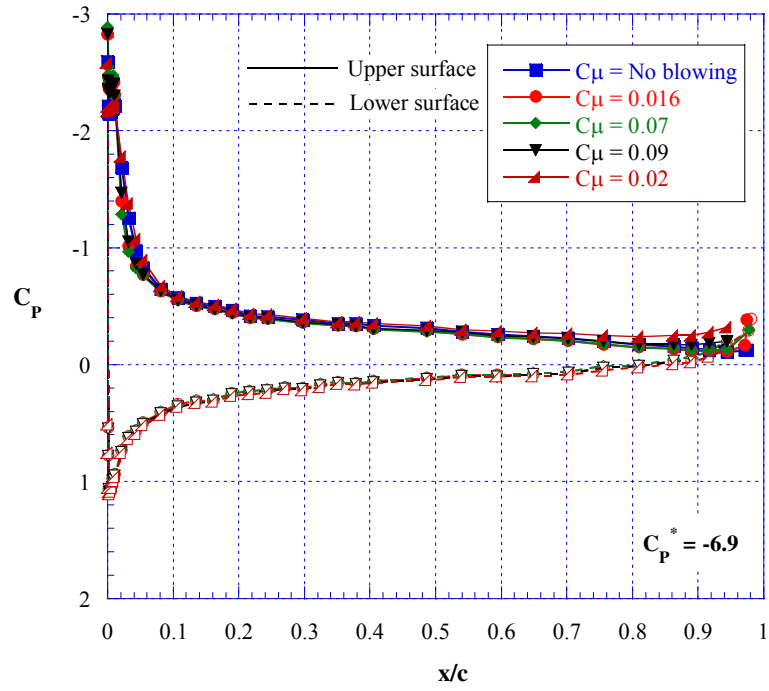


Figure 40 – Upper and lower chordwise pressure distribution, Coanda (1.78:1), slot ($h/c = 0.0012$), Mach = 0.3, $\alpha = 6^\circ$.

Dual Slot Blowing



(c)

Figure 40 – Concluded.

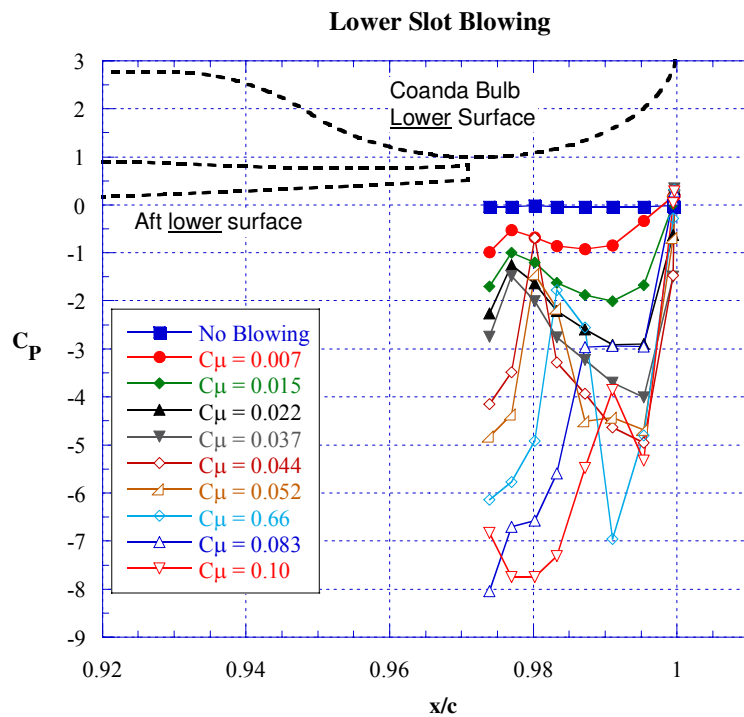
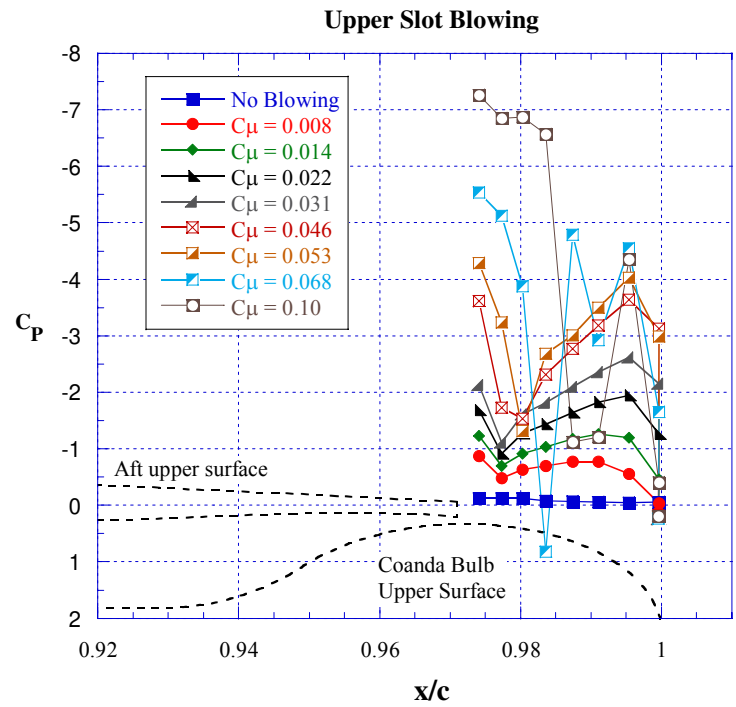


Figure 41 – Upper and lower surface Coanda bulb pressure distribution, Coanda (1.78:1), slot ($h/c = 0.0012$), Mach = 0.3, $\alpha = 6^\circ$.

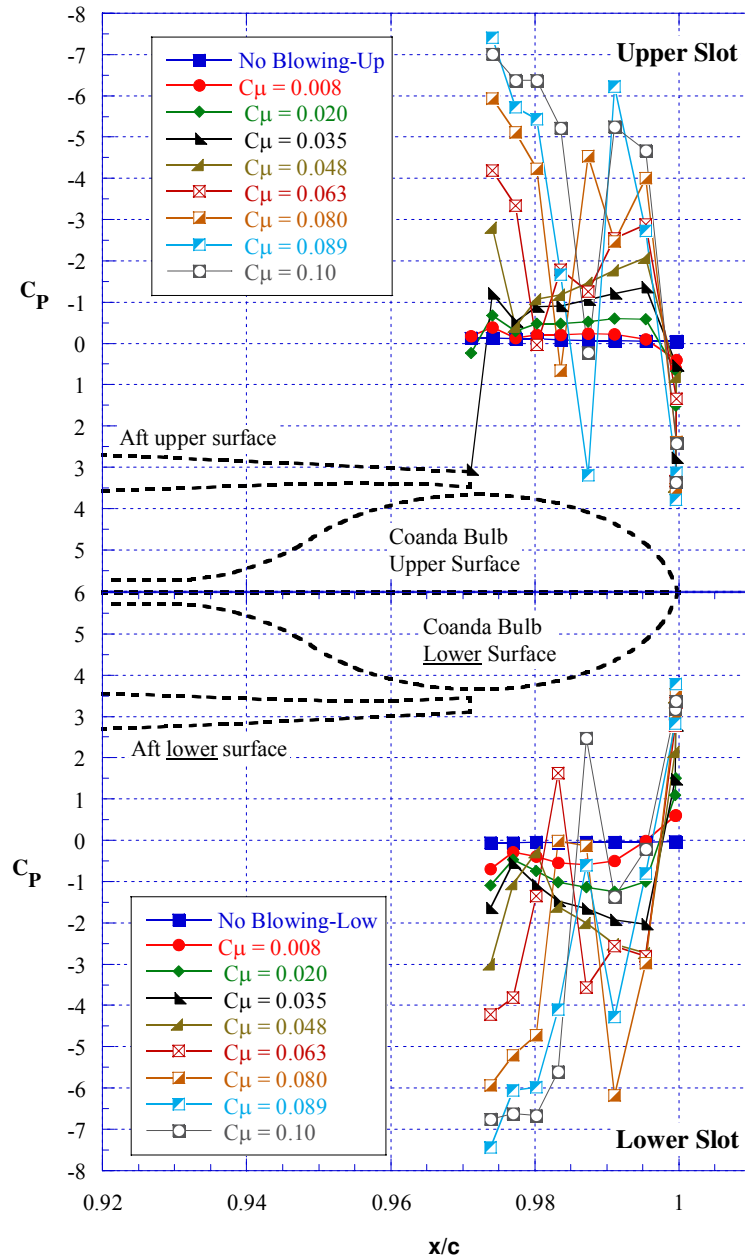


Figure 42 - Coanda bulb pressure distribution, dual slot blowing
 Coanda (1.78:1), slot ($h/c = 0.0012$), Mach = 0.3, $\alpha = 6^\circ$.

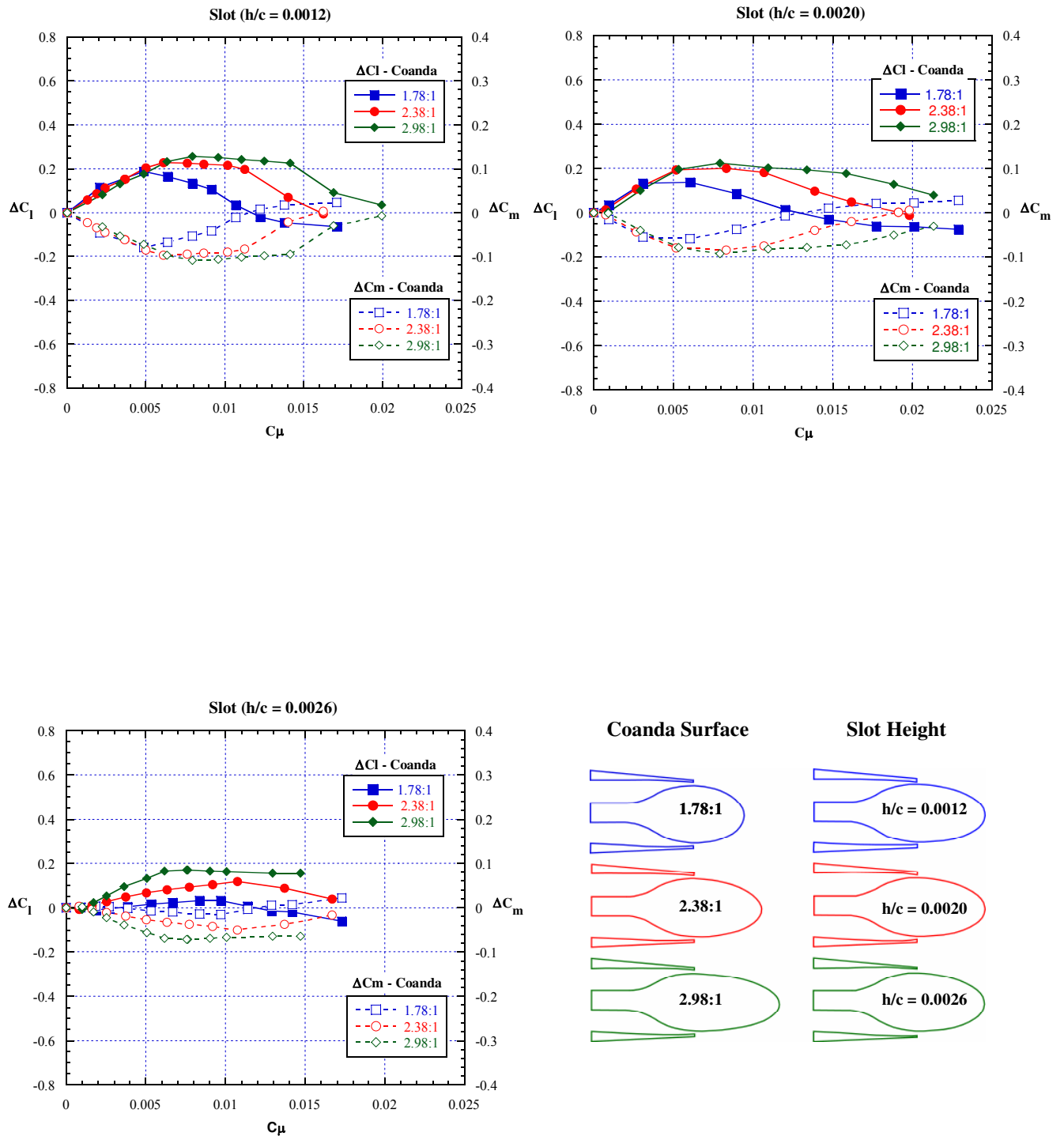


Figure 43 – ΔC_l & ΔC_m versus C_μ , Coanda surface effect, upper slot blowing, Mach = 0.8, $\alpha = 3^\circ$.

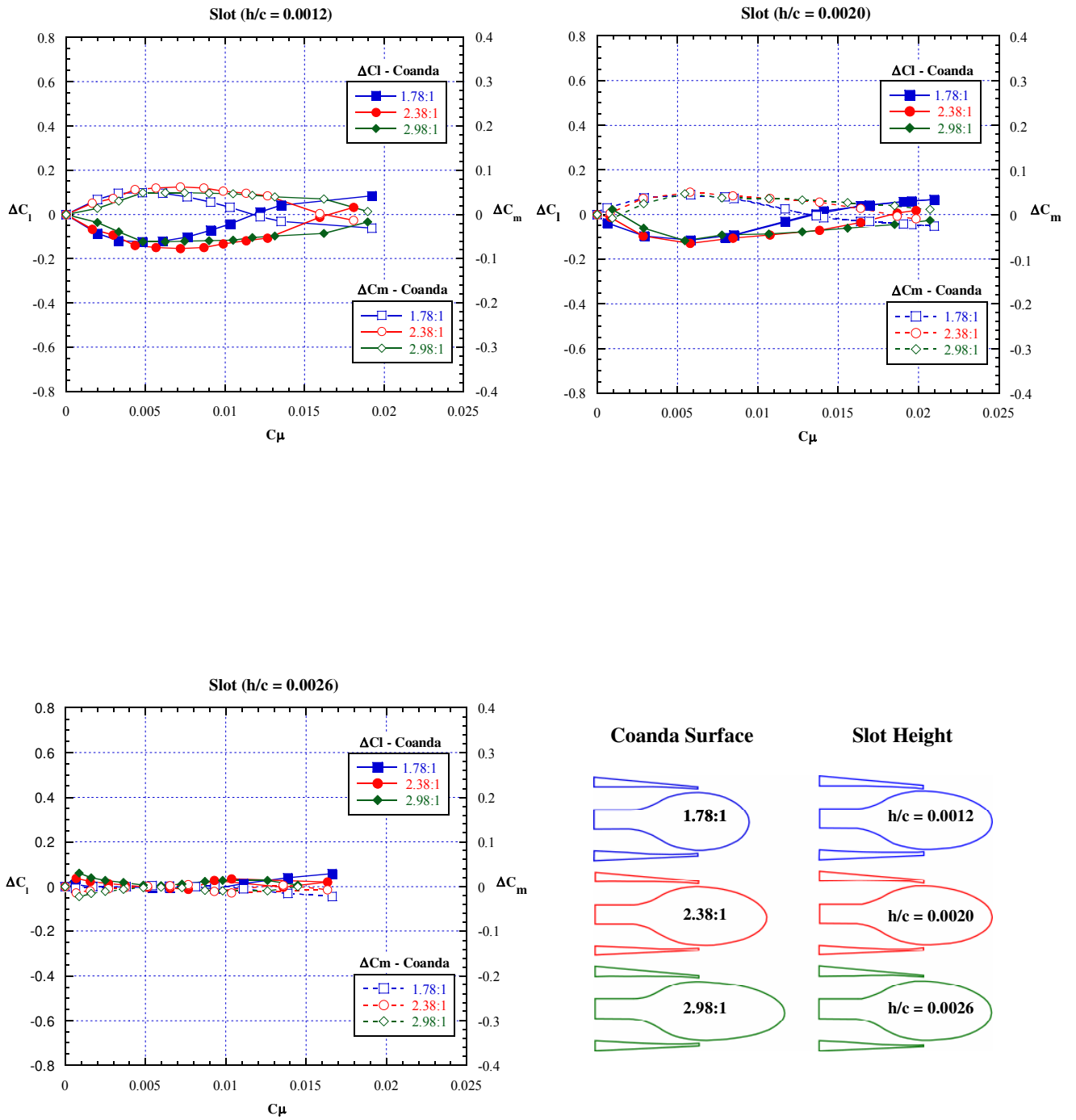


Figure 44 – ΔC_l & ΔC_m versus C_μ , Coanda surface effect, lower slot blowing, Mach = 0.8, $\alpha = 3^\circ$.

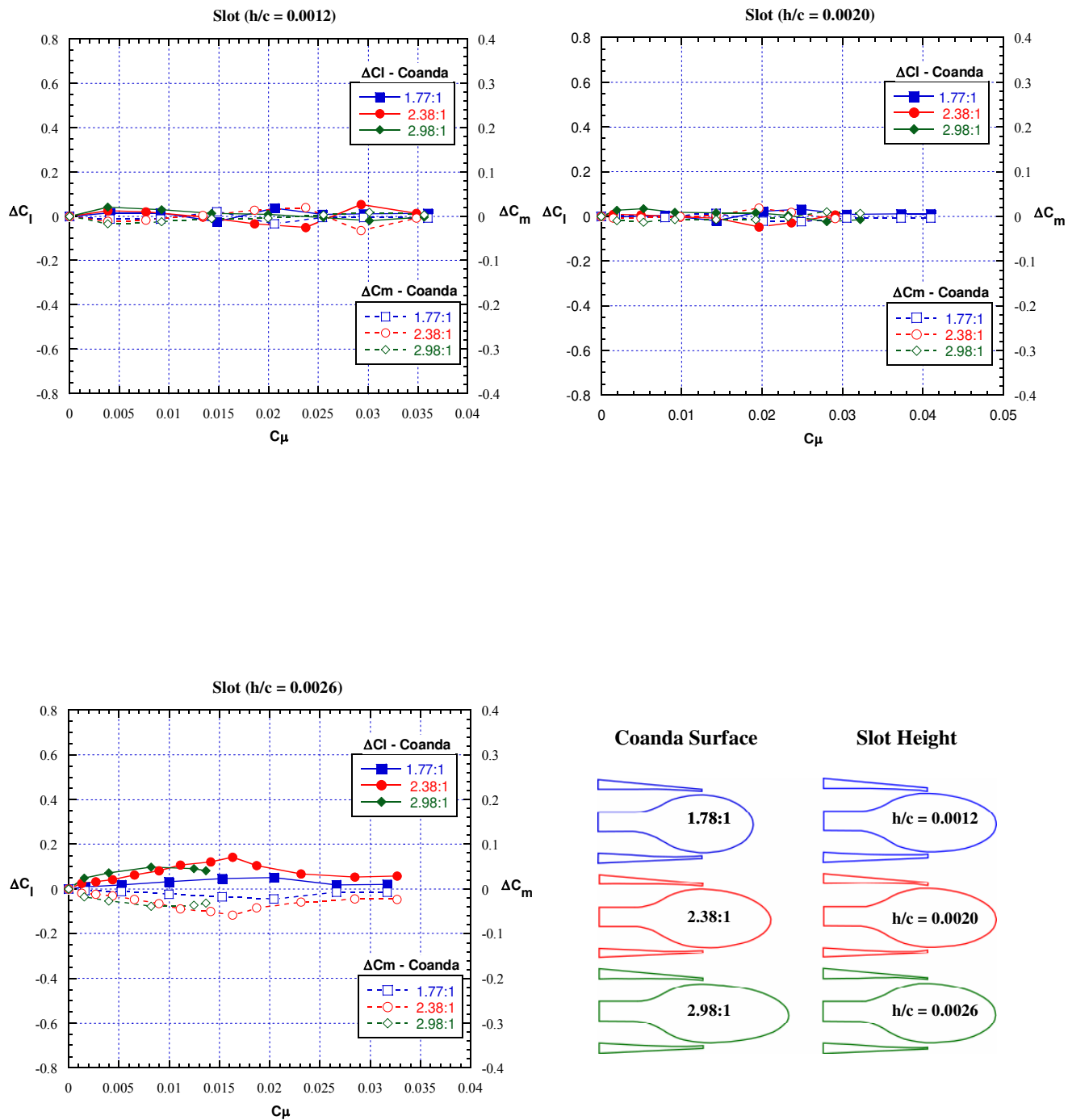


Figure 45 – ΔC_l & ΔC_m versus C_μ , Coanda surface effect, dual slot blowing, Mach = 0.8, $\alpha = 3^\circ$.

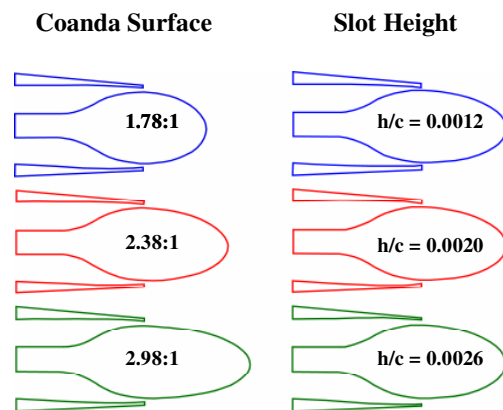
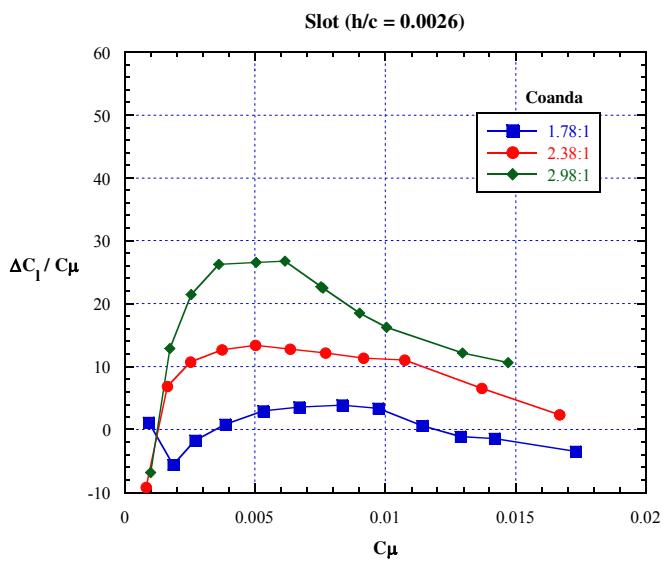
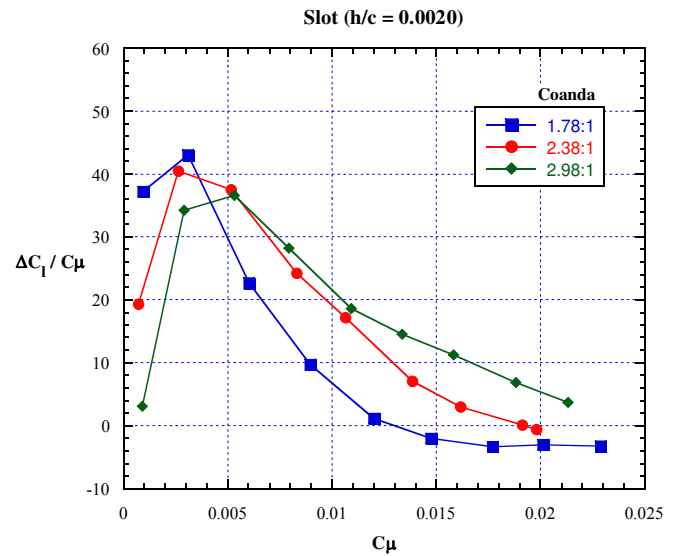
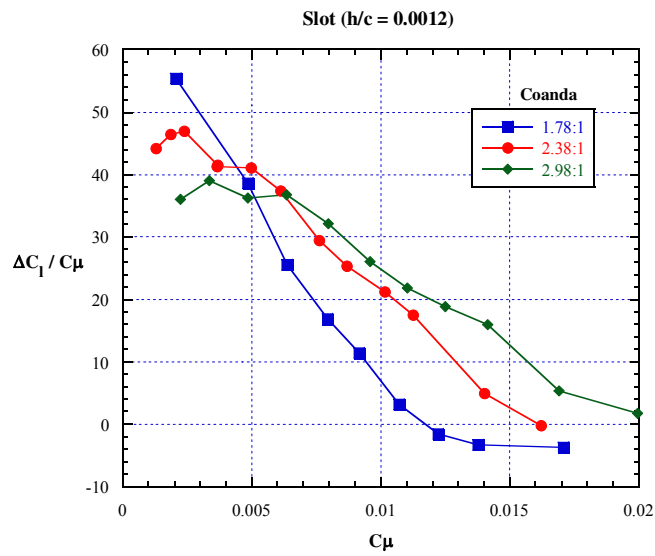


Figure 46 – Lift augmentation ratio versus C_{μ} , Coanda surface effect, upper slot blowing, Mach = 0.8, $\alpha = 3^\circ$.

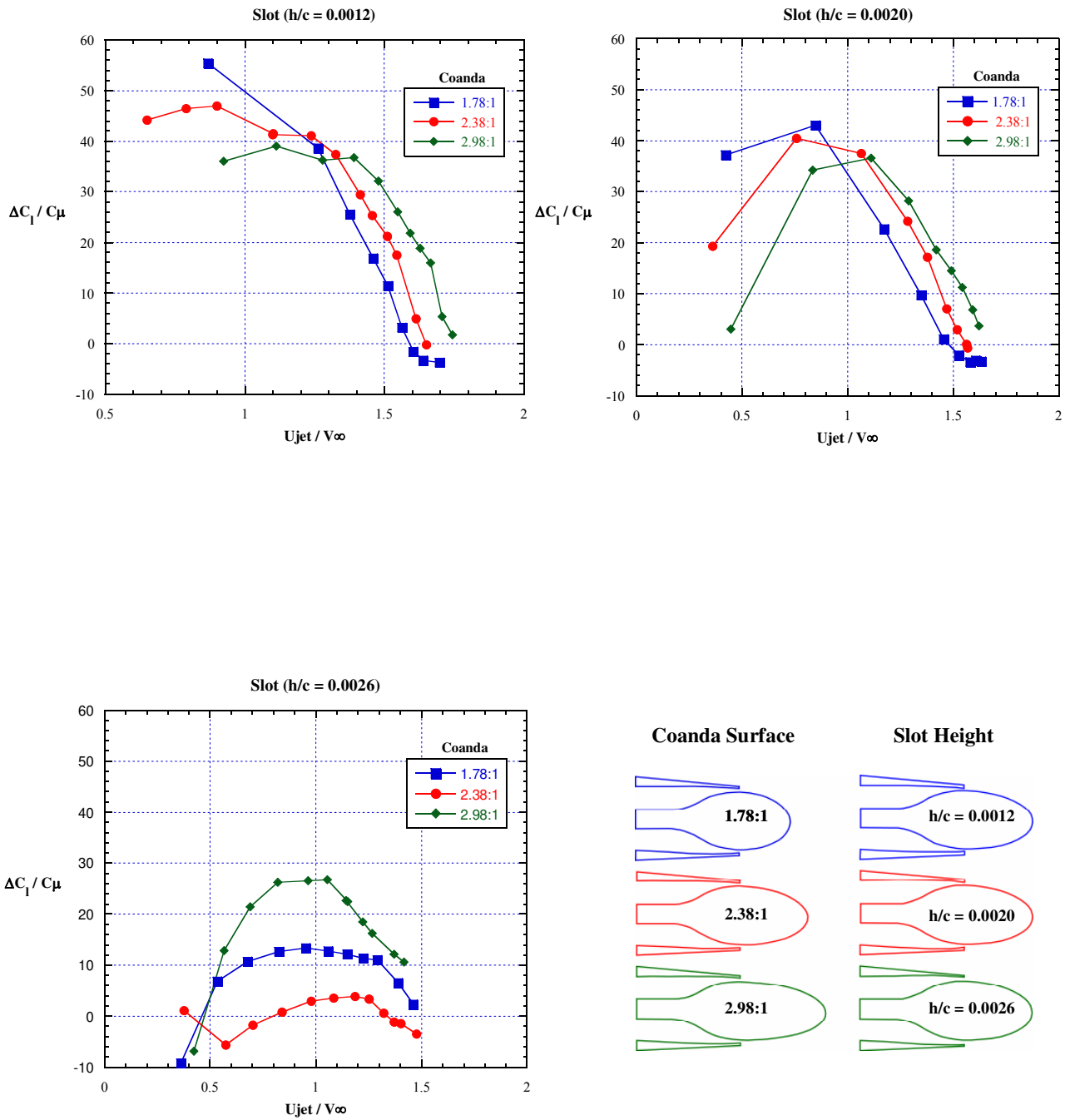


Figure 47 – Lift augmentation ratio versus velocity ratio, Coanda surface effect, upper slot blowing, Mach = 0.8, $\alpha = 3^\circ$.

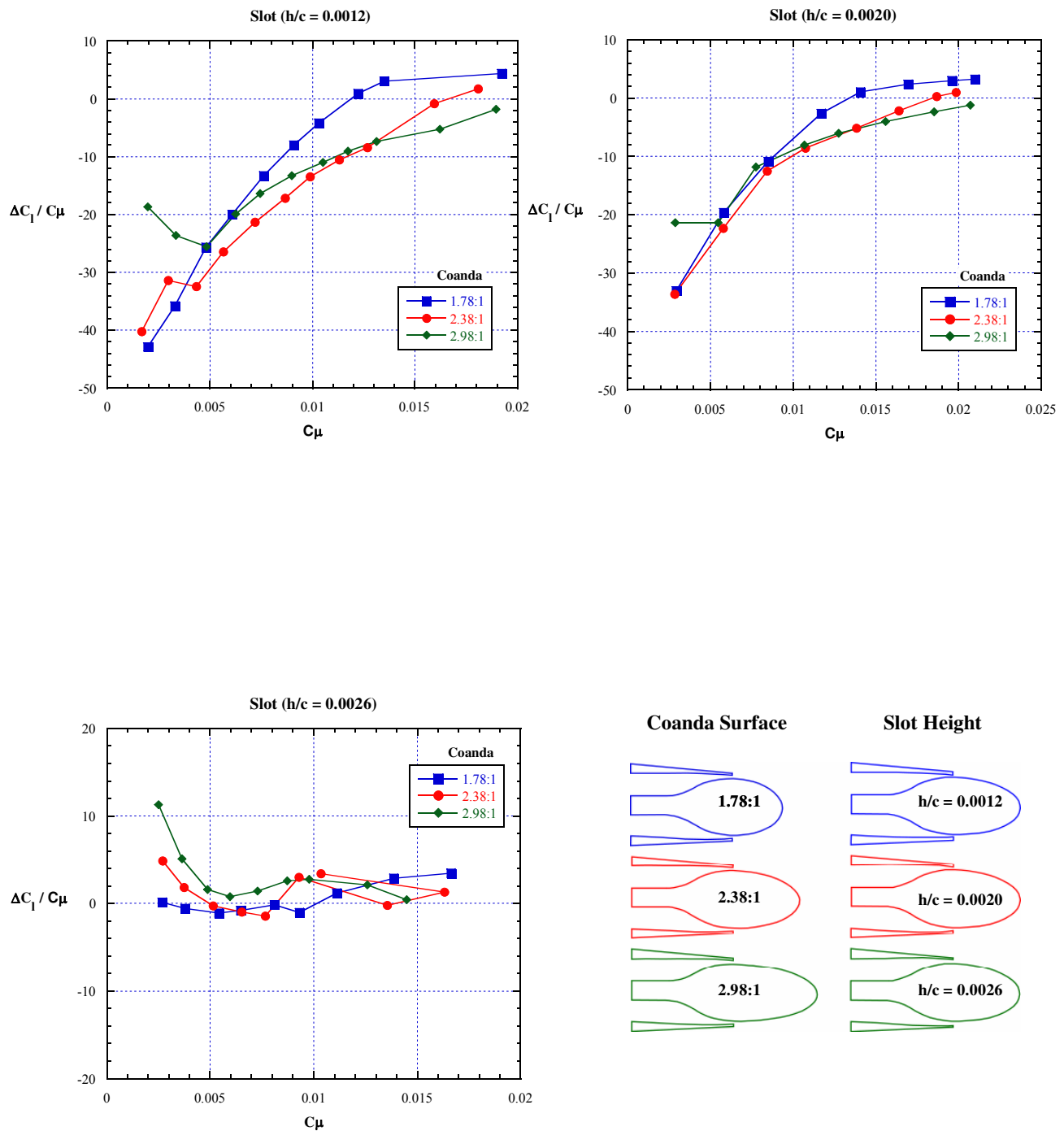


Figure 48 – Lift augmentation ratio versus C_{μ} , Coanda surface effect, lower slot blowing, Mach = 0.8, $\alpha = 3^{\circ}$.

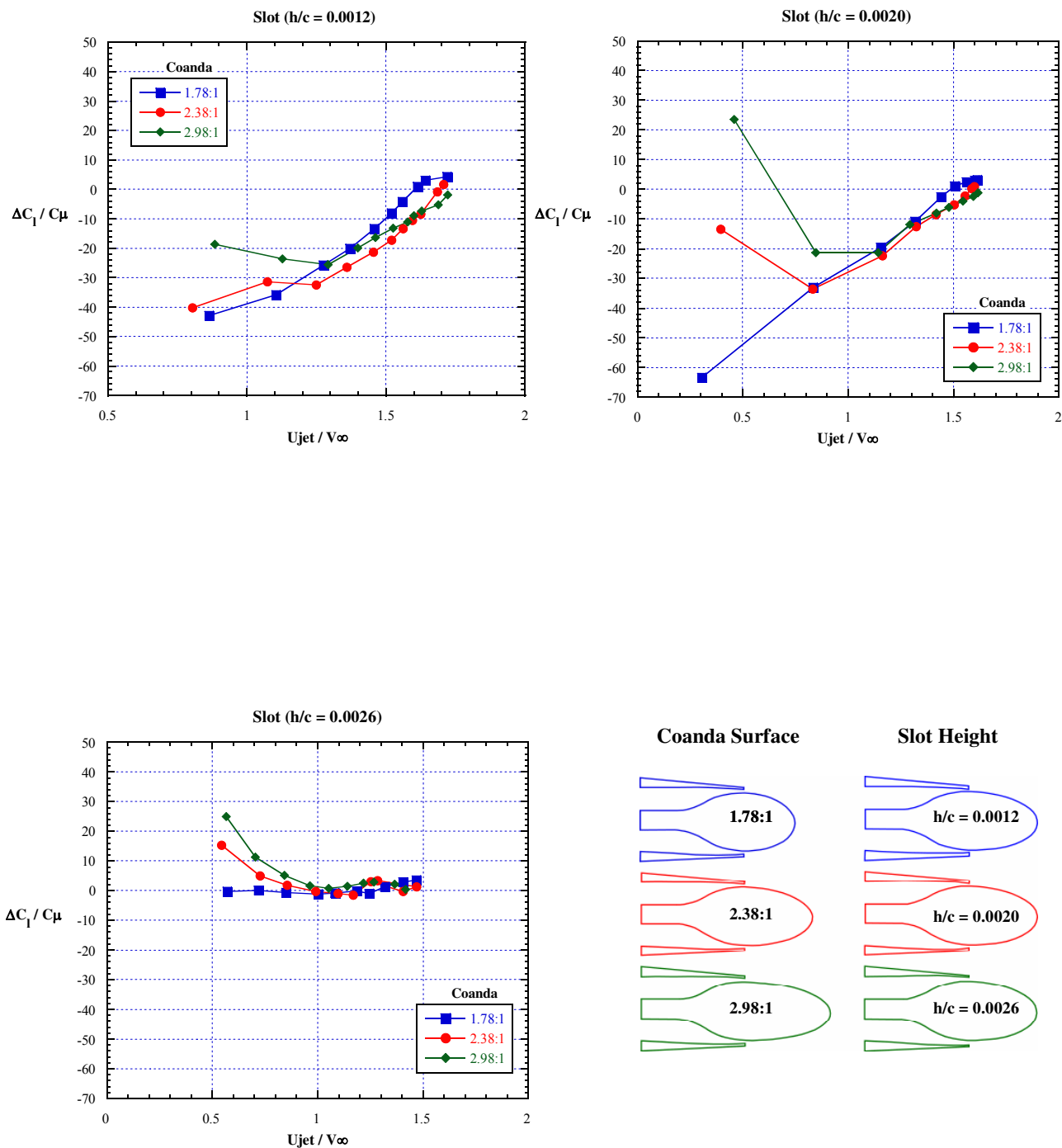


Figure 49 – Lift augmentation ratio versus velocity ratio, Coanda surface effect, lower slot blowing, Mach = 0.8, $\alpha = 3^\circ$.

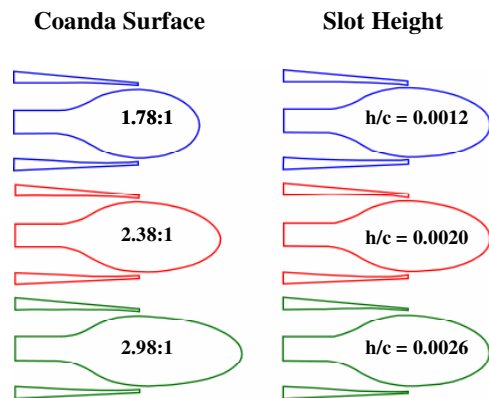
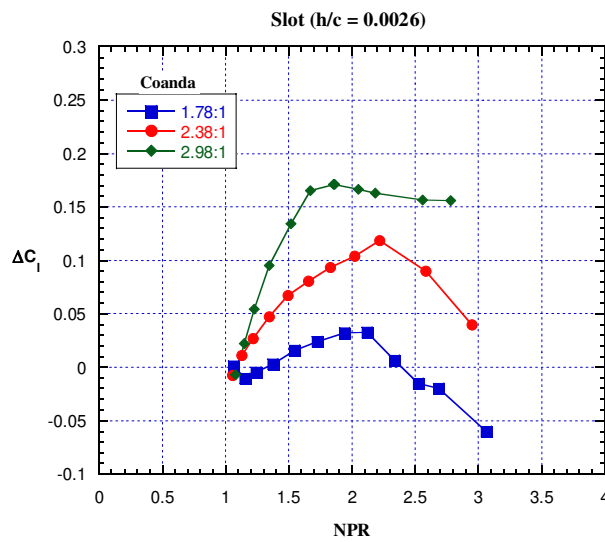
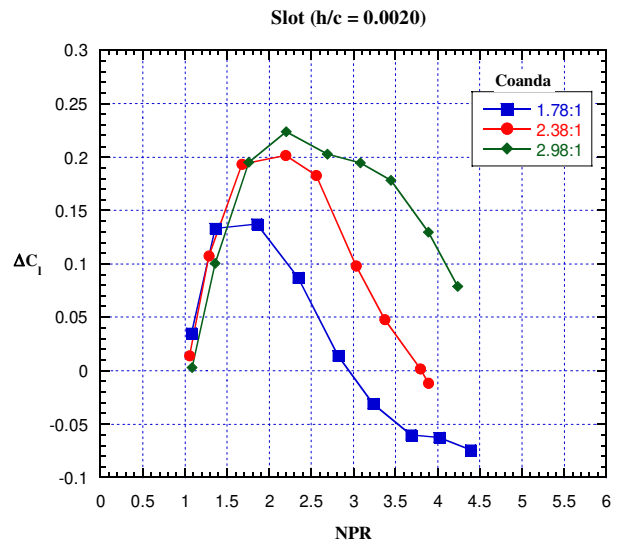
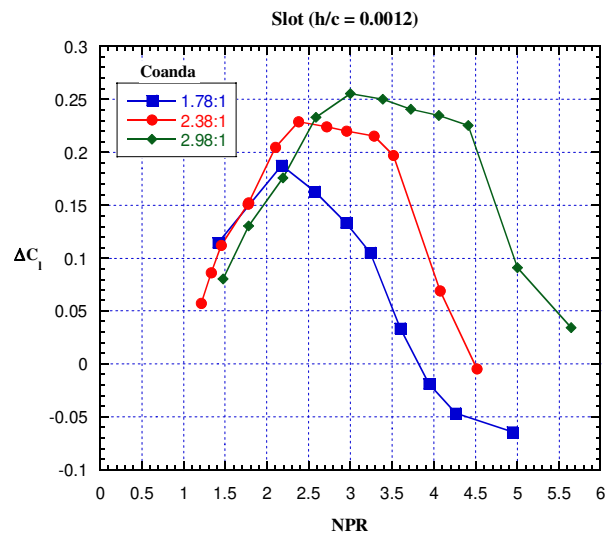


Figure 50 – ΔC_1 versus nozzle pressure ratio, Coanda surface effect, upper slot blowing, Mach = 0.8, $\alpha = 3^\circ$.

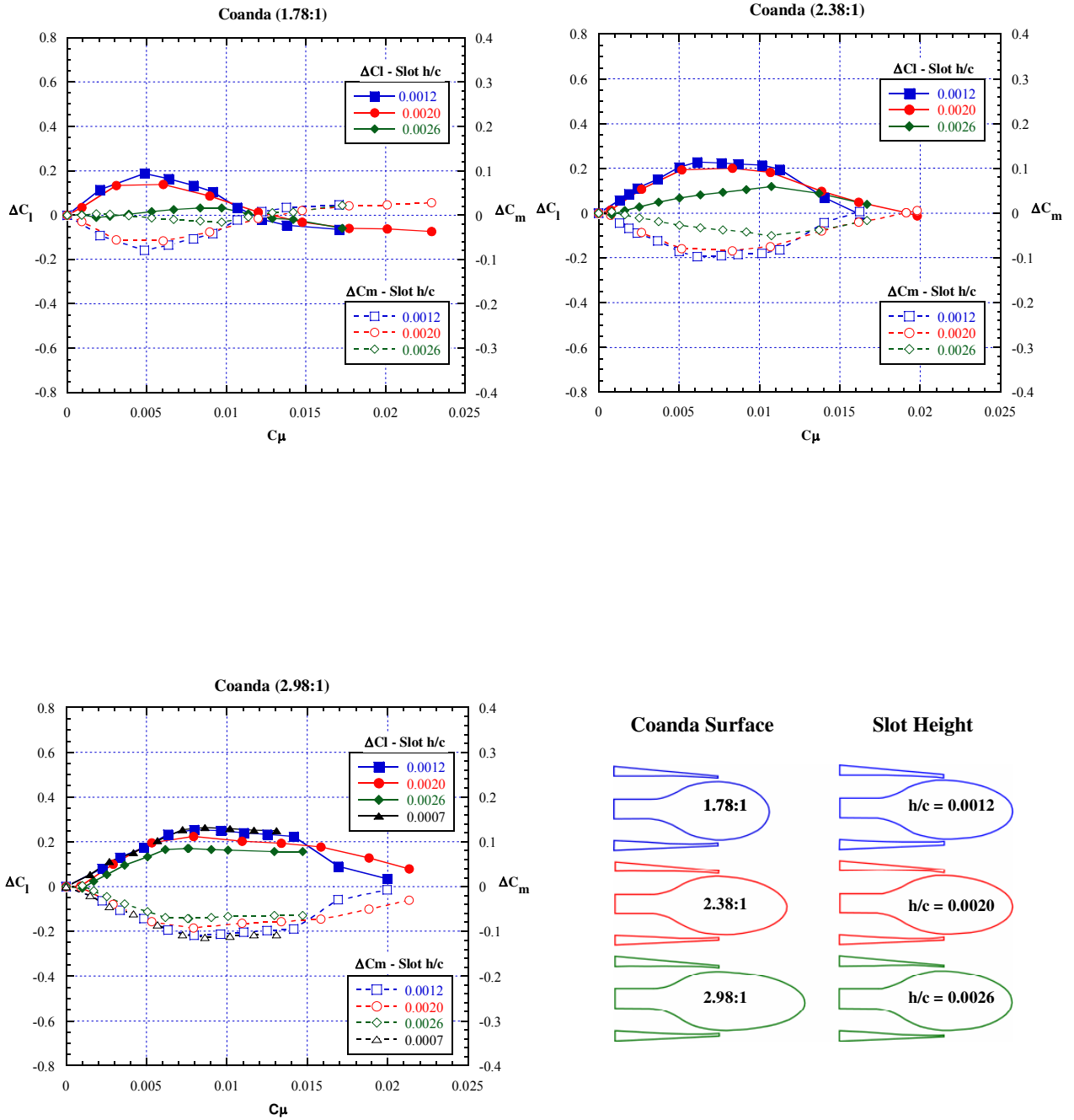


Figure 51 – ΔC_l & ΔC_m versus C_μ , slot height effect, upper slot blowing, Mach = 0.8, $\alpha = 3^\circ$.

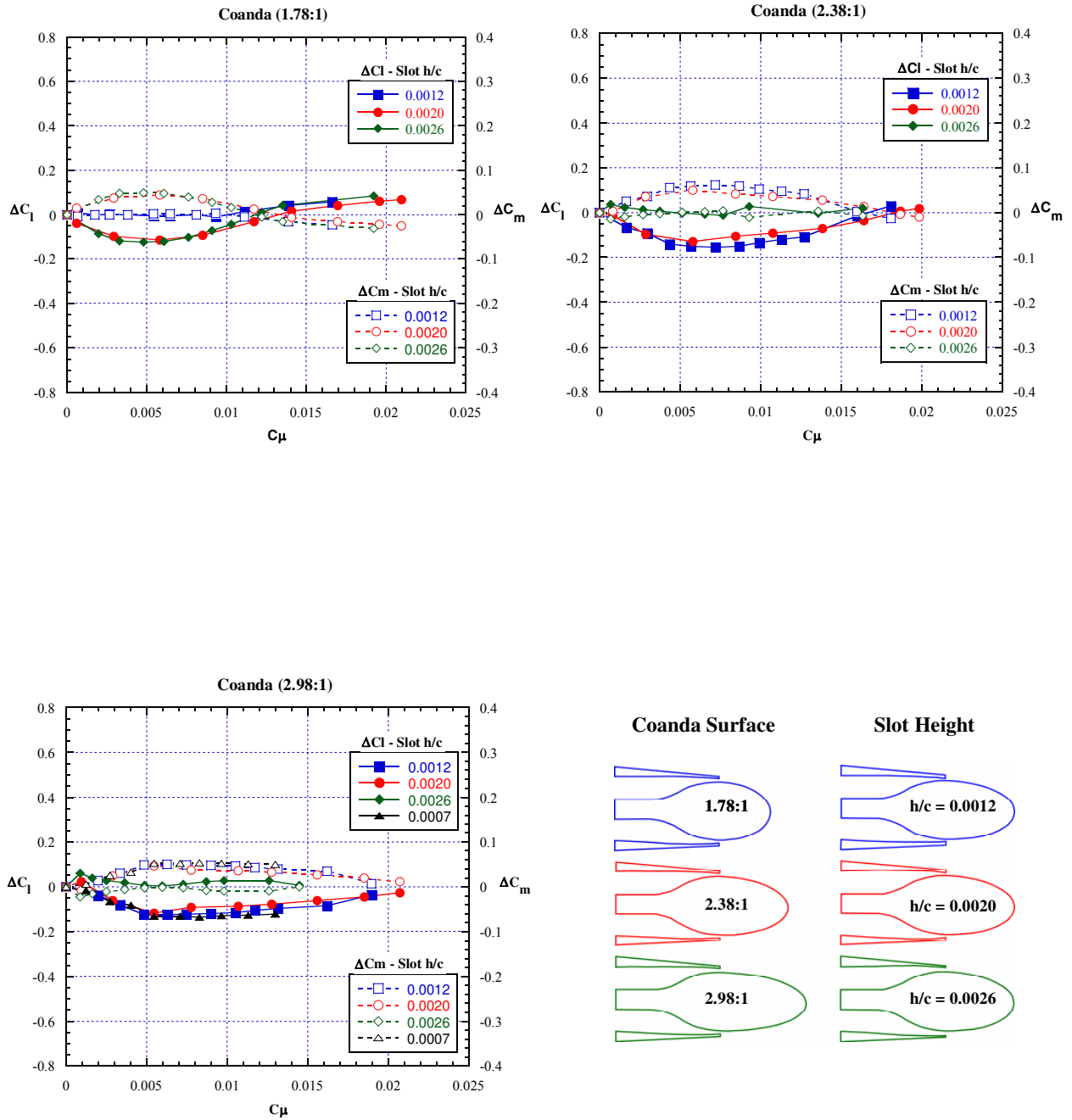


Figure 52 – ΔC_l & ΔC_m versus C_μ , slot height effect, lower slot blowing, Mach = 0.8, $\alpha = 3^\circ$.

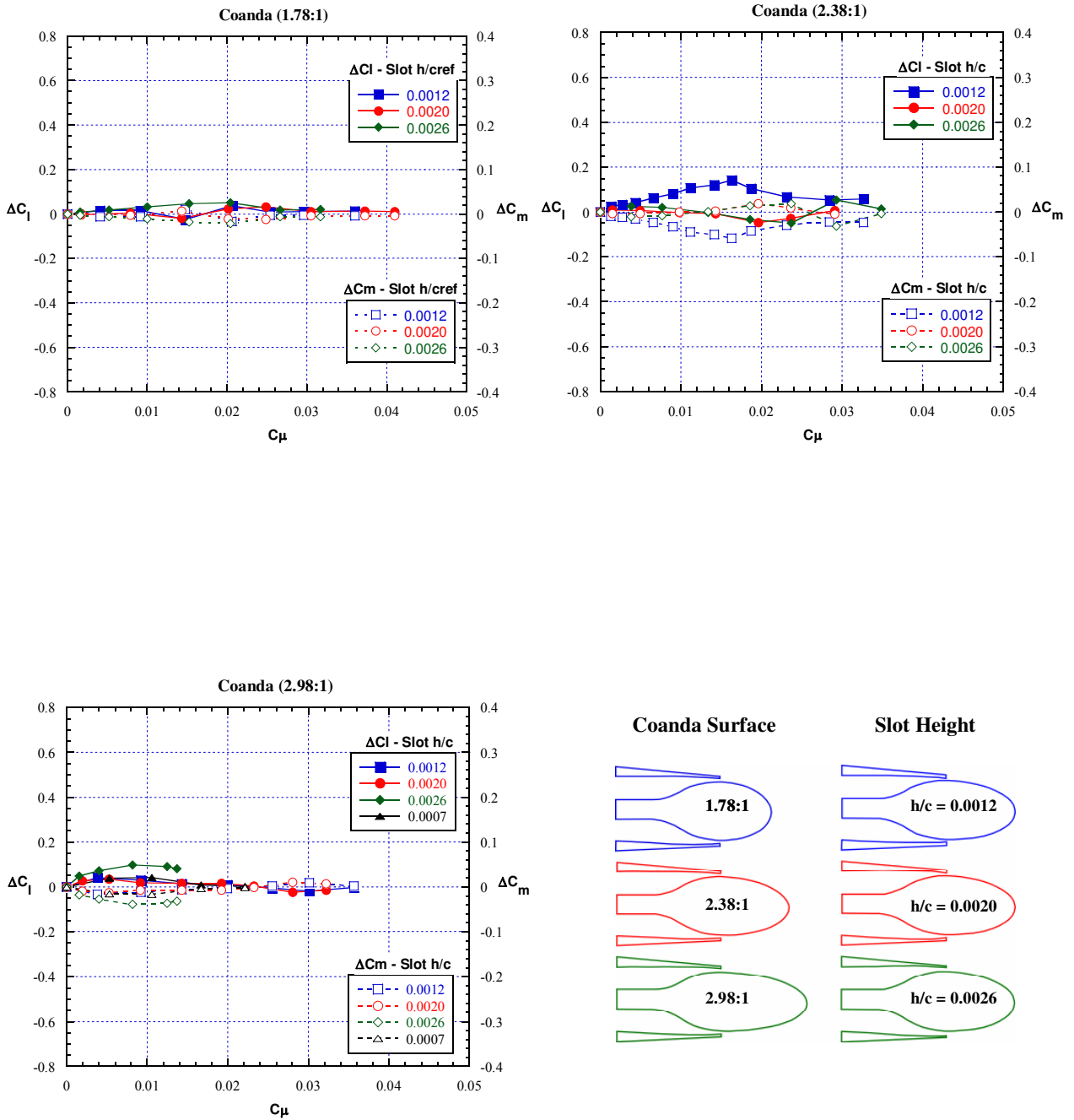


Figure 53 – ΔC_l & ΔC_m versus C_μ , slot height effect, dual slot blowing, Mach = 0.8, $\alpha = 3^\circ$.

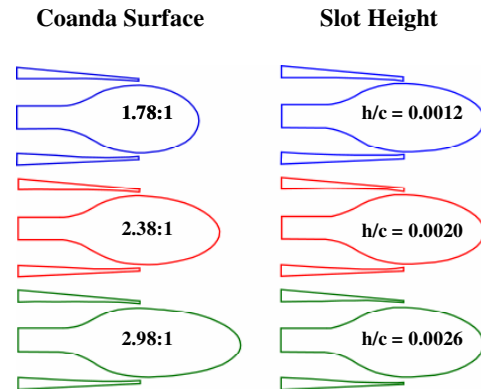
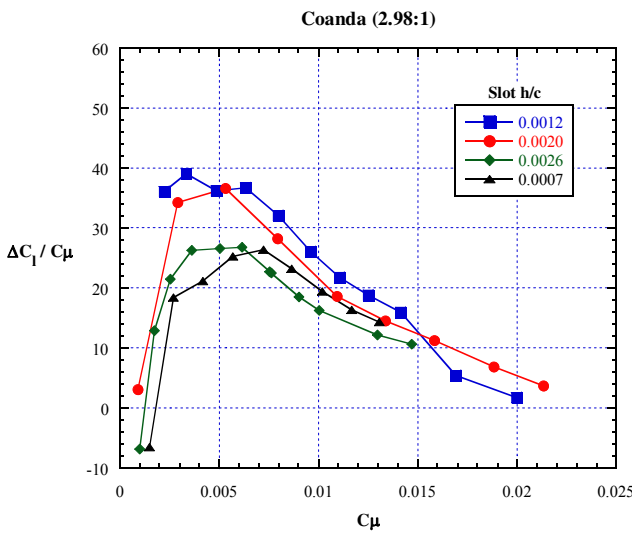
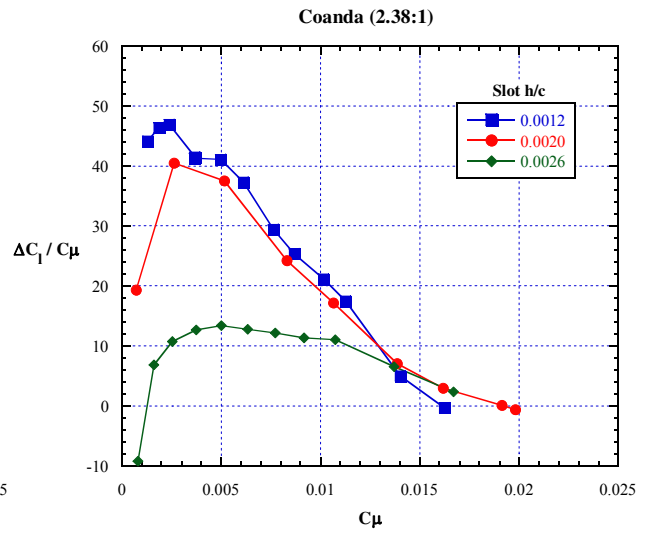
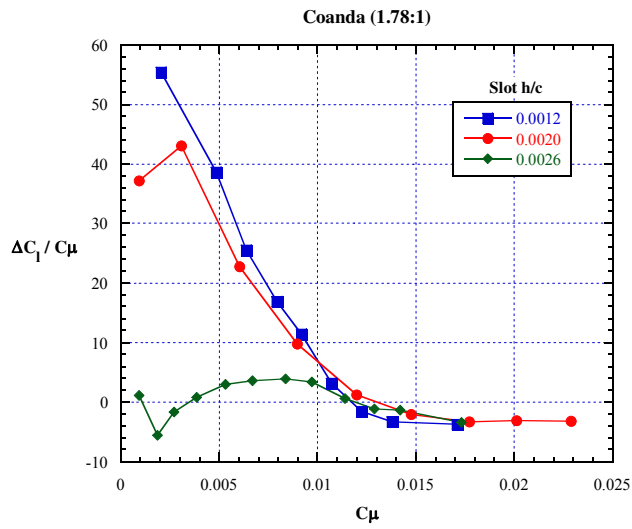


Figure 54 – Lift augmentation ratio versus C_{μ} , slot height effect, upper slot blowing, Mach = 0.8, $\alpha = 3^\circ$.

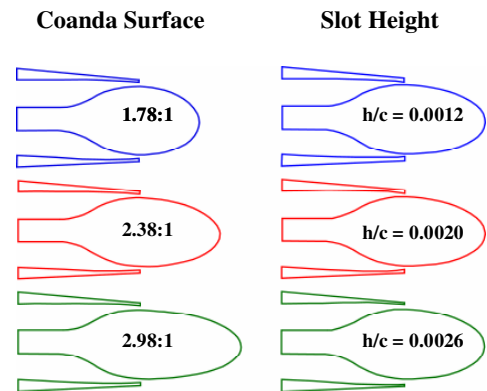
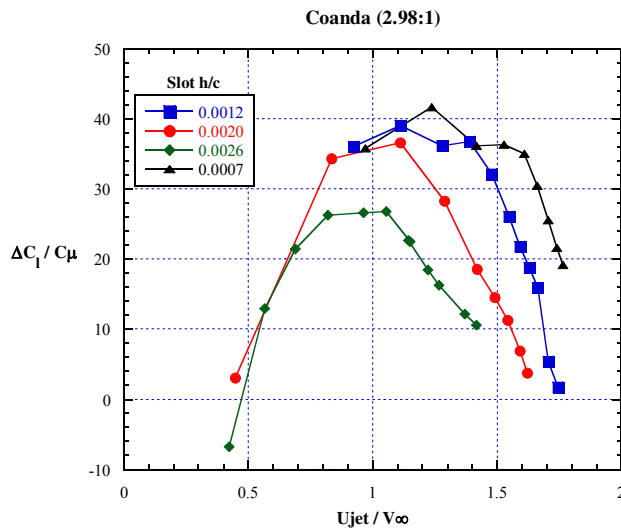
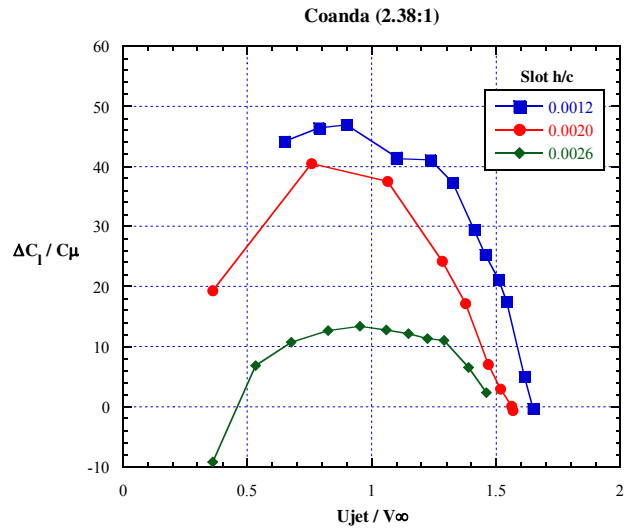
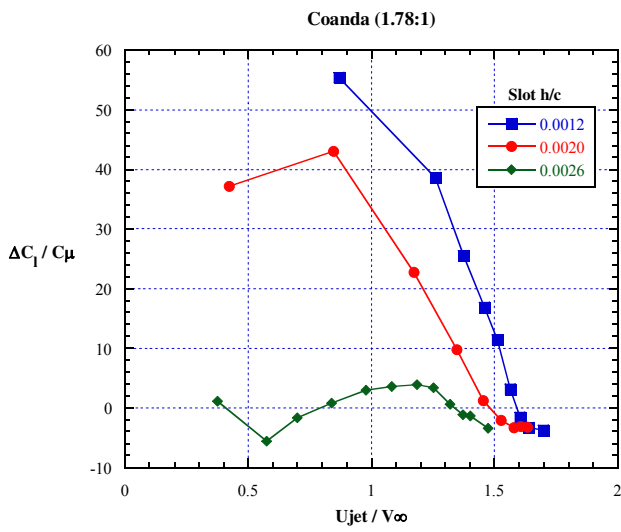


Figure 55 – Lift augmentation ratio versus velocity ratio, slot height effect, upper slot blowing, Mach = 0.8, $\alpha = 3^\circ$.

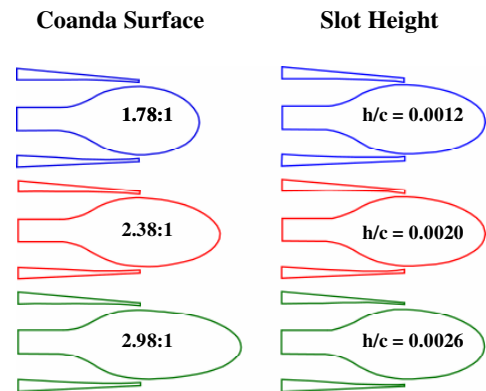
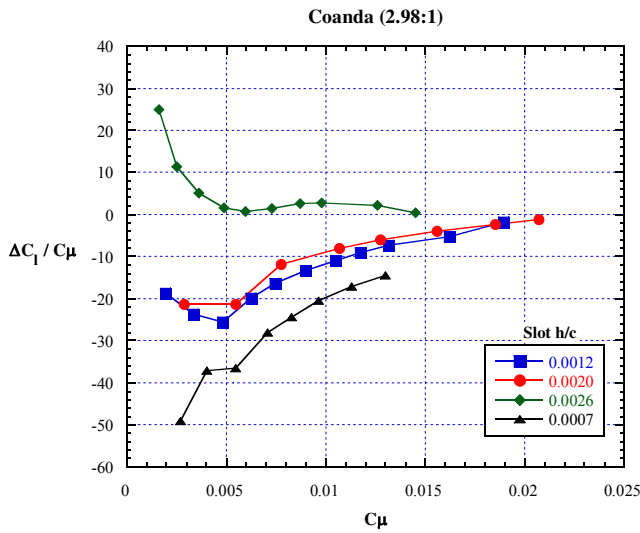
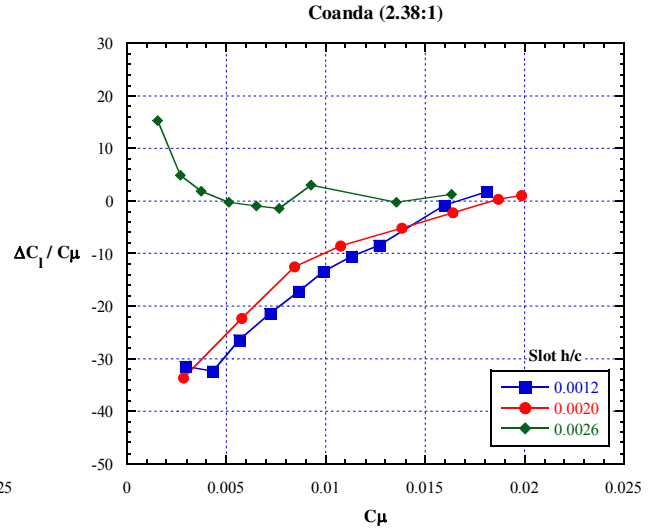
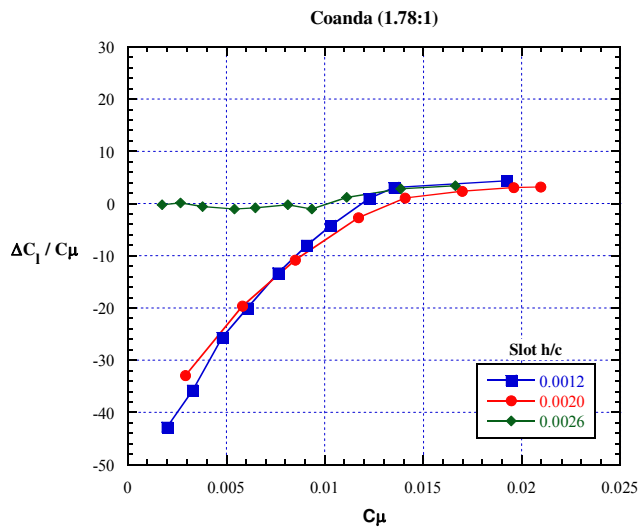


Figure 56 – Lift augmentation ratio versus C_{μ} , slot height effect, lower slot blowing, Mach = 0.8, $\alpha = 3^\circ$.

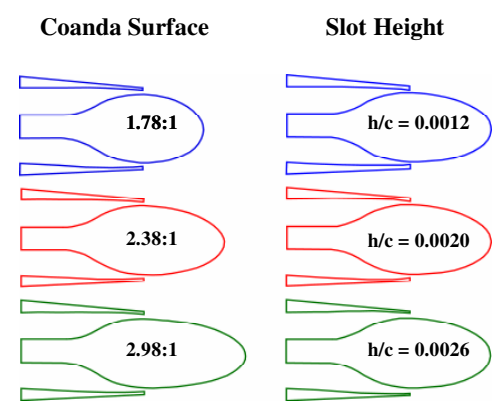
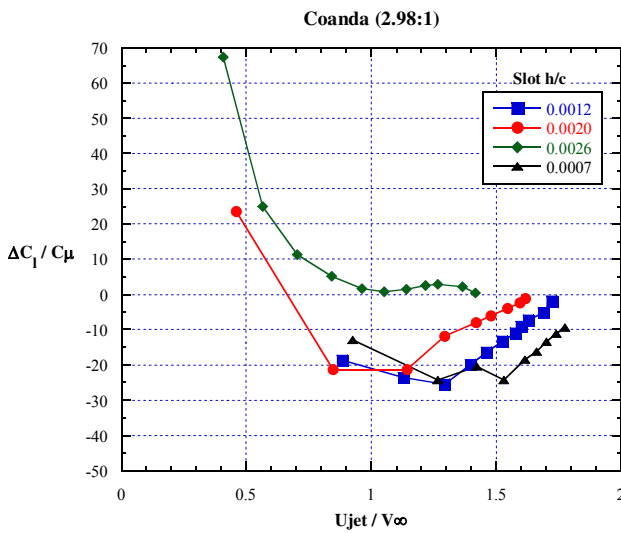
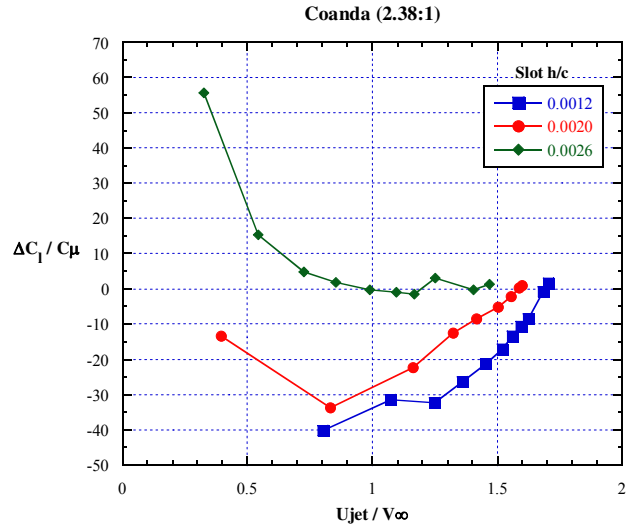
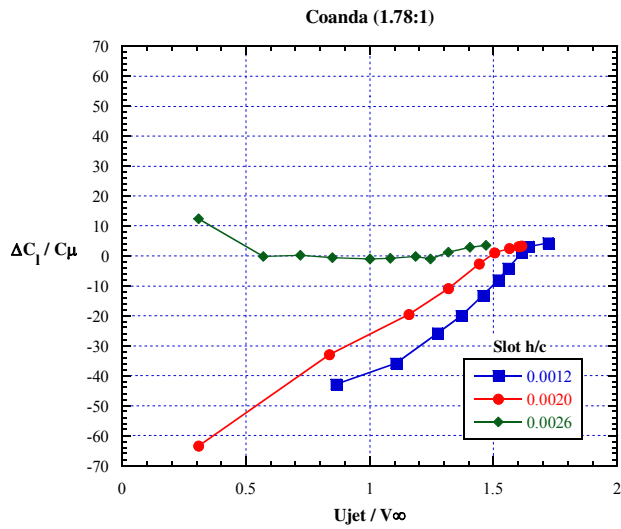


Figure 57 – Lift augmentation ratio versus velocity ratio, slot height effect, lower slot blowing, Mach = 0.8, $\alpha = 3^\circ$.

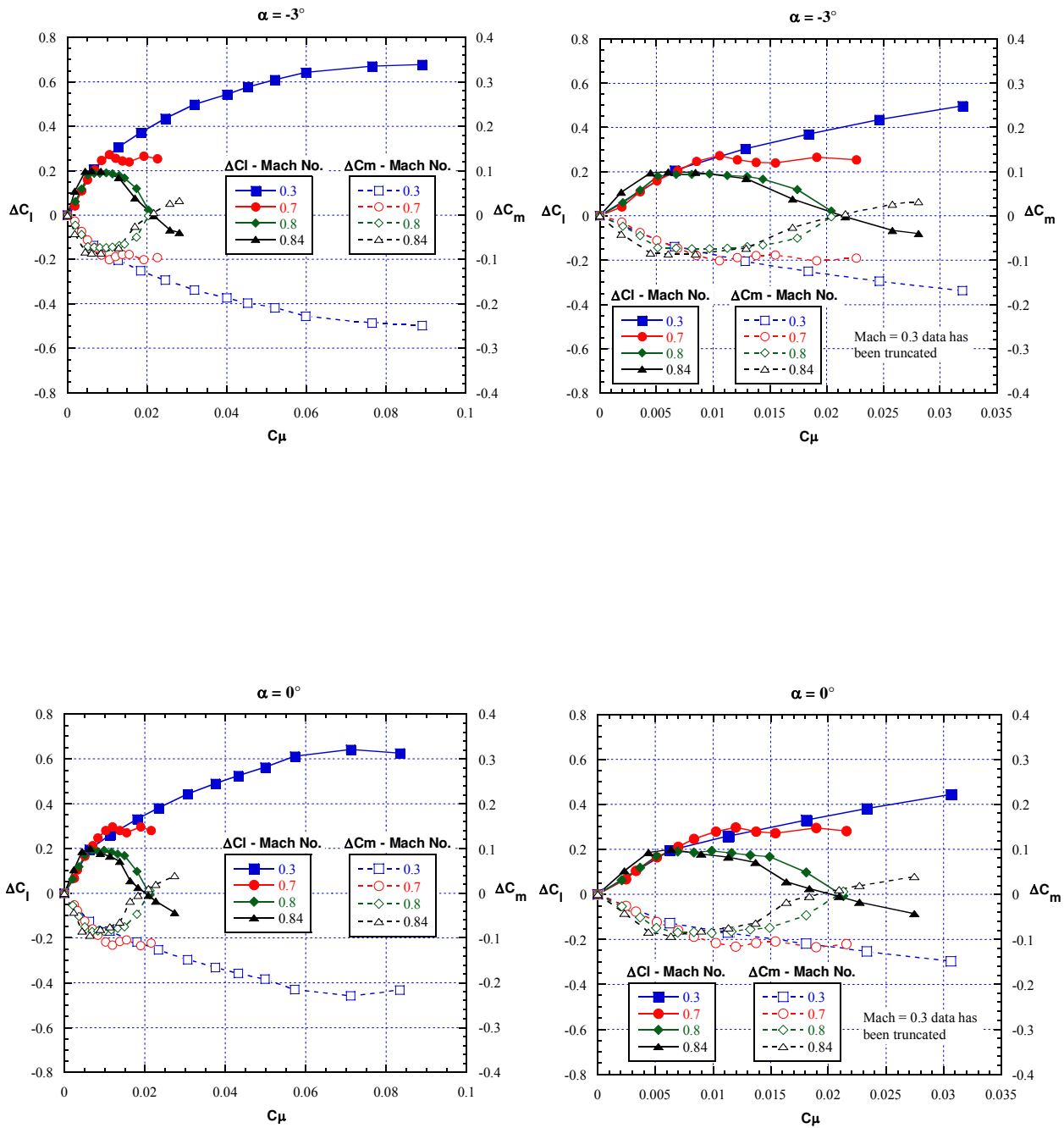


Figure 58 – ΔC_l & ΔC_m versus C_μ , Mach number effect, upper slot blowing, Coanda (2.98:1), slot ($h/c = 0.0012$).

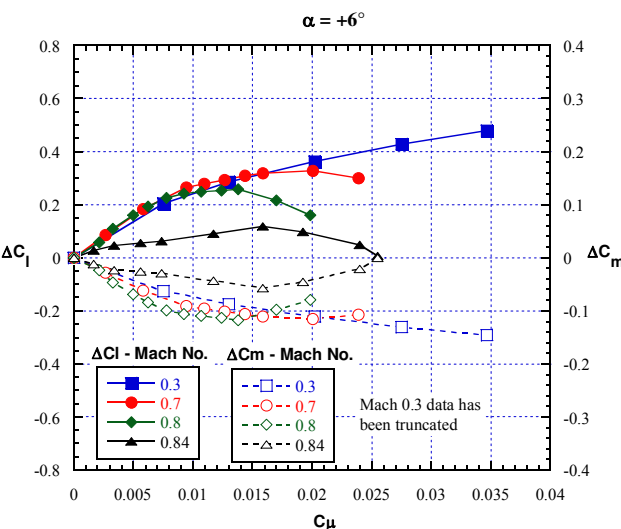
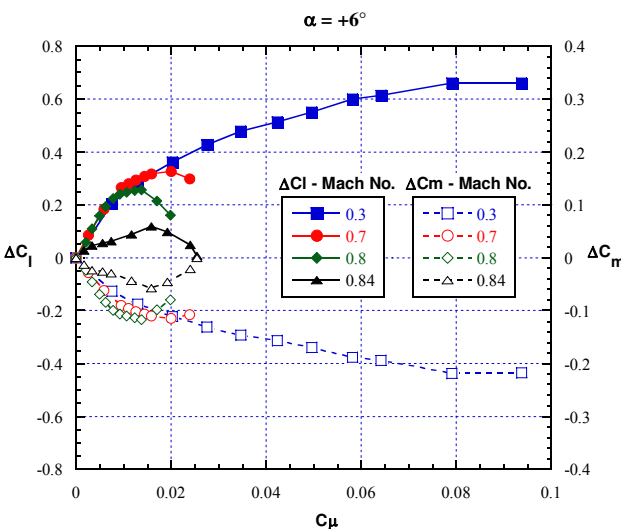
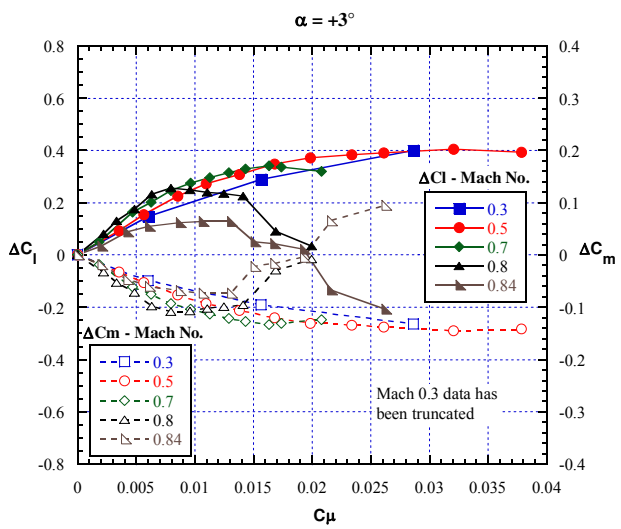
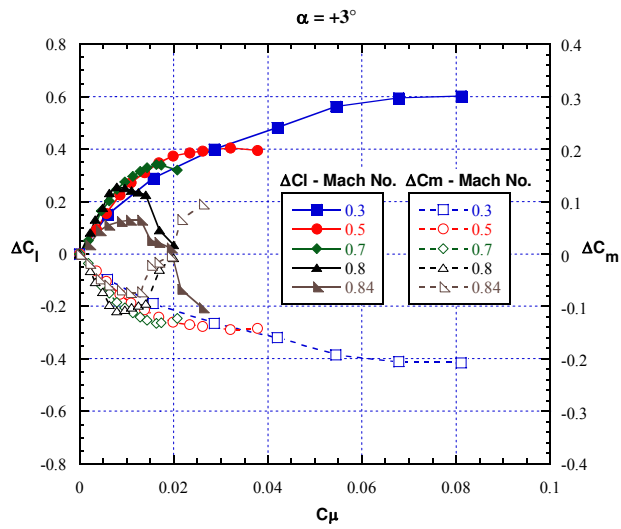


Figure 58 – Continued.

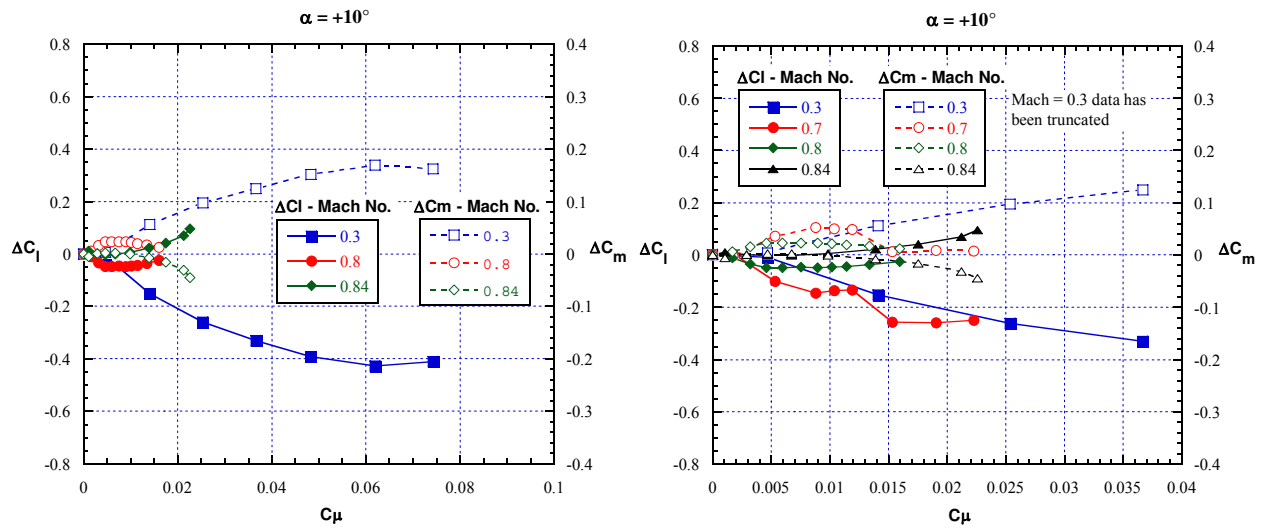


Figure 58 – Concluded.

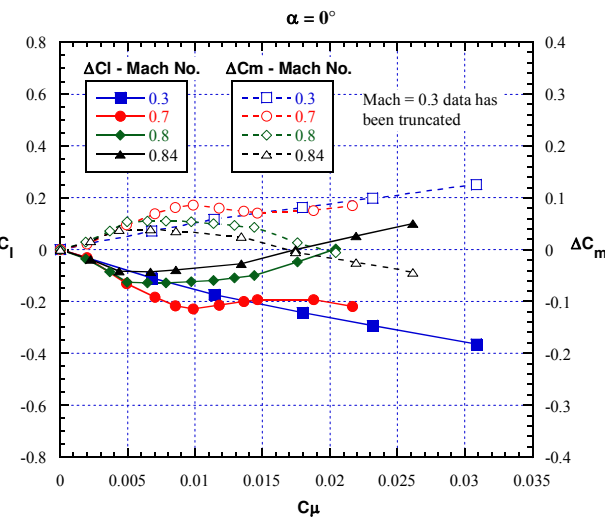
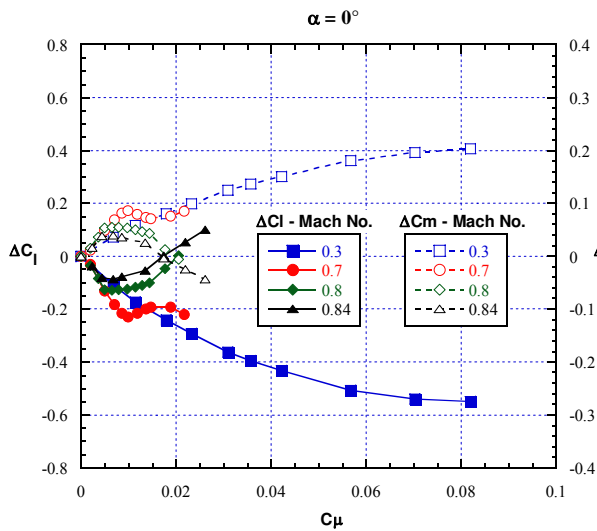
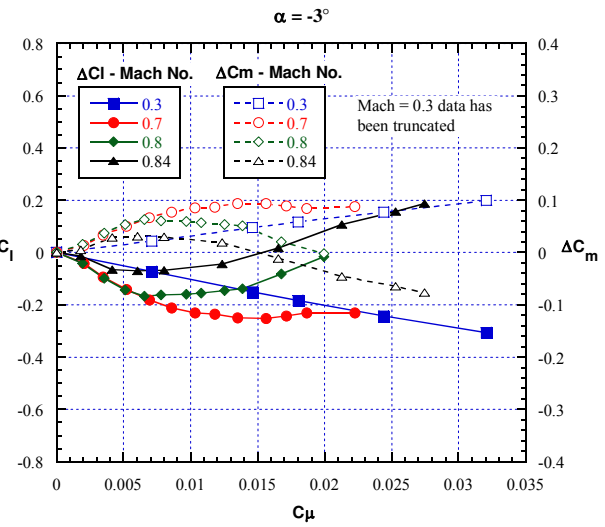
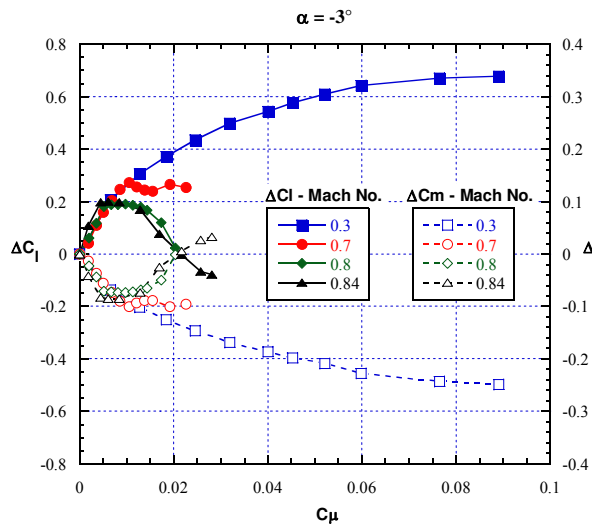


Figure 59 – ΔC_l & ΔC_m versus C_μ , Mach number effect, lower slot blowing, Coanda (2.98:1), slot ($h/c = 0.0012$).

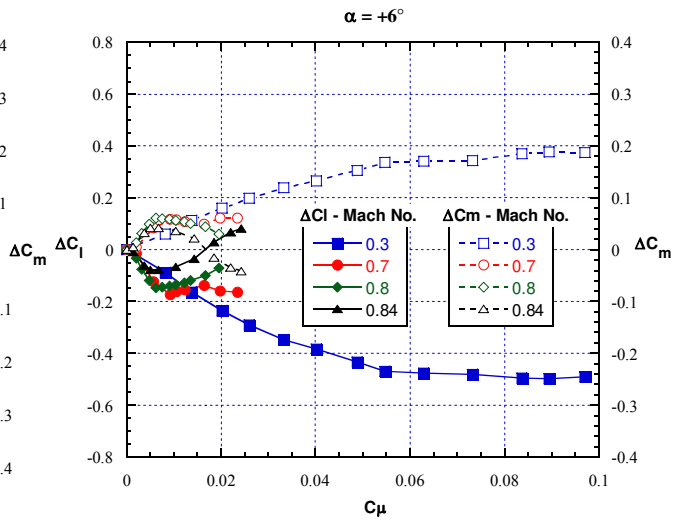
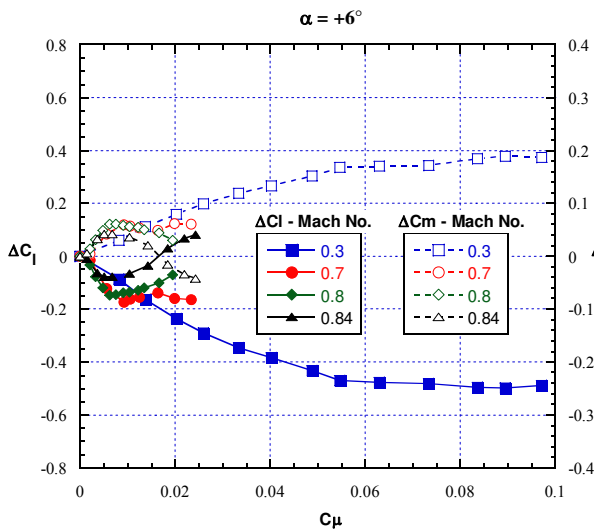
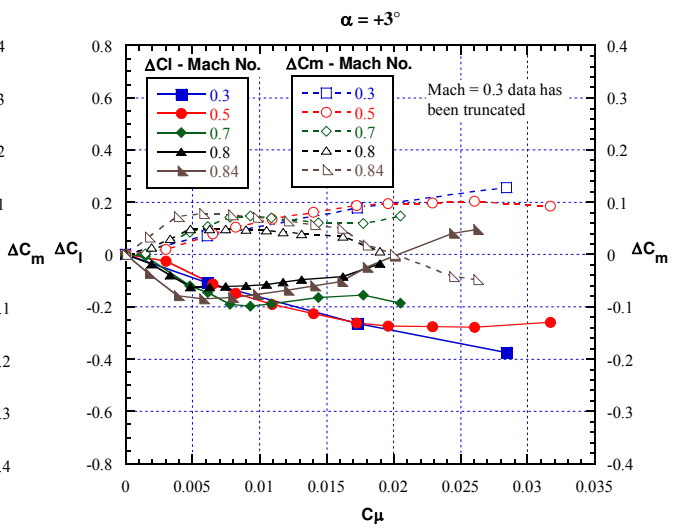
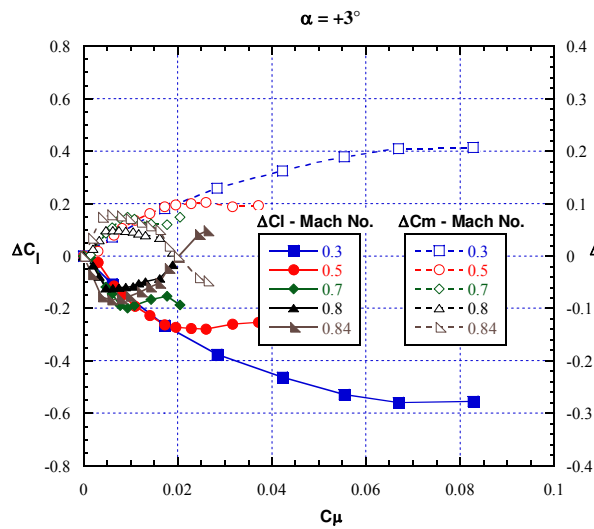


Figure 59 – Continued.

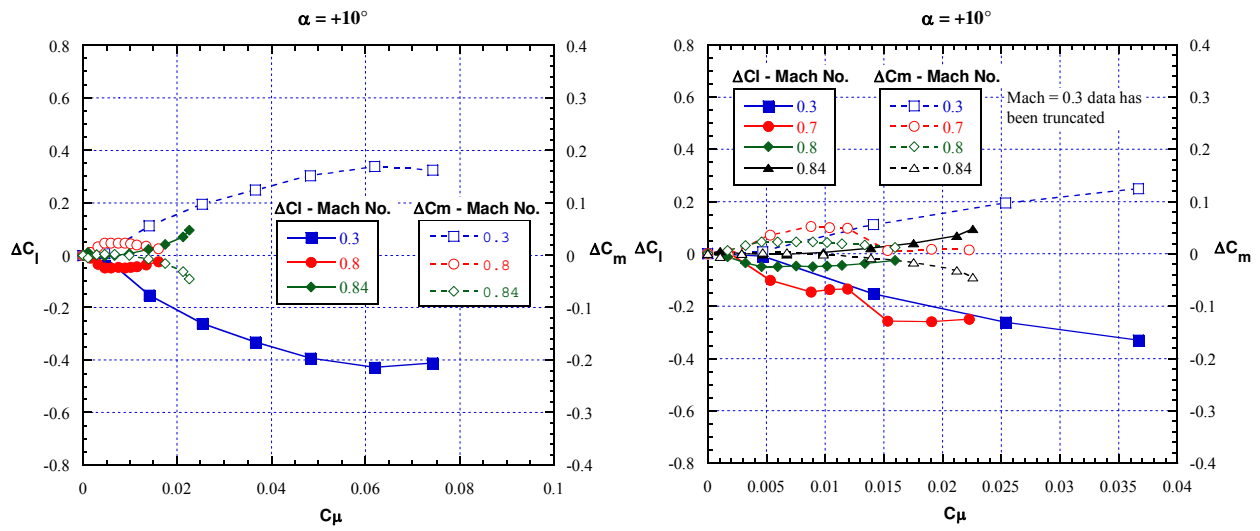


Figure 59 – Concluded.

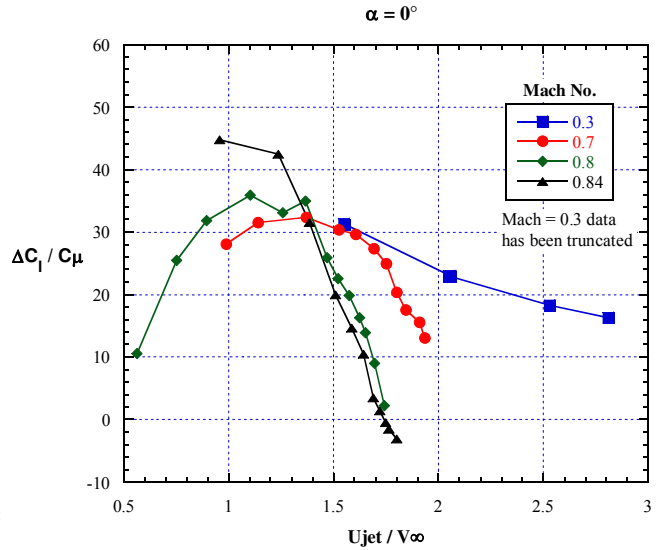
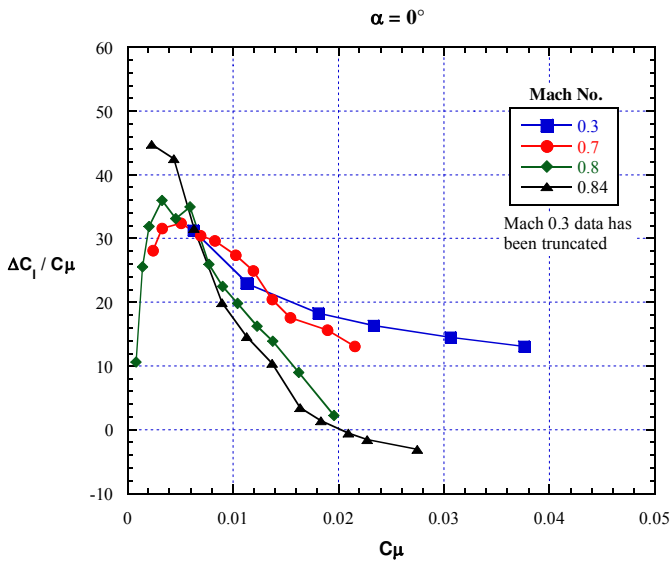
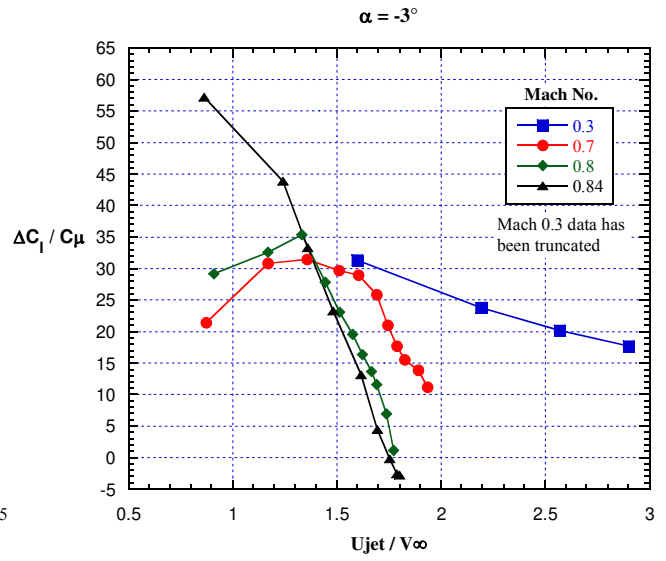
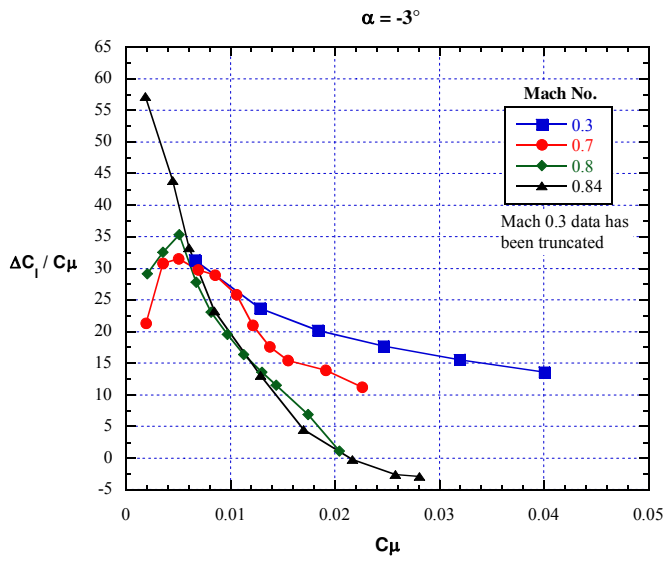


Figure 60 – Lift augmentation ratio versus C_μ or velocity ratio, Mach number effect, upper slot blowing, Coanda (2.98:1), slot ($h/c = 0.0012$).

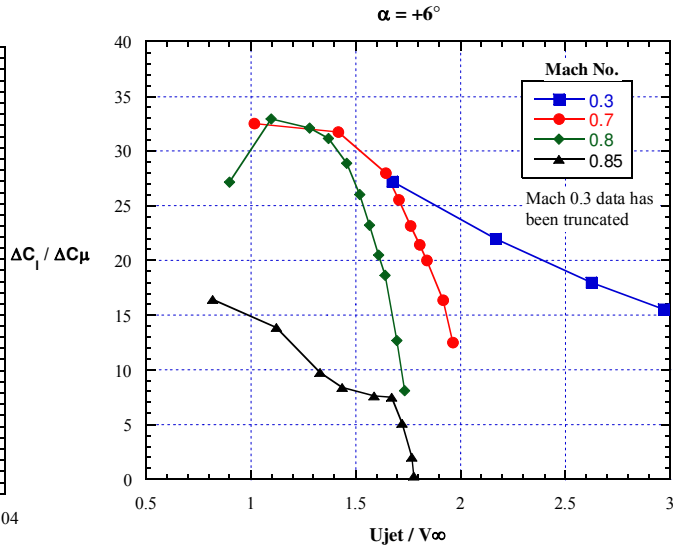
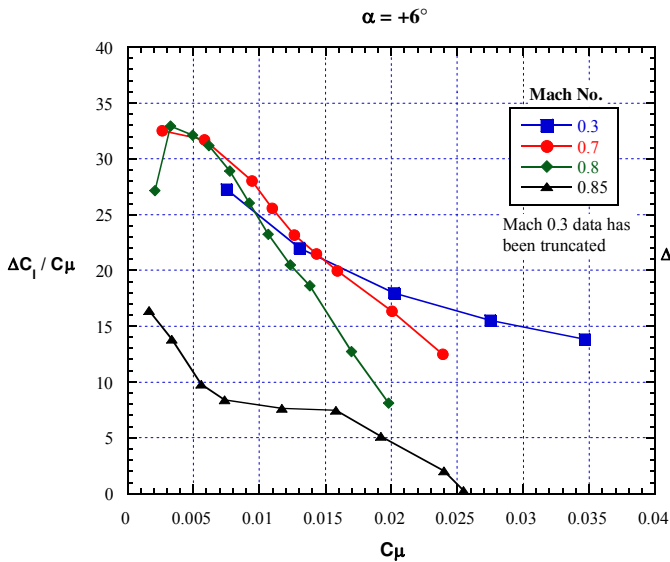
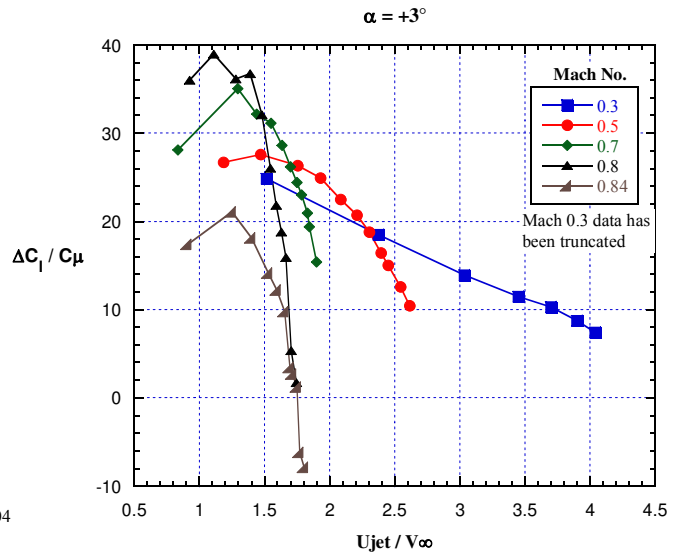
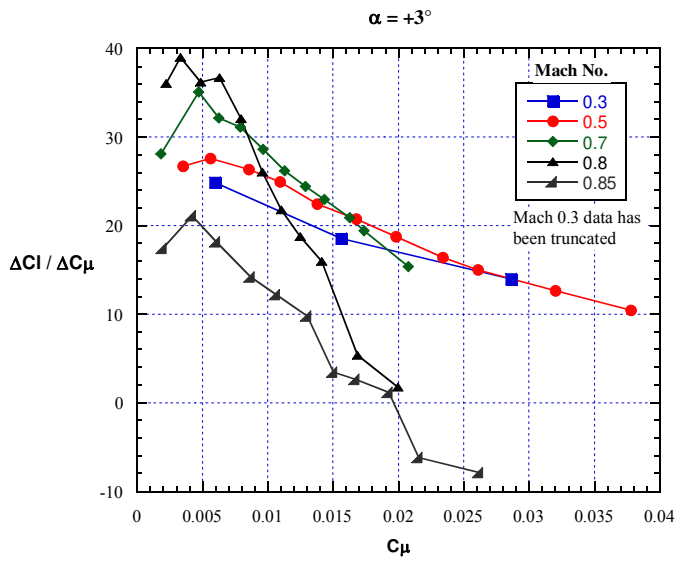


Figure 60 – Continued.

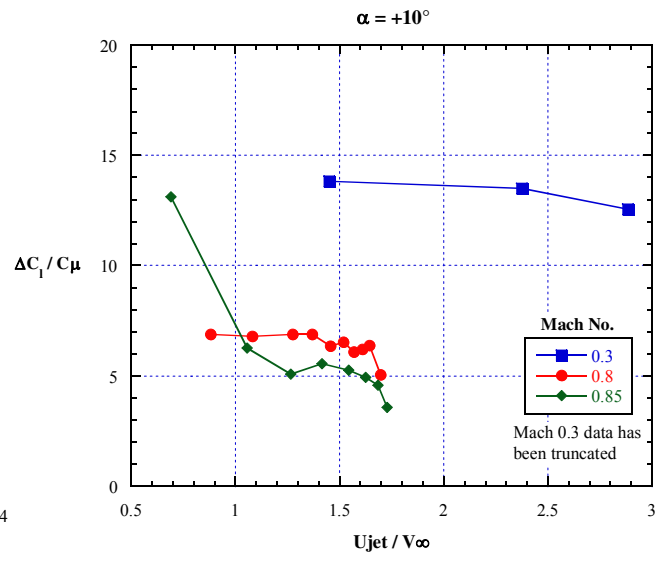
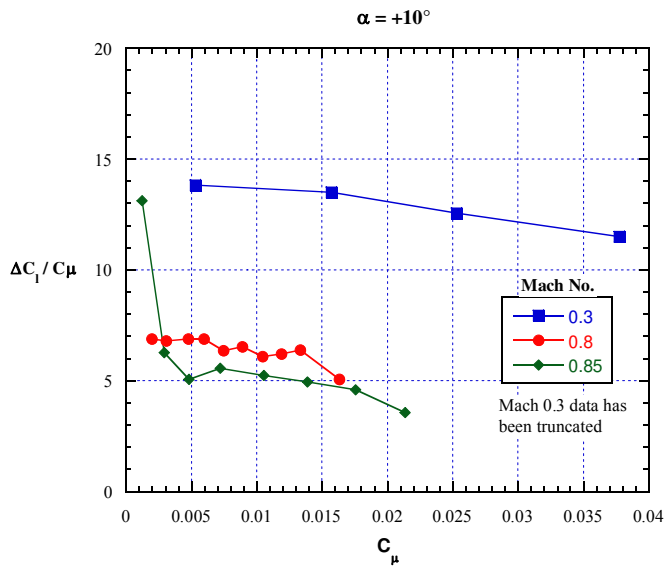


Figure 60 – Concluded.

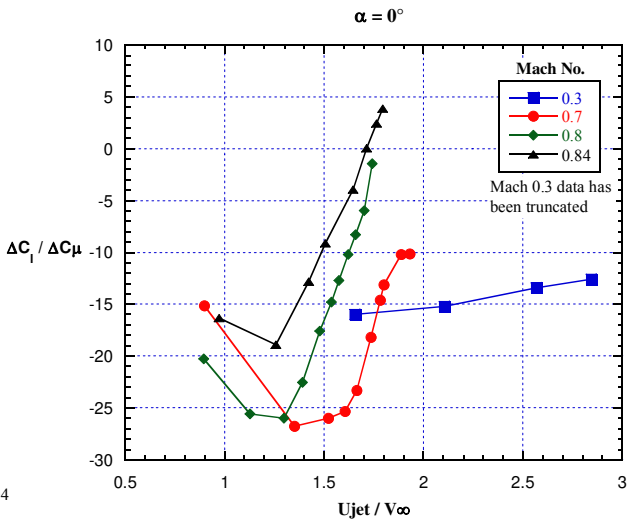
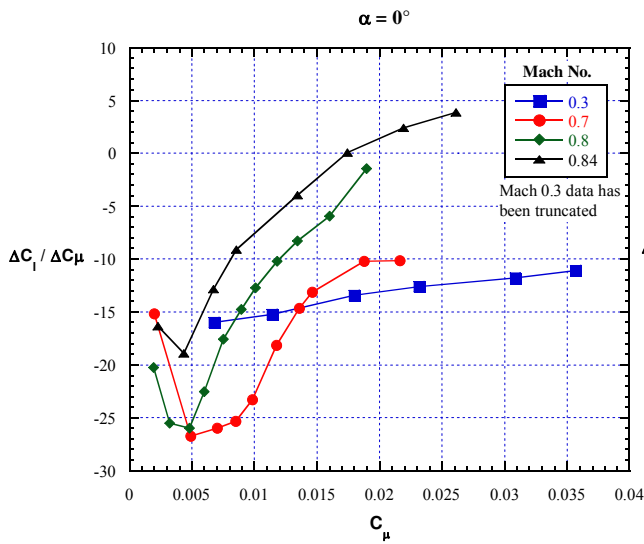
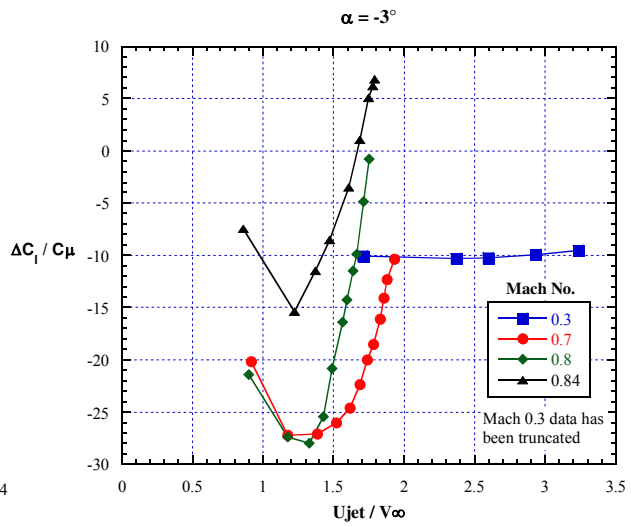
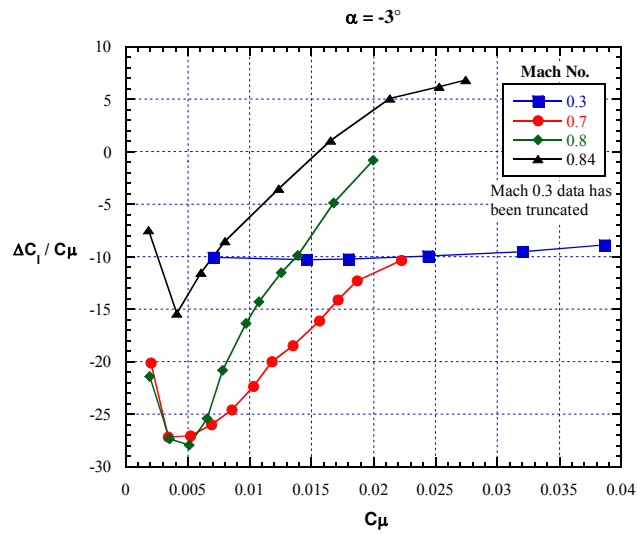


Figure 61 – Lift augmentation ratio versus C_μ or velocity ratio, Mach number effect, lower slot blowing, Coanda (2.98:1), slot ($h/c = 0.0012$).

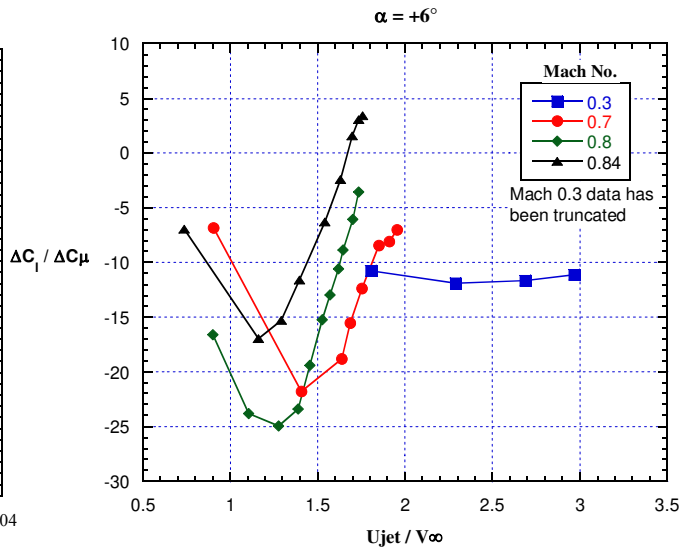
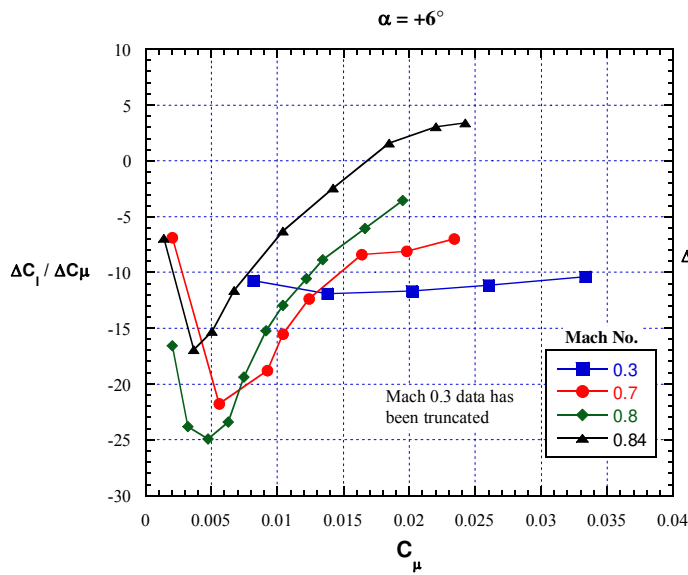
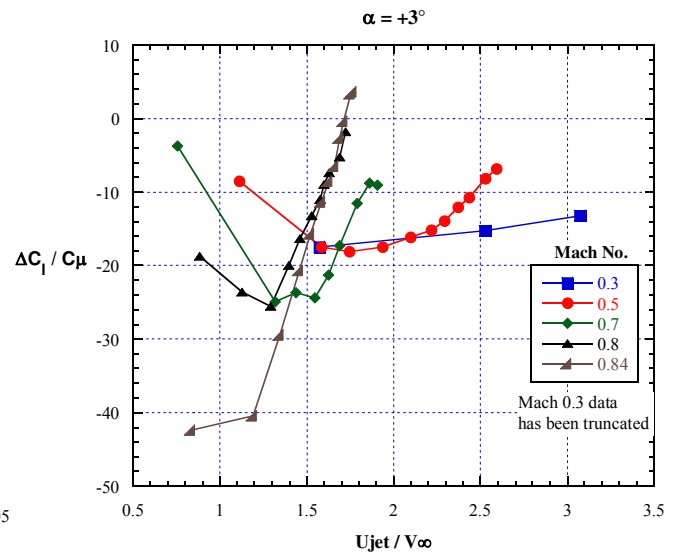
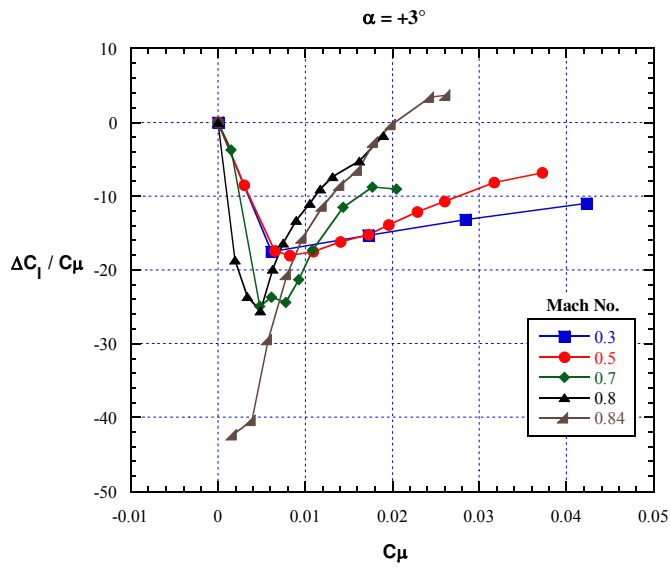


Figure 61 – Continued.

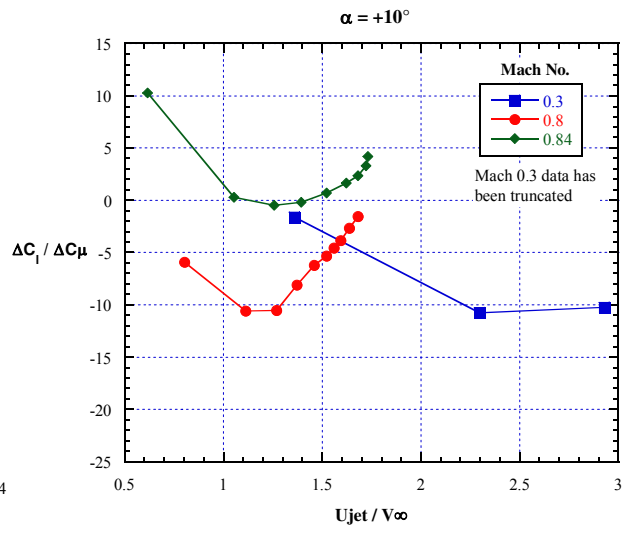
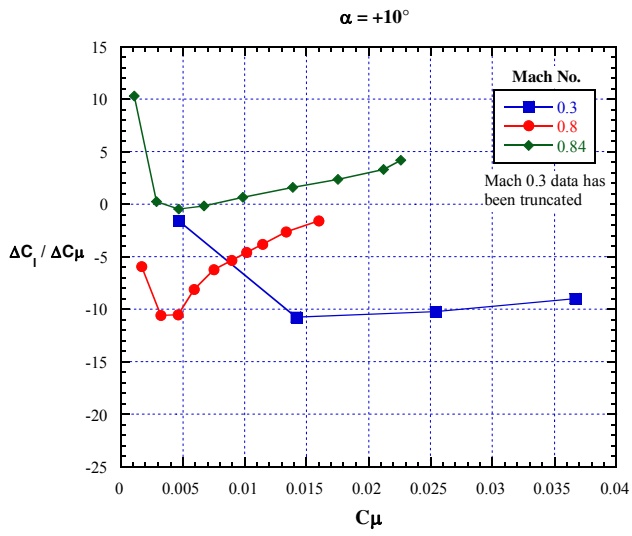


Figure 61 – Concluded.

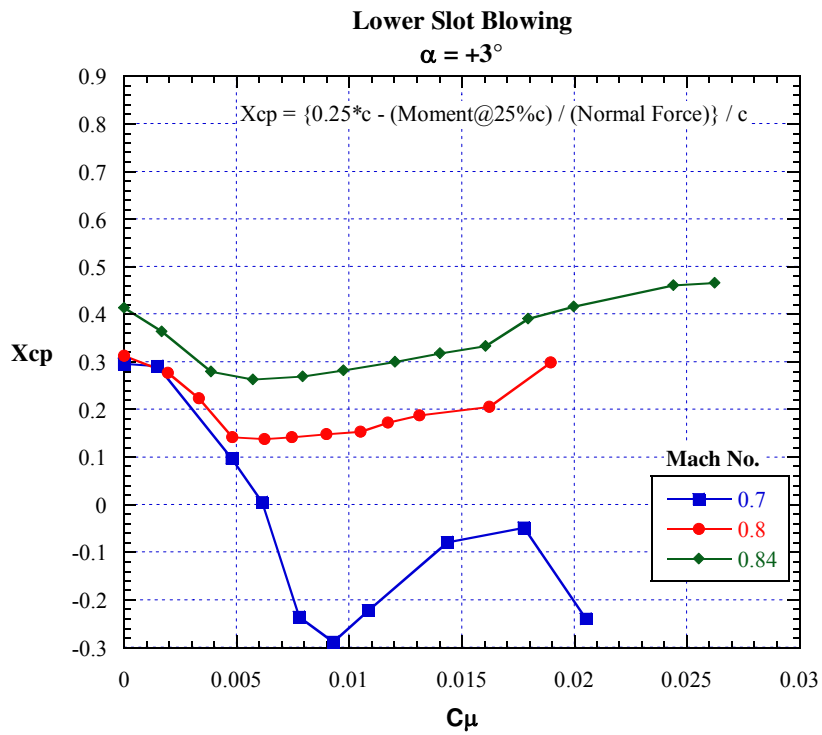
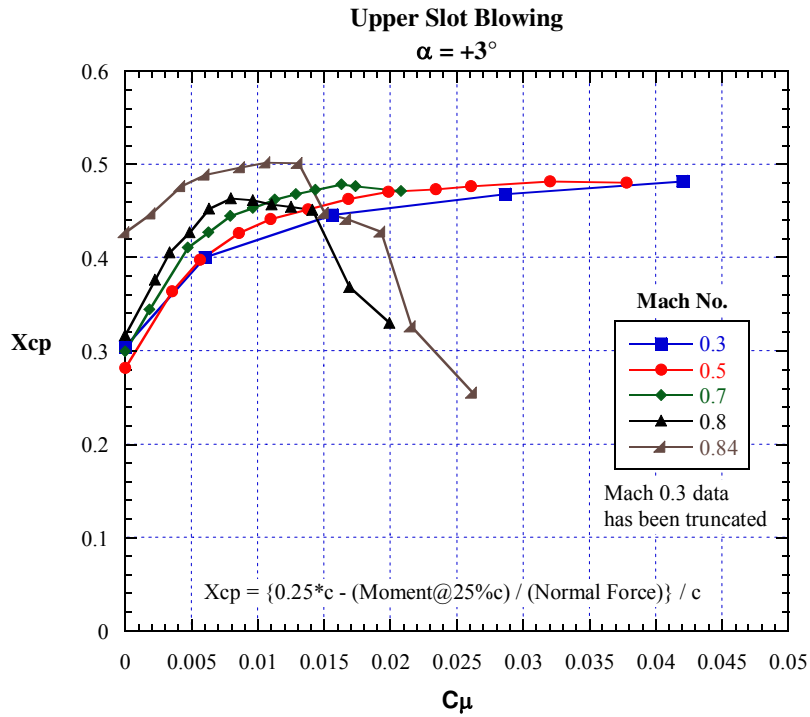


Figure 62 – Center of pressure location versus C_μ , Mach number effect, Coanda (2.98:1), slot ($h/c = 0.0012$).

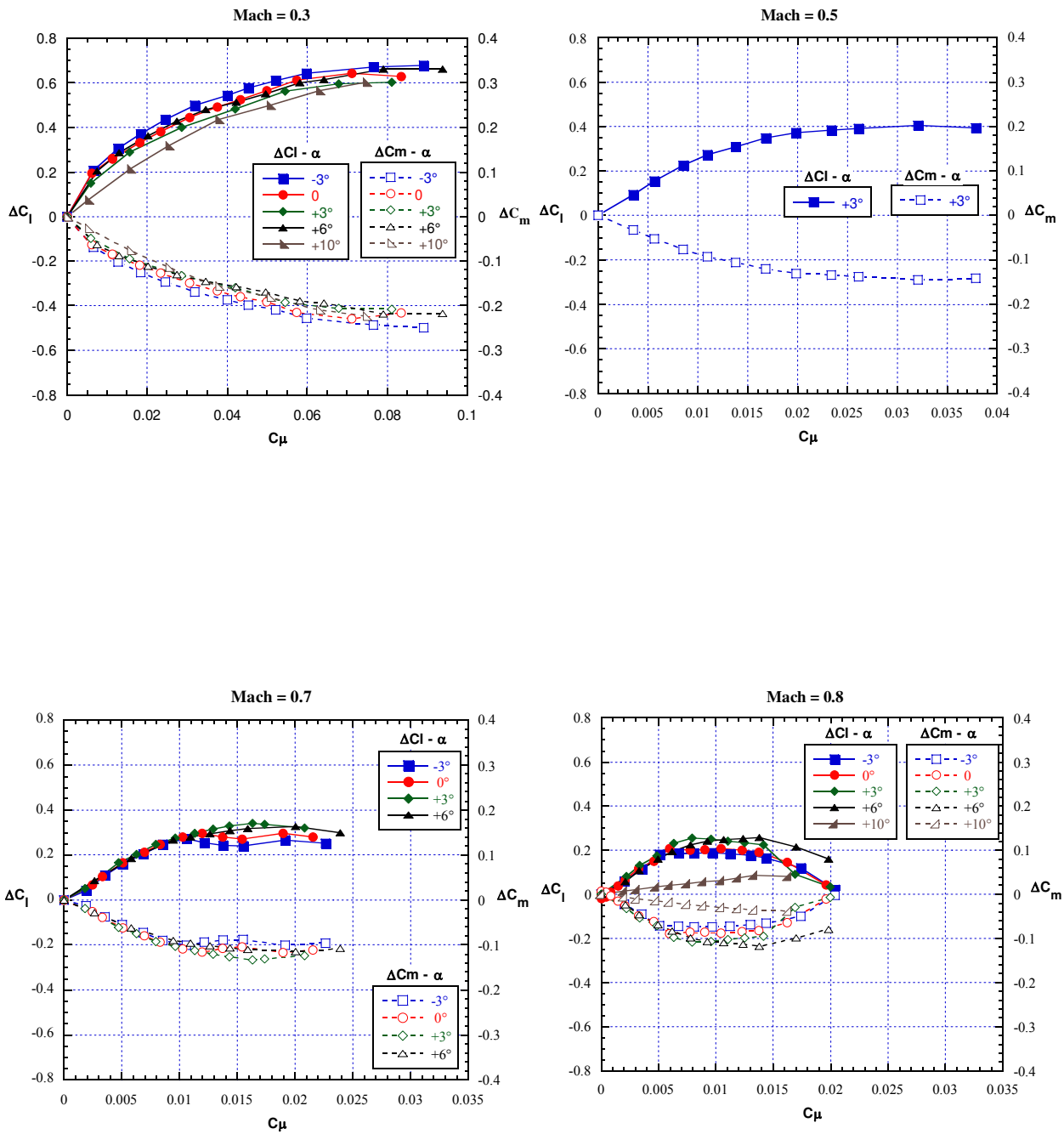


Figure 63 – ΔC_l & ΔC_m versus C_μ , angle of attack effect, upper slot blowing, Coanda (2.98:1), slot ($h/c = 0.0012$).

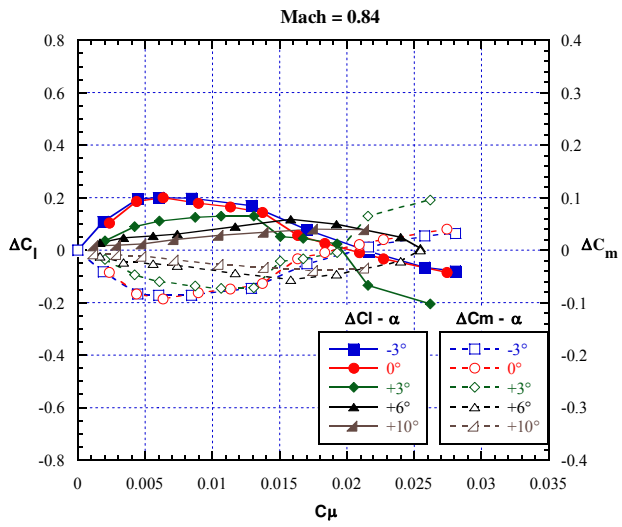


Figure 63 – Concluded.

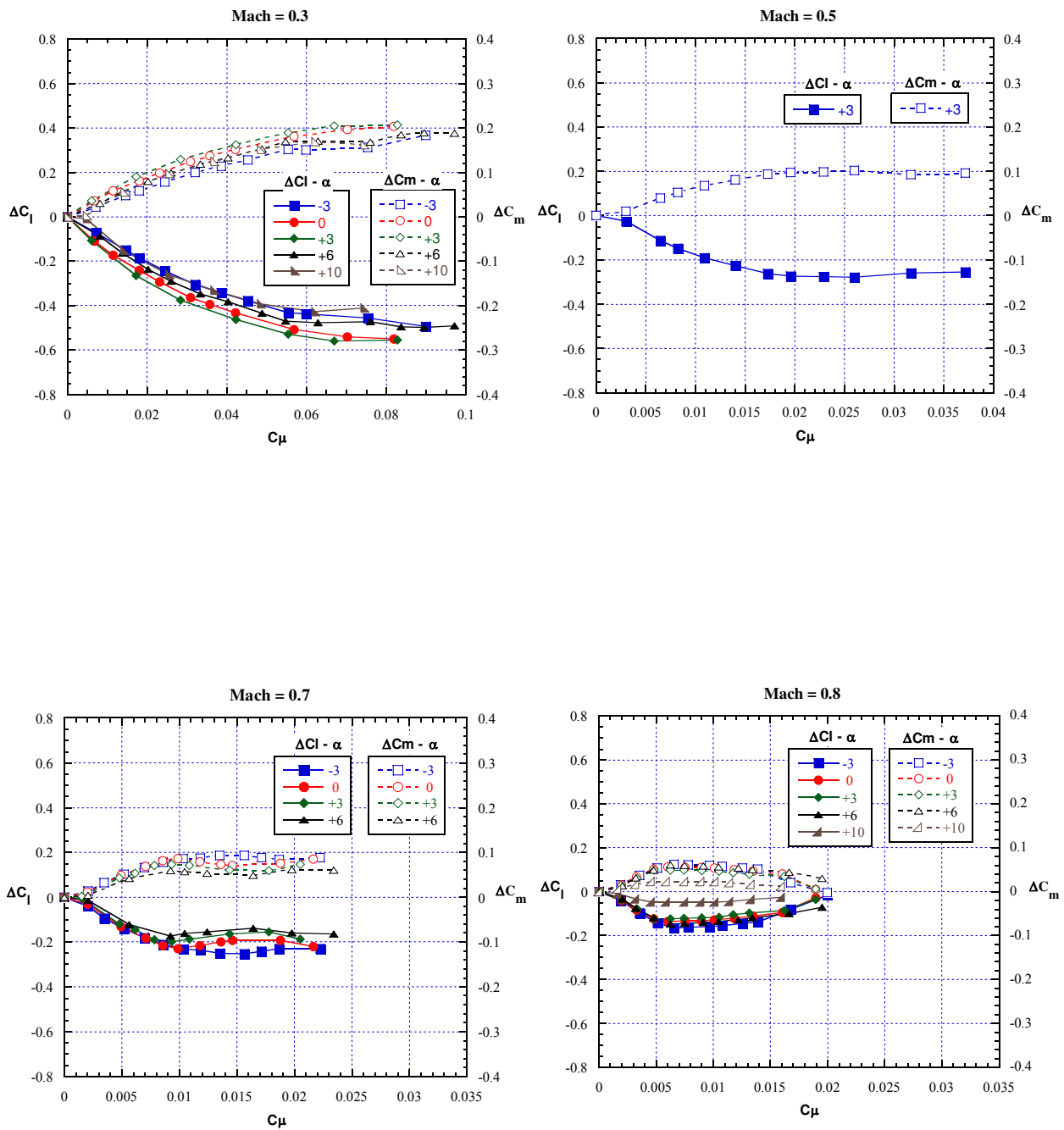


Figure 64 – ΔC_l & ΔC_m versus C_μ , angle of attack effect, lower slot blowing, Coanda (2.98:1), slot ($h/c = 0.0012$).

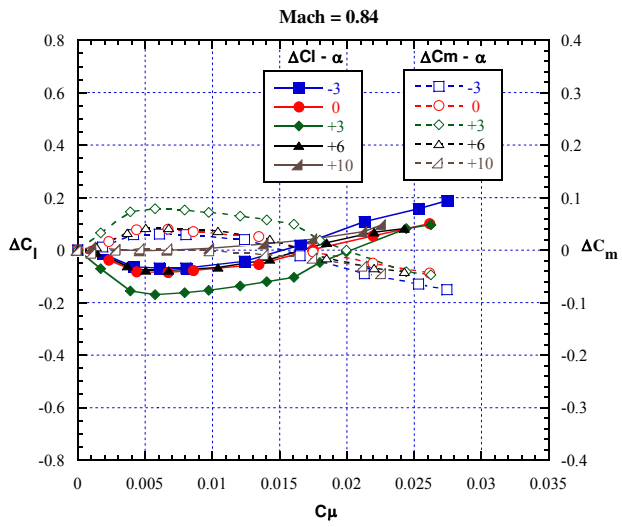


Figure 64 – Concluded.

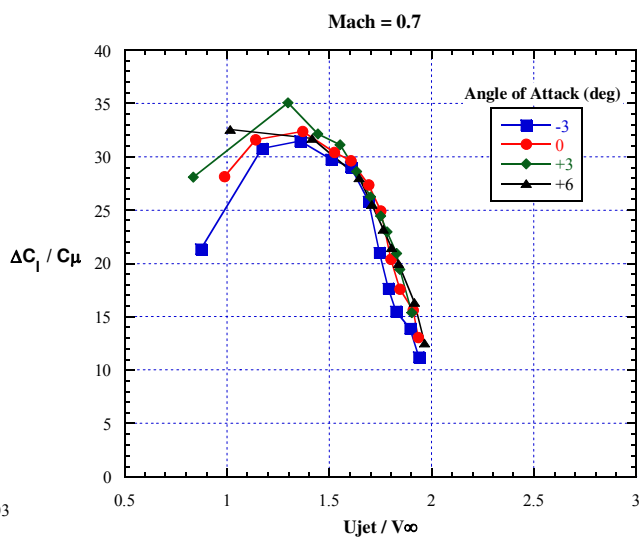
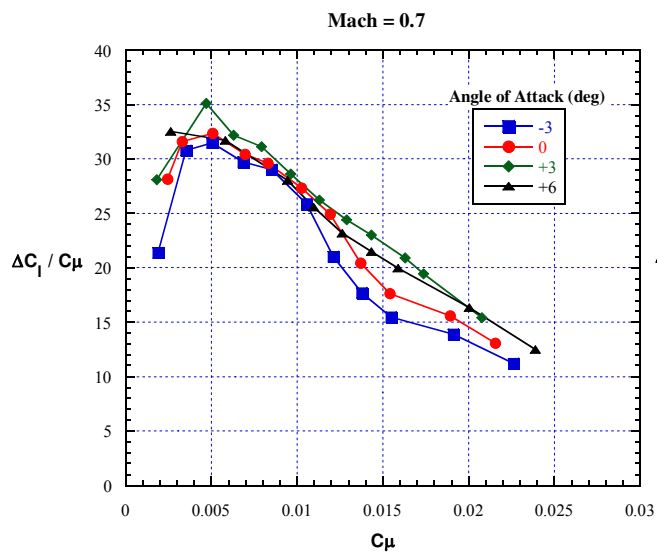
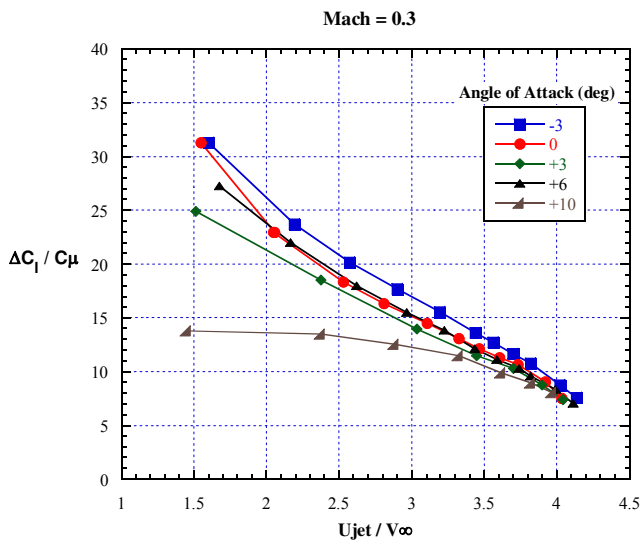
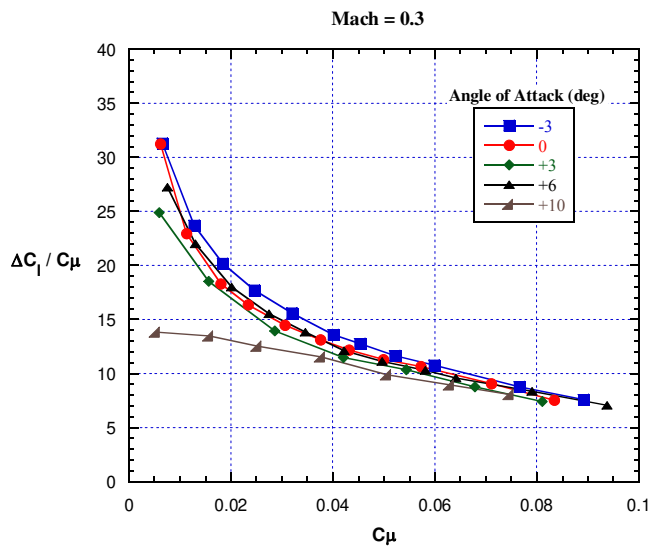


Figure 65 – Lift augmentation ratio versus C_{μ} or velocity ratio, angle of attack effect, upper slot blowing, Coanda (2.98:1), slot ($h/c = 0.0012$).

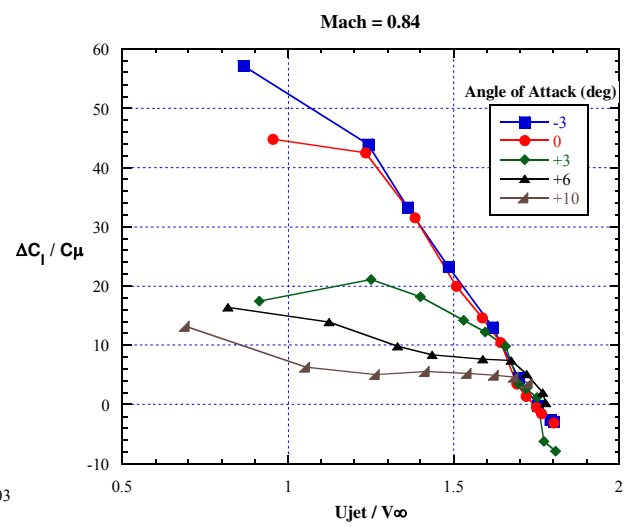
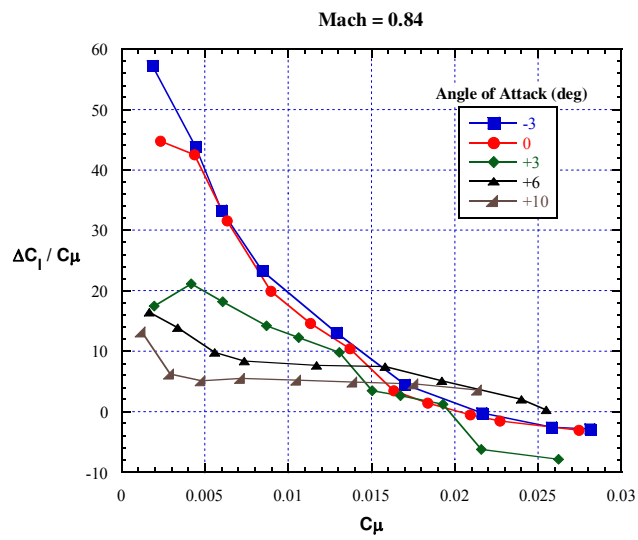
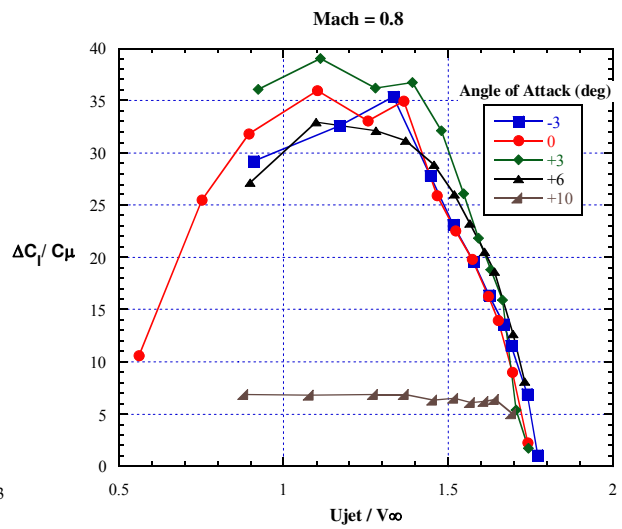
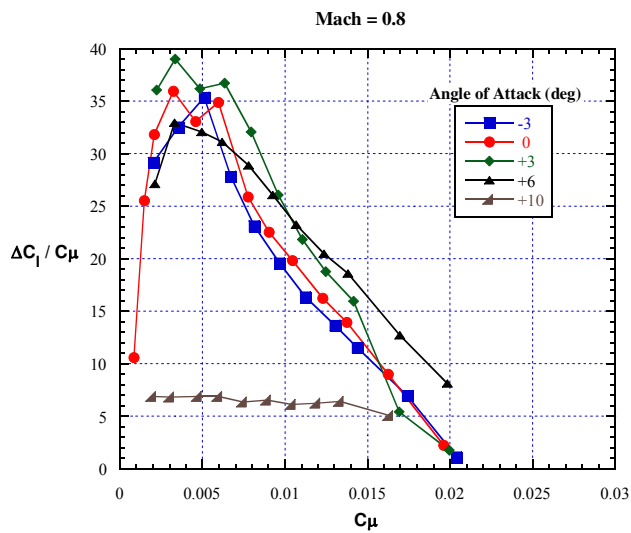


Figure 65 – Concluded.

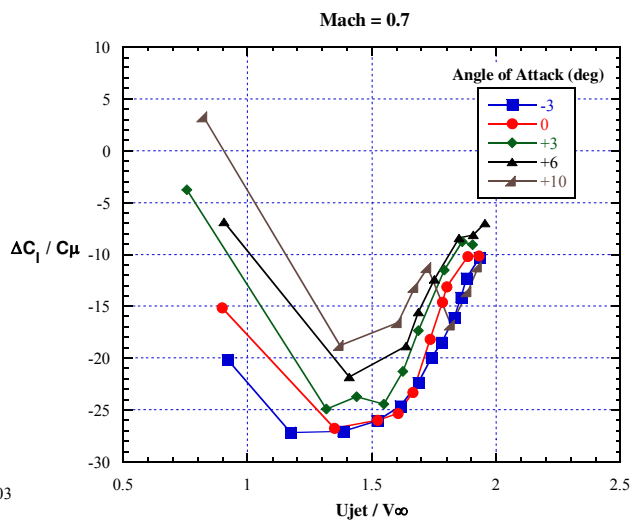
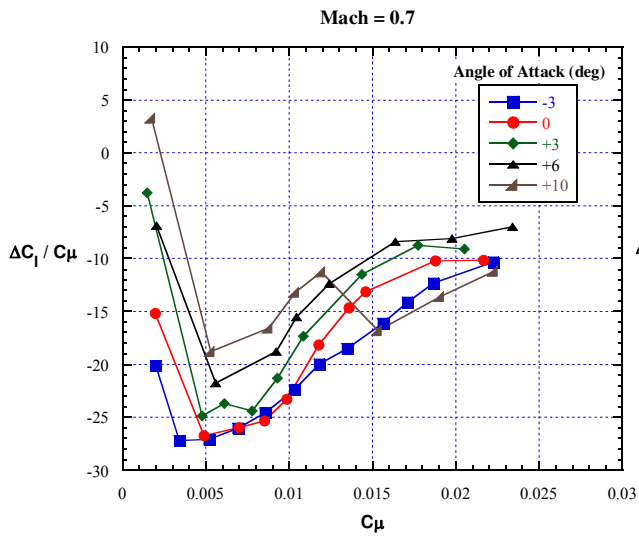
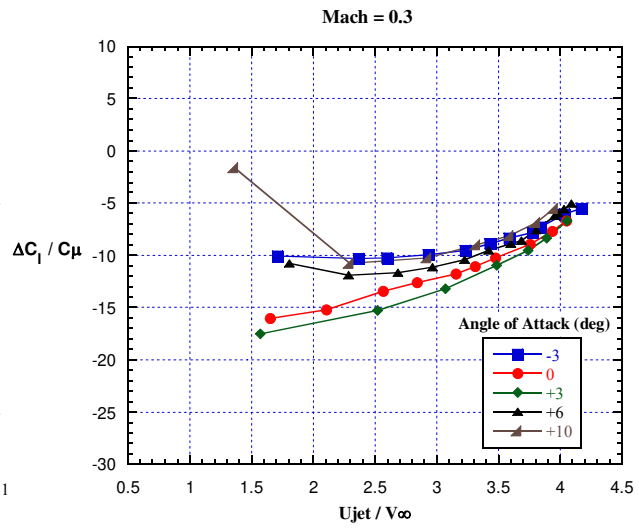
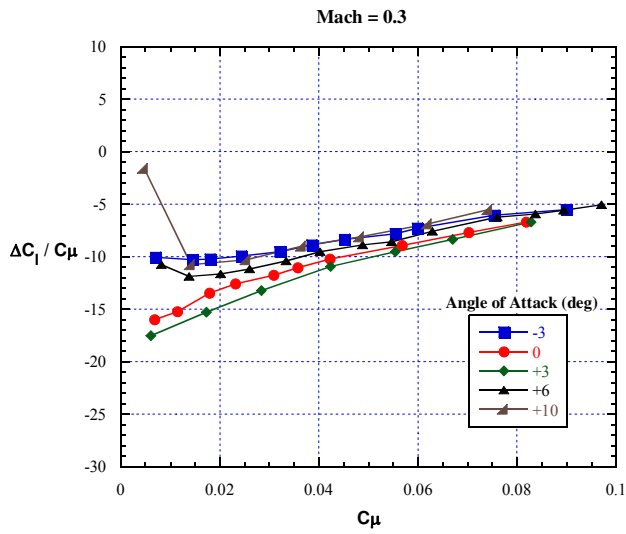


Figure 66 – Lift augmentation ratio versus C_{μ} or velocity ratio, angle of attack effect, lower slot blowing, Coanda (2.98:1), slot ($h/c = 0.0012$).

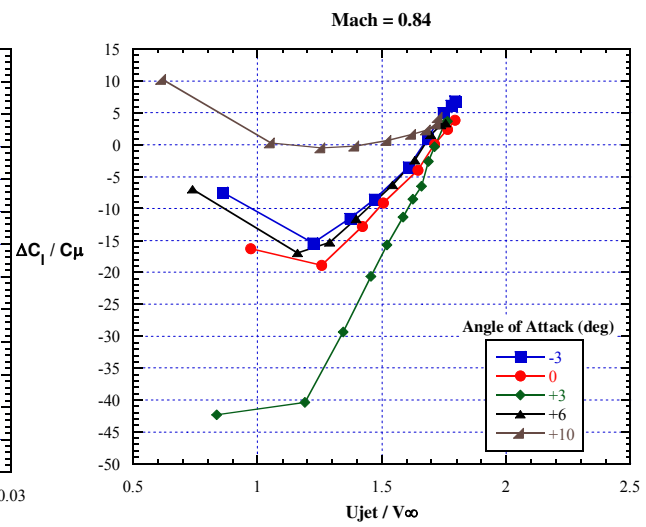
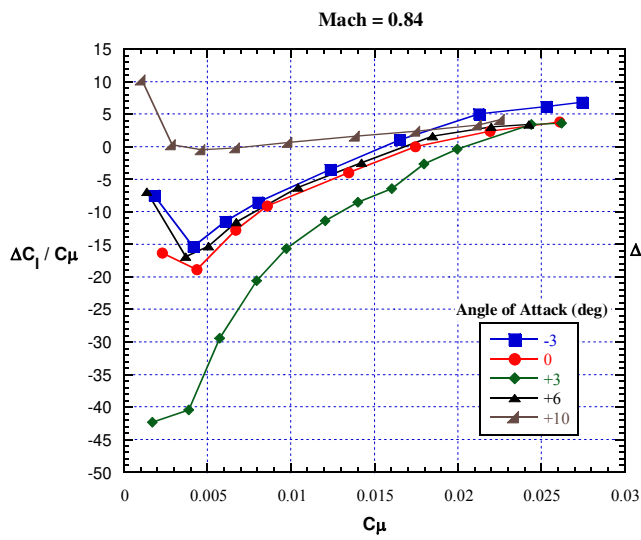
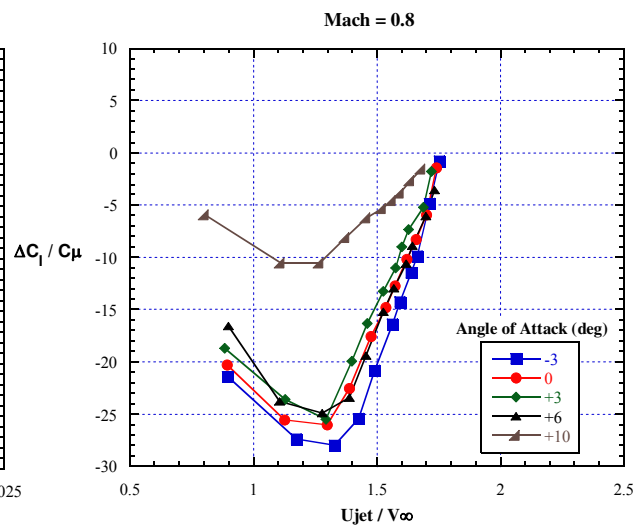
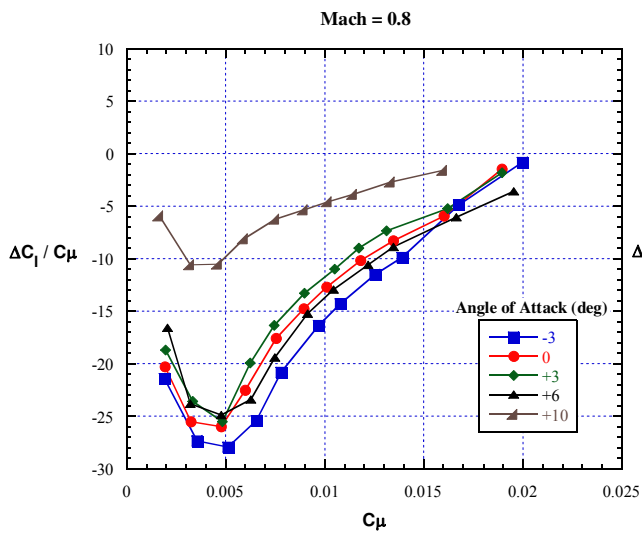


Figure 66 – Concluded.

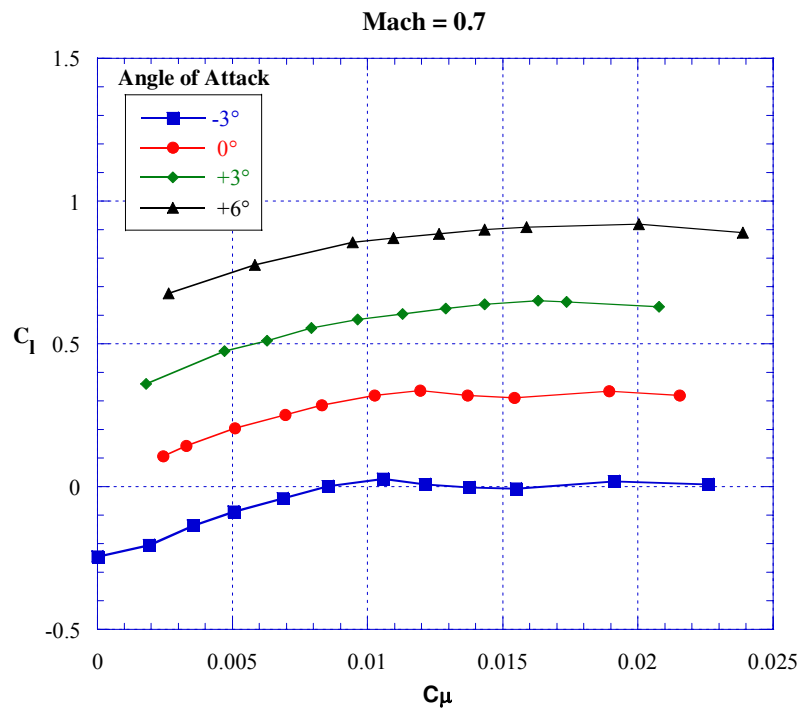
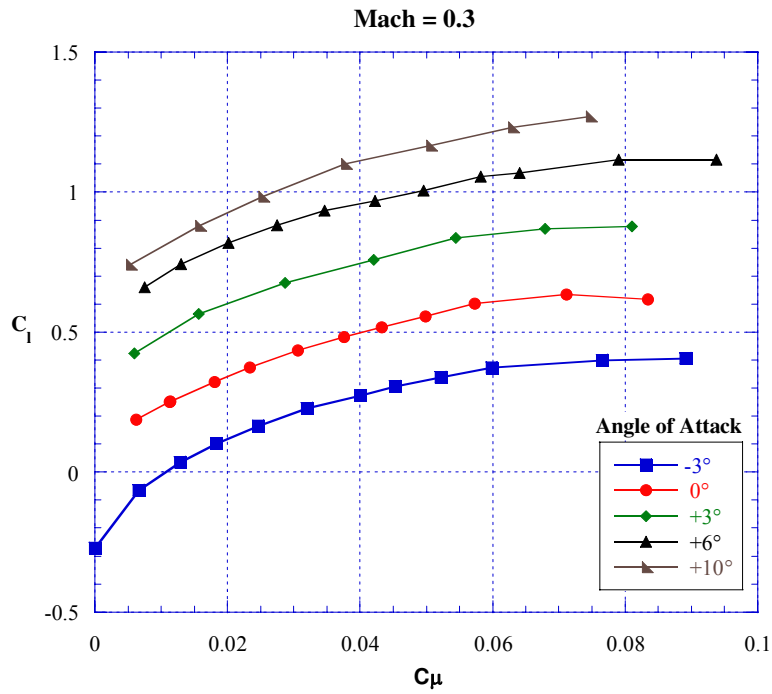


Figure 67 – C_1 versus C_μ , angle of attack effect, upper slot blowing, Coanda (2.98:1), slot ($h/c = 0.0012$).

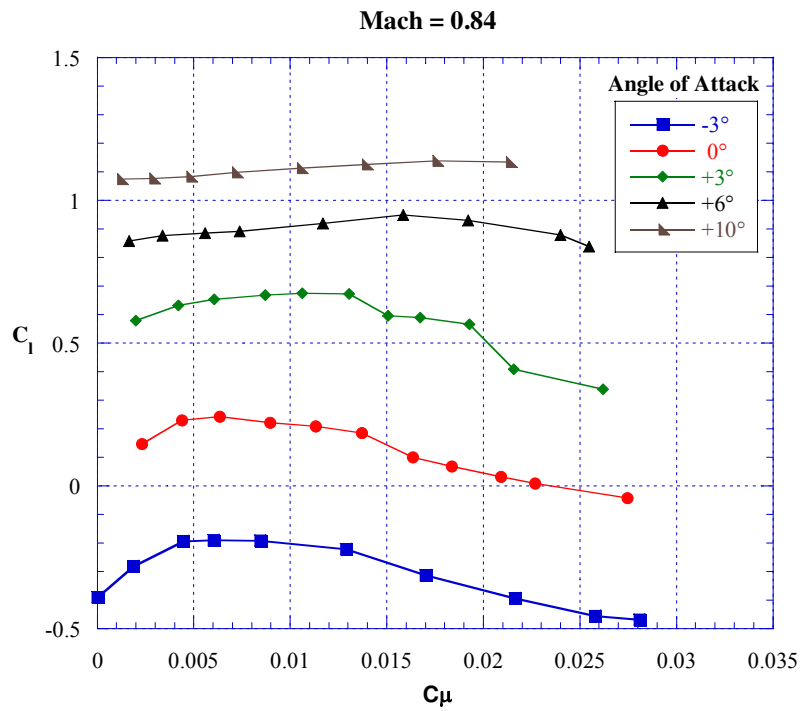
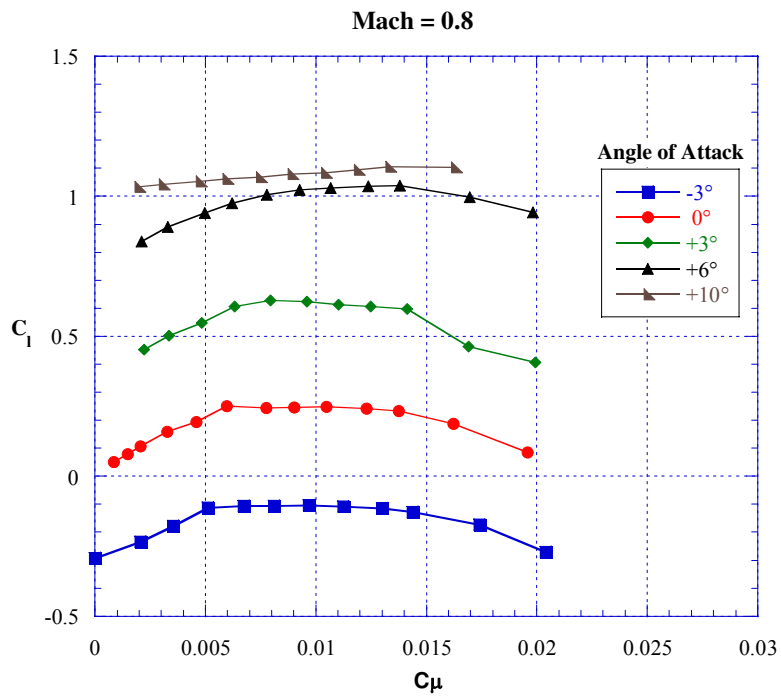


Figure 67 – Concluded.

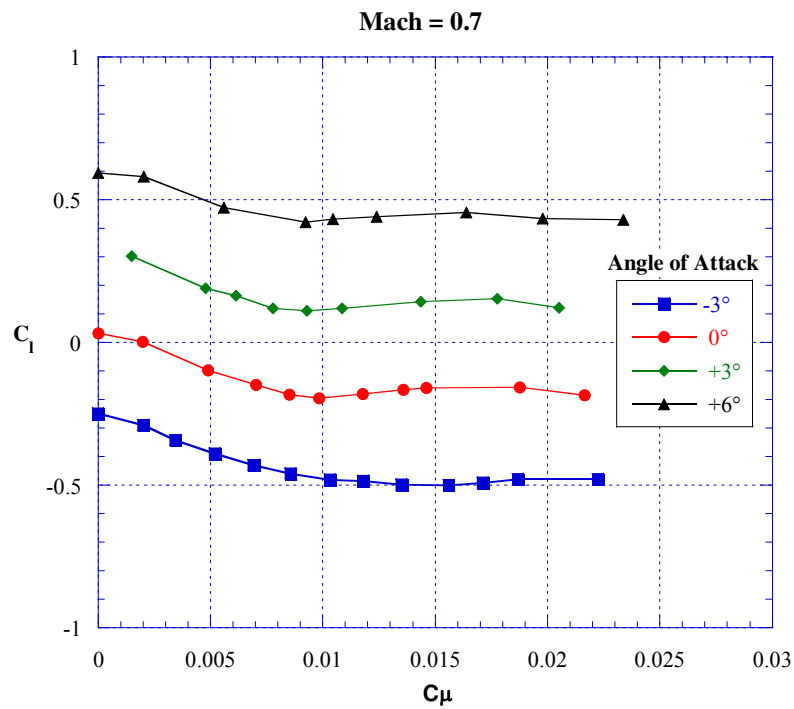
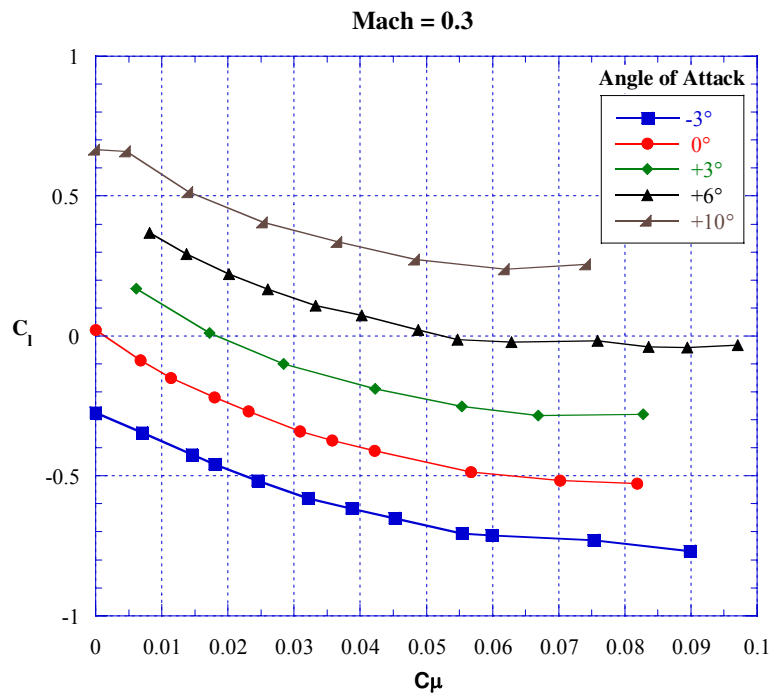


Figure 68 – C_l versus C_μ , angle of attack effect, lower slot blowing, Coanda (2.98:1), slot ($h/c = 0.0012$).

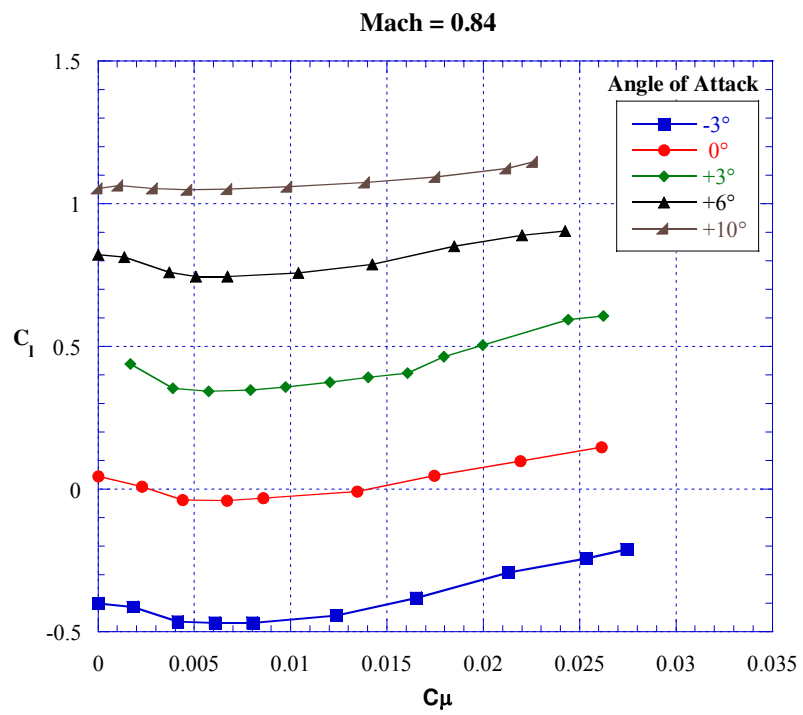
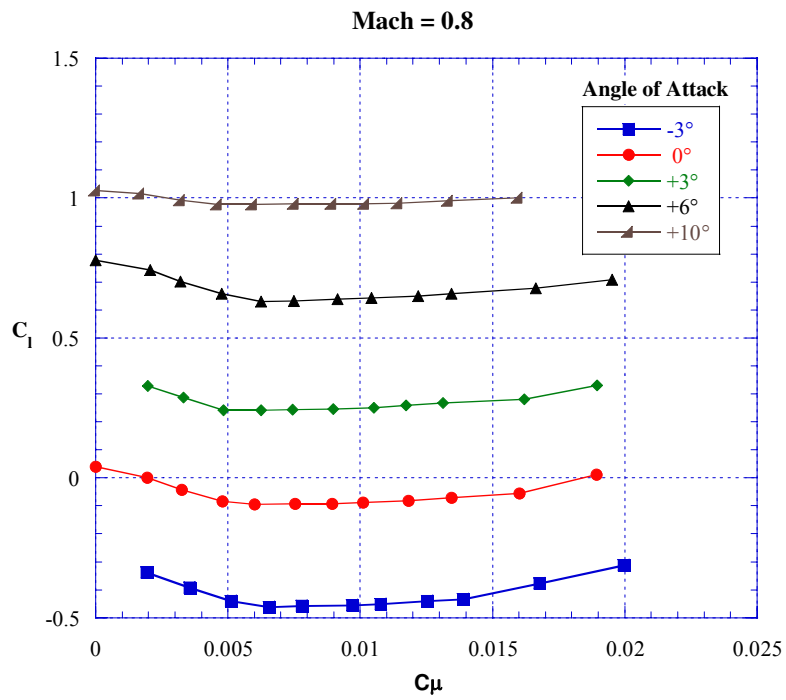


Figure 68 – Concluded.

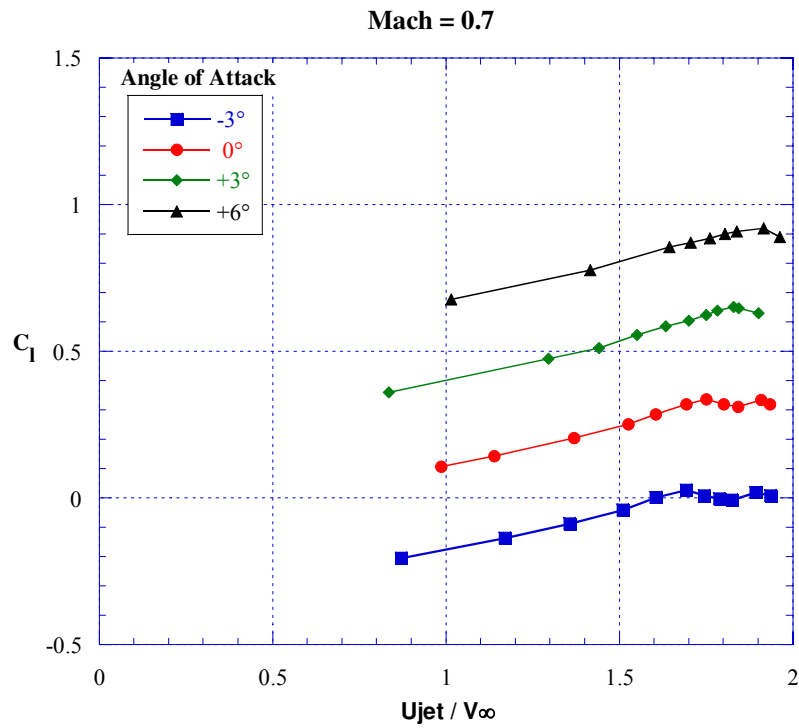
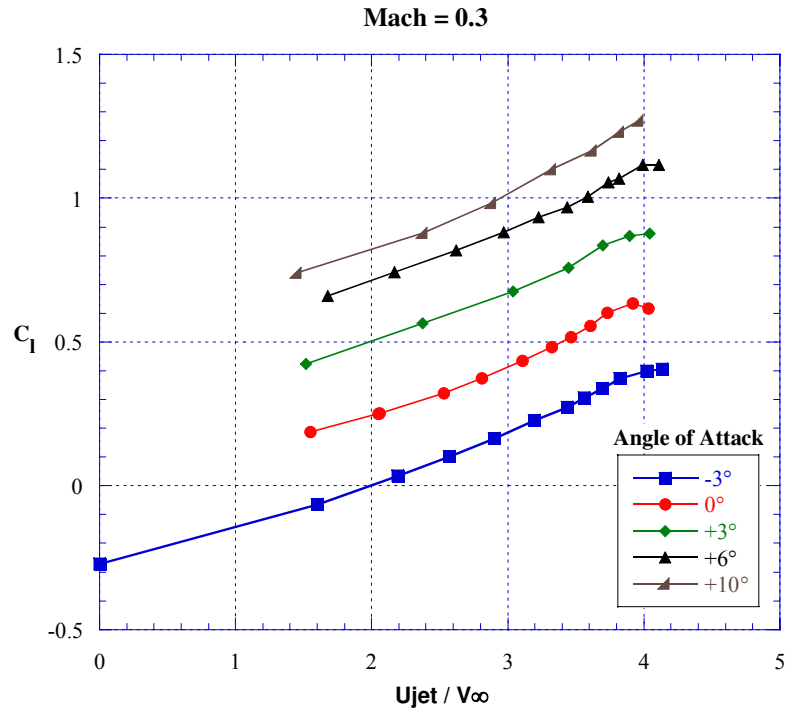


Figure 69 – C_1 versus velocity ratio, angle of attack effect, upper slot blowing, Coanda (2.98:1), slot ($h/c = 0.0012$).

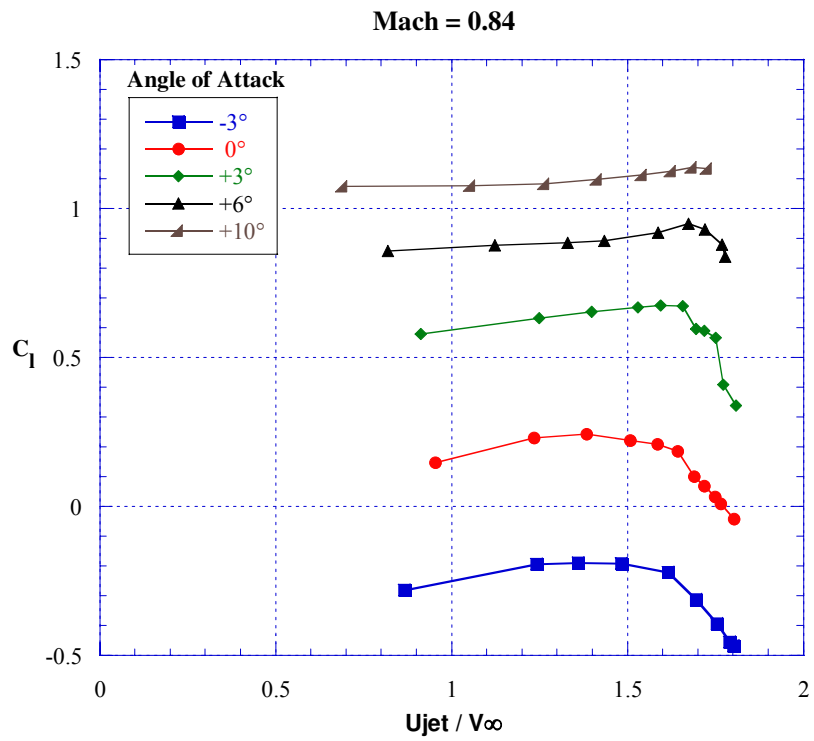
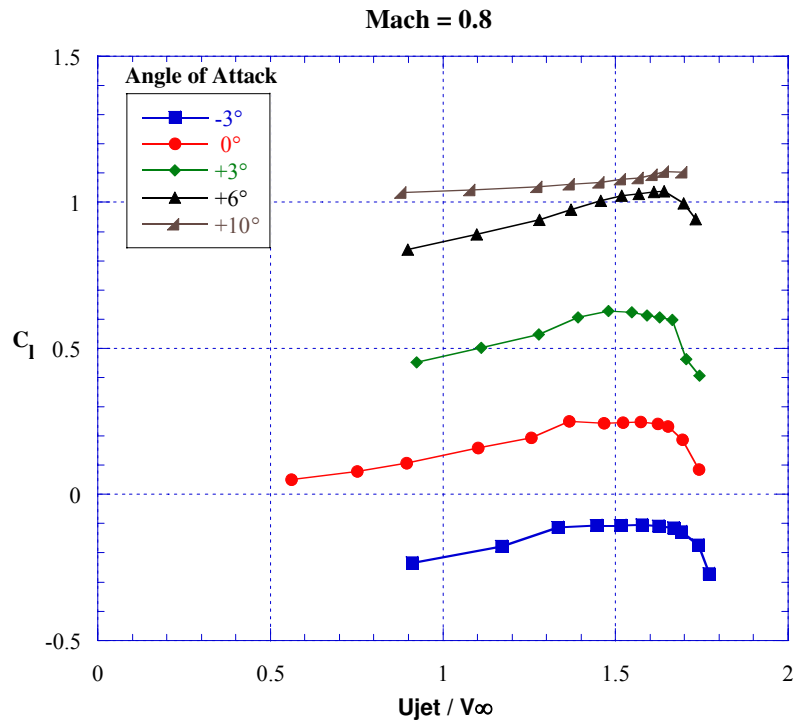


Figure 69 – Concluded.

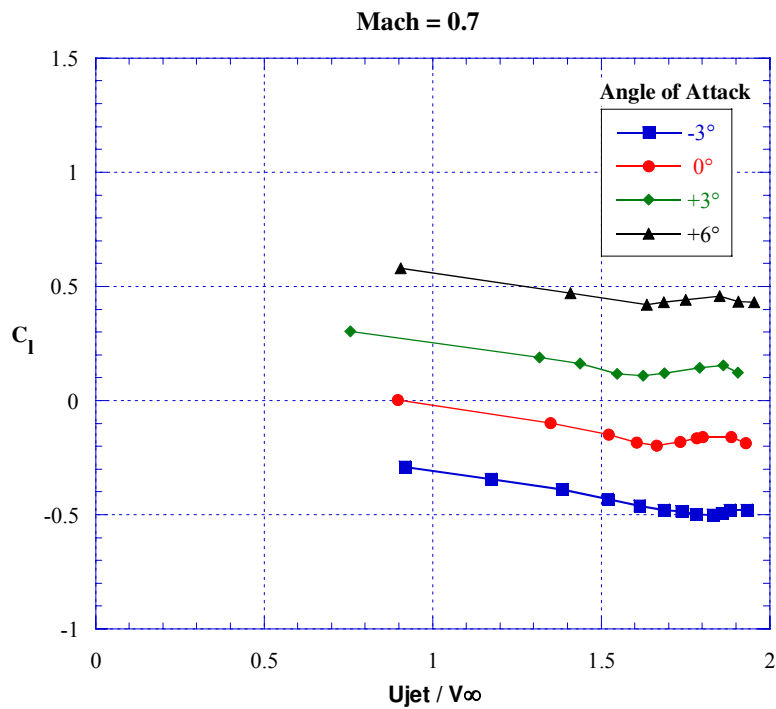
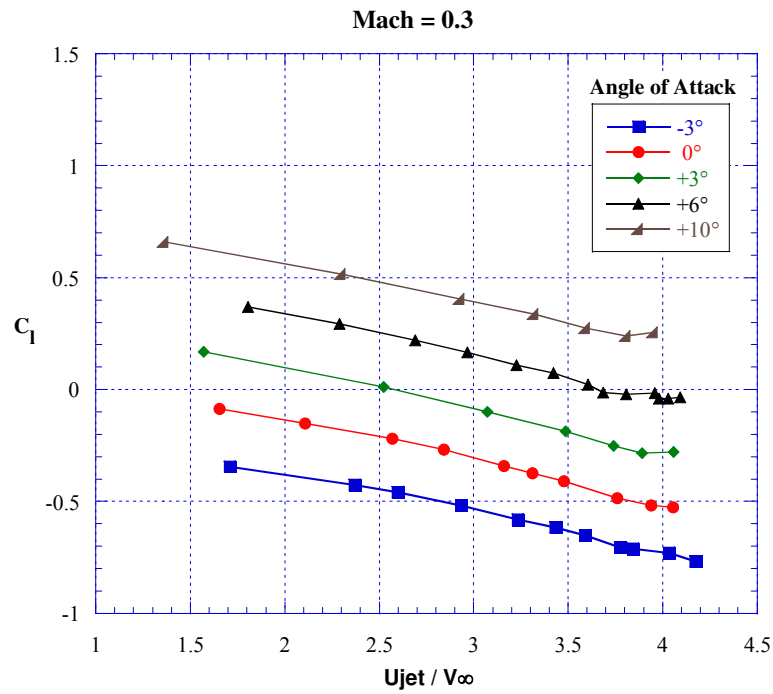


Figure 70 – C_1 versus velocity ratio, angle of attack effect, lower slot blowing, Coanda (2.98:1), slot ($h/c = 0.0012$).

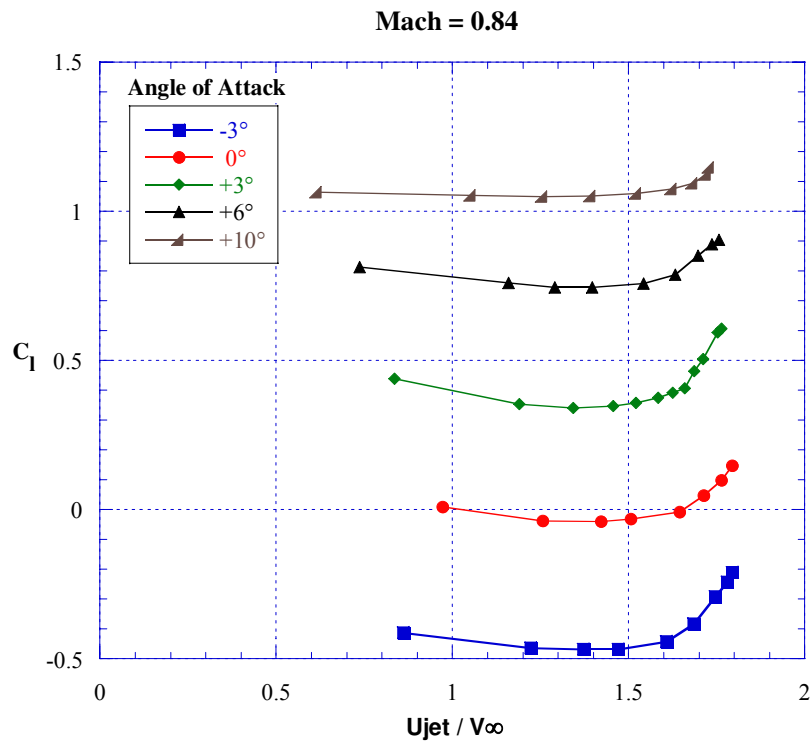
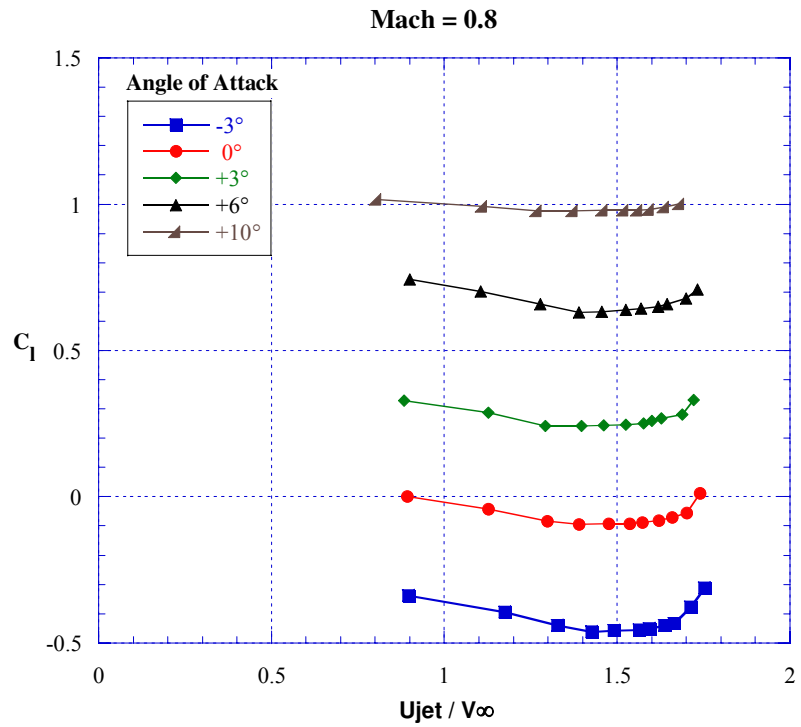


Figure 70 – Concluded.

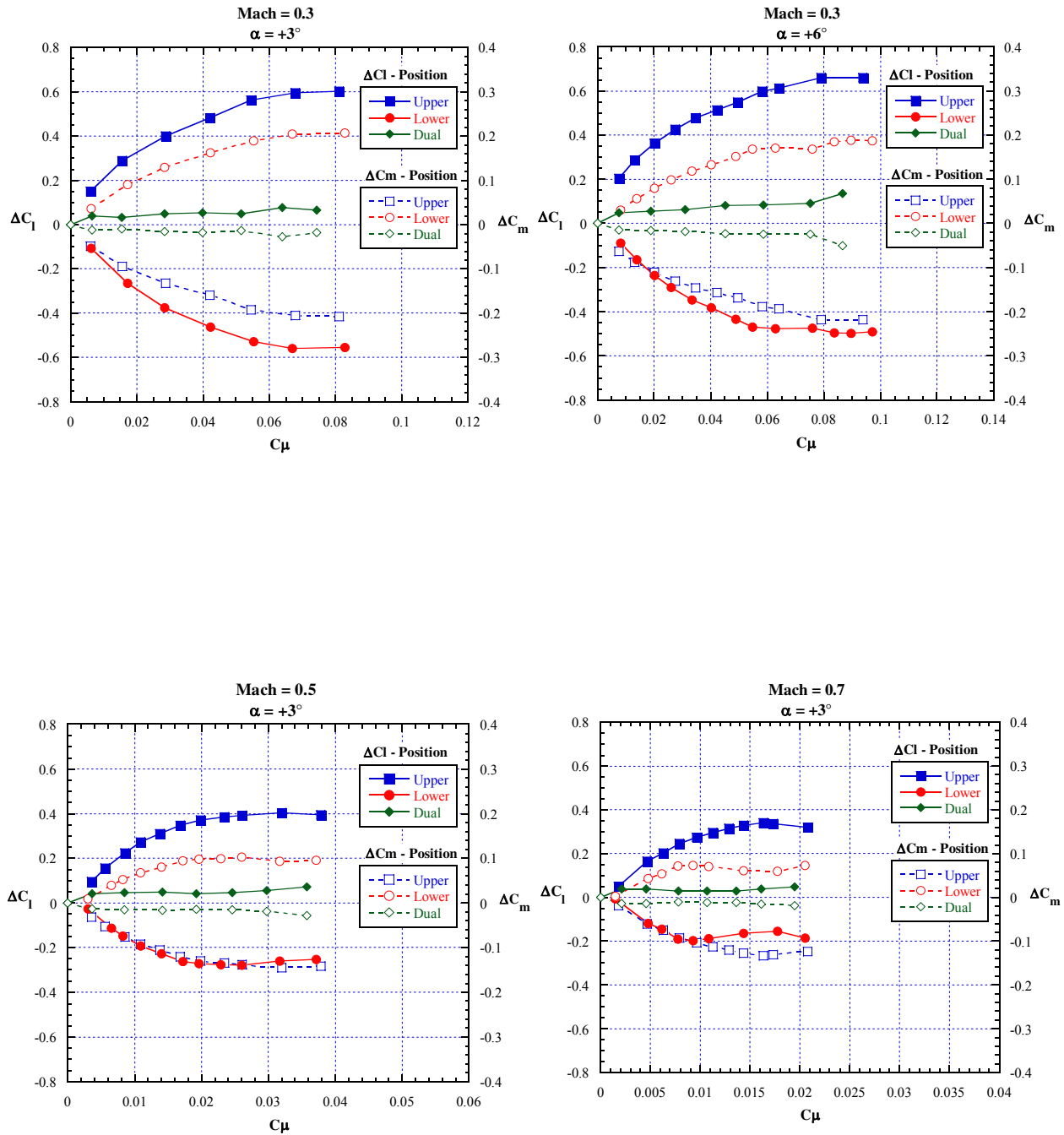


Figure 71 – ΔC_l & ΔC_m versus C_μ , slot position effect, Coanda (2.98:1), slot ($h/c = 0.0012$).

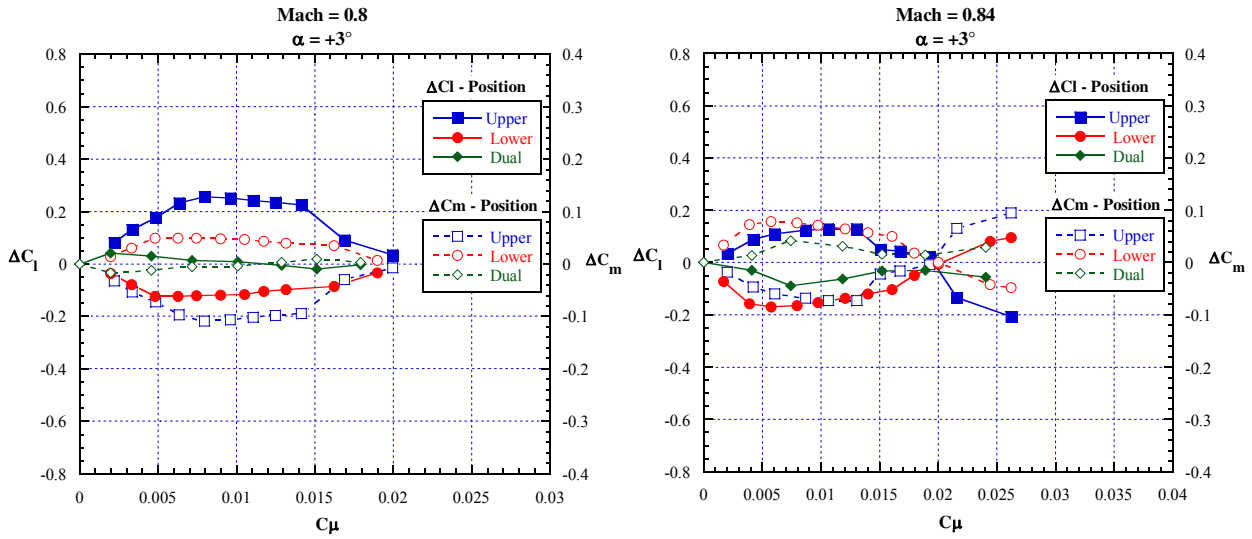


Figure 71 – Concluded.

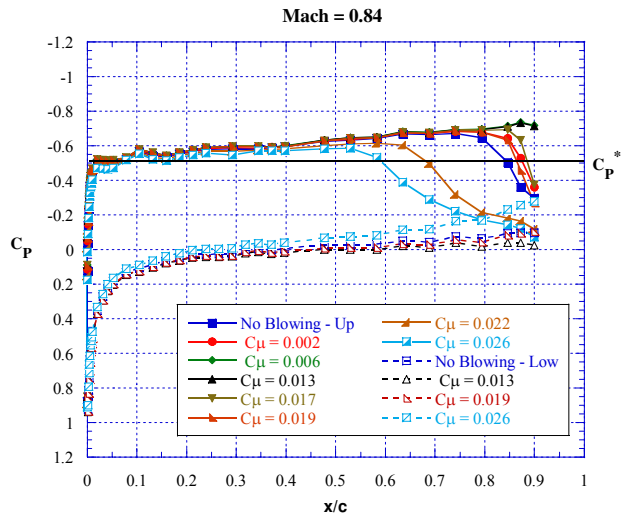
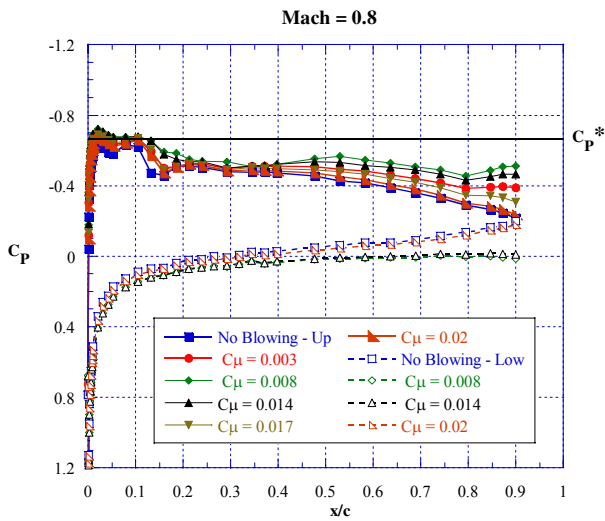
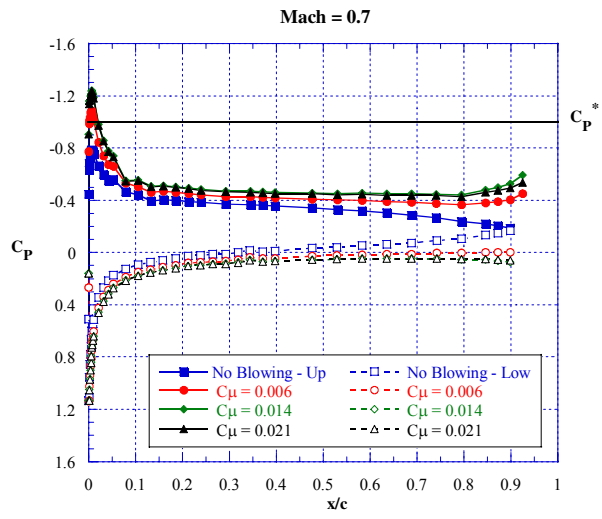
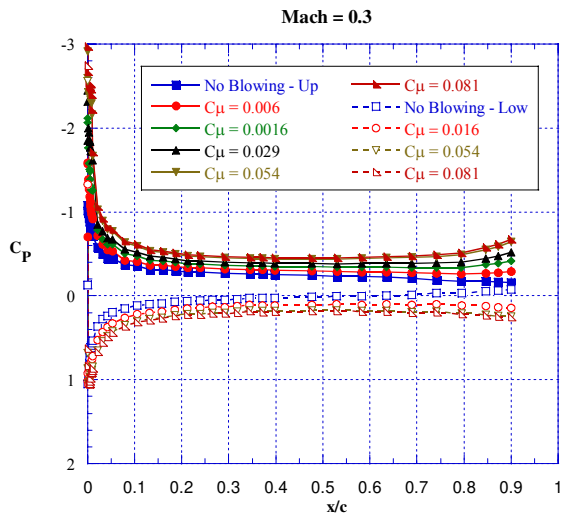


Figure 72 – Upper and lower chordwise surface pressure distribution, C_{μ} effect, upper slot blowing, Coanda (2.98:1), slot ($h/c = 0.0012$), $\alpha = 3^\circ$.

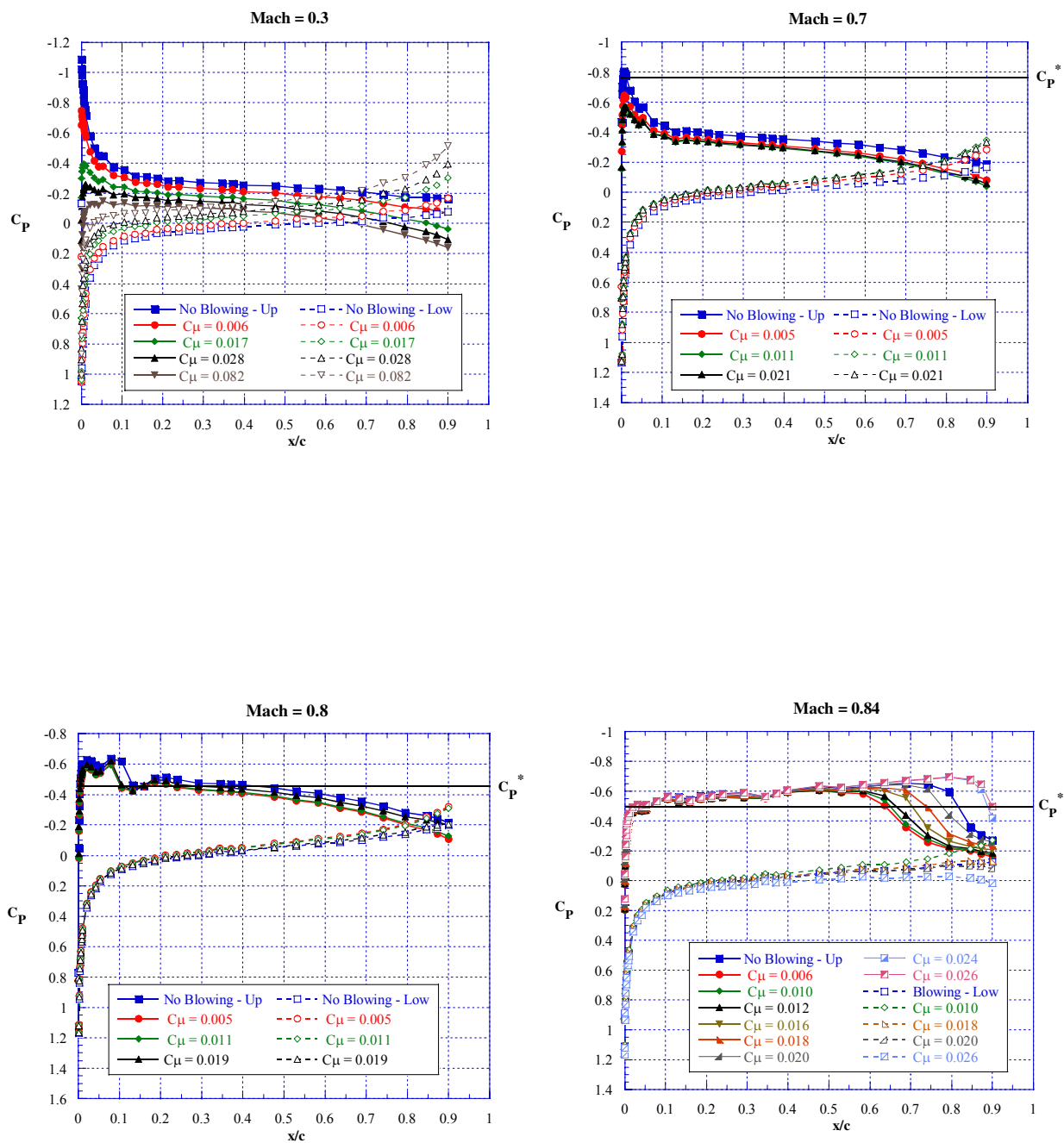


Figure 73 – Upper and lower chordwise surface pressure distribution, C_{μ} effect, lower slot blowing, Coanda (2.98:1), slot ($h/c = 0.0012$), $\alpha = 3^\circ$.

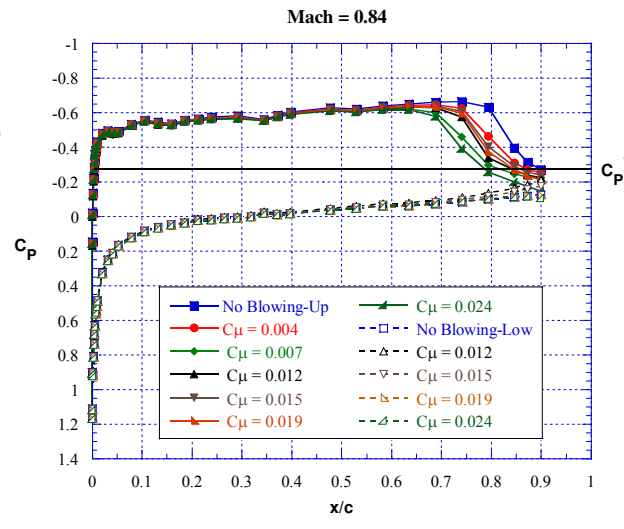
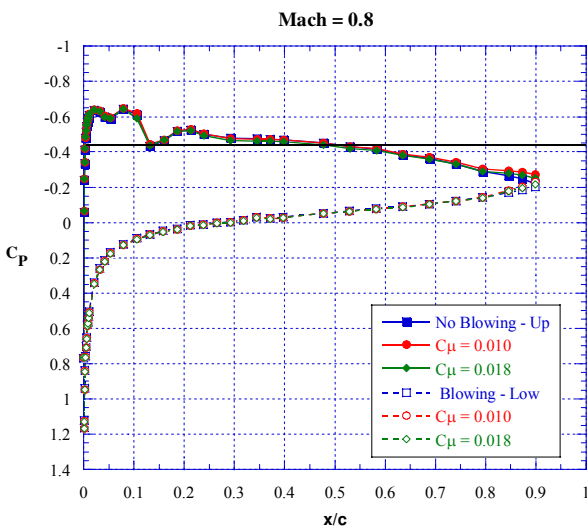
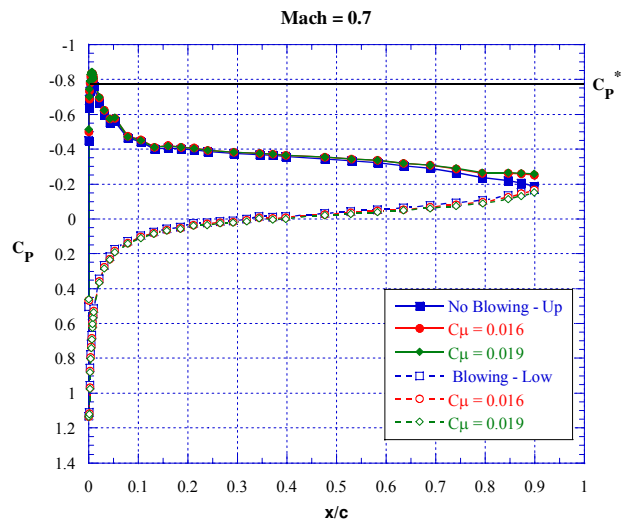
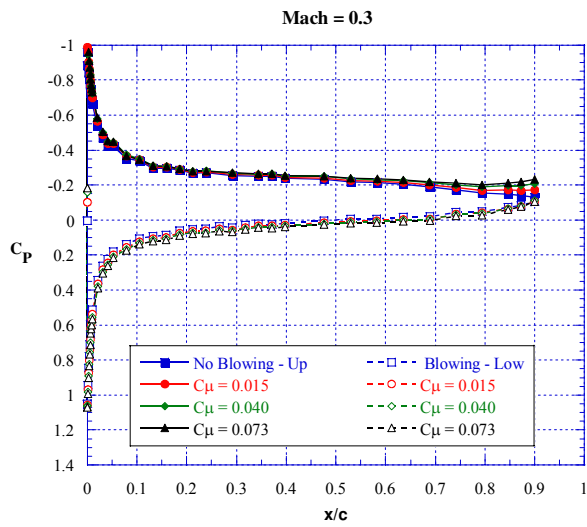


Figure 74 – Upper and lower chordwise surface pressure distribution, C_{μ} effect, dual slot blowing, Coanda (2.98:1), slot ($h/c = 0.0012$), $\alpha = 3^\circ$.

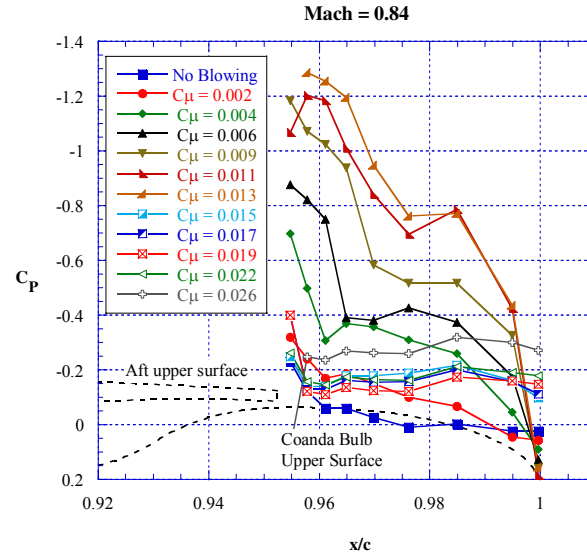
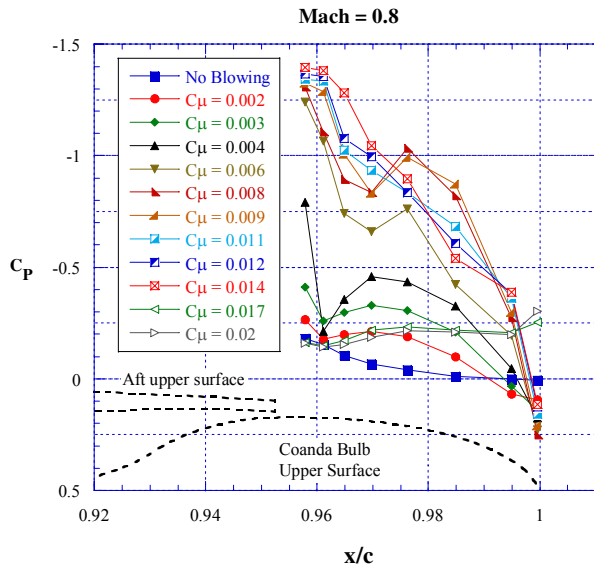
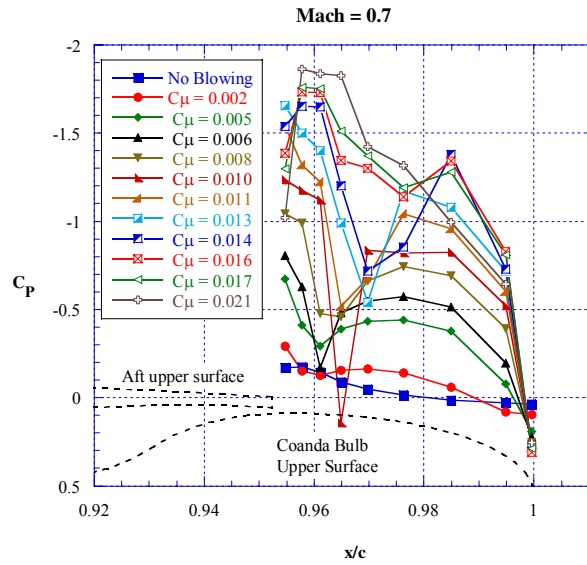
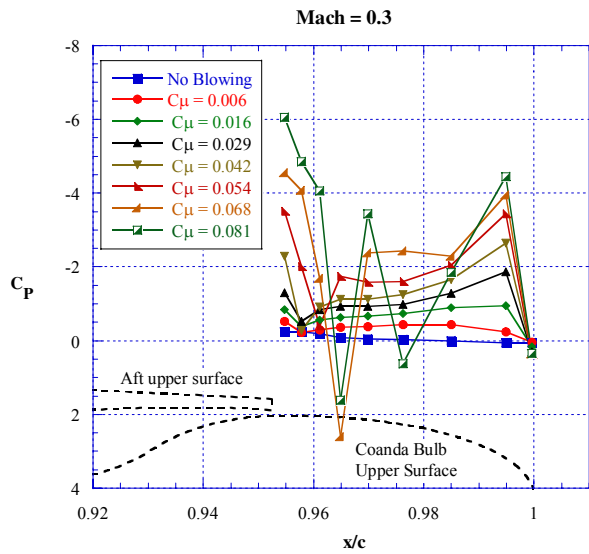


Figure 75 – Upper surface Coanda bulb pressure distribution, C_μ effect, upper slot blowing, Coanda (2.98:1), slot ($h/c = 0.0012$), $\alpha = 3^\circ$.

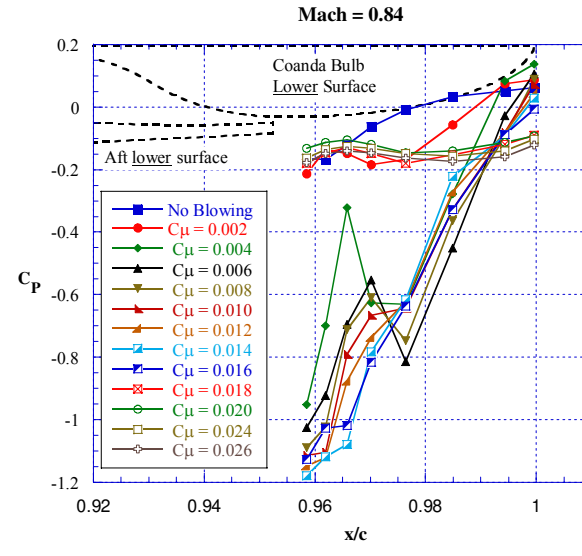
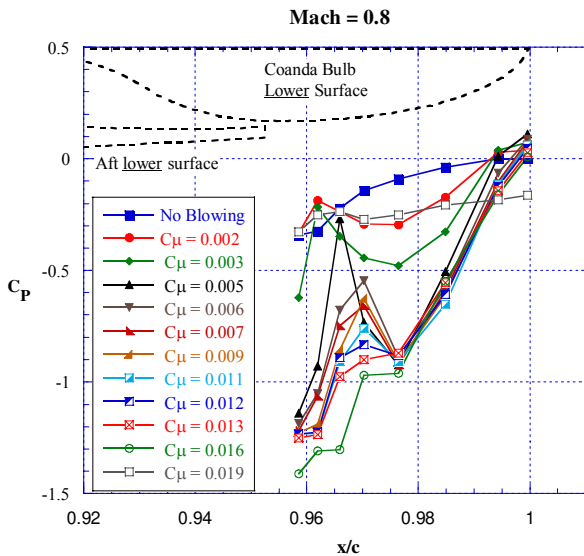
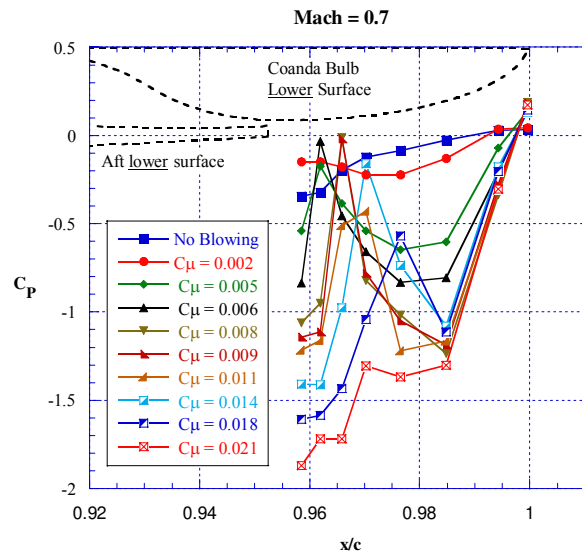
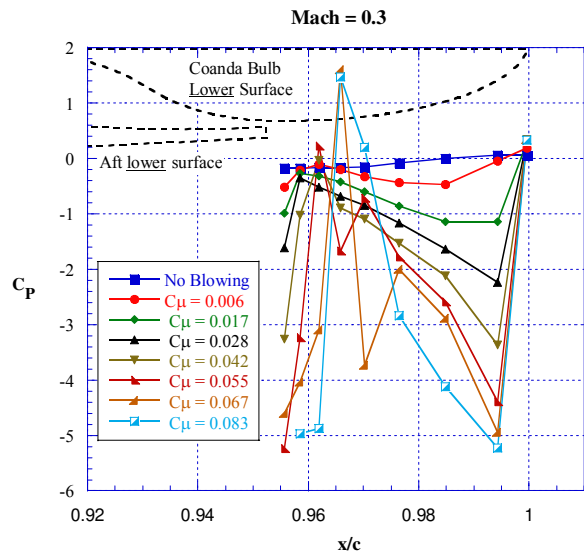


Figure 76 – Lower surface Coanda bulb pressure distribution, C_{μ} effect, lower slot blowing, Coanda (2.98:1), slot ($h/c = 0.0012$), $\alpha = 3^\circ$.

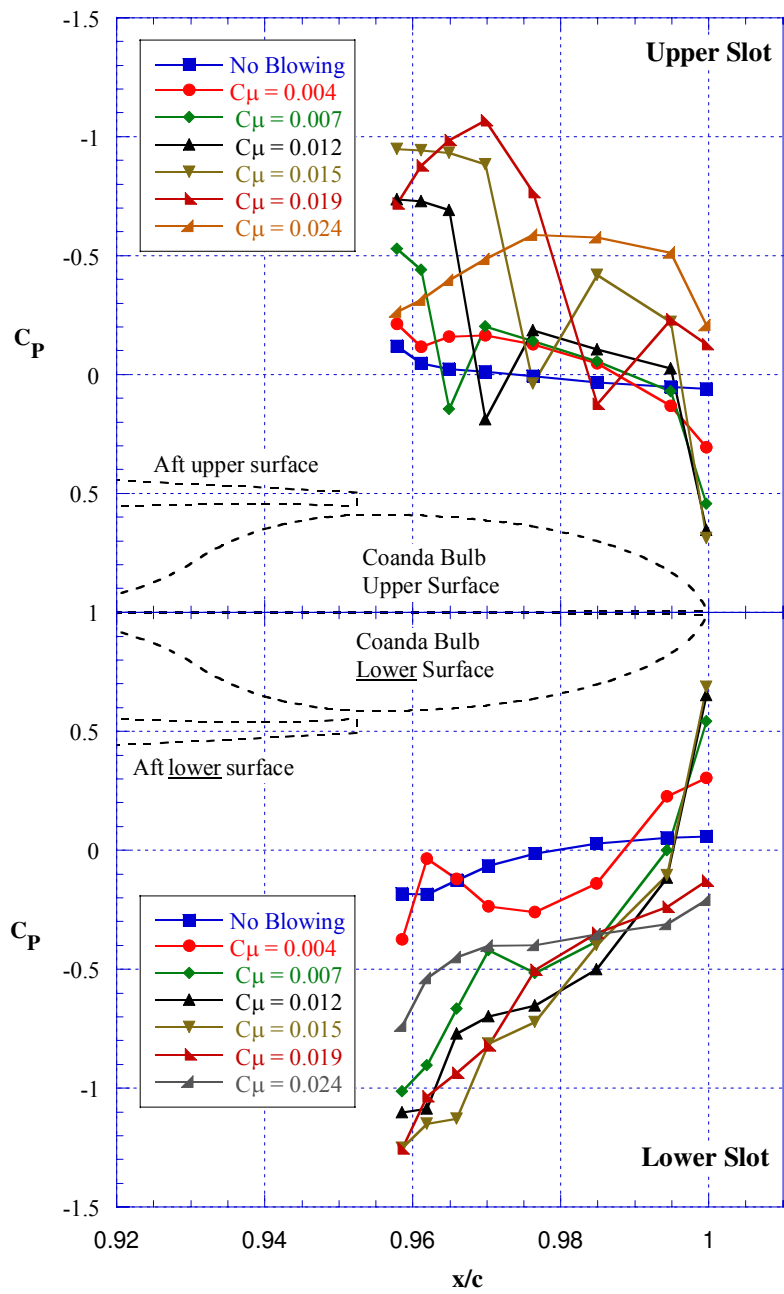


Figure 77 – Coanda bulb pressure distribution, dual slot blowing, Coanda (2.98:1), slot ($h/c = 0.0012$), Mach = 0.84, $\alpha = 3^\circ$.

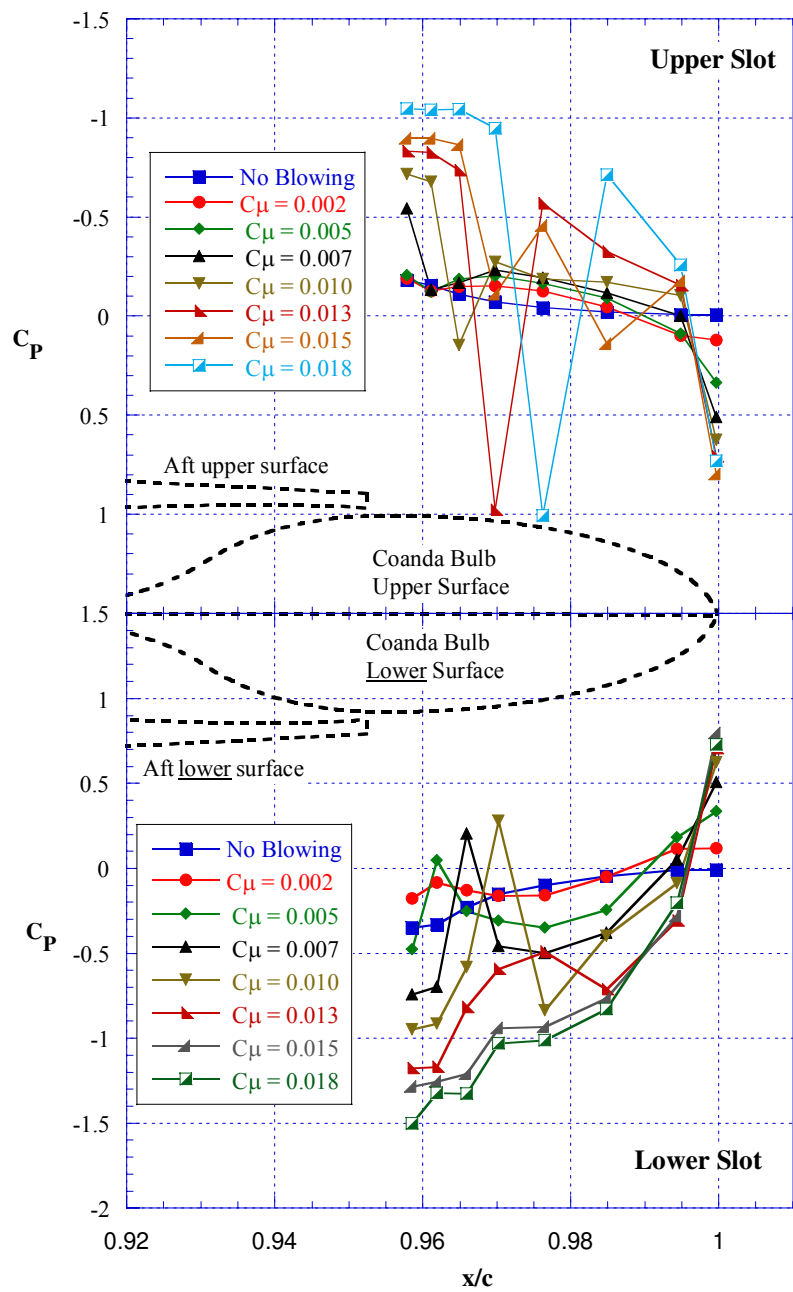


Figure 78 – Coanda bulb pressure distribution, dual slot blowing, Coanda (2.98:1), slot ($h/c = 0.0012$), Mach = 0.8, $\alpha = 3^\circ$.

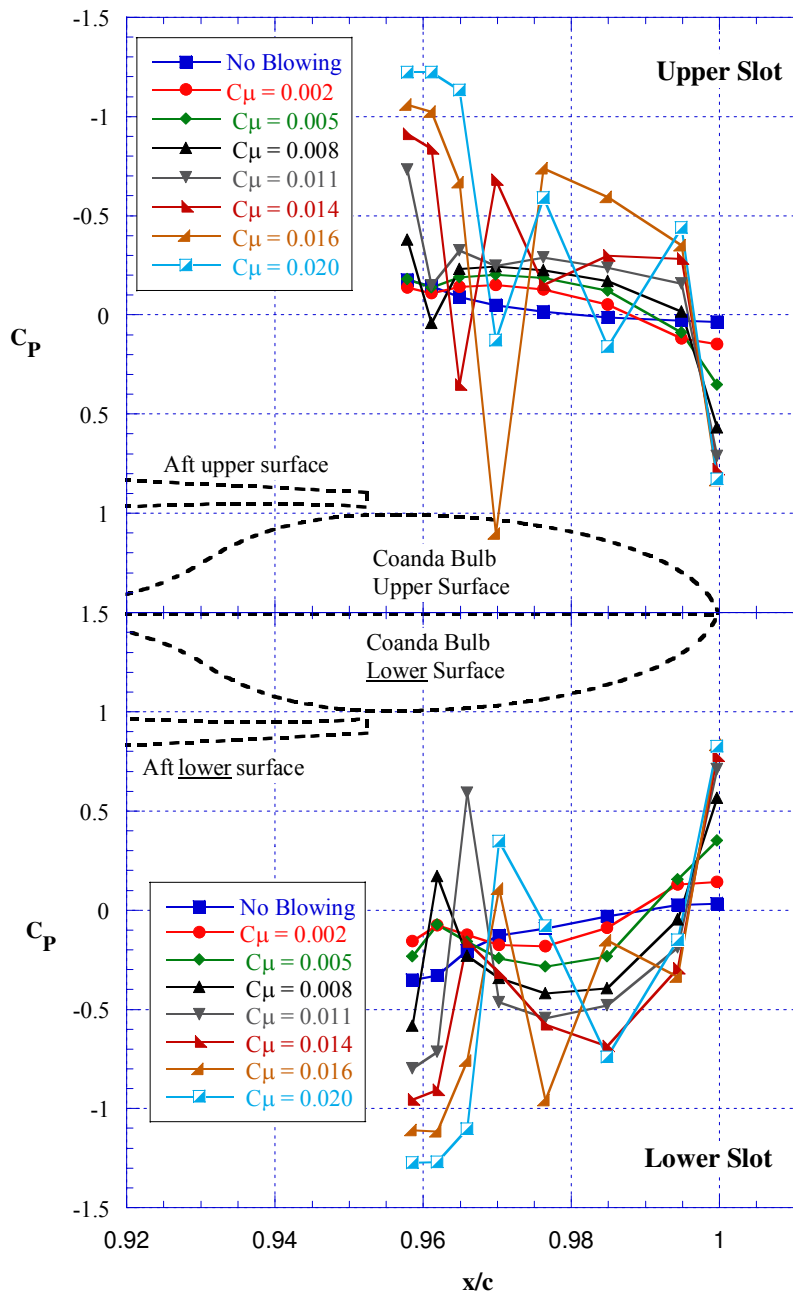


Figure 79 – Coanda bulb pressure distribution, dual slot blowing, Coanda (2.98:1), slot ($h/c = 0.0012$), Mach = 0.7, $\alpha = 3^\circ$.

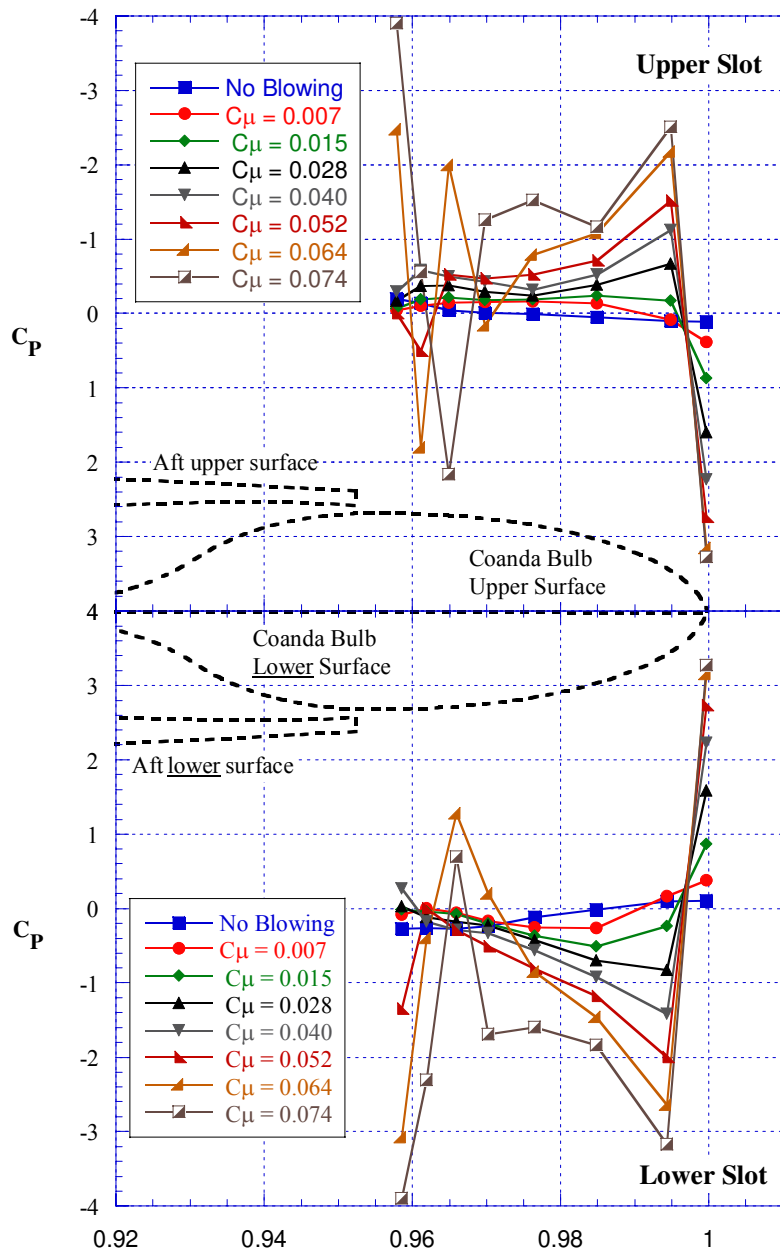


Figure 80 – Coanda bulb pressure distribution, dual slot blowing, Coanda (2.98:1), slot ($h/c = 0.0012$), Mach = 03, $\alpha = 3^\circ$.

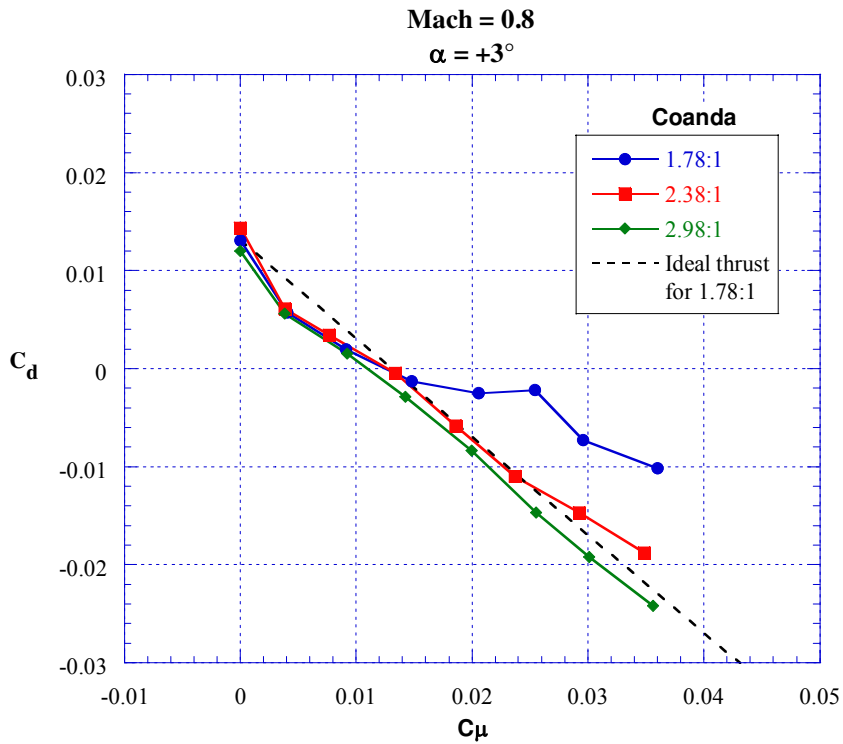
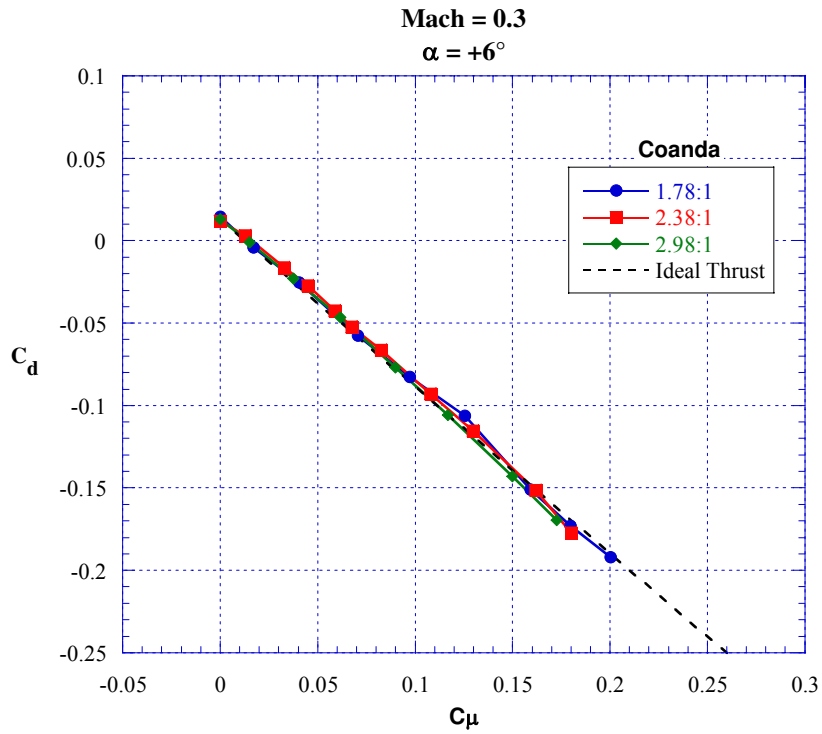


Figure 81 – C_d versus C_{μ} , Coanda surface effect, dual slot blowing, slot ($h/c = 0.0012$).

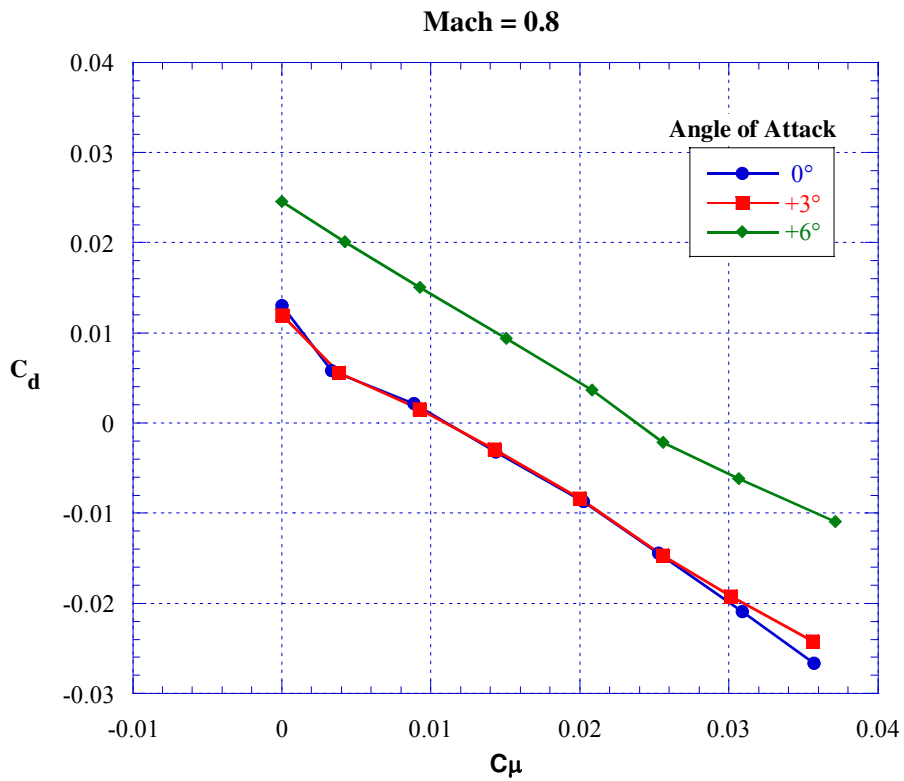
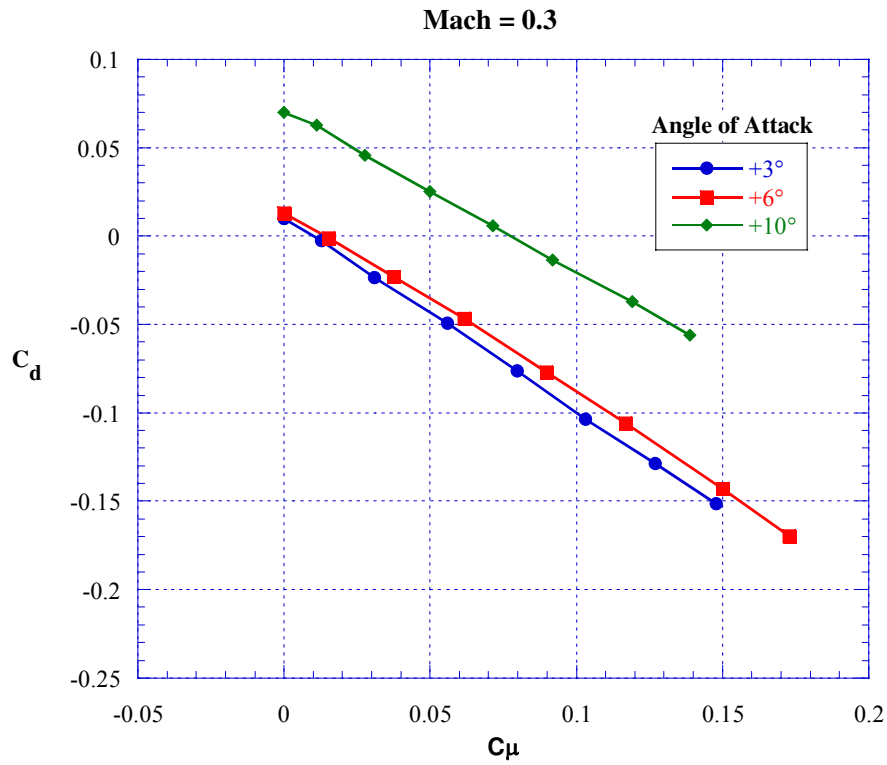


Figure 82 – C_d versus C_{μ} , angle of attack effect, dual slot blowing, Coanda (2.98:1), slot ($h/c = 0.0012$).

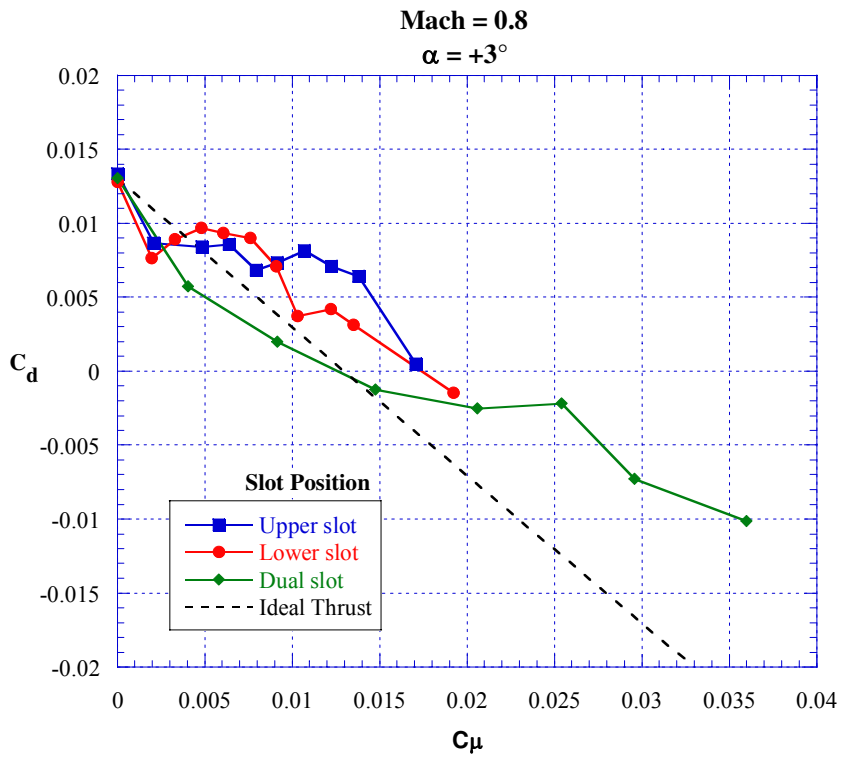
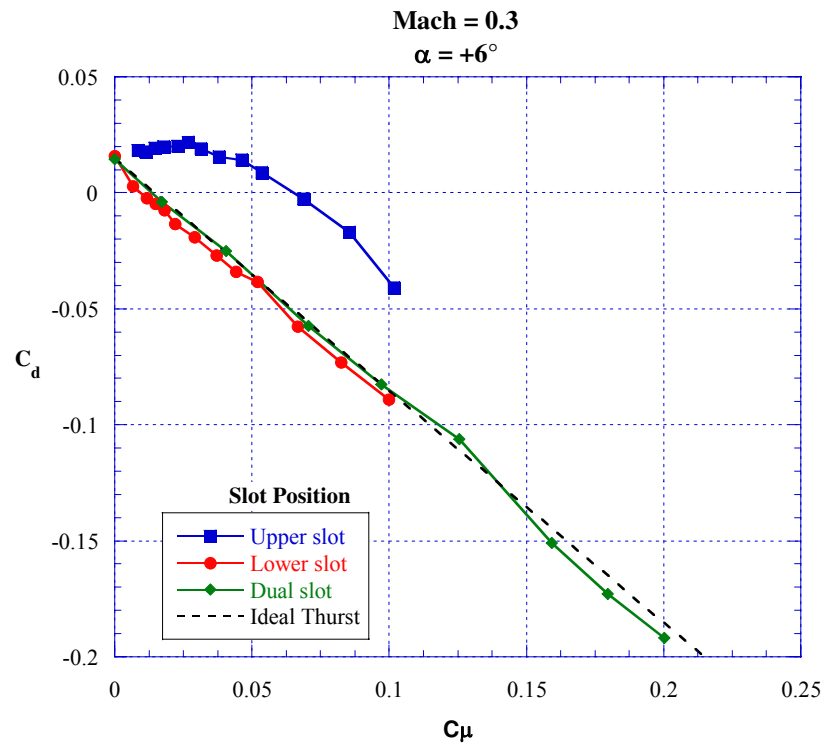


Figure 83 – C_d versus C_μ , slot position effect, Coanda (1.78:1), slot ($h/c = 0.0012$).

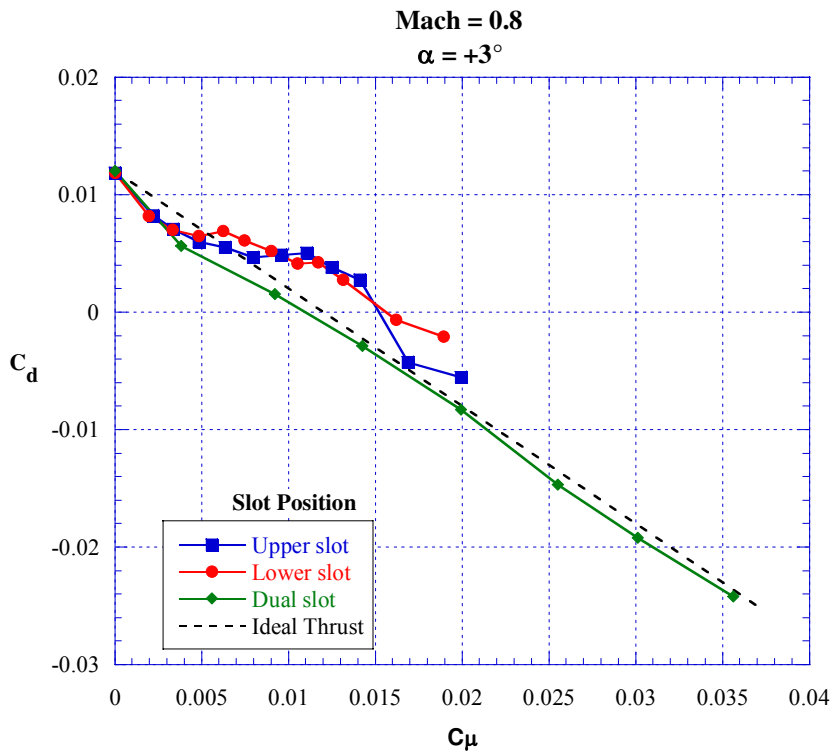
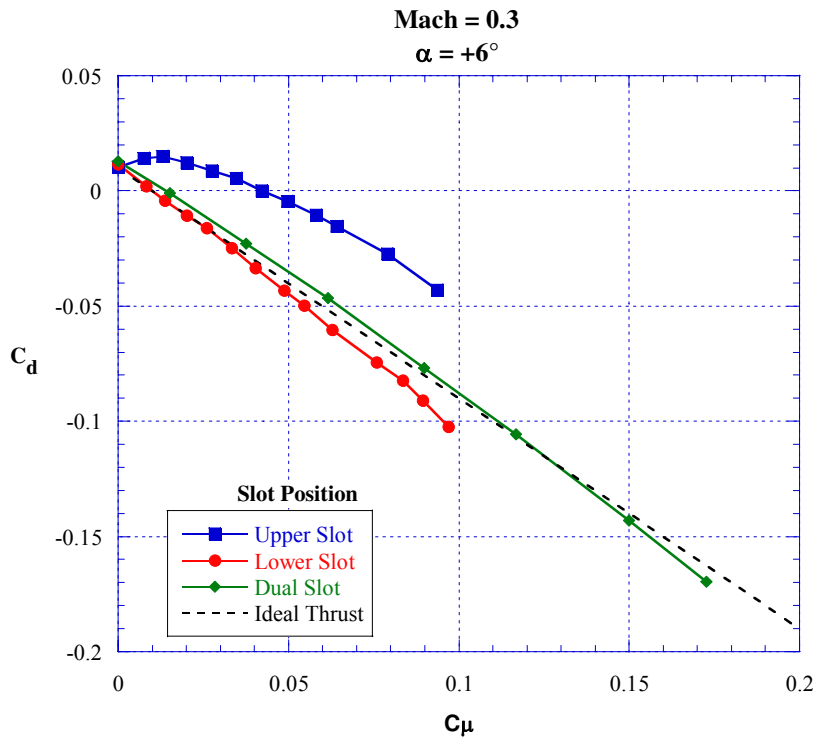


Figure 84 – C_d versus C_μ , slot position effect, Coanda (2.98:1), slot ($h/c = 0.0012$).

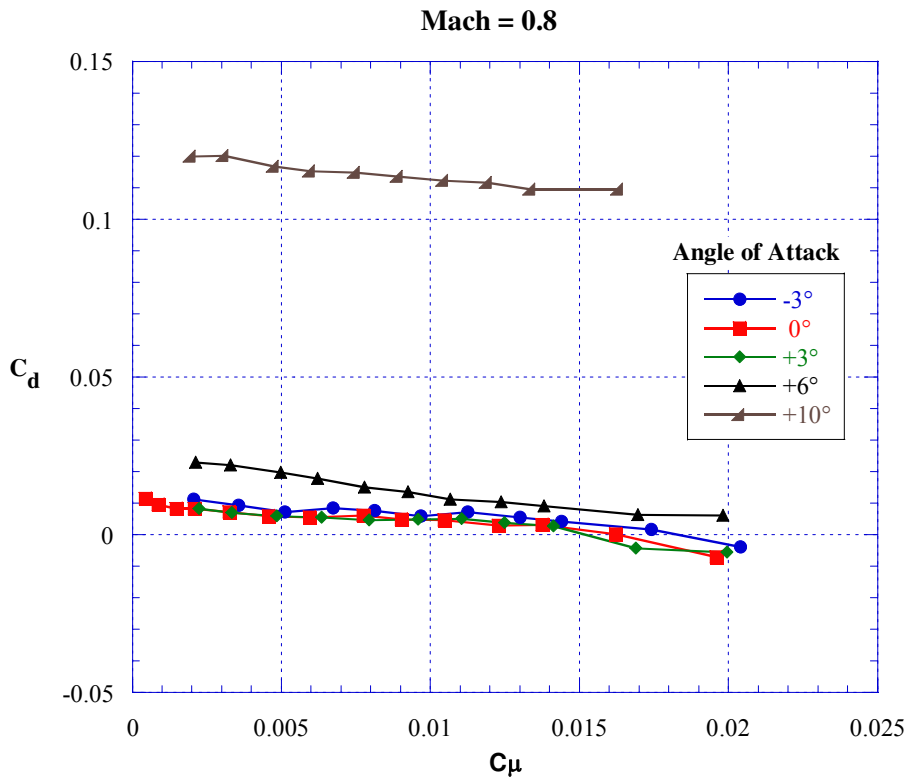
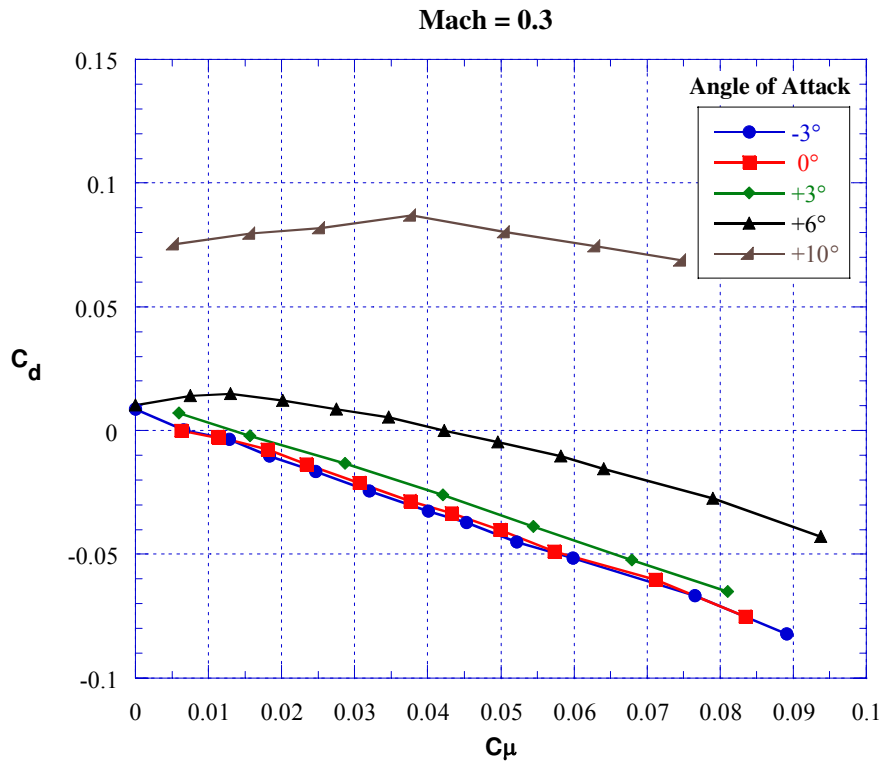


Figure 85 – C_d versus C_μ , angle of attack effect, upper slot blowing, Coanda (2.98:1), slot ($h/c = 0.0012$).

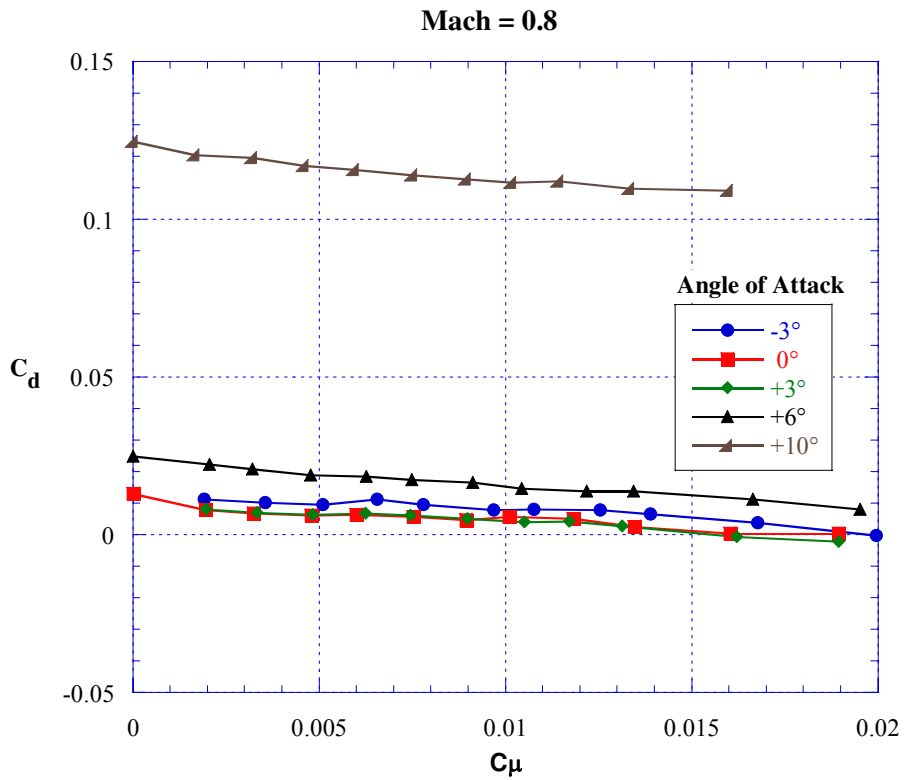
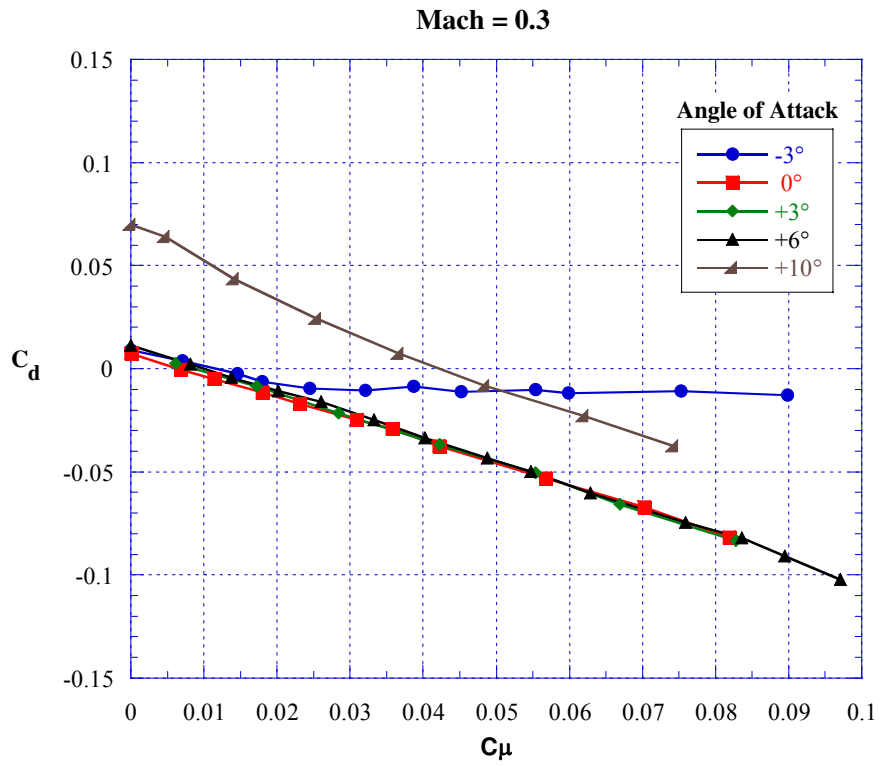


Figure 86 – C_d versus C_μ , angle of attack effect, lower slot blowing, Coanda (2.98:1), slot ($h/c = 0.0012$).

REPORT DOCUMENTATION PAGE				Form Approved OMB No. 0704-0188	
<p>The public reporting burden for this collection of information is estimated to average 1 hour per response, including the time for reviewing instructions, searching existing data sources, gathering and maintaining the data needed, and completing and reviewing the collection of information. Send comments regarding this burden estimate or any other aspect of this collection of information, including suggestions for reducing this burden, to Department of Defense, Washington Headquarters Services, Directorate for Information Operations and Reports (0704-0188), 1215 Jefferson Davis Highway, Suite 1204, Arlington, VA 22202-4302. Respondents should be aware that notwithstanding any other provision of law, no person shall be subject to any penalty for failing to comply with a collection of information if it does not display a currently valid OMB control number.</p> <p>PLEASE DO NOT RETURN YOUR FORM TO THE ABOVE ADDRESS.</p>					
1. REPORT DATE (DD-MM-YYYY)		2. REPORT TYPE		3. DATES COVERED (From - To)	
01- 03 - 2005		Technical Memorandum			
4. TITLE AND SUBTITLE Trailing Edge Blowing on a Two-Dimensional Six-Percent Thick Elliptical Circulation Control Airfoil Up to Transonic Conditions				5a. CONTRACT NUMBER	
				5b. GRANT NUMBER	
				5c. PROGRAM ELEMENT NUMBER	
6. AUTHOR(S) Alexander, Michael G.; Anders, Scott G.; Johnson, Stuart K.; Florance, Jennifer P.; and Keller, Donald F.				5d. PROJECT NUMBER	
				5e. TASK NUMBER	
				5f. WORK UNIT NUMBER 23-066-50-AE	
7. PERFORMING ORGANIZATION NAME(S) AND ADDRESS(ES) NASA Langley Research Center Hampton, VA 23681-2199				8. PERFORMING ORGANIZATION REPORT NUMBER L-19058	
9. SPONSORING/MONITORING AGENCY NAME(S) AND ADDRESS(ES) National Aeronautics and Space Administration Washington, DC 20546-0001				10. SPONSOR/MONITOR'S ACRONYM(S) NASA	
				11. SPONSOR/MONITOR'S REPORT NUMBER(S) NASA/TM-2005-213545	
12. DISTRIBUTION/AVAILABILITY STATEMENT Unclassified - Unlimited Subject Category 02 Availability: NASA CASI (301) 621-0390					
13. SUPPLEMENTARY NOTES An electronic version can be found at http://ntrs.nasa.gov					
14. ABSTRACT A wind tunnel test was conducted in the NASA Langley Transonic Dynamics Tunnel (TDT) on a six percent thick slightly cambered elliptical circulation control airfoil with both upper and lower surface blowing capability. Parametric evaluations of jet slot heights and Coanda surface shapes were conducted at momentum coefficients (Cm) from 0.0 to 0.12. Test data were acquired at Mach numbers of 0.3, 0.5, 0.7, 0.8, and 0.84 at Reynolds numbers per foot of 2.43 x 10 ⁵ to 1.05 x 10 ⁶ . For a transonic condition, (Mach = 0.8 at $\alpha = 3^\circ$), it was generally found the smaller slot and larger Coanda surface combination was overall more effective than other slot/Coanda surface combinations. Lower surface blowing was not as effective as the upper surface blowing over the same range of momentum coefficients. No appreciable Coanda surface, slot height, or slot blowing position preference was indicated transonically with the dual slot blowing.					
15. SUBJECT TERMS Circulation control; Coanda effect; Coanda trailing edge device; Control augmentation; Lift augmentation; Trailing edge blowing; Transonic; Wind tunnel test					
16. SECURITY CLASSIFICATION OF:			17. LIMITATION OF ABSTRACT	18. NUMBER OF PAGES	19a. NAME OF RESPONSIBLE PERSON
a. REPORT	b. ABSTRACT	c. THIS PAGE			STI Help Desk (email: help@sti.nasa.gov)
U	U	U	UU	134	19b. TELEPHONE NUMBER (Include area code) (301) 621-0390